Development of a cryogenic permanent magnet undulator at the ESRF

Charles Kitegi

EUROPEAN SYNCHROTRON RADIATION FACILITY
UNIVERSITE JOSEPH FOURIER – GRENOBLE

Development of a Cryogenic Permanent Magnet Undulator at the ESRF

Thèse
Pour obtenir le grade de docteur de l'Université Joseph Fourier
Discipline : Instrumentation

Présentée et soutenue publiquement par
Charles Kitegi
Le 18 décembre 2008

Composition du Jury

Johann Collot	Président
Marie-Emmanuelle Couprie	Rapporteur
Jean-Michel Ortega	Rapporteur
Joël Chavanne	Co-directeur
Dominique Givord	Membre du jury
David Lunney	Membre du jury

Abstract

In 2004, at SPring-8, Toru Hara proposed a new concept of undulator with a short period and a high field: the Cryogenic Permanent Magnet Undulator (CPMU). The purpose of this concept is to cool $Nd_2Fe_{14}B$ magnets at 150 K. This cooling allows magnets which have a higher remanence to be used, up to 40% higher than that of the magnets traditionally used in undulators.

In order to assess the technological possibility of producing such undulator, a 2 m long undulator with a 18 mm period has been proposed at the ESRF. This piece of work presents the design and the construction of this CPMU at the ESRF. First a magnetic model of the CPMU is introduced; it is based on measurements of the magnetization curve at cryogenic temperature performed at the Louis Néel Laboratory. This model forecasts an increase of the peak field of 8% and of the field integral of 0.2 Gm at around 150 K. A unique magnetic measurement bench has been developed at the ESRF. This bench allows both the in vacuum local field and field integral to be measured. Its design and construction are presented. Finally we have reviewed the measurements at room and cryogenic temperature. These measurements are in agreement with the magnetic model.

Remerciements

Ce travail a été effectué à la Facilité Européenne de Rayonnement Synchrotron (ESRF) dans le groupe élément d'insertions, sous la direction de Pascal Elleaume et de Joël Chavanne. Ils m'ont donné l'opportunité de participer à un projet innovant, ce qui a été très excitant. Leur présence, leurs conseils et leurs encouragements pendant ces années passées à l'ESRF, ont été indispensable pour mon apprentissage de la mesure magnétique et de la correction d'éléments d'insertion. Pour tout cela, je les remercie.

De nombreuses personnes ont apporté leurs compétences et permis le succès du projet. Je les remercie profondément : les magnéticiens (Joël Chavanne, Christophe Penel), les vidistes (Dominique Cognie, Michel Garrec, Michael Han, Roberto Kersevan), les cryogénistes (Michel Rossat et Franck Revol), le bureau d'étude (Damien Coulomb, Loïs Goirand, Bernard Plan, Bernard Ogier) et l'équipe magnétométrie du laboratoire Louis Néel (Do). L'aimable collaboration de chaque intervenant a été très enrichissante tant scientifiquement que humainement.

Un grand merci à Philippa Gaget et Anne Dely pour le temps passé à corriger l'anglais de mon manuscrit et leur précieuse aide dans l'organisation de ma soutenance.

Je tiens à remercier tout particulièrement le président du jury de thèse Johan Collot, les rapporteurs Marie-Emmanuelle Couprie et Jean Michel Ortega pour leur implication et leur méticulosité dans la lecture du manuscrit. Un merci chaleureux à Dominique Givord et David Lunney, j'ai été très honoré de leur participation au jury de thèse.

Cette aventure et la vie à Grenoble n'aurait pas été aussi sympathique sans la présence des gens du labo en particulier : Bertrand Cottin, Alexandra Flaven Bois, Nicolas Guillotin, Claude Joan, Fouhed Taoutaou, Thomas Perron, Reynald. Ils ont toujours été là en cas de coups durs !

Enfin je remercie mes proches et ma famille pour leur soutien. Je tiens en particulier à rendre hommage à Claire Marty pour son amour et son aide précieuse durant toutes ces années. Elle a partagé tous mes moments de doute. Sans sa présence à mes cotés, le chemin aurait été encore plus tortueux.

Table of contents

1. Introduction

Historically, scientists have widely used light and especially X-rays in many research areas, in order to probe materials and undercover their fundamental properties. Tubes were the traditional devices used to produce these X-rays until the discovery of the Synchrotron Radiation (SR). SR, i.e. the electromagnetic radiation emitted by relativistic electrons in a magnetic field, has deeply modified the production of X-rays.

SR sources

In 1898 Liénard and Wiechert first introduced the theory of SR and derived the energy loss expression of an electron in a circularly motion due to SR [1]. The practical observation of SR came 50 years later with the availability of the first ultra relativistic electron beams [2]. After World War II, particles accelerators underwent an intense development; SR was observed on a practical level in 1947 on the first electron synchrotron ever built, the 70 MeV electron synchrotron at the General Electric Company laboratory [3].

At that time, accelerators aimed at producing high energy particles for nuclear physics and high energy physics. Nevertheless it was quickly envisioned that the intense light produced in electron synchrotrons could have interesting aspects in physics [4]. Although the accelerators weren't dedicated to the SR, scientists first used the SR emitted in Bending Magnets (BM) for experiments.

Due to the increasing number of SR users, the so-called 2nd generation of SR facilities, i.e. accelerators facilities dedicated to the production of SR with BM, were built in the late seventies. In these facilities, the electron beam was stored for a few hours in a storage ring at its nominal energy. Users installed in dedicated labs located a few tens of meters away from the BM, collected the SR emitted on a continuous basis. Finally the 3rd generation of SR facilities were built in the late eighties. The locations around the world of the principal 2nd (CHESS, HASYLAB, SSRC) and 3rd generation (ESRF, SOLEIL, DIAMOND, SPring-8, APS…) SR sources are displayed in Figure 1.1 [5]. The electrons energy in SR sources varies from 1 GeV to 8 GeV.

Figure 1.1: Location of the SR facilities already in operation or planned around the world, picture from SOLEIL website (http://www.synchrotron-soleil.fr/portal/page/portal/Soleil/Liens).

The third generation of SR sources combines:

1. High current electron beam with small emittance (small size and divergence). Such an electron beam is necessary to produce a punctual and intense SR. The electron current stored in the storage ring is a few hundred of mA and the emittance is kept around the nanometer rad.

2. The usage of Insertion Devices (IDs) in order to produce very intense SR. IDs are magnetic assemblies which produce a periodic magnetic field. The field is perpendicular to the direction of the electron motion and drives the electrons in an oscillatory motion. Compared to BMs, the SR flux emitted in IDs is higher by 2 or 3 order of magnitude. IDs are installed in the so called straight sections, i.e. portions of storage ring free of magnets necessary to focus and drive the beam along the storage ring.

The European Synchrotron Radiation Facility (ESRF) belongs to the 3rd generation of SR sources. The ESRF accelerator complex is composed of a linac, a booster and the storage ring. Electron beam is first accelerated in the linac at 200 MeV. Electron beam is then transferred to the booster where it is accelerated at 6 GeV, its nominal energy. Finally electron beam is injected into the storage ring where it is stored at its nominal energy. The ESRF accelerator complex is schematically represented in Figure 1.2. It has been in operation since 1992. Table 1.1 lists the main parameters of the ESRF.

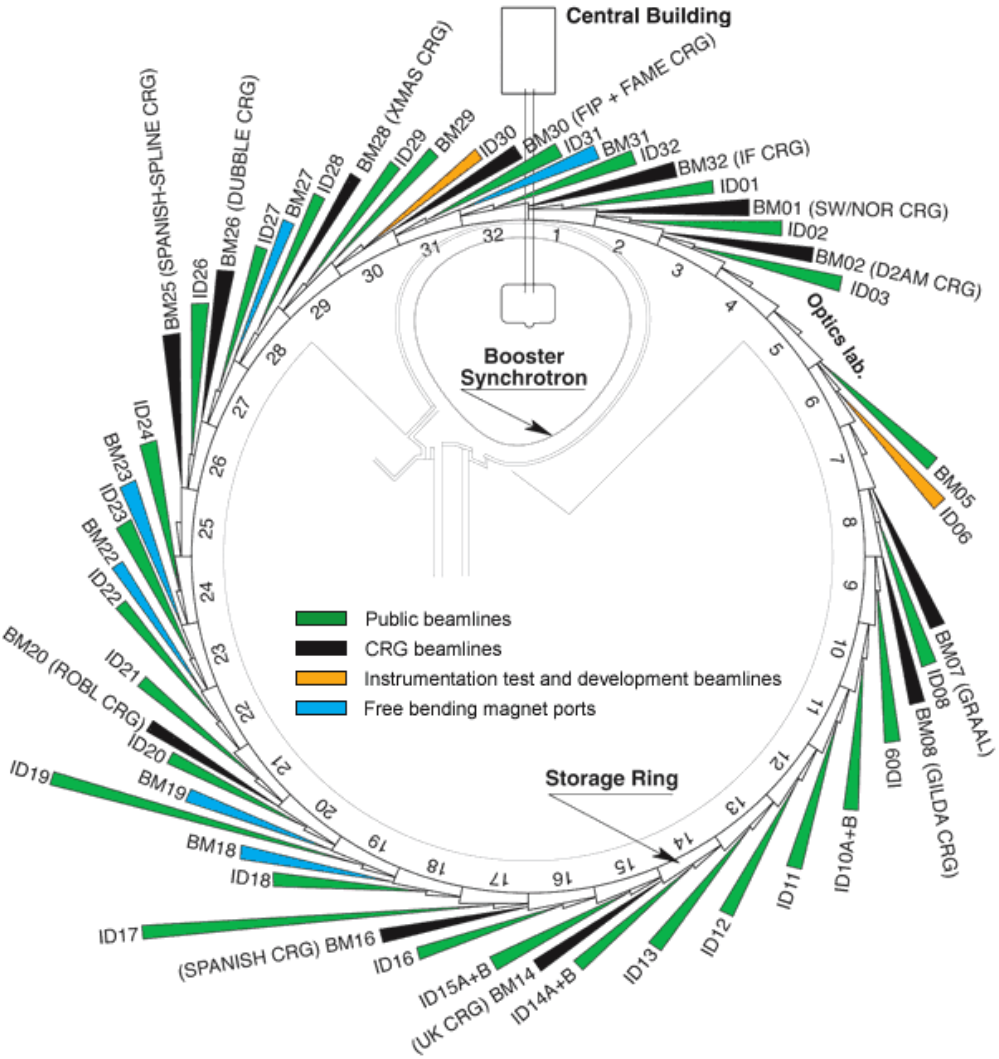

Figure 1.2: Schematic representation of the ESRF complex accelerator and the beamlines where users are installed to collect the SR.

Table 1.1: Main parameters of the electron beam in the ESRF storage ring.

	Emittance [nm rad]	RMS beam size (even/odd cells) [μm]	RMS beam divergence (even/odd cells) [μrad]
Vertical	0.04	7.9/8.3	3.2/3
Horizontal	4	402/59	10.7/90

Development of Insertions Devices

The SR emitted by ultra relativistic electrons which experience an oscillatory motion in an ID has been studied since the early years following the observation of SR at the General Electric Company laboratory [6], [7]. The SR emitted in any ID falls into two distinct regimes, the undulator or the wiggler regime. The wiggler regime is characterized by its broad spectrum; it extends from the infrared to the X-ray region. On the other side, in the undulator regime the spectrum reduces to a series of peaks with amplitude exceeding the wiggler regime by 2 orders of magnitude. This is the result of an interference process which occurs in the undulator regime.

IDs are naturally called wigglers or undulators according to the properties of the SR emitted. Undulators are short period and medium field devices while wigglers are long period and high field devices. ID technology has undergone substantial development since the early eighties together with the commercial availability of high performance magnets made of Samarium-Cobalt ($SmCo_5$, Sm_2Co_{17}) and more recently the Neodymium-Iron-Boron ($Nd_2Fe_{14}B$) magnets. Table 1.2 resumes the main properties of the undulators and wigglers installed at the ESRF.

Table 1.2: Main parameters of insertion devices installed at the ESRF.

	Period	Peak field	Energy range
Undulator	<40 mm	<1 T	1-100 keV
Wiggler	>70 mm	>1 T	1-150 keV

At the ESRF, and at the current stage of undulator technology, users are provided with a very intense photon flux at an energy level as high as 100 keV. Wigglers are used to produce intense photon flux with higher energy; they extend the spectrum up to 150 keV. As a result short period and high field undulators are necessary in order to extend the undulator spectrum to such a high energy level. In 2004, a new type of short period high field undulator was proposed at SPring-8, the Cryogenic Permanent Magnet Undulator (CPMU) [8]. It consists of operating an undulator based on Neodymium-Iron-Boron magnets cooled at cryogenic temperature. This technology allows the selection of $Nd_2Fe_{14}B$ magnets the remanence of which might be by 40% higher with respect to standard $Nd_2Fe_{14}B$ magnets used in conventional undulators. At the ESRF a full scale CPMU prototype has been build in order to investigate the technological difficulties inherent to 2 m long cooled devices and to validate the CPMU concept. This thesis reviews the design and the construction of the CPMU at the ESRF.

The chapter 2 is dedicated to the technology of insertion devices. The SR properties of wigglers and undulators are reviewed. The technological solutions to build, measure and correct IDs are presented.

The CPMU concept is introduced in the chapter 3 and the CPMU design is detailed. Emphasis is placed on the CPMU magnetostatic model and the thermal model. The selection of the temperature at which one cools the magnetic assembly is done according to the magnetostatic model. Then, the thermo-mechanical effects on the magnetic assembly are discussed.

The undulator is assembled and corrected first in air at room temperature in order to facilitate its production. In the chapter 4, we discuss the methodology used at the ESRF and present the field integral and the RMS phase error after correction.

Nevertheless it is planned to operate the CPMU at cryogenic temperature, consequently additional errors may appear at cryogenic temperature. A magnetic bench compatible with low temperature operation is therefore needed in order to validate the correction done at ambient temperature. This will be covered in the last chapter. Emphasis is given to the magnetic bench developed at the ESRF in order to perform measurements at cryogenic temperature. Finally magnetic measurements are compared to the theoretical model.

2. Properties and use of Insertion devices

In 3rd generation sources, insertion devices are installed on straight sections in order to deliver an intense radiation to users installed on beamlines. In this chapter we describe the SR properties of an insertion device. The technology to design, measure and correct an insertion device is also introduced. Most common IDs installed at the ESRF are described. First we will review the general physical quantities of electromagnetic radiation.

2.1. Synchrotron radiation

In this subchapter we will briefly review the electromagnetic field which an accelerated single relativistic electron produces. Afterwards we derive from the electromagnetic field the physical quantities of SR.

2.1.1. Origin of the Synchrotron radiation

Here we consider a source that produces electromagnetic field. The source radiates when the produced electromagnetic field carries an irreversible flow of energy away from the source, "to infinity". One deduces from a basic consideration of the Poynting vector that a source shall emit an electromagnetic field falling off like $1/r$ in order to emit radiation. An accelerated electron emits such an electromagnetic field [9]. More generally we call Synchrotron Radiation (SR) the radiation produced by an ultra relativistic charge accelerated in a magnetic field.

Electromagnetic field emitted by an ultra relativistic electron

Here we consider an ultra relativistic electron and a stationary observer, the electron and the observer are represented in Figure 2.1. We note $\vec{r}(\tau)$ the electron position at time τ and $\vec{n}(\tau)$ the unit vector which points toward the fixed observer located at the fixed position $\vec{R}$. D is the distance between the fixed observer and the electron, θ is the angle between the unit vector $\vec{n}(\tau)$ and the electron velocity $c\vec{\beta}(\tau)$.

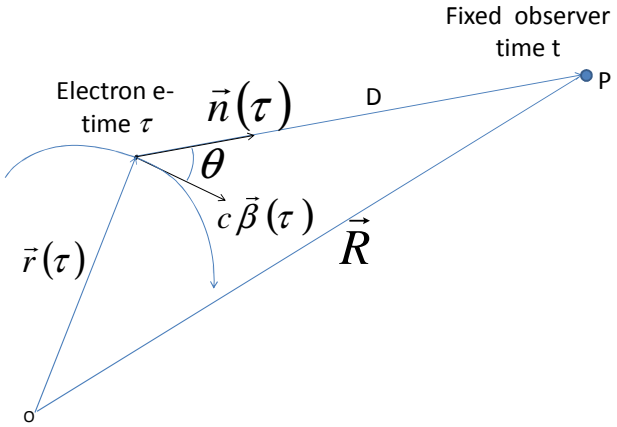

Figure 2.1: Electron and observer time.

The electron emits an electromagnetic field that propagates at the speed of light. Thus, the observer sees at time t, the electromagnetic field emitted at the earlier time τ. This time τ is the so called retarded time. The relation between the observer time and the retarded time is:

$$t = \tau + \frac{\left|\vec{R} - \vec{r}(\tau)\right|}{c} \tag{2.1}$$

The expression obtained for the electromagnetic field at the observer position and time is known as the Liénard-Wiechert field [9]:

$$\begin{aligned}\vec{E}(\vec{R},t) &= \vec{E}_c(\vec{R},t) + \vec{E}_r(\vec{R},t)\\ \vec{B}(\vec{R},t) &= \frac{\vec{n}\times\vec{E}(\vec{R},t)}{c}\end{aligned} \tag{2.2}$$

With:

$$\begin{aligned}\vec{E}_c(\vec{R},t) &= \frac{e}{4\pi\epsilon_0}\left(\frac{\vec{n}-\vec{\beta}}{D^2\gamma^2\left(1-\vec{n}\vec{\beta}\right)^3}\right)_{ret}\\ \vec{E}_r(\vec{R},t) &= \frac{e}{4\pi\epsilon_0 c^2}\left(\frac{\vec{n}\times\left(\vec{n}-\vec{\beta}\right)\times d\vec{\beta}/d\tau}{D\left(1-\vec{n}\vec{\beta}\right)^3}\right)_{ret}\end{aligned} \tag{2.3}$$

The subscript "ret" in equation (2.3) states that the expression in bracket is computed at the retarded time τ, this being the time at which the field was emitted. Consequently the computation of the electromagnetic field at the observer time and location $(\vec{R},t)$ requires knowledge of the electron position and velocity at the retarded time τ. Actually the retarded position and the velocity can be determined only in rare physical cases. Computing these values is the main difficulty of the Liénard-Wiechert field computation.

The electric and the magnetic fields are perpendicular to each other. Moreover the electric field is the sum of two different contributions:

- $\vec{E}_r$ is the radiated field or the acceleration field. This contribution vanishes for constant velocity. The synchrotron radiation arises from this contribution as it decays as *1/D*. Any ultra relativistic charged particle emits radiation whenever this particle is deflected, accelerated or decelerated.
- $\vec{E}_c$ is the velocity field or the Coulomb field. The field decays as $1/D^2$. Thus, the radiated power associated to this contribution stays in the electron vicinity. Because of the dependence order with respect to *D,* we ignore this contribution for large distances and we only consider the radiated field $\vec{E}_r$.

Equation (2.1) is useful to characterize some properties of SR emitted by ultra relativistic electrons. The ratio between the observer time and the retarded time is:

$$\frac{dt}{d\tau} = 1-\vec{n}(\tau)\cdot\vec{\beta}(\tau) = 1-\beta\cos\theta \tag{2.4}$$

According to equations (2.3) and (2.4), the maximum field is radiated when:

$$\frac{dt}{d\tau}\to 0 \tag{2.5}$$

This maximum is achieved for small θ, when the electron velocity points towards the observer. For an ultra relativistic electron, the time ratio then reduces to:

$$\frac{dt}{d\tau} = \frac{1}{2}\cdot\left(\frac{1}{\gamma^2}+\theta^2\right) \tag{2.6}$$

γ is the ratio of the electron energy E to its energy at rest m_0c^2:

$$\gamma = \frac{E}{m_0c^2} = \sqrt{\frac{1}{1-\beta^2}} \tag{2.7}$$

According to equation (2.6), the radiated field is maximal as far as the angle θ is small compared to $1/\gamma$. For instance, at the ESRF the energy electron is 6 GeV, we obtain $\gamma = 11742$ and

$\beta = 1 - 3.6 \cdot 10^{-9}$. The cone aperture is then a few thousandths of radians. Finally a deflected ultra relativistic electron emits a highly collimated radiation in a forward direction; the radiation is emitted in a narrow cone the aperture angle of which is approximately $1/\gamma$.

Laboratory frame and small angle approximation

In the following sections, we discuss the synchrotron radiation emitted in different insertion devices. First we will introduce the notations used to describe in the laboratory frame the electron motion and the direction of the SR emission, then we will detail the approximations made to compute the synchrotron radiation in insertion devices.

We will restrict our discussion to the "far field approximation" so that we ignore the velocity field. In the far field approximation we have:

- The magnetic and the electric field are perpendicular to the direction of observation.
- The observation direction $\vec{n}$ is independent of τ.

The electron motion in the laboratory frame is displayed in Figure 2.2. We assume that the observer direction and the electron velocity make a small angle with the Os axis which is called the longitudinal axis. Ox is defined as the axis in the horizontal plane which is perpendicular to the longitudinal axis Os ($Ox \perp Os$). Finally we define the Oz axis in the vertical plane so that the laboratory frame $Oxzs$ is direct.

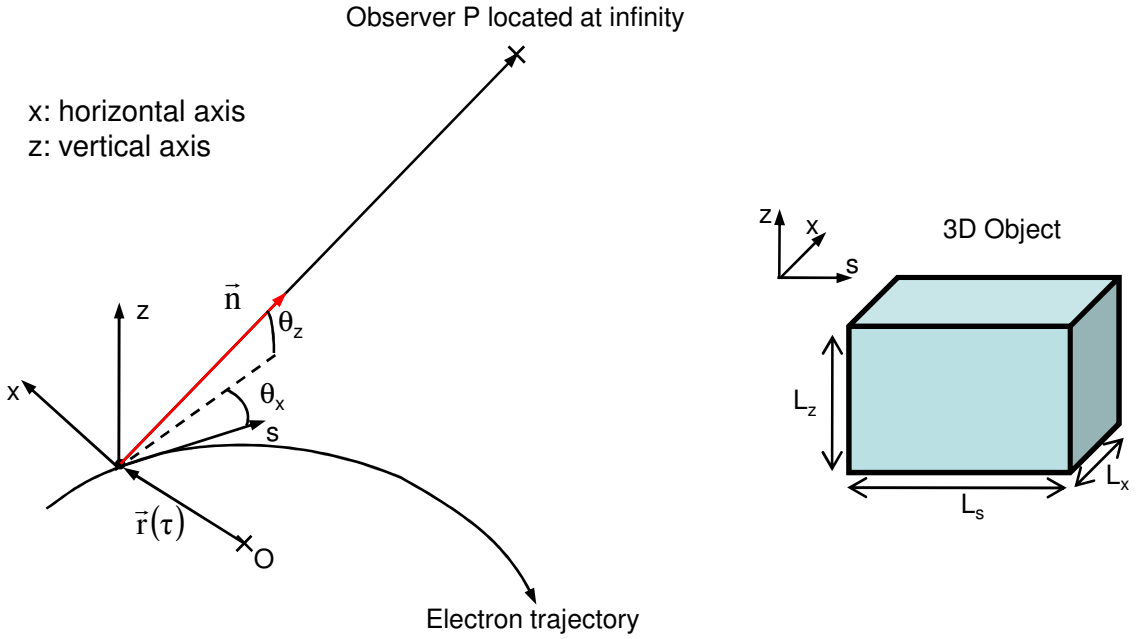

Figure 2.2: Electron motion in the laboratory frame. In the laboratory frame we note (L_x, L_z, L_s) the dimensions of any 3D object.

We note (L_x, L_z, L_s) the dimensions of any object in the laboratory frame. In the small angle approximation, the unit vector $\vec{n}$ and the electron velocity $\vec{\beta}$ are written as follows:

$$\begin{aligned} \vec{n} &\approx \left(\theta_x, \theta_z, 1 - \frac{\theta_x^2 + \theta_z^2}{2}\right) \\ \vec{\beta} &\approx \left(\beta_x, \beta_z, 1 - \frac{1 + \gamma^2\beta_x^2 + \gamma^2\beta_z^2}{2\gamma^2}\right) \end{aligned} \tag{2.8}$$

θ_x and θ_z are respectively the angle between $\vec{n}$ and axis $\vec{s}$ measured in the Oxs and the Ozs planes.

2.1.2. SR characterization

Hereafter we will present some useful notions, the spectral angular flux, polarization and brilliance. These characterize the synchrotron radiation emitted by an electron beam. The spectral angular flux quantifies the available amount of energy in a given direction. Since the electromagnetic field is a vector quantity, the SR interaction with a material may depend on the electromagnetic field orientation which is characterized by its polarization. Finally one will introduce the brilliance; this is the density function of photons in phase space.

We first derive the SR properties assuming a mono energetic filament electron beam. Mono energetic filament electron beam is an ideal beam where:

- All the electrons have the same energy and travel along the same trajectory.
- Electrons have random longitudinal positions.

The first condition ensures that two different electrons would emit similar field while the second one cancels any interference process between the electric fields which are emitted by different electrons.

However a mono energetic filament beam is an approximation, an ideal beam. Real beams in storage rings have a finite size, a divergence and an energy spread; beams are said to be thick. Thus electrons in storage ring have neither the same trajectory nor the same energy. The properties of synchrotron radiation which thick electron beam emits, is overviewed the sub-section "Thick beam with energy spread".

Angular spectral flux

Here we consider a filament mono energetic electron beam with intensity I. The total energy per unit solid angle radiated in the direction $\vec{n}$ is for each electron:

$$\frac{dW}{d\Omega}(\vec{n}) = \lim_{D\to\infty}\left(\varepsilon_0 c \int_{-\infty}^{+\infty} D^2\left|\vec{E}(\vec{R},t)\right|^2 dt\right) \tag{2.9}$$

The electric field $\vec{E}(\vec{R},\omega)$ in the spectral domain is the Fourier transform of the electric field $\vec{E}(\vec{R},t)$. In the far field approximation one has:

$$\vec{E}(\vec{R},\omega) = \frac{1}{2\pi}\int_{-\infty}^{+\infty}\vec{E}\,(\vec{R},t)exp(i\omega t)dt = -\frac{ie}{2\varepsilon_0 cD}exp\left(i\frac{\omega}{c}\vec{n}\cdot\vec{R}\right)\vec{H}(\vec{n},\omega) \tag{2.10}$$

With:

$$\vec{H}(\vec{n},\omega) = \frac{\omega}{2\pi}\int_{-\infty}^{+\infty}(\vec{n}-\vec{\beta})exp\left(i\omega\left(\tau-\frac{\vec{n}\cdot\vec{r}}{c}\right)\right)d\tau \tag{2.11}$$

Using the Parseval theorem, we can compute the radiated energy per unit solid angle with the electric field in the spectral domain. The radiated energy per unit solid angle is then:

$$\frac{dW}{d\Omega}(\vec{n}) = \frac{e^2}{4\pi\varepsilon_0 c}\int_0^{+\infty}\left|\vec{H}(\vec{n},\omega)\right|^2 d\omega \tag{2.12}$$

For a filament electron beam, we define the power generated per solid angle in the observer direction as the product of the energy radiated per unit angle multiplied by the total number of electrons per second I/e:

$$\frac{dP}{d\Omega}(\vec{n}) = \frac{\alpha hI}{2\pi e}\int_0^{+\infty}\left|\vec{H}(\vec{n},\omega)\right|^2 d\omega \tag{2.13}$$

α is the fine constant structure ($\alpha = e^2/(2\varepsilon_0 hc) \cong 1/137$) and h the Planck's constant. Finally the power per unit solid angle and per unit frequency is:

$$\frac{d^2P}{d\Omega d\omega}(\vec{n},\omega) = \frac{\alpha h I}{2\pi e}\left|\vec{H}(\vec{n},\omega)\right|^2 \tag{2.14}$$

For the radiation being emitted in photons with energy $\epsilon = h\omega/2\pi$, and a photon flux ϕ, the photons carry the power:

$$P = \phi\epsilon \tag{2.15}$$

Finally we deduce from (2.14) and (2.15), the number of photons per second per solid angle per relative frequency bandwidth emitted in the direction $\vec{n}$:

$$\frac{d^2\phi}{d\Omega\, d\omega/\omega}(\vec{n},\omega) = \frac{\alpha I}{e}\left|\vec{H}(\vec{n},\omega)\right|^2 \tag{2.16}$$

This quantity is usually called the angular spectral flux and is proportional to the squared vector field $\vec{H}(\vec{n},\omega)$. The spectral flux $\frac{d\phi}{d\omega/\omega}(\omega)$ represents the number of photons emitted per second per relative frequency bandwidth:

$$\frac{d\phi}{d\omega/\omega}(\omega) = \frac{\alpha I}{e}\int_{-\infty}^{+\infty}\int_{-\infty}^{+\infty}\left|\vec{H}(\theta_x,\theta_z,\omega)\right|^2 d\theta_x d\theta_z \tag{2.17}$$

The electromagnetic field is a vector quantity. Its interaction with a material might depend on the electric field orientation that is characterized by its polarization. We discuss now the polarization of an electromagnetic field.

Polarization

Any electromagnetic field may be broken up into a sum of monochromatic plane waves [10]. Thus we will first review the different polarization state of a planar monochromatic wave. We will consider a monochromatic electromagnetic wave with an angular frequency ω and wave vector $\vec{k}$ parallel to the observer direction. The electric field is contained in the plane perpendicular to the wave vector. The electric field describes a closed curve in the plane. The geometrical shape of the closed curve and the sense of the field rotation in the plane define the polarization state of the field. Generally the field extremity describes an ellipse in the wave plane; the polarization is elliptical. In some cases the ellipse is reduced to a circle/line, the wave has a circular/linear polarization. The polarization states are represented in Figure 2.3.

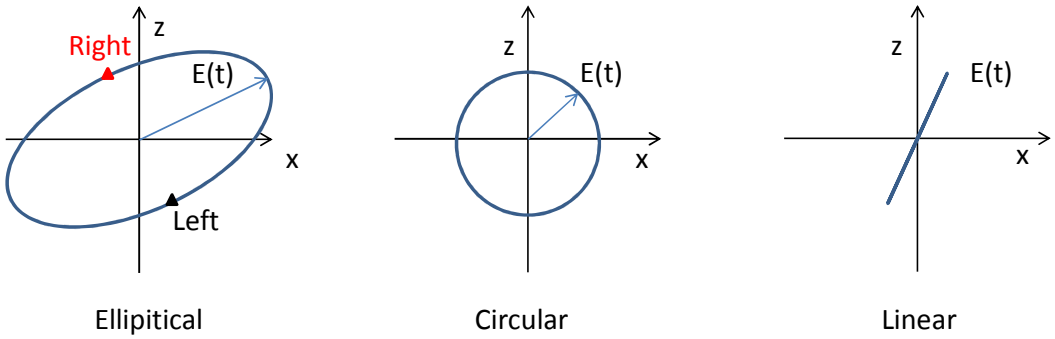

Figure 2.3: Different polarization states.

We can split up the wave polarization into two vectors. These two vectors form a polarization basis. The most commonly used bases are listed in Table 2.1. All these bases are made up of two orthogonal unit vectors.

Table 2.1: Principal polarization bases.

Vertical and horizontal polarization	Crossed linear polarization	Right and left handed circular polarization
$(\vec{u}_x, \vec{u}_z)$	$(\vec{u}_{45}, \vec{u}_{-45})$ $\vec{u}_{\pm 45} = \frac{\vec{u}_x \pm \vec{u}_z}{\sqrt{2}}$	$(\vec{u}_r, \vec{u}_l)$ $\vec{u}_{r\atop l} = \frac{\vec{u}_x \pm i\vec{u}_z}{\sqrt{2}}$

If $\vec{u}$ represents a polarization vector, the spectral angular flux associated with this polarization state is defined as:

$$\frac{d^2\phi}{d\Omega\, d\omega/\omega}(\vec{n}, \omega, \vec{u}) = \frac{\alpha I}{e}\left|\vec{H}(\vec{n}, \omega) \cdot \vec{u}^*\right|^2 \tag{2.18}$$

$\vec{u}^*$ is the $\vec{u}$ complex conjugate. One could choose any of the three bases listed in Table 2.1 in order to compute the flux I_u with polarization unit vector $\vec{u}$. For instance we note I_x (I_z) the flux with horizontal (vertical) polarization. Similarly we note I_{45}, I_{-45}, I_r and I_l the fluxes with crossed linear polarization and right and left handed circular polarization.

Stokes developed a polarization characterization based on the measurement of intensity in the three polarization basis. One defines the Stokes parameters as [11]:

$$\begin{aligned} s_0 &= I_x + I_z \\ s_1 &= I_x - I_z \\ s_2 &= I_{45} - I_{-45} \\ s_3 &= I_r - I_l \end{aligned} \tag{2.19}$$

The first Stokes parameter is positive and measures the total intensity. The others measure the balance of the intensity measured in the three bases introduced above. The Stokes parameters s_1, s_2, s_3 vary from -1 to 1 and are not independent. For a fully polarized light, they satisfy the relation:

$$s_0^2 = s_1^2 + s_2^2 + s_3^2 \tag{2.20}$$

We define the polarization rates I_1, I_2, I_3 as the Stokes parameters normalized to the total intensity.

$$I_1 = s_1/s_0 \qquad I_2 = s_2/s_0 \qquad I_3 = s_3/s_0 \tag{2.21}$$

The equality in equation (2.20) is broken whenever the wave is partially depolarized. For instance, the natural light is fully depolarized. Its polarized fluxes I_x, I_z, I_{45}, I_{-45}, I_r and I_l are equal consequently the Stokes parameters s_1, s_2, s_3 are equal to zero. It is then useful to define the polarization degree p as:

$$p = \sqrt{\frac{s_1^2 + s_2^2 + s_3^2}{s_0^2}} \tag{2.22}$$

Its value varies from 0 to 1. The polarization of the synchrotron radiation emitted in the different insertion devices is discussed in section 2.2.

Spectral brilliance

The spectral brilliance or the brilliance $\mathcal{B}(s, \vec{y}, \vec{y}', \omega, \vec{u})$ of a SR source is the phase space density of the photon flux. It measures the number of photons with the frequency ω and the polarization state $\vec{u}$ at the position $\vec{y} = (x, z)$ which propagates in the direction $\vec{y}' = (\theta_x, \theta_z)$. The brilliance unit is the number of photons per second, per 0.1% spectral bandwidth, per unit solid angle and per unit source size.

The brilliance is invariant in any ideal optical photon beam transport system such as a drift space or a lens free of geometrical aberrations; it is a fundamental property of SR source.

By definition any information about the SR emitted in a source is contained in this quantity so that one derives any other SR quantity from the brilliance. For instance the spectral angular flux $\frac{d^2\phi}{d\Omega d\omega/\omega}(\vec{y}', \omega, \vec{u})$ is related to the brilliance according to:

$$\frac{d^2\phi}{d\Omega\, d\omega/\omega}(\vec{y}', \omega, \vec{u}) = \int_{-\infty}^{+\infty}\int_{-\infty}^{+\infty} \mathcal{B}(s, \vec{y}, \vec{y}', \omega, \vec{u})\, d^2\vec{y} \tag{2.23}$$

K. J. Kim first introduced a general definition of the brilliance from the electric $\vec{E}(\vec{y}, \omega)$ field by means of the Wigner distribution function [12], [13]. P. Elleaume showed that with such definition, the brilliance is expressed in terms of the dimensionless vector $\vec{H}$ [14]:

$$\begin{aligned}\mathcal{B}(s, \vec{y}, \vec{y}', \omega, \vec{u}) = \frac{\alpha I}{e}\left(\frac{\omega}{2\pi c}\right)^2 \int_{-\infty}^{+\infty}\int_{-\infty}^{+\infty} \left(\vec{H}\left(\vec{y}' + \frac{\vec{\xi}'}{2}, \omega\right)\vec{u}^*\right)\left(\vec{H}^*\left(\vec{y}' - \frac{\vec{\xi}'}{2}, \omega\right)\vec{u}\right) \\ \times \exp\left(-i\frac{\omega}{c}(\vec{y}' + s\vec{y}')\vec{\xi}'\right) d^2\vec{\xi}'\end{aligned} \tag{2.24}$$

Thick beam with energy spread

In the storage ring, electrons are grouped in bunches [15]. It can be demonstrated from the equation of electron motion in a storage ring that the longitudinal motion of an electron beam is decoupled from the transverse one. We will therefore describe the longitudinal and the transversal beam distribution independently.

Longitudinal positions of electrons in a bunch are uncorrelated and follow a Gaussian distribution with an RMS length σ_s [16]. We first assume a mono energetic filament beam but with a Gaussian longitudinal distribution. It can be demonstrated that electrons emit an incoherent electric field with the wavelength λ if one has [14]:

$$\sigma_s \gg \frac{\lambda}{2\pi}\sqrt{\ln(N_e - 1)} \tag{2.25}$$

N_e is the number of electrons per bunch. At the ESRF, the spectrum range extends from 0.1 eV to 100 keV. This corresponds to a wavelength smaller than a millimetre. Since the electron bunch length is in the order of a few millimetres, one may ignore the interference process in SR emitted by thick electron beams.

In the transverse plane, a thick electron beam has a finite size. Furthermore electrons do not have the same energy. We note γ the energy of an electron and γ_0 the average energy; the relative energy deviation δ is:

$$\delta = \frac{\gamma - \gamma_0}{\gamma_0} \tag{2.26}$$

Because of the finite beam size and the energy deviation, electrons may have different trajectories and velocities so that different electrons in thick beam emit different $\vec{E}(\vec{R}, \omega)$. A description of transverse beam distribution is required to properly compute the SR properties of a thick beam; one then uses a density function $\rho(\vec{Y}, \vec{Y}', s, \delta)$. This function describes at the position s, the electron distribution in phase space $\vec{Y} = (x, z), \vec{Y}' = (\beta_x, \beta_z)$, the density function depends also on the energy deviation δ. For a thick beam, one derives any quantity $\mathcal{Q}_t$ introduced previously (the electric field, the angular flux, the flux, the brilliance…) from the filament beam quantity $\mathcal{Q}$. $\mathcal{Q}_t$ is the convolution product between $\mathcal{Q}$ and the density function $\rho(\vec{Y}, \vec{Y}', s, \delta)$:

$$\mathcal{Q}_t(\vec{y},\vec{y}',\omega,\vec{u}) = \int \mathcal{Q}\left((\vec{y}-\vec{Y})(1+\delta),(\vec{y}'-\vec{Y}')(1+\delta),s,\frac{\omega}{(1+\delta)^2},\vec{u}\right) \times (1+\delta)^4 \rho(\vec{Y},\vec{Y}',s,\delta) d^2\vec{Y} d^2\vec{Y}' d\delta \quad (2.27)$$

In conclusion, the vector field $\vec{H}(\vec{n},\omega)$ is of primary interest and a powerful parameter. Indeed knowledge of this is sufficient to characterize the SR emitted by a filament electron beam. It is clear from equation (2.18) that the vector field $\vec{H}(\vec{n},\omega)$ contains the polarization state and the spectral flux information. Moreover the vector field also contains both the near and the far field information [14]. Dealing with thick beam requires the additional use of the electron beam density function.

2.2. Synchrotron radiation emitted in ID

Hereafter we will look at the properties of radiation which is emitted by an electron beam throughout an insertion device. The SR properties are derived from the vector field $\vec{H}(\vec{n},\omega)$. The inspiration for this section mainly comes from the lecture given by P. Elleaume and R. P. Walker in [14], [17], [18] and [19].

Ultra relativistic electron beam emits SR whenever one bends its trajectory. A constant magnetic field is the most simple field geometry used to deflect an ultra relativistic electron beam trajectory; this constant field is produced by using a bending magnet. By combining short bending magnets of opposite polarity, one drives the electron into an oscillating trajectory perpendicular to the magnetic field. As a result, the synchrotron radiation emitted from each bending magnet accumulates along the average electron velocity, providing therefore a very high spectral flux. This is the basis of insertion devices; IDs are periodic magnetic devices and produce a periodic magnetic field. In addition, an interference process between the SR emitted in each ID period may further increase the spectral flux; where the interference process is predominant one calls the IDs undulators. The other devices are called wigglers. One should mention that the interference process only concerns the SR emitted by each single electron in the different ID periods; the SR emitted by several electrons is incoherent.

First we describe the SR emitted in bending magnets and wigglers where we ignore the interference process. Finally we will review the SR emitted in undulators.

2.2.1. Bending magnet and wiggler radiation

Bending magnet radiation

We assume that the bending magnet produces a vertical magnetic field $\vec{B}(0,B_0,0)$ and the electron velocity parallel to the magnetic field is null. The electron motion is a circle in the horizontal plane. We analyse the bending magnet radiation emitted around the retarded time $\tau = 0$ in a direction perpendicular to the acceleration. The observation direction makes an angle θ_z with the horizontal plane $(O,\vec{x},\vec{s})$. The electron position at the retarded time $\tau = 0$ defines the origin O. Considering the small angle approximation exposed in section 2.1.1, one has:

$$\vec{n} = \left(0,\theta_z,1-\frac{\theta_z^2}{2}\right)$$
$$\vec{\beta} = \beta\left(\omega_0\tau,0,1-\frac{{\omega_0}^2\tau^2}{2}\right) \quad (2.28)$$
$$\vec{r} = \left(-\frac{c^2\tau^2}{2\rho},0,\beta c\tau-\frac{c^3\tau^3}{6\rho^2}\right)$$

With ρ the radius curvature and ω_0 the angular frequency of the circular motion:

$$\rho = \frac{mc\gamma}{eB} \qquad \omega_0 = \frac{c}{\rho} \quad (2.29)$$

One computes the dimensionless vector $\vec{H}(H_x,H_z)$ by inserting equation (2.28) in equation (2.11):

$$H_x = i\frac{\omega}{\omega_c}\frac{\sqrt{3}}{2\pi}\gamma\left(1+\gamma^2{\theta_z}^2\right)K_{2/3}(\xi)$$
$$H_z = \frac{\omega}{\omega_c}\frac{\sqrt{3}}{2\pi}\gamma^2\theta_z\sqrt{1+\gamma^2{\theta_z}^2}K_{1/3}(\xi) \qquad (2.30)$$

$K_{2/3}$ and $K_{1/3}$ are the Bessel modified functions, the subscripts $2/3$ and $1/3$ indicate the order of the Bessel functions. ω_c is the so called critical frequency defined as:

$$\omega_c = \frac{3c\gamma^3}{2\rho} \qquad \xi = \frac{\omega\rho}{3c}\left(\frac{1}{\gamma^2}+{\theta_z}^2\right)^{3/2} \qquad (2.31)$$

The critical frequency ω_c shares in two equal parts the spectral radiated power. A critical wavelength λ_c and a critical energy ϵ_c are associated to the critical frequency. Their expressions are in practical units:

$$\lambda_c[nm] = \frac{1.86}{B[T]E^2[GeV]} \qquad \epsilon_c[keV] = 0.665B[T]E^2[GeV] \qquad (2.32)$$

The spectral angular flux is:

$$\frac{d^2\phi}{d\Omega\, d\omega/\omega}(\vec{n},\omega) = \frac{\alpha I}{e}(|H_x|^2+|H_z|^2) \qquad (2.33)$$

Figure 2.4 displays the angular distribution of ${H_x}^2$ and ${H_z}^2$ as a function of the normalized vertical angle. ${H_x}^2$ (${H_z}^2$) is maximum (null) on the axis, thus the BM on axis radiation is horizontally polarized. ${H_z}^2$ is maximum off axis. At a wide angle, both ${H_z}^2$ and ${H_x}^2$ decrease to 0, the intensity radiation tends to zero. The opening angle of the radiation decreases with the photon energy.

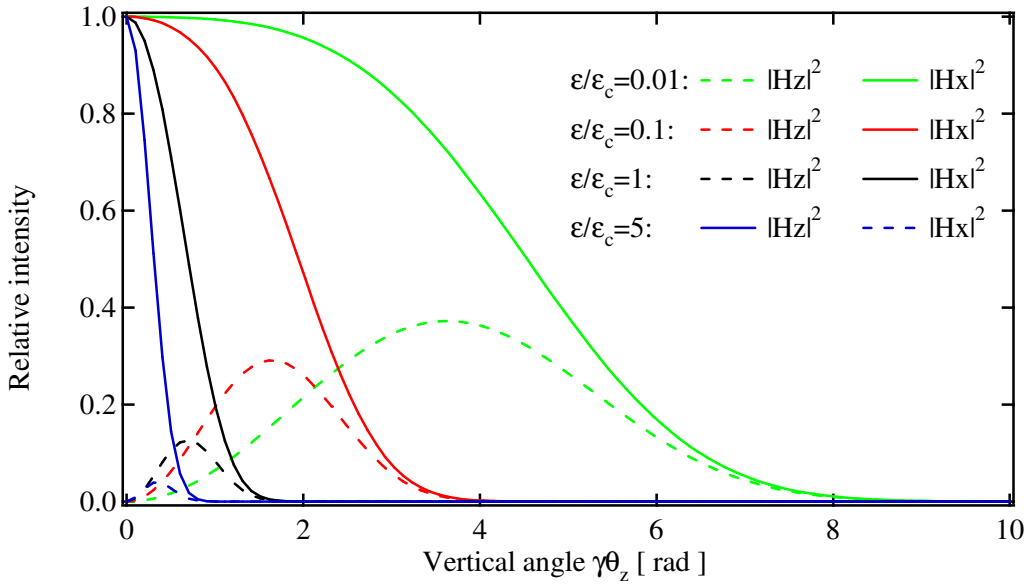

Figure 2.4: Angular distribution of the horizontal ${H_x}^2$ and vertical ${H_z}^2$ polarized radiation as a function of the normalized vertical angle for several photon energies. The electron energy is 6 GeV and $B_0 = 0.8\,T$.

In equation (2.30) H_x is imaginary while H_z is real; there is a 90° phase shift between the vertical and the horizontal field components. The electromagnetic field observed outside the orbit plane exhibits a circularly polarized component. The polarization rates I_1, I_2 and I_3 are:

$$I_1 = \frac{|H_x|^2-|H_z|^2}{|H_x|^2+|H_z|^2} \qquad I_2 = 0 \qquad I_3 = \pm\frac{2|H_x|\times|H_z|}{|H_x|^2+|H_z|^2} \qquad (2.34)$$

Wiggler radiation

The wiggler is a periodic magnetic assembly. It produces a strong magnetic field and has therefore a rather long period. Typical wigglers designed at the ESRF have a period larger than 80 mm; they produce magnetic field with peak field amplitude higher than 0.7 T. Wigglers period number varies from 5 to 20. We assume the field to be:

$$\vec{B}\left(0, -B_0 \sin\left(\frac{2\pi}{\lambda_0}s\right), 0\right) \tag{2.35}$$

Interference in wigglers is negligible. Hence we assimilate the wiggler as being the sequence of $2N$ bending magnets with opposite polarity, one behind the other; N is the number of periods. Since we ignore the interference, the photon emission from a wiggler is simply the sum of the intensities emitted in each bending magnet. This leads to an emission increase of $2N$ compared to standard bending magnets. Figure 2.5 compares the spectral flux emitted in a bending magnet and in a wiggler.

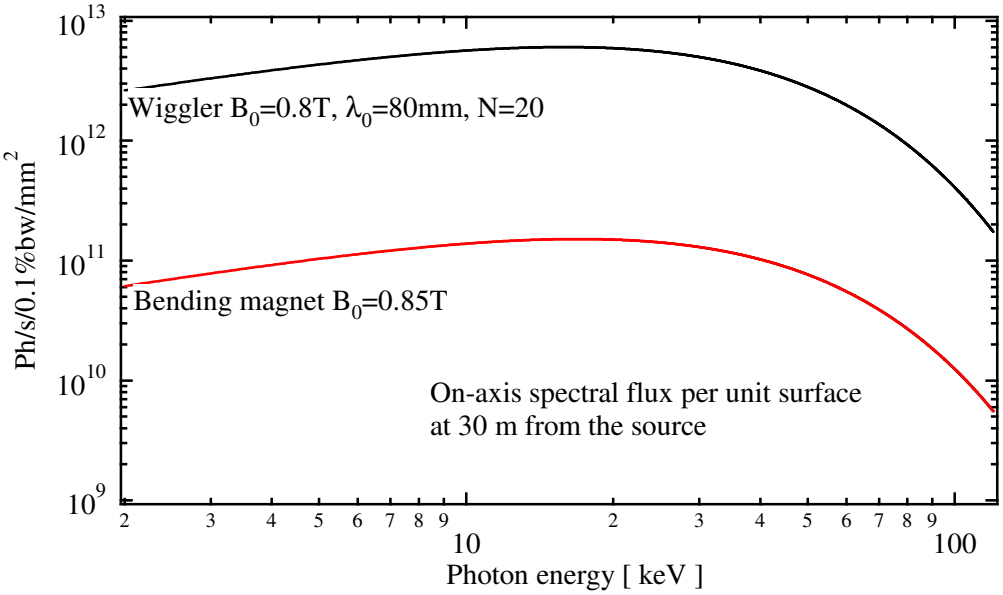

Figure 2.5: Spectral photon flux generated by a 200 mA, 6 GeV electron beam for a 0.85 T bending magnet and a 0.8 T wiggler with 20 periods. The wiggler period is 80 mm.

The opposite polarities of the two bending magnets destroy the circularly polarized component of the wiggler radiation. In addition an observer located off-axis would collect the wiggler radiation with a natural depolarized component. The polarization rates I_1, I_2 and I_3 are:

$$I_1 = \frac{|H_x|^2 - |H_z|^2}{|H_x|^2 + |H_z|^2} \qquad I_2 = I_3 = 0 \tag{2.36}$$

Off axis H_z is not null while H_x decreases, I_1 is different to 1. Off axis the wiggler radiation is naturally and partially depolarized. At a wide angle both $H_x$and H_z are asymptotically equal, the radiation is fully depolarized.

The on axis brilliance of wiggler radiation generated by a thick electron beam can be estimated as [19]:

$$\mathcal{B} \approx \left.\frac{d^2\phi}{d\Omega\, d\omega/\omega}\right|_{\theta_z=0} \frac{N}{2\pi\sqrt{\sigma_z'^2 + \sigma_R'^2}\sqrt{\sigma_x^2 + a^2 + L^2\,\sigma_x'^2/12}\sqrt{\sigma_z^2 + L^2\,\sigma_z'^2/12}} \tag{2.37}$$

Where L is the wiggler length, σ_z, σ_z' (σ_x, σ_x') are the vertical (horizontal) RMS electron beam size and divergence. $\left.\frac{d^2\phi}{d\Omega d\omega/\omega}\right|_{\theta_z=0}$ is the angular spectral flux in the orbit plane produced by a filament

electron beam in a bending magnet with field B_0. σ_R' is the RMS standard deviation of angular divergence of the bending magnet radiation. It can be shown that at photon energies close to the critical energy, one may express σ_R' as [18]:

$$\sigma_R' = \frac{0.565}{\gamma}\left(\frac{\omega}{\omega_c}\right)^{-0.425} \tag{2.38}$$

a is the amplitude of the sinusoidal motion of the electron in the horizontal plane:

$$a = \frac{\lambda_0 K}{2\pi\gamma} \tag{2.39}$$

2.2.2. Undulator radiation

Here we focus on undulator radiation emitted in the direction $\vec{n}$. An undulator produces a transverse and periodic magnetic field $\vec{B}(B_x(s), B_z(s), 0)$ along its longitudinal axis $\vec{s}$. λ_0 is its period length and N its number of periods. In the small angle approximation one has:

$$\begin{gathered}\vec{n} = (\theta_x, \theta_z) \\ \vec{r} = (0, 0, c\tau) \\ \vec{\beta} = \left(\beta_x, \beta_z, 1 - \frac{1 + \gamma^2\beta_x^2 + \gamma^2\beta_z^2}{2\gamma^2}\right)\end{gathered} \tag{2.40}$$

With:

$$\beta_x = \frac{e}{\gamma mc}\int_{-\infty}^{s} B_z(s')ds' \qquad \beta_z = -\frac{e}{\gamma mc}\int_{-\infty}^{s} B_x(s')ds' \tag{2.41}$$

At any undulator period an electron is deflected and emits an electromagnetic wave at frequency ω. In the following period this electromagnetic wave will interfere with a newly emitted wave at frequency ω. Whenever the phase advance between both waves is an integer multiple of 2π, the interference is constructive otherwise it is partially destructive. This is the interference condition. As a result, the vector field and the spectral angular flux are made up of a series of harmonics with frequency equal to a multiple integer of ω_1, the fundamental frequency. A radiation emitted at the fundamental frequency ω_1, has a 2π phase advance from one period to the next. The fundamental frequency ω_1 depends on the observation direction (θ_x, θ_z):

$$\omega_1(\theta_x, \theta_z) = \frac{4\pi c\gamma^2}{\lambda_0\left(1 + K_x^2/2 + K_z^2/2 + \gamma^2(\theta_x^2 + \theta_z^2)\right)} \tag{2.42}$$

In practical units, the photon energy at the fundamental frequency is:

$$\epsilon(\theta_x, \theta_z)[keV] = 9.498\frac{E^2[GeV]}{\lambda_0[mm]\left(1 + K_x^2/2 + K_z^2/2 + \gamma^2(\theta_x^2 + \theta_z^2)\right)} \tag{2.43}$$

E is the electron beam energy. K_x and K_z are the deflection parameters. They are dimensionless and defined as:

$$K_i = \sqrt{\frac{2\gamma^2}{\lambda_0}\int_0^{\lambda_0} \beta_i^2 ds} \;\; ; i = x, z \tag{2.44}$$

One computes the dimensionless vector $\vec{H}(\theta_x, \theta_z, \omega)$ by inserting equation (2.40) into equation (2.11). The periodicity of the magnetic field and consequently that of the electron velocity, allows the

split of $\vec{H}(\theta_x, \theta_z, \omega)$ into an integral over each undulator period. When the origin of the laboratory is located in the middle of the undulator, one may write $\vec{H}(\theta_x, \theta_z, \omega)$ as follows [14]:

$$\vec{H}(\theta_x, \theta_z, \omega) = N\vec{H}_{\lambda_0}(\theta_x, \theta_z, \omega)\frac{\sin\left(\pi N(\omega/\omega_1)\right)}{N\sin\left(\pi(\omega/\omega_1)\right)} \tag{2.45}$$

With:

$$\vec{H}_{\lambda_0}(\theta_x, \theta_z, \omega) = \frac{\omega}{2\pi\gamma c}\int_0^{\lambda_0} \vec{v}(s)exp\left(i\phi(s,\omega)\right)ds$$

$$\phi(s,\omega) = \frac{\omega}{2c\gamma^2}\int_0^{s}\left(1+\vec{v}^2(s')\right)ds' \tag{2.46}$$

$$\vec{v} = \gamma(\beta_x - \theta_x)\vec{u}_x + \gamma(\beta_z - \theta_z)\vec{u}_z$$

The vector $\vec{H}(\theta_x, \theta_z, \omega)$ is the product of two terms:

- The first term $\vec{H}_{\lambda_0}(\theta_x, \theta_z, \omega)$ represents the flux produced in one period. $\vec{H}_{\lambda_0}$ is the vector field $\vec{H}$ with the integral in equation (2.11) being limited to a single period of the insertion device. The vector field $\vec{H}_{\lambda_0}$ is emitted in the observer direction at the frequency ω. Usually this term varies smoothly with the frequency.

- The $\frac{\sin\left(\pi N(\omega/\omega_1)\right)}{N\sin\left(\pi(\omega/\omega_1)\right)}$ term is called the interference term. Figure 2.6 represents the interference term for 50 periods. This term is responsible for the harmonic peak series. For each peak, the amplitude is proportional to the squared number of periods. This is the signature of the interference process.

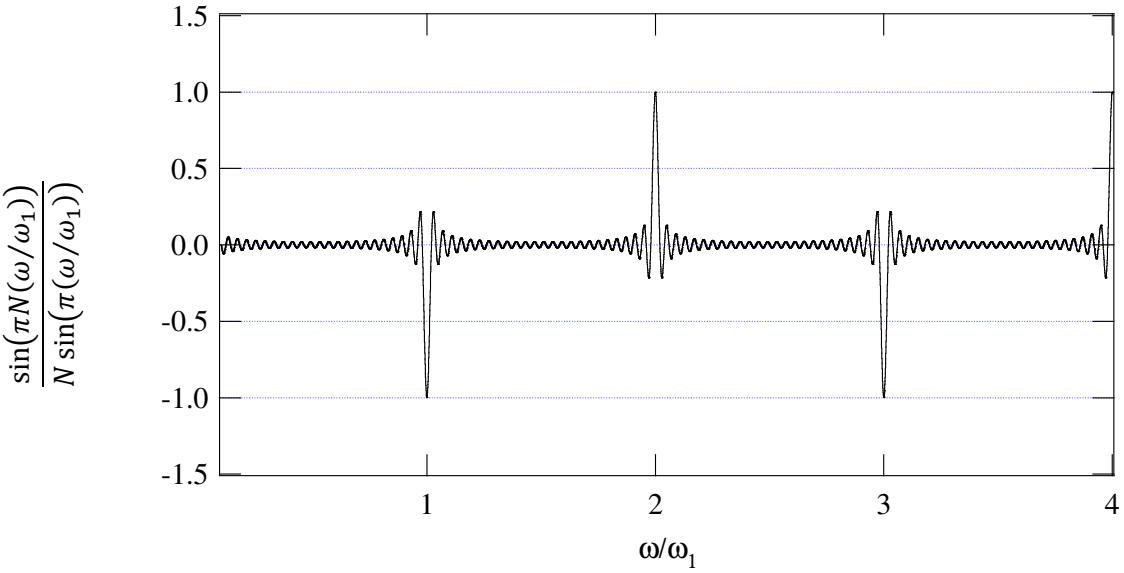

Figure 2.6: Graph of the $\frac{\sin\left(\pi N(\omega/\omega_1)\right)}{N\sin\left(\pi(\omega/\omega_1)\right)}$ term as a function of ω/ω_1 for 50 periods.

The spectral angular flux defined in equation (2.16) is for a filament beam [17]:

$$\frac{d^2\phi}{d\Omega\, d\omega/\omega}(\theta_x, \theta_z, \omega) = \frac{\alpha I}{e}N^2\left|\vec{H}_{\lambda_0}(\theta_x, \theta_z, \omega)\right|^2 \times \left(\frac{\sin\left(\pi N(\omega/\omega_1)\right)}{N\sin\left(\pi(\omega/\omega_1)\right)}\right)^2 \tag{2.47}$$

For the on axis resonant frequency $\omega = n\omega_1(0,0)$ angles, the spectral flux $\frac{\mathrm{d}\phi_n}{d\omega/\omega}$ is [17]:

$$\frac{d\phi_n}{d\omega/\omega} = \iint_{\Omega} \frac{d^2\phi}{d\Omega\, d\omega/\omega} d\Omega = \frac{\pi}{2}\alpha \frac{IN}{en}\frac{1}{\gamma^2}\left(1 + \frac{{K_x}^2}{2} + \frac{{K_z}^2}{2}\right)\left|\vec{H}_{\lambda_0}(0,0,n\omega_1)\right|^2 \tag{2.48}$$

On odd harmonics of the undulator radiation emitted by a thick electron beam, the on axis brilliance can be approximated as [17]:

$$\mathcal{B} \approx \frac{\frac{d\phi_n}{d\omega/\omega}}{4\pi^2 \Sigma_X \Sigma_{X'} \Sigma_Z \Sigma_{Z'}} \tag{2.49}$$

Where Σ_X, $\Sigma_{X'}$ (Σ_Z, $\Sigma_{Z'}$) are the horizontal (vertical) RMS photon beam size and divergences in the middle of the undulator. They are approximated as a function of the RMS electron beam sizes σ_z, $\sigma_{z'}$, σ_x and $\sigma_{x'}$ as follows [17]:

$$\begin{aligned} {\Sigma_{X'}}^2 &= \sigma_{x'}^2 + \frac{\lambda}{2L} & {\Sigma_{Z'}}^2 &= \sigma_{z'}^2 + \frac{\lambda}{2L} \\ {\Sigma_X}^2 &= {\sigma_x}^2 + \frac{\lambda L}{8\pi^2} & {\Sigma_Z}^2 &= {\sigma_z}^2 + \frac{\lambda L}{8\pi^2} \end{aligned} \tag{2.50}$$

Where L is the length of the undulator and λ is the wavelength associated to ω.

Planar undulator

The planar undulator produces a vertical sinusoidal magnetic field along the electron beam path. We assume the field to be:

$$\vec{B}\left(0, -B_0\, sin\left(\frac{2\pi}{\lambda_0}s\right), 0\right) \tag{2.51}$$

The electron undulates along the x axis. We derive the electron velocity β_x, β_z from the Lorentz force:

$$\beta_x = \frac{K_z}{\gamma}\cos\left(\frac{2\pi}{\lambda_0}s\right) \qquad \beta_z = 0 \qquad K_z = \frac{eB_0\lambda_0}{2\pi mc^2} \tag{2.52}$$

One deduces from equations above a practical interpretation of the deflection parameter K_z: K_z/γ represents the amplitude of the horizontal velocity. In practical units one has:

$$K_z = 0.0934 B_0[T]\lambda_0[mm] \tag{2.53}$$

Figure 2.7 and Figure 2.8 show the electric field and the radiation spectrum for two different K_z. On the axis, the positive and negatives pulses of the electric field $\vec{E}(\vec{R}, t)$, are equidistant. As a result the on axis spectrum doesn't contain even harmonics. The on axis spectral angular flux vanishes for even harmonics. For small value $K_z \ll 1$ the electric field is nearly sinusoidal. The radiation spectrum reduces to the fundamental frequency. On the other side for large deflection parameter K_z, the electric field is made of a periodic sharp peak. Thus the spectrum contains high harmonics.

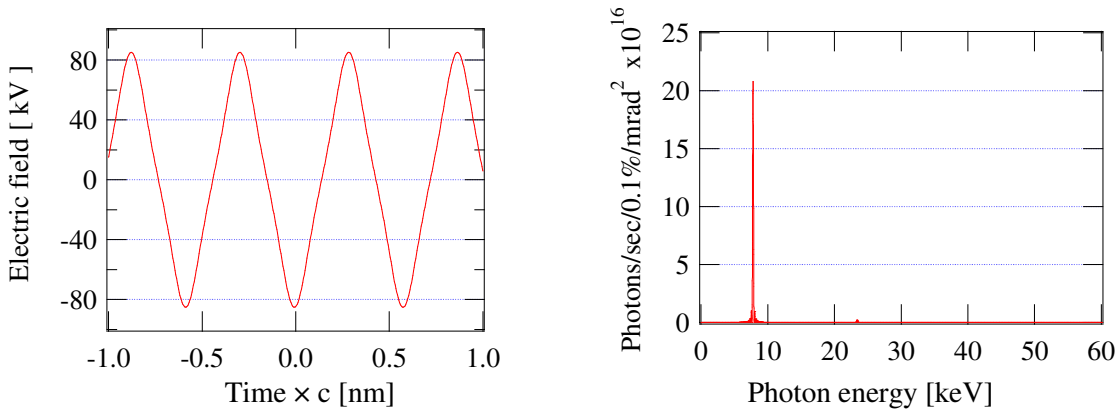

Figure 2.7: Horizontal electric field emitted by a single electron and spectral angular flux produced by a filament beam (I = 200 mA, E = 6 GeV) in a periodic magnetic field with $K = 0.3$. Calculation computed using B2E [10].

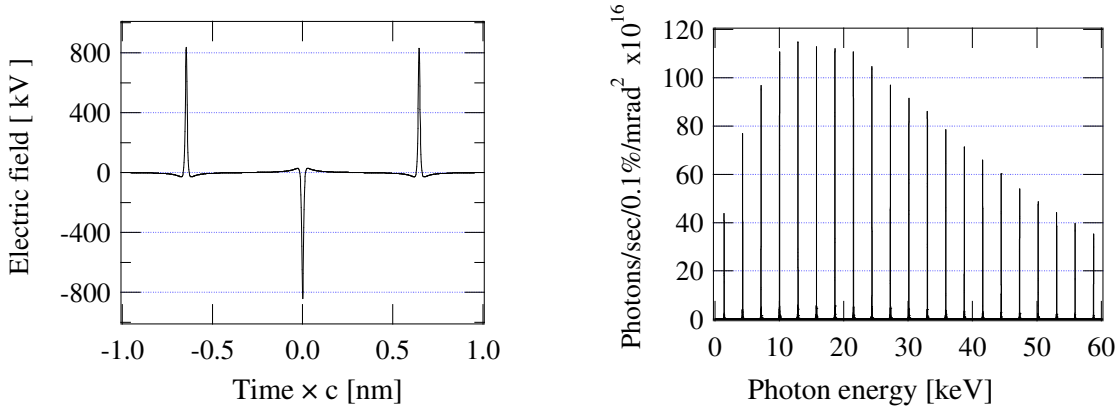

Figure 2.8: Horizontal electric field emitted by a single electron and spectral angular flux produced by a filament beam (I = 200 mA, E = 6 GeV) in a periodic magnetic field with $K = 3$. Calculation computed using B2E [10].

The electric field has no vertical component for an observer located in the horizontal plane (z=0), the SR is then horizontally polarized. Actually an observer in any direction sees a linear polarized light. However the plane of polarization depends on the emission direction and the harmonic number. Such a planar magnetic field cannot produce circularly polarized light [20].

Ellipsoidal undulator

A periodic magnetic field, which combines horizontal and vertical components, is sufficient to produce an elliptical polarization. Indeed the horizontal component introduces a vertical acceleration. This acceleration produces a vertical field component even when the observer is on the axis. The magnetic field is:

$$\vec{B} = \left(B_{x_0} \sin\left(\frac{2\pi}{\lambda_0} s + \varphi\right), B_{z_0} \sin\left(\frac{2\pi}{\lambda_0} s\right), 0\right) \tag{2.54}$$

The deflection parameter K_x and K_z are:

$$K_x = \frac{eB_{x_0}\lambda_0}{2\pi mc^2} \qquad K_z = \frac{eB_{z_0}\lambda_0}{2\pi mc^2} \tag{2.55}$$

Like a planar undulator, the on axis spectral angular flux vanishes for even harmonics. For a filament electron beam, the spectral angular flux is maximal on the axis. The filament beam radiates

SR on the axis with elliptical polarization. The polarization rates of any odd harmonic can be expressed as:

$$I_1 = \frac{\left(B_{x_0}/B_{z_0}\right)^2 - 1}{\left(B_{x_0}/B_{z_0}\right)^2 + 1} \quad I_2 = \frac{2\left(B_{x_0}/B_{z_0}\right)\cos\varphi}{\left(B_{x_0}/B_{z_0}\right)^2 + 1} \quad I_3 = \frac{2\left(B_{x_0}/B_{z_0}\right)\sin\varphi}{\left(B_{x_0}/B_{z_0}\right)^2 + 1} \tag{2.56}$$

The polarization is purely circular $(I_1, I_2 = 0)$ when the vertical and horizontal components have the same amplitude with a $\pi/2$ phase. Electrons then have a helicoidal motion in the undulator and their longitudinal velocity β_s is constant. With a constant velocity, only one frequency can fulfill the interference condition introduced above. Finally the spectrum of a purely circular polarized radiation is reduced to only one harmonic. This offers poor energy tunability for the users. Consequently, in practice, we choose to use an elliptical polarization rather than a purely circular one, so that the spectrum contains a broader range of harmonics. We create the elliptical polarization by using vertical and horizontal magnetic field components that do not have the same amplitude.

We have overviewed the SR emitted by an ultra relativistic electron beam in three different magnetic devices, the bending magnet, wiggler and undulator. In addition, we showed we can choose the polarization state thanks to the selection of the field geometry and the observation direction. Now we come to the selection of the most appropriate ID according to its usage. Depending on their research field, scientists are interested in photons within a specific energy spectrum. One would naturally design the device which produces the highest brilliance in this energy range. Figure 2.9 compares the brilliance produced by a typical wiggler and a typical undulator. One observes that the undulator brilliance decreases rapidly at high photon energy. On the other side the wiggler brilliance is rather flat on a large photon energy range. Finally wigglers are necessary to produce high energy photons with high brilliance.

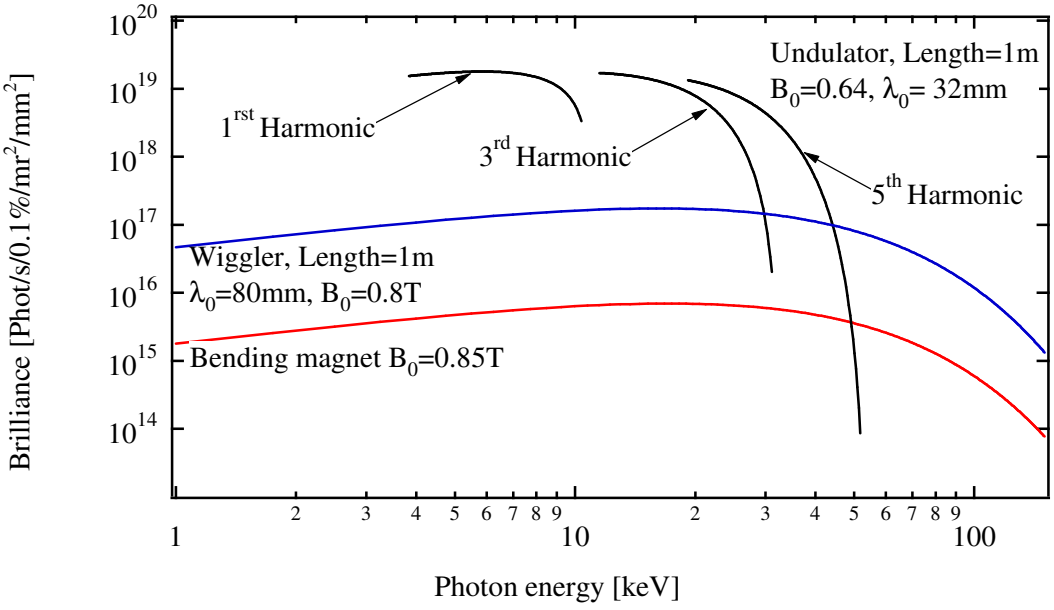

Figure 2.9: Brilliance achievable at the ESRF with standard wiggler and undulator computed with SRW. One varies the undulator magnetic gap in order to tune the photon energy. Computation dome using SRW [21]; the beam parameters are those of the ESRF even straight section, listed in Table 2.2 presented in section 2.3.1.

2.3. Magnetic properties of ID

We will then introduce the magnetic quantities that fully characterize the radiation properties, as well as the effect on the electron beam. These quantities are of primary interest for the realization and

the optimization of a real insertion device. An ID has to fulfil two requirements in order to be installed on the storage ring. It should produce radiation of the highest intensity for the users without disturbing the electron beam dynamics in the storage ring. The RMS phase error is used to quantify the effect of magnetic errors on the radiation intensity. It is only relevant for undulators in which interference is predominant. On the other side, the perturbations, which an insertion device induces, are mainly related to its field integrals. We will now review these two magnetic quantities.

2.3.1. Field integrals

Magnets in the storage ring drive and focus the electron beam. The reference particle experiences a closed trajectory, which is called the closed orbit [16]. Electrons, which deviate from the closed orbit, oscillate in the transverse plane around the reference particle. The transverse oscillations are the so called betatron oscillation. The transverse position of an electron in a storage ring free of magnetic errors is [16]:

$$\begin{aligned} x(s) &= A_x\sqrt{\beta_{b_x}(s)}\cos\left(\int\frac{1}{\beta_{b_x}(s)}ds+\delta_x\right) \\ z(s) &= A_z\sqrt{\beta_{b_z}(s)}\cos\left(\int\frac{1}{\beta_{b_z}(s)}ds+\delta_z\right) \end{aligned} \tag{2.57}$$

$\beta_{b_x}\ (\beta_{b_z})$ is the horizontal (vertical) beta function (not to be confused with the transverse electron velocities β_x and β_z). The constants A_x, A_z, δ_x and δ_z are defined by the initial position of the electron. The horizontal (vertical) tune $\nu_x\ (\nu_z)$ is the number of horizontal (vertical) betatron oscillation per turn:

$$\nu_i = \frac{1}{2\pi}\oint\frac{ds}{\beta_{b_i}(s)} \qquad i = x,z \tag{2.58}$$

Insertion devices and user instrumentation are aligned with respect to the closed orbit. An installed insertion device which might disrupt the electron beam dynamics would displace the electron beam closed orbit; electrons then oscillate around the perturbed closed orbit. As a result this would misalign the radiation axis of any installed insertion device. Therefore, any insertion device which disturbs the closed orbit would disrupt every single user of the synchrotron facility.

Net angle and position offset

The net angle $\theta(\theta_x,\theta_z)$ and position offset $\Delta(\Delta_x,\Delta_z)$ of an electron recorded between the entrance and the exit as it crosses an undulator is deduced from the Lorentz equation. To the first order in $1/\gamma$, the net angle and the position offset are given by:

$$\begin{aligned} \theta_x &= \frac{e}{\gamma mc}I_z + o\left(\frac{1}{\gamma^2}\right) & \theta_z &= -\frac{e}{\gamma mc}I_x + o\left(\frac{1}{\gamma^2}\right) \\ \Delta_x &= \frac{e}{\gamma mc}J_z + o\left(\frac{1}{\gamma^2}\right) & \Delta_z &= -\frac{e}{\gamma mc}J_x + o\left(\frac{1}{\gamma^2}\right) \end{aligned} \tag{2.59}$$

Where $\vec{I} = (I_x, I_z)$ and $\vec{J} = (J_x, J_z)$ are the first and the second field integral along s:

$$I_i = \int_{-\infty}^{+\infty} B_i(s)\,ds \qquad J_i = \int_{-\infty}^{+\infty} ds \int_{-\infty}^{s} B_i(s')\,ds' \qquad i = x,z \tag{2.60}$$

The angle and the position offset are respectively proportional to the first field integral and the second field integral. IDs with non zero on axis field integrals disturb the closed orbit. Practically, one

can tolerate the fact that a "perturbing" ID causes an angle and a position offset smaller than 10% of the beam size and divergence [15]. Such limits lead to the following relations [22]:

$$\begin{aligned} I_x &\leq \frac{\gamma mc}{5e}\sin(\pi\nu_z)\sqrt{\frac{\varepsilon_z}{\beta_{b_z}}} & J_x &\leq \frac{\gamma mc}{5e}\sin(\pi\nu_z)\sqrt{\beta_{b_z}\varepsilon_z} \\ I_z &\leq \frac{\gamma mc}{5e}\sin(\pi\nu_x)\sqrt{\frac{\varepsilon_x}{\beta_{b_x}}} & J_z &\leq \frac{\gamma mc}{5e}\sin(\pi\nu_x)\sqrt{\beta_{b_x}\varepsilon_x} \end{aligned} \tag{2.61}$$

ε_x (ε_z) is the horizontal (vertical) emittance of the electron beam. β_{b_x} (β_{b_z}) is the horizontal (vertical) beta function in the middle of straight section. Table 2.2 lists the value of the transverse emittances, the tunes and the beta function in the middle of the straight sections.

Table 2.2: Horizontal and vertical emittances, tunes and beta functions in the middle of the straight sections at the ESRF.

	Even straight section	Odd straight section
Horizontal emittance ε_x / Vertical emittance ε_z [m rad]	3.9 10^{-9}/2.5 10^{-11}	
Horizontal tune ν_x / Vertical tune ν_z	0.44/0.39	
Horizontal beta β_{b_x} / Vertical beta function β_{b_z} [m]	0.5/2.73	35.2/2.52

The electron beam parameters at the ESRF lead to the following upper limits for the field integrals:

$$\begin{cases}\theta_x \leq 2\ \mu rad \\ I_z \leq 0.4\ Gm\end{cases} \quad \begin{cases}\Delta_x = 9\ \mu m \\ J_z \leq 1.8\ Gm^2\end{cases} \quad \begin{cases}\theta_z \leq 0.5\ \mu rad \\ I_x \leq 0.1\ Gm\end{cases} \quad \begin{cases}\Delta_z = 1.5\ \mu m \\ J_x \leq 0.3\ Gm^2\end{cases} \tag{2.62}$$

Multipole expansion of the first field integral

The magnetic field in the undulator gap or in the aperture of storage ring magnets is given by solving the Maxwell's equation in vacuum:

$$\vec{\nabla}\cdot\vec{B} = 0 \qquad \vec{\nabla}\times\vec{B} = 0 \tag{2.63}$$

Since we solve the same Maxwell's equation to compute the magnetic field in an ID gap or in the aperture of a conventional magnet, we may apply the harmonic analysis widely used in accelerator magnet technology to IDs [23]. Because of the cylindrical geometry of magnet apertures, one usually expresses $\vec{I}$ using the following Fourier expansion in a cylindrical basis (r, θ):

$$\begin{aligned} I_r &= \sum_{k=1}^{\infty} kr^{k-1}(-A_k\cos(k\theta) + B_m\sin(k\theta)) \\ I_\theta &= \sum_{k=1}^{\infty} kr^{k-1}(B_k\sin(k\theta) + A_k\cos(k\theta)) \end{aligned} \tag{2.64}$$

A_m and B_m are the constant coefficients known respectively as the skew and the normal multipoles. The development becomes in the Cartesian system (x, z, s):

$$I_x = \sum_{k=1}^{\infty} -A_k \sum_{j=0}^{\frac{k-1}{2}} (-1)^j \binom{k-1}{2j} z^{2j} x^{k-2j-1} + B_k \sum_{j=0}^{\frac{k-1}{2}} (-1)^j \binom{k-1}{2j+1} z^{2j+1} x^{k-2j-2}$$
$$I_z = \sum_{k=1}^{\infty} A_k \sum_{j=0}^{\frac{k-1}{2}} (-1)^j \binom{k-1}{2j+1} z^{2j+1} x^{k-2j-2} + B_k \sum_{j=0}^{\frac{k-1}{2}} (-1)^j \binom{k-1}{2j} z^{2j} x^{k-2j-1} \quad (2.65)$$

In other words, equations (2.64) and (2.65) state that, whatever the coordinate system used, the insertion device integral might be split up into a sum of usual multipole components used to focus and drive the beam in the accelerator. As a result, one could investigate the disruption that an insertion device induces on the beam dynamics by breaking it up into the sum of its multipole components and computing the effect of each component. Table 2.3 lists the usual multipole components used to focus and drive the beam in the accelerator [23].

Table 2.3: Integral field components for 2D multipoles up to sextupole.

Multipole of order k	Skew lenses	Normal lenses
Dipole k=1	$I_x = -A_1$ $I_z = 0$	$I_x = 0$ $I_z = B_1$
Quadrupole k=2	$I_x = -2A_2 x$ $I_z = 2A_2 z$	$I_x = 2B_2 z$ $I_z = 2B_2 x$
Sextupole k=3	$I_x = -3A_3(x^2 - z^2)$ $I_z = 6A_3 zx$	$I_x = 6B_3 zx$ $I_z = 3B_3(x^2 - z^2)$

Every multipole component must be corrected in order to cancel the undulator effect on the beam dynamics. The process done to correct any multipole component of the field integral is called "multipole shimming".

An efficient multipole correction is based on a well known property of the Maxwell equations. It can be demonstrated that the field integral $\vec{I}(I_x, I_z)$ in an undulator gap or in an aperture of an accelerator magnet, satisfies the 2D Maxwell's equation in vacuum [10]:

$$\frac{\partial I_x}{\partial x} + \frac{\partial I_z}{\partial z} = 0 \qquad \frac{\partial I_x}{\partial z} - \frac{\partial I_z}{\partial x} = 0 \quad (2.66)$$

Equation (2.66) is equivalent to the Cauchy condition. Consequently the first field integral may be represented in vacuum with an analytical function of a complex variable [22]. One defines an analytical function $\tilde{I}(\xi)$ of the complex variable $\xi = x + iz$:

$$\tilde{I}(\xi) = I_x(x, \mathrm{z}) - iI_z(x, \mathrm{z}) \quad (2.67)$$

In vacuum the complex integral $\tilde{I}$ is continuously derivable and admits a Taylor series expansion. The Taylor series around the insertion device axis is:

$$\tilde{I}(\xi) = \sum_{n=0}^{\infty} \frac{\xi^n}{n!} \tilde{I}^n(0) \qquad \tilde{I}^n(0) = \frac{d^n}{d\xi^n} \tilde{I}(0) \quad (2.68)$$

The field integral representations using either the multipole expansion or the Taylor series are equivalent. Therefore one relates the multipole components A_n and B_n to the successive complex field integral derivatives $\tilde{I}^{(n)}(0)$:

$$A_n = -\frac{1}{(n-1)!}\Re\left(\tilde{I}^{(n-1)}(0)\right) = -\frac{1}{(n-1)!}\frac{d^{n-1}}{dx^{n-1}}I_x(0)$$
$$B_n = \frac{1}{(n-1)!}\Im\left(\tilde{I}^{(n-1)}(0)\right) = \frac{1}{(n-1)!}\frac{d^{n-1}}{dx^{n-1}}I_z(0) \tag{2.69}$$

According to equation (2.69), the multipole components A_n and B_n vanish whenever we cancel the successive x-derivatives of I_x and I_z. The Cauchy integral formula provides a powerful tool to cancel the I_x and I_z derivatives. Indeed the complex field integral $\tilde{I}$ satisfies the Cauchy integral formula, over any contour delimiting a region free of magnetic source. Thus for any complex variable ξ inside the contour $\mathcal{C}$, one has:

$$\tilde{I}^{(n)}(\xi) = \frac{n!}{2i\pi}\oint_{\mathcal{C}}\frac{\tilde{I}(w)}{(w-\xi)^{n+1}}dw \tag{2.70}$$

For a field integral equal to zero on the contour $\mathcal{C}$, the field integral is null within the surface bounded by the contour $\mathcal{C}$. An efficient multipole shimming then consists of cancelling the field integral along a particular contour. This process is exposed in detail in section 2.4.4.

2.3.2. Phase error

Besides disturbing the electron dynamics in the storage ring, magnetic errors in undulators cause a reduction in the SR intensity.

The on axis electric field emitted in a perfect planar undulator is displayed in Figure 2.10. This is a series of peaks equally spaced; T_i refers the successive times when an observer located on the axis and at infinite receives the $2N$ peaks of the electric field. The corresponding spectrum is represented in Figure 2.11, it contains numerous harmonics. Magnetic errors in the undulator shift the times T_i, change the fundamental frequency of the undulator radiation and introduce destructive interference. As a result errors reduce the radiation intensity on the harmonics of the X-ray spectrum.

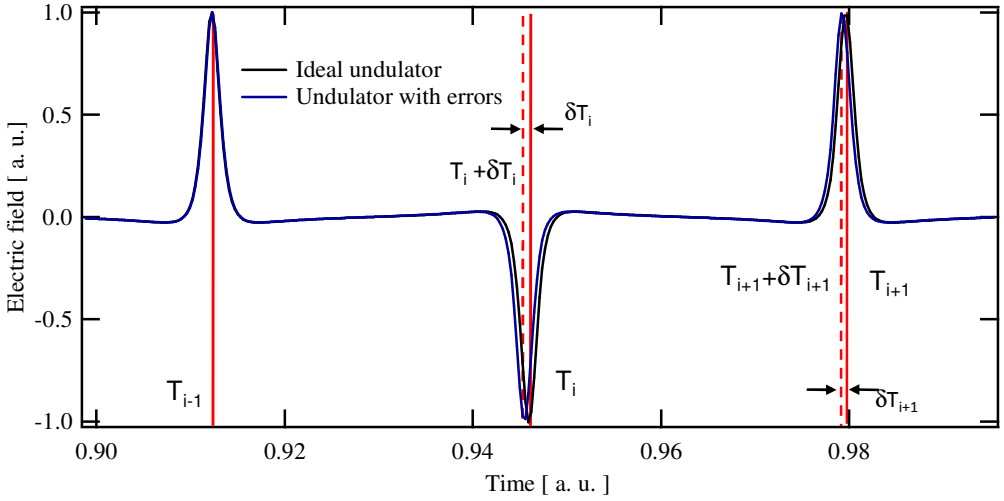

Figure 2.10: The on axis electric field emitted by a single 6 GeV electron propagating through an ideal (black curve) planar undulator ($K = 1.88, \lambda_0 = 20\,mm, N = 48$). It is a series of peaks equally spaced. Errors in the magnetic field shown in Figure 2.12 cause a shift of the electric field peaks. Computation made using B2E.

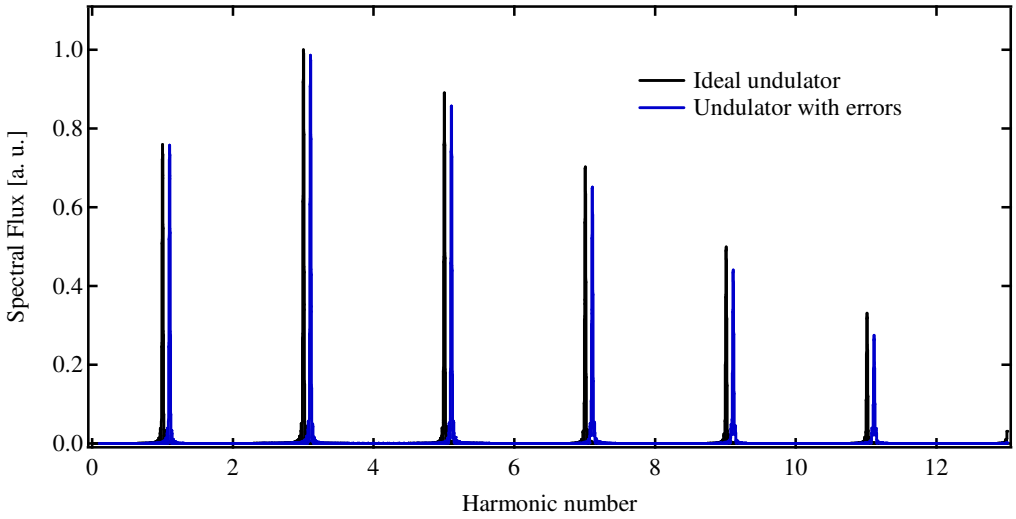

Figure 2.11: The on axis spectrum produced by a filament electron beam (I = 200 mA, E = 6 GeV) for an ideal undulator ($K = 1.88, \lambda_0 = 20\,mm, N = 48$) and for an undulator with localized amplitude errors shown in Figure 2.12. Computation made using B2E.

RMS Phase error

In order to study the impact of magnetic error on undulator spectrum, one uses the phase ϕ_i instead of the time delay T_i. The phase ϕ_i measures the slippage of one optical wavelength between the electron and the light [24]. The phase ϕ_i is defined as:

$$\phi_i = \frac{\omega_1}{c} \int_0^{i\lambda_0/2} \left(\frac{1}{\beta_s} - 1\right) ds \tag{2.71}$$

Where β_s is the longitudinal velocity of electrons and ω_1 the fundamental frequency of the undulator radiation. As one assumes the magnetic field of a real planar undulator with magnetic errors is to be written as:

$$B_z = -B_{z_0} \sin\left(\frac{2\pi}{\lambda_0} s\right) + \delta B_z(s) \qquad \delta B_z(s) \ll 1 \tag{2.72}$$

$\delta B_z(s)$ represents the magnetic field error. The longitudinal velocity β_s is:

$$\beta_s(s) \approx 1 - \frac{1}{\gamma^2} - \frac{K^2}{2\gamma^2}\left(\cos\left(\frac{2\pi}{\lambda_0} s\right) + \delta_x(s)\right)^2 \tag{2.73}$$

With:

$$\delta_x(s) = \frac{1}{\lambda_0 B_{z_0}} \int_{-\infty}^{s} \delta B_z(u)\, du \tag{2.74}$$

$\delta_x(s)$ is the normalized integral of the magnetic field error $\delta B_z(s)$; it measures the angle error which introduces the magnetic field error $\delta B_z(s)$ at the position s. The phase ϕ_i defined in (2.71) then becomes:

$$\phi_i = i\pi + \delta\phi_i \tag{2.75}$$

With:

$$\delta\phi_i = \frac{2\pi K^2}{\lambda_0\left(1+\frac{K^2}{2}\right)}\int_0^{i\frac{\lambda_0}{2}}\left(\left(\delta_x(s)\right)^2 - \frac{\delta B_z(s)}{\pi B_{z_0}}\sin\left(\frac{2\pi}{\lambda_0}s\right)\right)ds \tag{2.76}$$

$\delta\phi_i$ is the phase error; it describes the deviation of one optical wavelength $\left(\lambda_1 = c/\omega_1\right)$ from the ideal slippage due to errors. A magnetic field error $\delta B_z(s)$ contributes twice to the phase error $\delta\phi_i$. Magnetic errors introduce some modulation $\delta B_z(s)$ in the undulator field; the effect of the modulation is contained in the sinus term in (2.76). In general this term is dominant on-axis. In addition electrons may experience a trajectory with angle errors. The squared term $\left(\delta_x(s)\right)^2$ in (2.76) resumes the effects of angle errors on the phase error, meaning that a small phase error requires a straightforward electron trajectory within the undulator.

For randomly distributed phase errors, the reduction of flux and brilliance on the spectrum harmonic n is given by $I_n(\sigma)$ [25]:

$$I_n(\sigma) = exp(-n^2\sigma^2) \tag{2.77}$$

Where σ, the so called RMS phase error, is the RMS value of the $2N$ phase errors $\delta\phi_i$:

$$\sigma = \sqrt{\frac{1}{2N}\sum_{i=1}^{2N}{\delta\phi_i}^2} \tag{2.78}$$

We consider hereafter some typical magnetic errors on periodic magnetic field. As plotted on the left graph in Figure 2.12, we assume a linear magnetic field amplitude variation, i.e. a taper, and some localized variations. In both cases the maximum variation of the field amplitude is 0.5%. The phase error $\delta\phi_i$ of the electric field, which a 6 GeV electron would emit throughout the different magnetic fields, is also displayed. The RMS phase error achieved with the tapered field is 3 times higher than the RMS phase error induced by localized peak field errors. Magnetic errors, which spread over a large number of periods, have a greater impact on the RMS phase error than the localized magnetic errors.

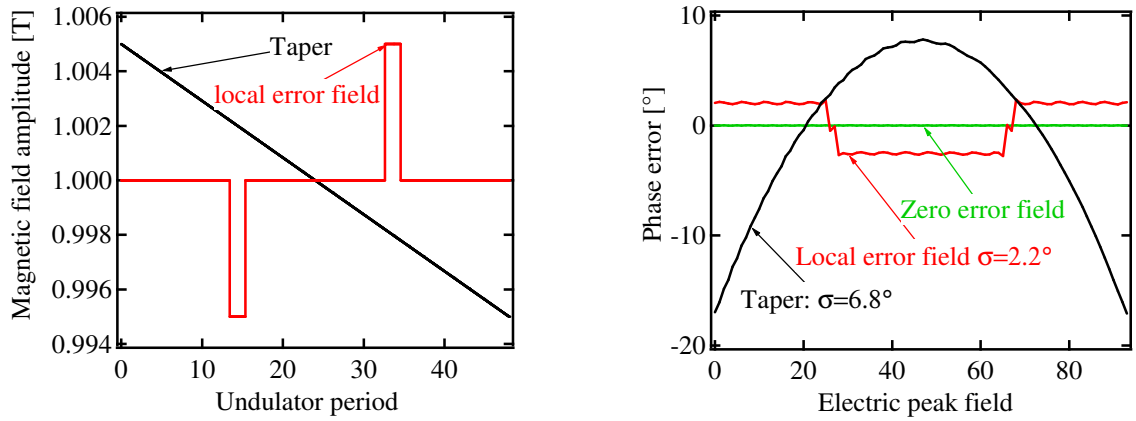

Figure 2.12: Magnetic fields deviation (left plot) of a periodic field $(K = 1.88, \lambda_0 = 20mm, N = 48)$ and associated phase error (right plot). The black curve corresponds to a linear decrease of the peak field along the length (tapered undulator); the red curve corresponds to localized field errors. In each case the maximum variation of the field amplitude is 0.5%. The computation is done using B2E.

The 5th and 7th harmonics of the on axis spectral flux, achieved with the different magnetic errors, are displayed in Figure 2.13. Compared to zero field error, the on axis spectral flux with the 6.8° phase error is already reduced by nearly 35% on the 5th harmonic. Therefore an undulator with such a high RMS phase error can't produce high energy photons. The spectral flux with the 2.2° phase error is

only reduced by nearly 10% on the 7th harmonic. Consequently 2° is acceptable RMS phase error value to produce a high energy undulator.

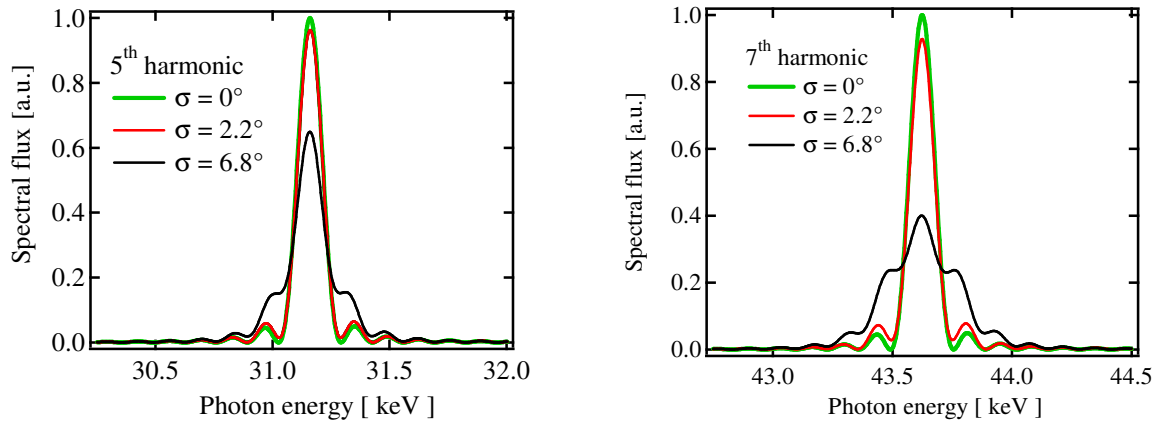

Figure 2.13: Impact of the different magnetic errors shown in Figure 2.12 on the 5th harmonic (left plot) and the 7th harmonic of the spectral flux (right plot). Computation done with B2E assuming a 6 GeV filament beam (I=200 mA, E=6 GeV).

According to the photon energy range the scientists are interested in, they select specific harmonics in the undulator radiation spectrum. Since the reduction of the radiation intensity increases with the harmonic number and the RMS phase error, one understands that an undulator with a RMS phase error of 6° is well suited for scientists working with the first harmonics of the undulator radiation spectrum. On the other hand, it is necessary to lower the maximum value of the RMS phase error σ_{max} to 2.5° as the undulator is dedicated to scientists working with high order harmonics. The process done to reduce the RMS phase error is called the phase or spectrum shimming. This process allows the correction of the magnetic errors which have the heaviest weight on the RMS phase error.

To sum up, an insertion device allows the production of intense radiation. In addition, we can choose the polarization state thanks to the selection of the field geometry. However, in practice the device has some magnetic errors. Errors in the undulator field are corrected in order to:

- Minimize the undulator field integrals at any gap value. Field integrals must be kept below the upper limits given in equation (2.62) in order to avoid large beam dynamics perturbations.
- Keep the RMS phase error σ below a maximum value σ_{max} in order to provide the users with a very intense photon flux. Regarding the use of the undulator, σ_{max} is fixed between 2° and 6°.

Table 2.4 summarizes the maximum value admitted at the ESRF for the first field integral, the second field integral and the RMS phase error.

Table 2.4: Maximum value admitted at the ESRF for the first field integral, the second field integral and the RMS phase error.

Horizontal first field integral I_x	Vertical first field integral I_z	Horizontal double field integral J_x	Vertical double field integral J_z	RMS phase error
0.1 Gm	0.4 Gm	0.3 Gm^2/ 1.5 µm	1.8 Gm^2/ 9 µm	2°-6°

2.4. Technology

In this sub chapter, we review the different existing technological solutions to produce IDs. Since most IDs are made of permanent magnets, an emphasis is placed on permanent magnet material. We also present the numerical method used at the ESRF to design an insertion device. Finally the magnetic measurement benches and the magnetic correction techniques are exposed. This subchapter is mainly inspired by the lecture given by J. Chavanne [22].

2.4.1. Permanent magnets

Fundamental magnetism

One characterizes ferromagnetic material with a spontaneous magnetization and a Curie temperature. The spontaneous magnetization is the magnetization which a ferromagnetic material exhibits naturally without any magnetic source. The Curie temperature is the temperature threshold above which a ferromagnetic material no longer exhibits a spontaneous magnetization. Only few elements exhibit ferromagnetic properties at ambient temperature. The magnetic elements are mainly the transition Metals (M) such as Fe, Ni and Co and the Rare earth elements (R) also called the lanthanides.

The magnetic properties of a material arise from the electronic structure of the elements of which it is constituted. The magnetic electrons in transition metals are located on the 3d electronic shell in the atomic structure. The spin moments of the 3d electrons govern the 3d magnetism. In metals such electrons provide a high magnetization (up to 2.16 T for the Fe at ambient temperature) and a high Curie temperature. The magnetic electrons are itinerant and are very sensitive to the surrounding electric field. One can show that it leads to a low magnetic anisotropy.

The magnetic electrons involved in the rare earth magnetism populate the 4f level. Electrons on the 4f level are localized, giving rise to high magnetocrystalline anisotropy. The magnetic ordering temperature of R elements is below room temperature, except for Gd whose Curie temperature is 293 K. The spin and the orbital moments of 4f electrons contribute to the total magnetic moments of R elements. The spin-orbit interaction, which forces the parallel alignment of the spin and orbital moments of the 4f electrons, dominates the 4f magnetism. For light R elements (Pr, Nd and Sm), the coupling between moments is anti parallel whereas it is parallel for heavy R elements (Gd to Tm).

M-rich R-M compounds

The magnetic properties of M and R elements are complementary so that one may associate their properties in R-M compounds. On one side, the large M-M interactions in the R-M compounds may provide the R-M compounds with a high Curie temperature, above room temperature. On the other side, the R-M interactions allow the large magnetocrystalline anisotropy, which characterizes the R ions, to be maintained at room temperature and above.

The large R-M interaction arises from a subtle mechanism called the “hybridization” which involves the M-3d electrons and the R-5d electrons. The hybridization is directly at the origin of the coupling between the spin moments of M-3d and R-4f electrons. The coupling is systematically anti parallel.

The anti parallel coupling in R-M interactions together with the spin-orbit coupling in R ions causes a ferromagnetic coupling of R and M total moments for light R elements whereas the coupling between R and M total moments is antiferromagnetic for heavy R elements [26]. Depending on the crystallographic structure of the R-M compound, only Nd, Pr and Sm ions are potentially interesting to develop high performance magnets based on R-M compounds.

From compounds to magnets

High-performance modern magnets are based on M-rich R-M compounds. As explained above they necessarily combine a high spontaneous magnetization and a strong magnetic anisotropy at room temperature [26]. As detailed above the M-M and the R-M interactions provide the large magnetization at ambient temperature while the ordering of R and M ions in uniaxial crystal provides the necessary anisotropy. Only few R-M alloys exhibit all the required properties for the production of high performance magnet. These are the SmCo alloys ($SmCo_5$ and Sm_2Co_{17}) and the ternary alloy $Nd_2Fe_{14}B$ [27].

The crystallographic structure of SmCo alloys and $Nd_2Fe_{14}B$ are sketched in Figure 2.14 and Figure 2.15. The easy axis of SmCo alloys is oriented along the c-axis. In order to produce Sm_2Co_{17} one substitutes some Sm with Co in the Sm_2Co_{17} crystal. Depending on the Sm substitution with Co in the Sm network, the Sm_2Co_{17} structure is rombohedral or a hexagonal. The crystallographic structure of $Nd_2Fe_{14}B$ is complex. At ambient temperature, the easy axis of $Nd_2Fe_{14}B$ crystals is oriented along the c-axis.

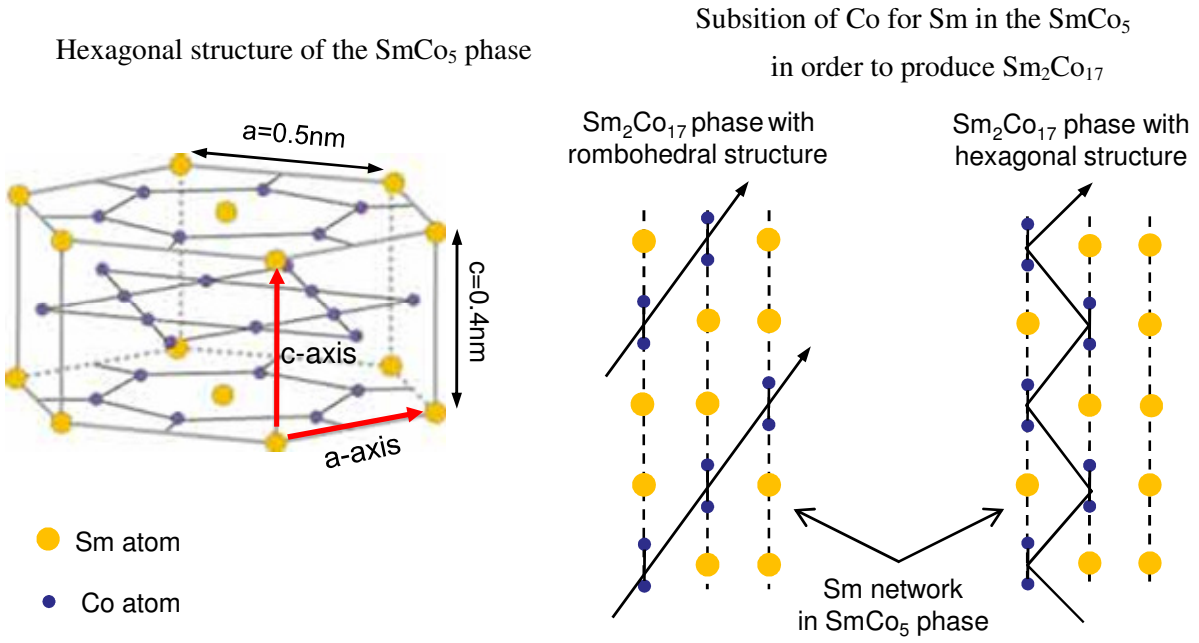

Figure 2.14: Structure of the $SmCo_5$ and Sm_2Co_{17} phases. The black arrows locate the substitution in the Sm network.

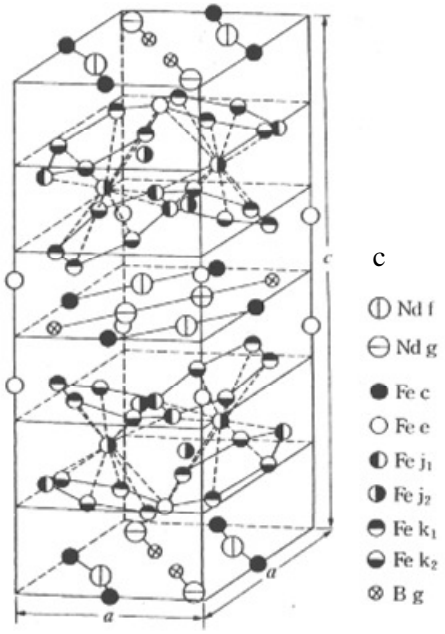

Figure 2.15: Structure of the $Nd_2Fe_{14}B$ phase, picture from Okayama university web page (http://www.magnet.okayama-u.ac.jp/magword/neomax/index.html).

The large anisotropy of R-M alloys is not sufficient to ensure that magnets based on these alloys have a large coercive field. Indeed magnetization reversal might occur in magnet defects. It is then necessary to develop special microstructures in magnet in order to avoid the propagation of the magnetization reversal in the whole magnet volume. This is the art of the permanent magnets manufacturing process.

Permanent magnet manufacturing process

The most common technology used to manufacture magnets is the powder metallurgy. This process allows the production of magnets with a high coercive field and high remanence. Figure 2.16 details this process.

The magnets produced by powder metallurgy may be seen as an assembly of independent grains. The grain axes are distributed around the macroscopic easy axis according to a Gaussian distribution. The Gaussian distribution variance is a few degrees. The grain size is typically a few tens of microns. In the thermally demagnetized state, the grains are divided into several uniformly magnetized domains. The magnetization direction alternates from one domain to the next. The region between domains in which the magnetization reverses is called a Bloch wall. In a wall the magnetization direction rotates progressively. After the magnet has been saturated, local demagnetization takes places on local defect in the magnet microstructure. The development of a coercive magnet requires the prevention of the creation and growth of domains (nucleation) with reversed magnetization in the magnet. The growth of reversed magnetization walls might be blocked on some defects present in grains (pinning process). The magnet coercive process is identified as the process which limits the magnetization reversal. The Sm_2Co_{17} coercive process is the pinning process. The nucleation is the mechanism involved in the coercive process of the $SmCo_5$ and $Nd_2Fe_{14}B$.

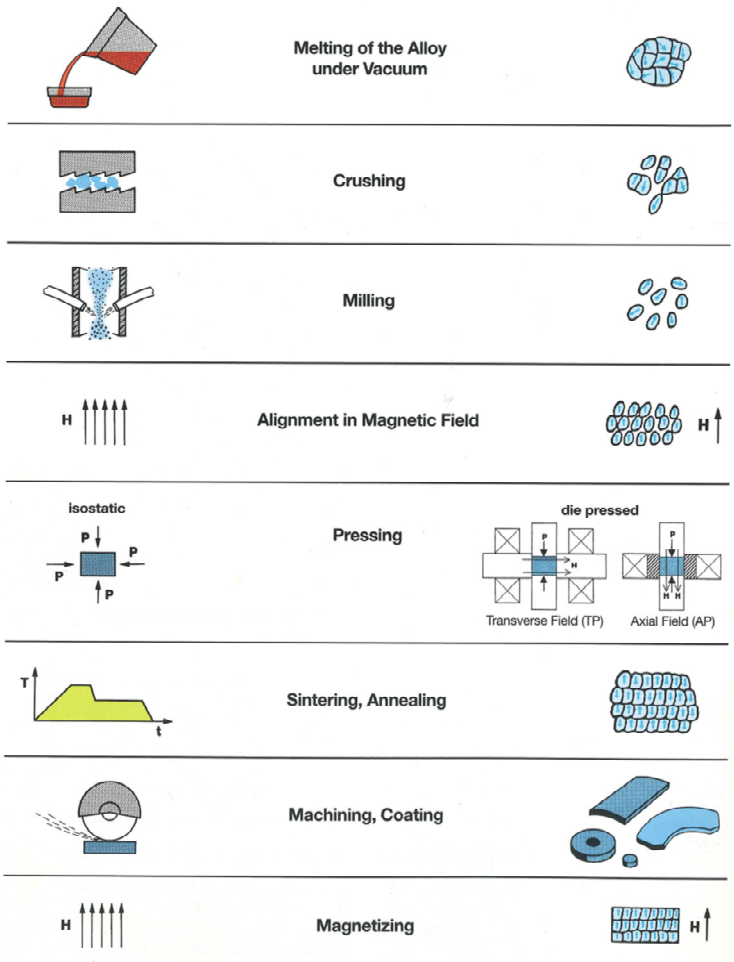

Figure 2.16: Production steps of rare-earth magnets, picture from Vacuumschmelze catalogue.

Table 2.5 lists the main permanent magnet parameters at ambient temperature produced by powder metallurgy. $Nd_2Fe_{14}B$ magnets hold the strongest remanent field B_r and offer the largest remanent field selection compared to SmCo magnets. All of them present relative permeabilities $\mu_{r\parallel}$ and $\mu_{r\perp}$ closed to unity. Their relative variation of the coercive field is negative.

Table 2.5: Remanent field, relative permeability, coercive field of the different R-M magnets at ambient temperature.

Alloy	B_r [T]	$\mu_{r\parallel}$	$\mu_{r\perp}$	$H_{cj}[kA/m]$	Curie temperature[°C]	$\Delta H_{cj}/H_{cj}\,\Delta T\ [K^{-1}]$
$SmCo_5$	0.9-1.01	1.05	1.15	1500-2400	750	-0.002
Sm_2Co_{17}	1.04-1.12	1.05-1.08		800-2000	800	-0.002/-0.005
$Nd_2Fe_{14}B$	1.0-1.4	1.04-1.06	1.15-1.17	1000-3000	310-370	-0.005

Magnets manufactured by powder metallurgy may exhibit magnetization inhomogeneities inside their volume. These magnetic errors are sources of field errors in insertion devices. The procedure used to characterize the magnet errors is discussed in section 4.1.

2.4.2. Insertion device technology

Current coils and permanent magnets are the two available sources of magnetic field. Additionally soft iron might be used to drive and concentrate the magnetic field. The most commonly used technology to build insertion devices is based on permanent magnet material. Current coil technology is dedicated to the production of long/ low field devices [28] or superconducting wigglers [29].

Permanent magnet undulator

Figure 2.18 presents various periodic permanent magnet arrangements to produce planar vertical field. K. Halbach [30] first proposed to build a pure permanent magnet undulator (PPM) with two parallel arrays of permanent magnets. The magnetization rotation from one block to the next by 90° allows a sinusoidal magnetic field with a period λ_0 to be built along the longitudinal axis. To increase the peak field along the axis, one may use soft iron poles with horizontally magnetized blocks (hybrid undulator). Both devices produce linear polarized radiation. Almost all undulators (more than 95%) installed at the ESRF use these designs.

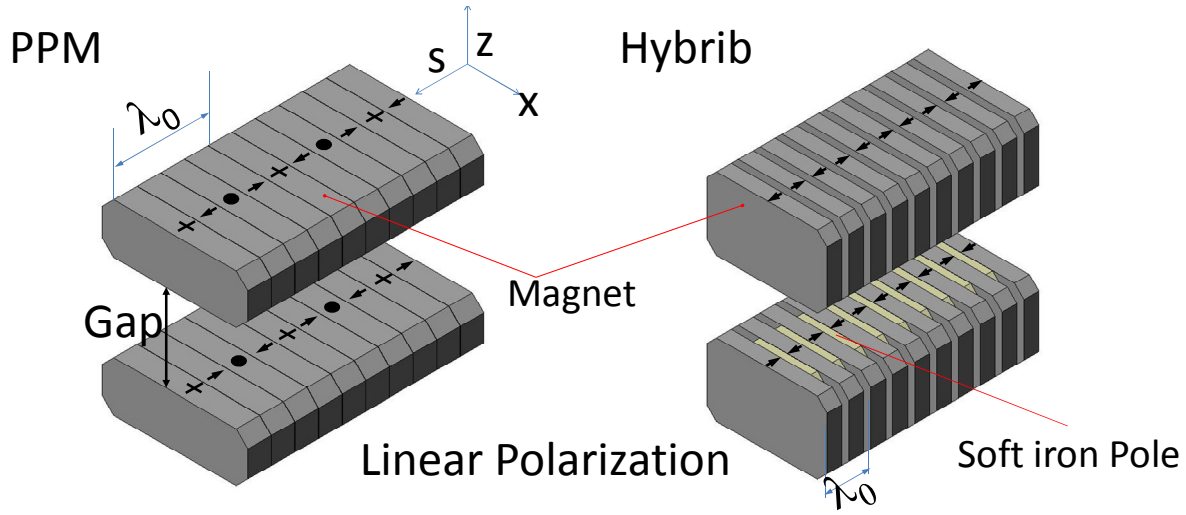

Figure 2.17: Halbach pure permanent magnet (PPM) undulator type (left) and hybrid undulator (right). Both devices produce planar vertical field.

The crossed undulator [31], [32] and the elliptical multipole wiggler [33] have been the first undulators used to produce light with circularly polarization. They consist of a superposition of two distinctive devices, one horizontally and one vertically polarized. In this scheme, magnet arrays on the lateral sides of the storage ring vacuum chamber are needed. The lateral size of the vacuum chamber limits then the minimum gaps of crossed undulators.

At the end of the eighties, P. Elleaume proposed the HELIOS design [34]. It was the first compact design with two parallel arrays of permanent magnets; this makes the production of both horizontal and vertical magnetic fields possible. The upper array produces the horizontal magnetic field component while the lower one produces the vertical magnetic field component. Moreover the longitudinal translation of the upper girder sets the phase between both magnetic field components. The HELIOS undulator is drawn in Figure 2.18. We note d the longitudinal shift of the upper girder with respect to the lower girder, B_{x_0} (B_{z_0}) is the horizontal (vertical) field amplitude on the HELIOS axis. The on axis horizontal and vertical magnetic field in an HELIOS may be written as:

$$B_x = B_{x_0}\cos\left(\frac{2\pi}{\lambda_0}(s+d)\right) \qquad B_z = B_{z_0}\cos\left(\frac{2\pi}{\lambda_0}s\right) \tag{2.79}$$

As $d = 0$, the phase between horizontal and vertical magnetic field is null, the polarization is linear. The field amplitudes do not depend on the longitudinal shift. Thus, the polarization of the radiation is changed independently of the radiation energy.

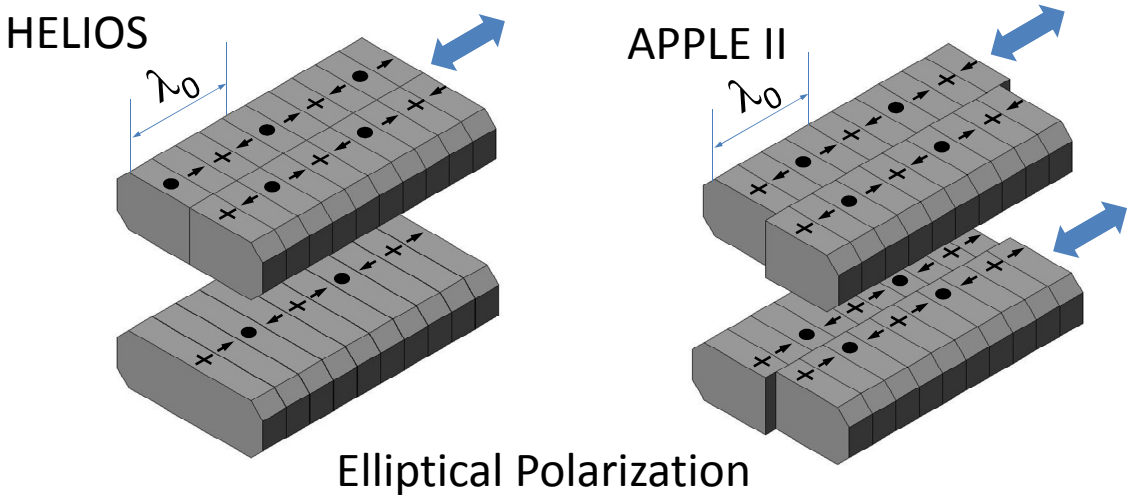

Figure 2.18 : The HELIOS and APPLE-II permanent magnet undulators. The translation of one array (HELIOS) or two arrays (APPLE-II) allows the production of both vertical and horizontal magnetic fields.

More recently the APPLE-II design has been proposed to produce ellipsoidal magnetic fields with higher peak fields [35]. The APPLE-II consists of two pairs of magnet arrays as shown in Figure 2.18. One pair of magnet arrays can move longitudinally, the top left and the bottom right magnet array. The other set of magnet arrays is fixed. Each set creates a magnetic field whose horizontal (vertical) amplitude is B_{x_0} (B_{z_0}). The longitudinal shift between the movable and fixed arrays causes a phase between the magnetic fields created by each set. If we note d the longitudinal shift between fixed and movable arrays, the field created by the four magnet arrays is [20]:

$$\vec{B} = \left(-2B_{x_0}\sin\left(\frac{\pi d}{\lambda_0}\right)\cos\left(\frac{2\pi s}{\lambda_0}+\frac{\pi d}{\lambda_0}\right), 2B_{z_0}\cos\left(\frac{\pi d}{\lambda_0}\right)\sin\left(\frac{2\pi s}{\lambda_0}+\frac{\pi d}{\lambda_0}\right)\right) \tag{2.80}$$

The phase between the horizontal and the vertical field component is always equal to $\pi/2$. The polarization then is almost always elliptical. It is linear as $B_x = 0$ or $B_z = 0$, meaning respectively $d = 0$ or $d = \lambda_0/2$. The polarization may also be circular as:

$$d = \frac{\lambda_0}{\pi}\tan^{-1}\left(\frac{B_{z_0}}{B_{x_0}}\right) \tag{2.81}$$

Since the field amplitude of B_x and B_z depends on the longitudinal shift d, the polarization of the radiation cannot be adjusted independently of the radiation energy. Therefore setting up the polarization without modifying the radiation energy implies to tune the gap of the APPLE-II accordingly.

Helical undulators present a broader variation of the peak field off axis, compared to the planar ones. This may have a strong impact on beam dynamics [36]. In order to limit this, helical undulators with 6 magnet arrays have been built. In this case the upper and lower central arrays generate a vertical field while the outer four arrays generate a horizontal field. The longitudinal shift between the four outer arrays and the central ones set the phase between the horizontal and the vertical component of the magnetic field.

Opening and closing the gap change the magnetic peak field and so forth the deflection parameter. To do so, the undulator is mounted on a mechanical support. Such mechanical supports are specially designed to keep the arrays parallel despite the large magnetic attraction between them. Assuming a

planar undulator with a sinusoidal field with a peak field B_{z_0}, length L and width W, the force between the two girders is [22]:

$$F = \frac{1}{4\mu_0} B_{z_0}^2 LW \tag{2.82}$$

The magnetic forces between arrays can reach a few 10^5N. Figure 2.19 presents a PPM mechanical support developed at the ESRF.

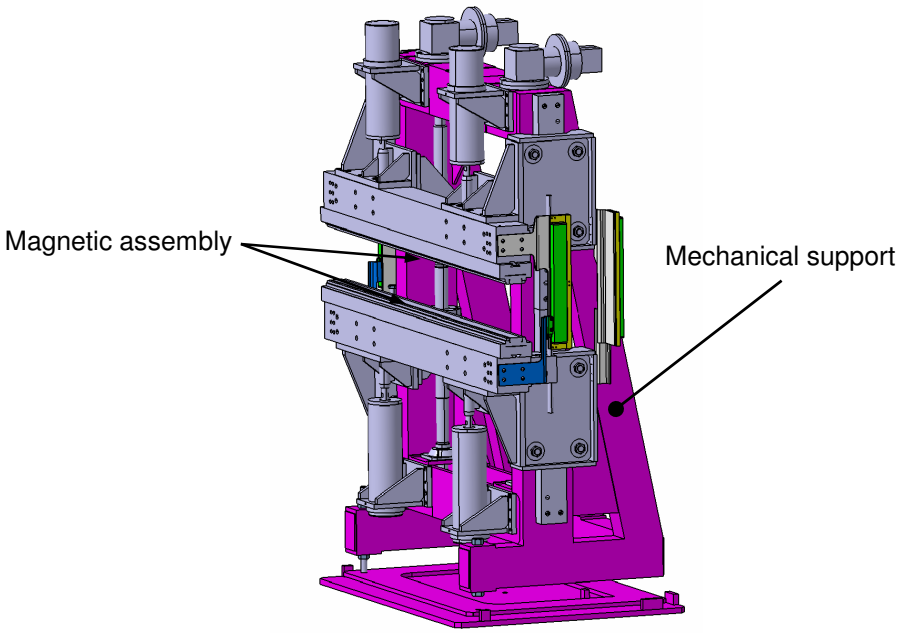

Figure 2.19: Standard mechanical support developed at the ESRF.

Electromagnet undulator

Usually the ElectroMagnetic undulators (EM) are made of Copper coils that drive the field in soft iron poles. This technology is similar to the one used to build accelerator magnets such as quadrupoles and sextupoles. It does not require a mechanical support which allows a variable gap. Indeed the current in coils sets the peak field. For a given gap and short period, the peak field B_{EM} of an EM undulator is usually smaller than B_{PPM}, the peak produced by a PPM undulator. Assuming a 2D model of both PPM and EM undulators, their peak field ratio is [22]:

$$\frac{B_{EM}}{B_{PPM}} \approx 0.11\mu_0 \frac{\lambda_0 J}{B_r} \tag{2.83}$$

Where B_r is the magnet remanent field and J the density current. Getting the same peak field as the one of a PPM design with a 35 mm period made of $Nd_2Fe_{14}B$ magnets with $B_r = 1.2\ T$, requires current density in the coils to be 244 A/mm^2. Such a current density is far beyond the maximum current density achievable at room temperature (20 A/mm^2). Consequently at room temperature, the EM undulators are limited to long periods, low field devices. Superconducting coils handle such current density so that one designs superconducting wigglers; the achievable peak field might be as high as 10 T [37]. One interest of the EM is the production of elliptically polarized light with a fast switching of the polarization state by using an AC current.

2.4.3. Field computation

Magnetic field computation allows the magnetic design optimization of an insertion device. The numerical simulation and the magnetic optimization of an insertion device are generally performed in

two steps. One first designs the periodic part to ensure that the insertion device provides the required peak field amplitude with the smallest magnet volume. Generally, the magnetic field periodicity and symmetry ensures a zero field integral. However the symmetry is broken at the extremity. Thus some field integrals may be generated at the extremity. The undulator extremity is designed to minimize them. We first review the integral method used to compute the magnetic fields of insertion devices. Planar designs (PPM and hybrid) are then given as a magnetic calculation illustration.

Integral method

The Finite Element Method (FEM) has been successfully implemented to solve a large number of physical problems. Within the FEM software, the undulator geometry is meshed in order to compute the magnetic field on each node of the meshes. In particular the geometry needs to be meshed to infinity in order to compute the insertion device field integral. An accurate FEM computation would result in a large number of nodes. An alternative approach, the integral method is well suited to solve magnetostatic problems with opened geometries.

A volume V uniformly magnetized according to $\vec{M}$ with an arbitrary shape produces a magnetic field $\vec{B}$ at a point $P(x,z,s)$ that can be written as:

$$\vec{B}(P) = Q(V,P)\vec{M} \tag{2.84}$$

The field integral $\vec{I}(x,z)$ can also be expressed in the matrix form:

$$\vec{I}(P) = G(V,P)\vec{M} \tag{2.85}$$

Q and G are 3×3 matrix which depends on the volume geometry and its relative position with the point P. The expressions of Q and G have been derived analytically for general shapes such as rectangles [10] and general polyhedrons [38]. The integral method approach consists then of dividing any magnet or soft material into N small volumes so that the magnetization in each small magnet is considered to be uniform. With the integral method, the magnetic field $\vec{B}(P)$ and the field integral $\vec{I}(x,z)$ is simply the sum of the fields or the field integrals that each single volume produces:

$$\vec{B}(P) = \sum_{i=1}^{N} Q(V_i,P)\vec{M}_i \qquad\qquad \vec{I}(P) = \sum_{i=1}^{N} G(V_i,P)\vec{M}_i \tag{2.86}$$

The problem now is to determine the magnetization in each small volume V_i. In any material, the magnetization depends on the local magnetic field $\vec{H}$ through the material property $\vec{M}(\vec{H})$:

$$\vec{M}(\vec{H}) = \vec{M}_0 + \chi\vec{H} \tag{2.87))}$$

$\vec{M}_0$ is the material remanent magnetization and χ the material susceptibility possibly dependant on $\vec{H}$. Finally the magnetic field $\vec{H}_i$ in the centre i of each small volume V_i must be first computed in order to find out the magnetization $\vec{M}_i(\vec{H}_i)$. The magnetic field $\vec{H}_i$ in the centre i originates from the magnetization $\vec{M}_j(\vec{H}_j)$ of all small volumes V_j and its expression is:

$$\vec{H}_i = \sum_{j=1}^{N} Q_{ij}(V_j,i)\,\vec{M}_j(\vec{H}_j) = \sum_{j=1}^{N} Q_{ij}(V_j,i)\left(\vec{M}_{0\,j} + \chi\vec{H}_j\right) \tag{2.88}$$

$Q_{ij}(V_j,i)\vec{M}_j(\vec{H}_j)$ represents the volume V_j contribution to the magnetic field $\vec{H}_i$ at the position i. The magnetization determination in each small volume V_i implies solving the N following equations:

$$\vec{M}_i = \vec{M}_{0_i} + \chi\vec{H}_i = \vec{M}_{0_i} + \chi\sum_{k=1}^{N}\left(\delta_{ik}I_3 - Q_{ik}(V_k,i)\right)^{-1}\left(\sum_{j=1}^{N} Q_{ij}(V_j,i)\,\vec{M}_{0\,j}\right) \tag{2.89}$$

The matrix I_3 is the 3×3 unity matrix and δ_{ik} the Kronecher symbol. Actually one builds for N volumes a $3N \times 3N$ matrix $\left(\delta_{ik}I_3 - Q_{ik}(V_k,i)\right)^{-1}\left(\sum_{j=1}^{N} Q_{ij}(V_j,i)\,\vec{M}_{0\,j}\right)$ called the interaction matrix.

The magnetization determination in the magnetic source volume reduces to the inversion of the interaction matrix. However, whenever the geometry is divided in a few hundred small volumes, the interaction matrix becomes too large and ill conditioned to allow a direct inversion. The so called computer code RADIA [39], which is based on this integral approach, implements an iterative procedure to determine the magnetization inside each small volume. The iteration stops when the magnetization $\vec{M}_i$ is stable in each small volume to a specified precision. RADIA is used for the design of insertion devices at the ESRF.

We now present an example of PPM and hybrid design of a planar undulator with an 18 mm period. We name PPM18 (HYB18) the PPM (hybrid) design. The permanent magnet is made of $Nd_2Fe_{14}B$ material. The soft material considered for the HYB18 design is a low carbon steel. Figure 2.20 displays the magnetization curves used to describe the $Nd_2Fe_{14}B$ magnets and the low carbon steel XC06.

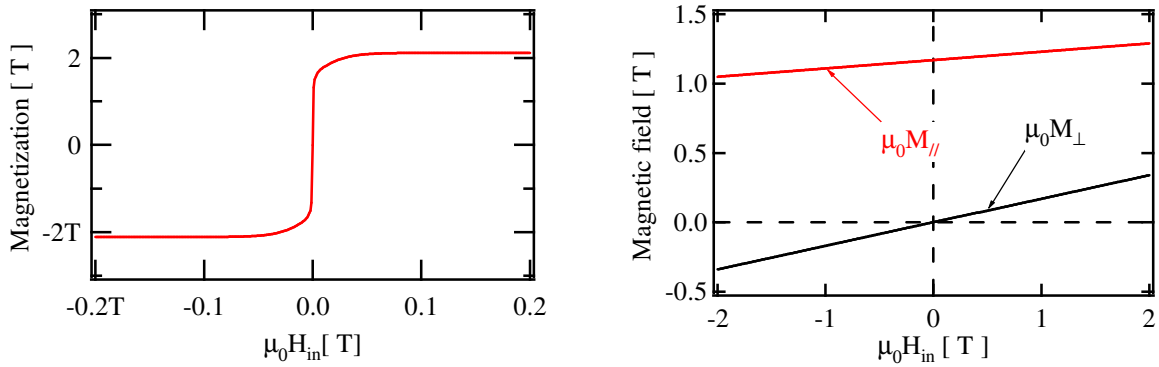

Figure 2.20: Description in RADIA of the pole (low carbon steel XC06, left plot) and magnet ($Nd_2Fe_{14}B$, right plot) material. The permanent magnet is made of $Nd_2Fe_{14}B$ material with a 1.17 T remanence and a susceptibility of 0.06 (0.15) parallel (perpendicular) to the easy axis.

Periodic part design

The Halbach PPM and the hybrid undulators are the most commonly used insertion devices, thus we will use their design process as an example. The design of the periodic part of ID aims to obtain the highest on axis amplitude B_0. Another constraint is to target constant field amplitude along the transverse horizontal axis, in order to minimize effect on the beam dynamics [40]. Designing the periodic part of such devices means optimizing their geometrical parameters. Figure 2.21 compares the peak field attainable with PPM18 and HYB18 designs as a function of the magnet volume per period. For each magnet volume, the geometries are optimized to produce the highest field. As the magnet volume increases, the PPM18 peak field reaches a limit while the HYB18 peak field still increases. Consequently the main constraint in designing PPM18 is to minimize the magnet volume (it limits the cost and size of the device). On the other side designing HYB18 geometry means producing the highest field for a given magnet volume.

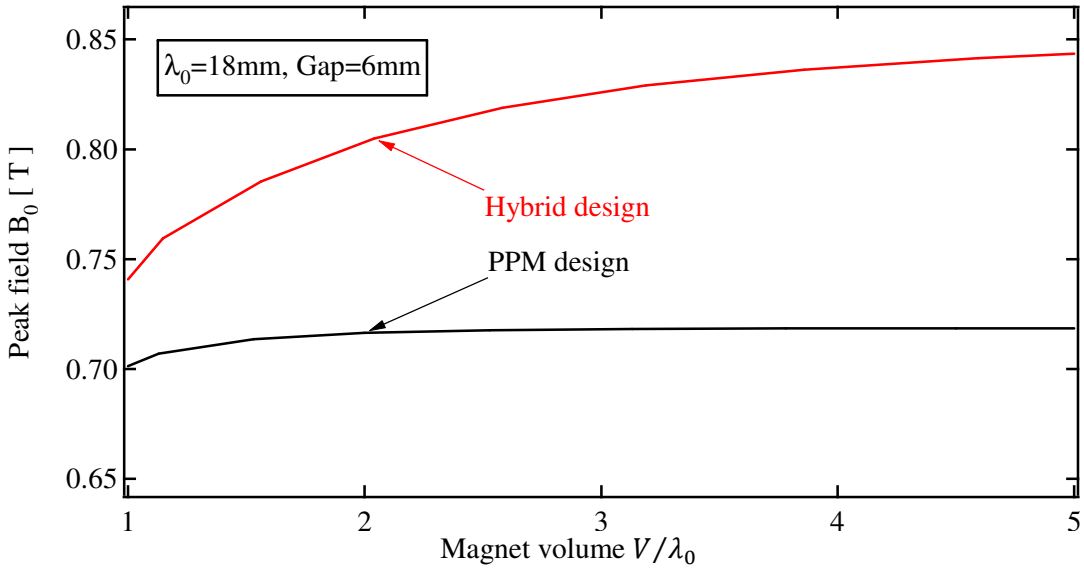

Figure 2.21: Comparison between peak fields reachable with a hybrid undulator (red curve) and a PPM undulator (black curve). Magnet dimension: $\left(2\sqrt{V/2\lambda_0}, \sqrt{V/2\lambda_0}, \lambda_0/4\right)$ for the PPM design. Magnet dimension for the hybrid design $\left(\sqrt{0.134V}, \sqrt{0.268V}, 6.2\right)$.

Figure 2.22 represents 1/8th of a PPM period on the left side, as well as 2 PPM periods on the right side. It can be observed that by applying relevant symmetries on the elementary geometry (the 1/8th of the PPM period), one can build the whole periodic part of the PPM undulator. Thus, the magnetic field of the periodic part might be computed from this elementary geometry, allowing a fast computation of the magnetic field. Concerning the parameters to adjust in order to optimize the design, here the magnet thickness L_s is constant and equals $\lambda_0/4$. Therefore the only free parameters left are the magnet width L_x and height L_z.

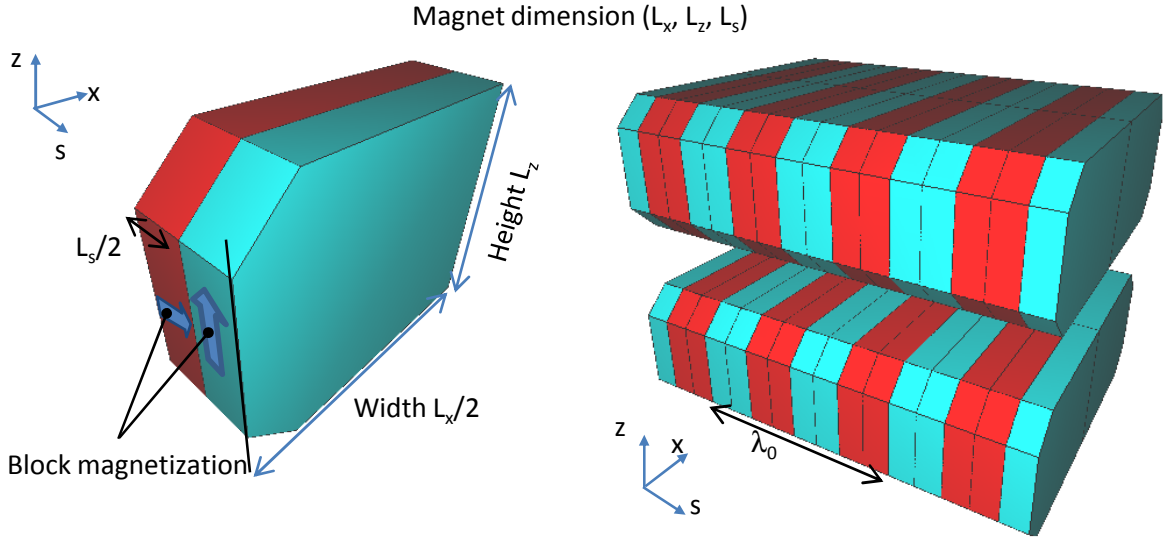

Figure 2.22: 1/8th period of PPM18 undulator (left) designed with RADIA. The parameters to be optimized are the height and width of magnets. Symmetries are applied on the 1/8th period to build the periodic part with RADIA (right). The gap is fixed at 6 mm.

Figure 2.23 represents the variation of the PPM18 on axis field amplitude as a function of the magnet width and height. The width has a stronger impact on the magnetic performance than the height. Indeed widening the magnets from $0.5\lambda_0$ to $2\lambda_0$ increases the field amplitude by more than

20%. On the other hand the same height enlargement only increases the field amplitude by less than 5%. Moreover greater magnet width ensures better field homogeneity. The on axis field amplitude reaches a limit when the magnet height is larger than $2\lambda_0$. However the field amplitude decreases by less than 3% as the magnet width is reduced from $2\lambda_0$ to λ_0. Such width reduction leads to a much more compact design with a negligible reduction in the on axis field amplitude. This leads to the usual selection of a magnet width somewhere between λ_0 and $2\lambda_0$. We use similar considerations to set the magnet height.

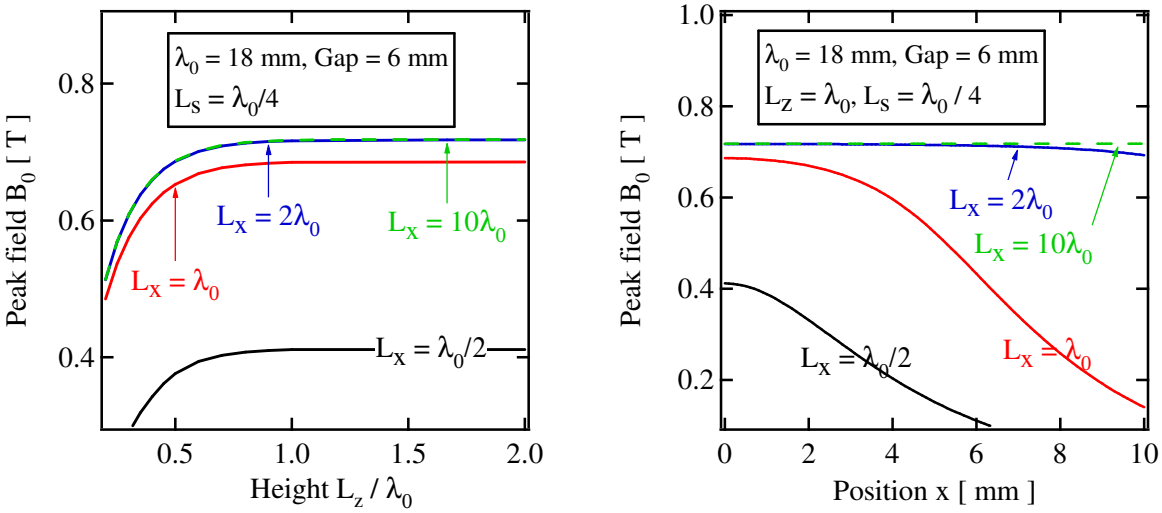

Figure 2.23: Variation of the PPM18 on axis field amplitude (left plot) and off axis (right plot) for different heights and widths. The computations are performed with RADIA.

Figure 2.24 represents the elementary geometry and a full period of the hybrid undulator HYB18 with 18 mm period. Designing a hybrid undulator is more complex than designing a PPM since we need to optimize more parameters. The parameters to be optimized are $(L_{x_m}, L_{z_m}, L_{s_m})$ and $(L_{x_p}, L_{z_p}, L_{s_p})$, which are the respective dimensions of magnets and poles.

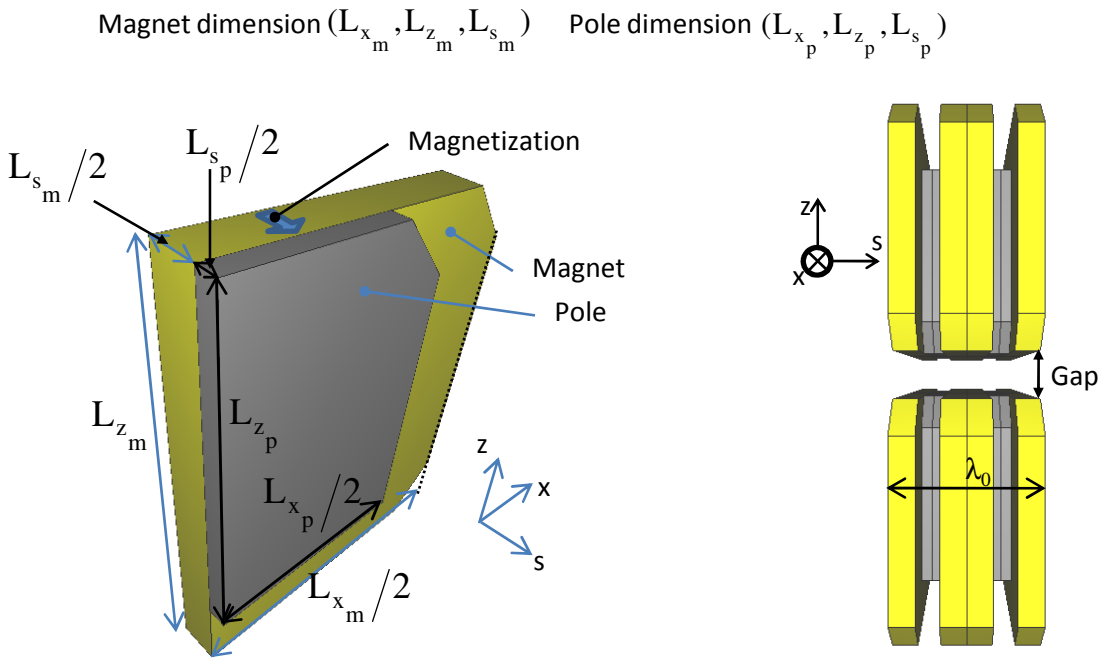

Figure 2.24: 1/8th period (left) and a full period (right) of a HYB18 designed with RADIA.

A hybrid design is optimized in a similar way as for a PPM design. Table 2.6 presents the chosen dimensions of pole and magnet for the HY18 design. The optimization of the geometrical parameters (height, width and thickness of magnet and pole) leads to hybrid design with narrow pole. We will now detail the variation of the magnetic peak field with the different geometrical parameters.

Table 2.6: Geometrical parameters of pole and magnet.

	Magnet	Pole
Width L_x [mm]	50	32
Height L_z [mm]	30	24
Thickness L_s [mm]	6.2	2.8

Figure 2.25 represents the variation of on axis peak field amplitude as a function of the magnet width and height. The field amplitude increases with magnet volume and becomes almost constant as the magnet transverse dimension exceeds the pole transverse dimension. It is a common practice to choose the magnet dimension which allies small size and high peak field.

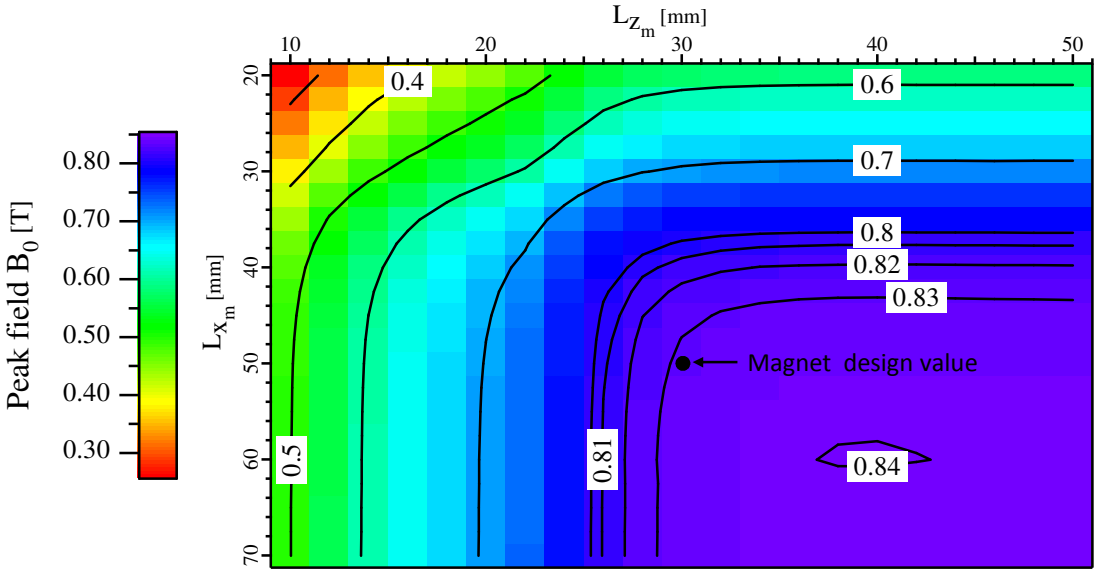

Figure 2.25: On axis peak field variation with the magnet width L_{x_m} and height L_{z_m}. The inserts label the contour lines of the on axis peak field (black lines). The computations are performed with RADIA. Magnet dimension is $(L_{x_m}, L_{z_m}, 6.2\ mm)$, the pole dimension $(32\ mm, 24\ mm,\ 2.8\ mm)$. The undulator gap is closed at 6 mm.

Figure 2.26 displays the on axis peak field as a function of the pole width and height. The peak field is almost constant as the pole width (height) is smaller than 50 mm (30 mm). Indeed, for smaller pole dimension, the peak field varies from 0.8 T to 0.840 T meaning an optimization of 5%. We choose the pole height (24 mm) which maximizes the peak field. The design pole width (32 mm) is much larger than the width (18 mm) which maximizes the peak field. Indeed it is necessary to select a wide pole in order to get constant off axis field amplitude. With this design the peak field is equal to 0.832 T, meaning a peak field difference with the maximum achievable less than 1%.

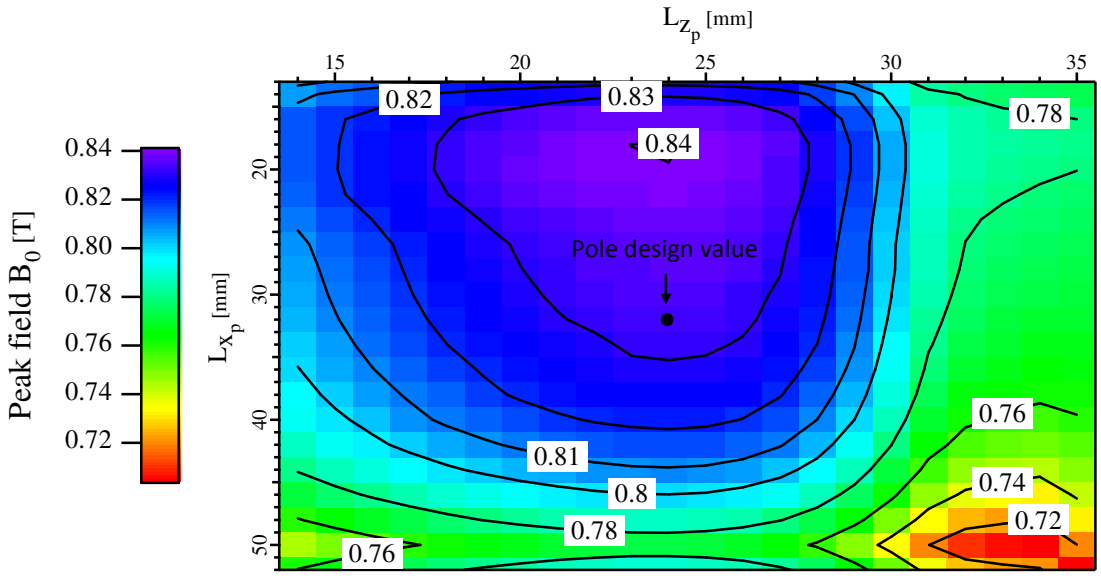

Figure 2.26: On axis peak field variation with the pole width L_{x_p} and height L_{z_p}. The inserts label the contour lines of the on axis peak field (black lines). The computations are performed with RADIA. Pole dimension $\left(L_{x_p}, L_{z_p}, 2.8\ mm\right)$. Magnet dimension $(50\ mm, 30\ mm,\ 2.8\ mm)$. The undulator gap is closed at 6 mm.

Figure 2.27 displays the off axis field homogeneity along the horizontal axis as a function of the magnet volume. The field homogeneity increases with the magnet width. The field is nearly constant off axis over 10 mm with a 50 mm magnet width.

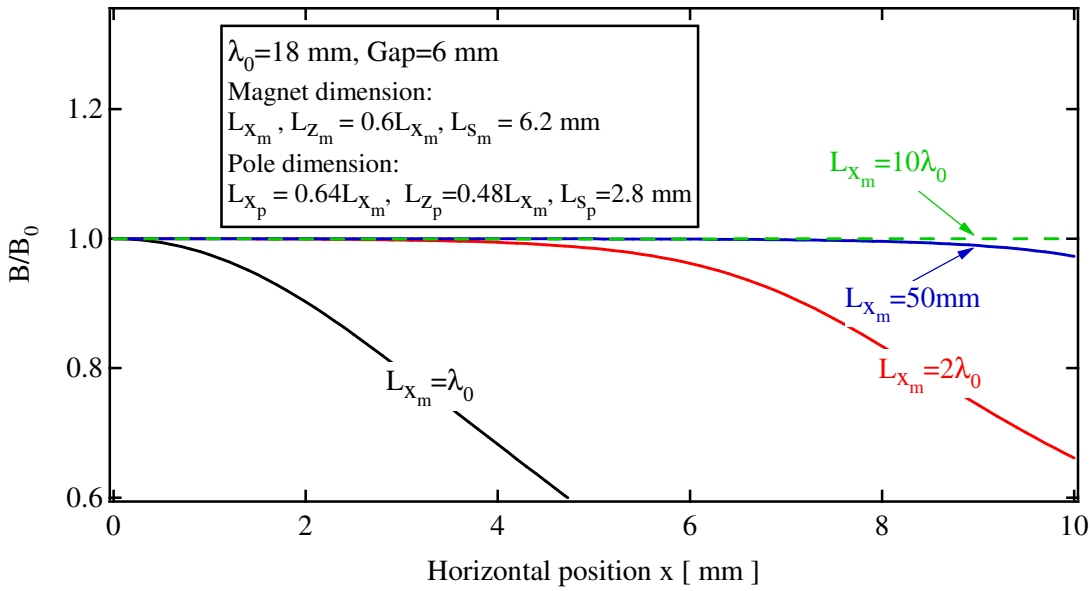

Figure 2.27: Field homogeneity along the horizontal axis as a function of magnet width. The computations are performed with RADIA.

The on axis magnetic field is not a pure sinusoidal and contains higher harmonics. Its decomposition in Fourier series is:

$$B_z = \sum_{n=1}^{\infty} B_n \sin\left(\frac{2n\pi}{\lambda_0} s\right) \tag{2.90}$$

B_n is the amplitude of the nth magnetic field harmonic. As the magnetic field is made of several harmonics, the deflection parameter becomes [41]:

$$K_x = \sqrt{\sum_{n=1}^{\infty} \left(\frac{e\lambda_0 B_n}{n2\pi mc^2}\right)^2} \tag{2.91}$$

Because of the $1/n$ term in brackets, high harmonics have a reduced impact on deflection parameter. The presence of high harmonics change the deflection parameter K_x; this causes a shift of the fundamental harmonic in the X-ray spectrum. Therefore the thickness of magnets and poles should be optimized in order to maximize the first harmonic of the magnetic field while keeping the higher order harmonic as small as possible. This is a particularity of the HYB18 design. Actually the magnetic field of PPM undulator also contains several harmonics. However the $\lambda_0/4$ PPM structure ensures that high order harmonics have rather low amplitude [42]. Figure 2.28 displays the variation of the peak field and the first harmonic as a function of the magnet thickness. Concerning the maximum peak field (first harmonic) is achieved for a magnet width equal to 6.5 mm (6.2 mm).

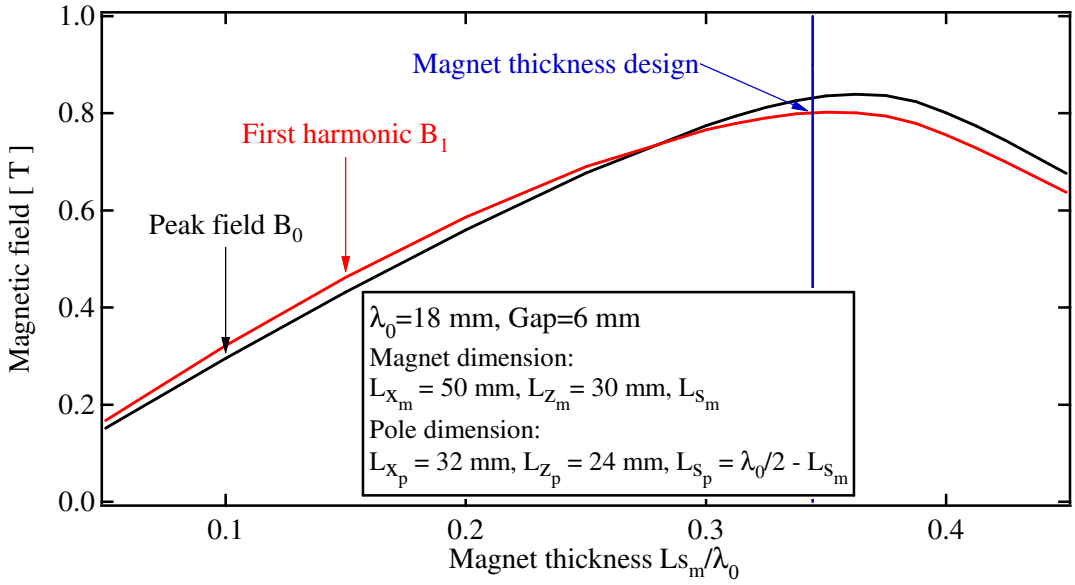

Figure 2.28: Variation of the on axis peak field and first harmonic with the pole and magnet thickness. The computations are performed with RADIA.

The main advantage of the hybrid design is the higher peak field that can be achieved for a given gap and a given period. Figure 2.29 presents the variation of the field amplitude with respect to g/λ_0, the ratio of the gap over the period assuming PPM and hybrid design with a 18 mm period. For small g/λ_0, the field diverges from pure sinusoid and the higher peak field arises from higher harmonics. As far as peak field is concerned, hybrid design is clearly advantageous for small g/λ_0. Thus devices with a small gap or a large period are designed with poles made of soft material.

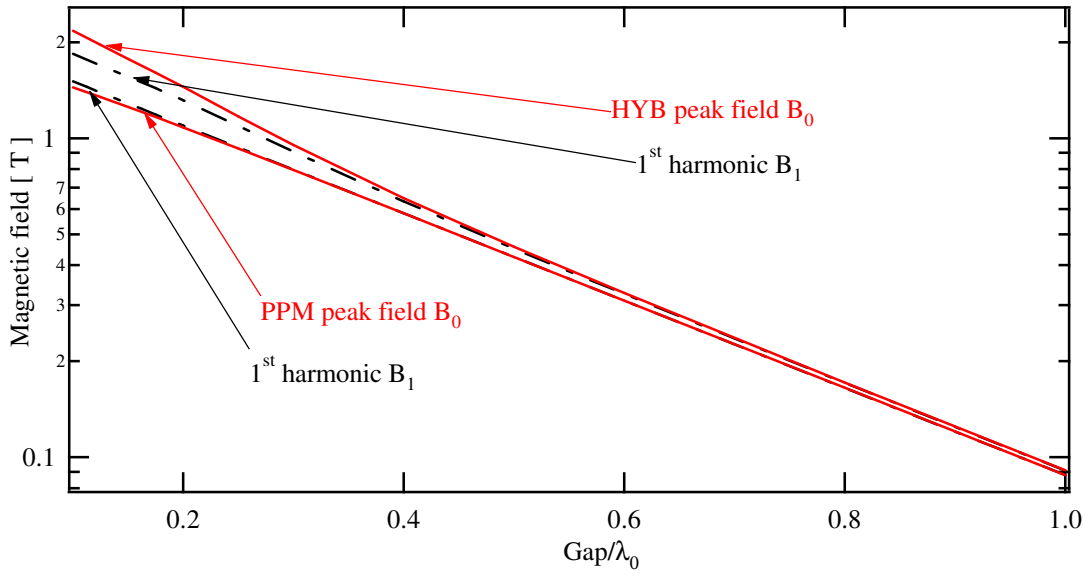

Figure 2.29: Peak field and first harmonic variation for a 18 mm period undulator. PPM and HYB designs are considered. The computations are performed with RADIA.

Field termination

In an undulator, the symmetry of the periodic part ensures a zero field integral $\vec{I}$. However at its extremities the symmetry is broken and a field integral $\vec{I}$ may be produced. The field integral depends on the magnetic gap and on the permeability of magnetic materials used. If one considers an insertion device made of magnetic material with zero susceptibility, its extremity design is rather simple and is a pure geometrical problem. On the other hand, designing extremity with materials, which have non zero susceptibility, is a full 3D magnetostatic problem.

At the ESRF, insertion devices are generally designed in such a way that both extremities generate a field integral with opposite signs. Such an insertion device has a zero field integral and is said to be antisymmetrical. In the meantime it produces a double field integral $\vec{J}$. As a result, a design with low integral at each extremity is necessary to ensure small values for both $\vec{I}$ and $\vec{J}$ at any gap. The field integral generated at the extremities can be broken up into three contributions:

$$\vec{I} = \vec{I}_{down} + \vec{I}_{up} + \vec{I}_{int} \tag{2.92}$$

$\vec{I}_{down}(\vec{I}_{up})$ is the field integral produced by the lower (upper) magnetic array assuming the upper (lower) girder is removed. Because of the material relative permeability, each magnetic array modifies the magnetization of the other one at a small gap value. As a result the field integral may differ from the sum of the upper and the lower girder. This difference $\vec{I}_{int}$ is called the interaction. The interaction is rather low for PPM design and may be large for hybrid design. The interaction tends to be zero at large gap values.

Both $\vec{I}_{down}$ and $\vec{I}_{up}$ are sensitive to the magnet position and magnetization. This offers some tools to correct them. On the other side the interaction is almost insensitive to magnets position and magnetization so there is no easy way to correct it efficiently. Additionally the interaction has a specific dependence on ID gap which is often difficult to correct with conventional methods (shimming). Optimum design of termination is therefore needed to minimize the interaction variation with the gap.

Several PPM terminations have been developed at the ESRF [22], [43]. Figure 2.30 represents two of them. The most complicated PPM termination uses magnets whose magnetization has an angle with the horizontal axis in the range of 30°-45°. The adjustable parameters are the end magnet width and

the magnetization angle. Such end field structures have been specifically designed to segment the undulators without significant loss on the spectral flux. Indeed if one considers two PPMs with an air gap in between, this type of end structure is also optimized to minimize the phase advance variation with the gap from one PPM to the other. Instead of assembling several meters long PPM, one builds smaller undulators that are phased together. The PPM segmentation also eases the design of the mechanical support. The other structure represented in Figure 2.30 uses two magnet blocks, one horizontally magnetized and the other one vertically magnetized. The vertically magnetized end magnet has its longitudinal dimension which is equal to one half of standard magnets used in the periodic part. The thickness of the end magnet with the horizontal magnetization is approximately $3\lambda_0/20$. Thanks to this end structure we obtain a small variation of the field integral with the gap. This has mostly been used for PPM in-vacuum undulators. In-vacuum undulators are discussed in section 3.1.1.

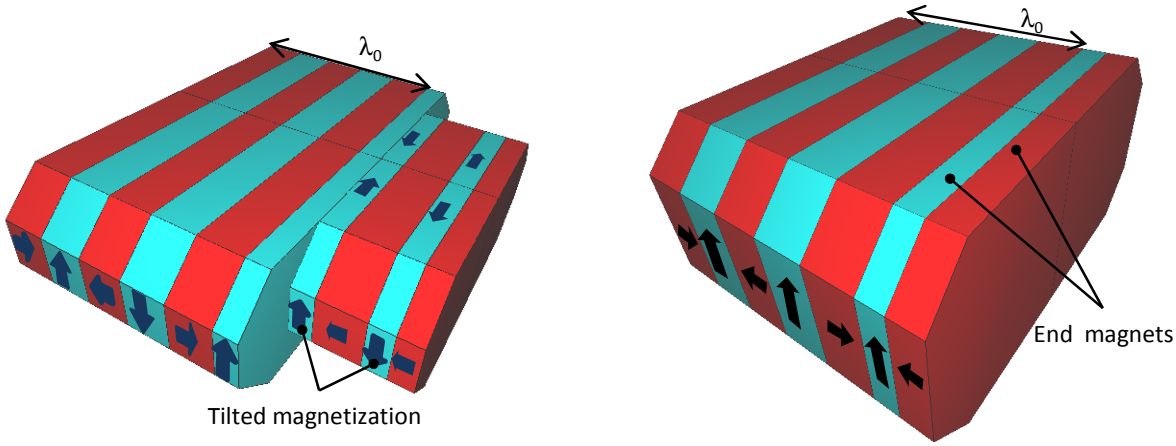

Figure 2.30: PPM design terminations. The left PPM termination design uses magnets with tilted magnetization. The right PPM termination design uses two magnets with vertical or horizontal magnetization.

Designing a hybrid end field termination is more complex than for a PPM. The hybrid termination optimization minimizes only the field integral variation. Figure 2.31 represents the hybrid end structure and is designed with two narrow magnets (magnet A and B) and one thin pole. The parameters to play with, in order to minimize the field integral, are the air gaps and the thickness of the end pole and magnets. The dimensions of pole and magnets are listed in Table 2.7.

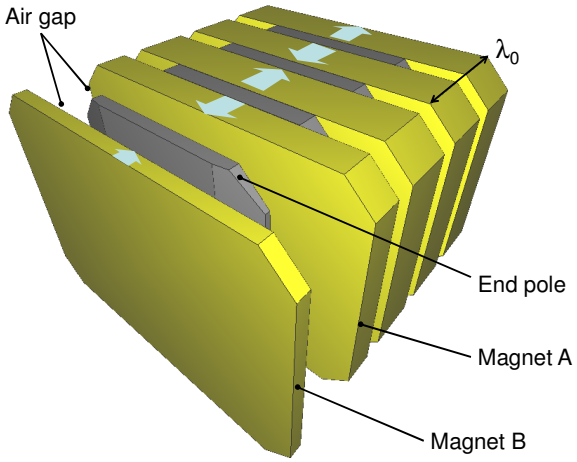

Figure 2.31: HYB18 design termination. The hybrid termination is made of two narrow magnets (A and B) and one pole. The pole is placed in an air gap between ends magnet.

Table 2.7: Air gaps and thickness of end magnets and pole for HYB18 termination.

L_s (mag. A/ mag. B/ pole)	4.75 mm / 2 mm/ 1.85 mm
Air gap between mag. A and pole	2.7 mm
Air gap between pole and mag. B	3.75 mm

Figure 2.32 represents the field integral achieved per extremity with both designs described above. The interaction and the field integral per girder achieved with the PPM18 design are rather low, less than 2 Gcm. Hence the field integral per extremity is also low. The hybrid extremity optimization keeps the field integral below 10 Gcm. The field per extremity is maintained at any gap below the maximum tolerated value reported in equation (2.59). However, in practice, magnetic correction on both girders may lower the field integral to a smaller value. Now we will introduce the magnetic measurement and correction.

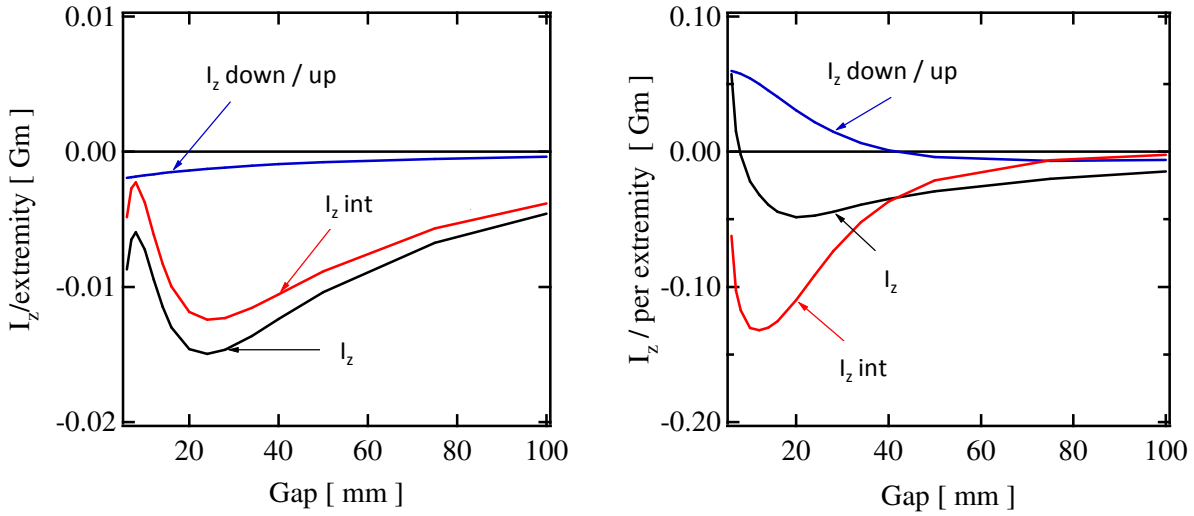

Figure 2.32: Field integral variation with the magnetic gap per extremity for the PPM18 (left plot) and the HYB18 (right plot).

2.4.4. Magnetic field measurement and correction

The field integrals and the RMS phase error characterize the effect of magnetic errors on the closed orbit and on the spectral flux. Hence measurement of both magnetic quantities is necessary to characterize magnetic errors. We detail hereafter the different measurement benches to perform field integral and local field measurement.

Field integrals measurement

The field integral measurement benches are based on the magnetic flux measurement that a closed loop intercepts [22], [44]. The wire used for the loop is a conductor. As a magnetic flux variation through loop surface induces a voltage at the loop extremities, the loop is moved within the magnetic source. Finally the created voltage is then integrated. Two loop geometries are used at the ESRF to measure the field integral:

- The rotating coil.
- The stretch wire.

Figure 2.33 represents the rotating coil geometry which is used to measure the undulator field integrals. The geometry is a large rectangular coil along the longitudinal axis. Practically speaking, the rotating coil is built using a multiturn wire which is stretched between two synchronized rotation

stages. The coil can be rotated around its longitudinal and translated along its own vertical and horizontal axis. In order to measure the second field integral, the coil is twisted so that its cross section is no longer rectangular. Later on, we express the magnetic flux through the different coil geometries.

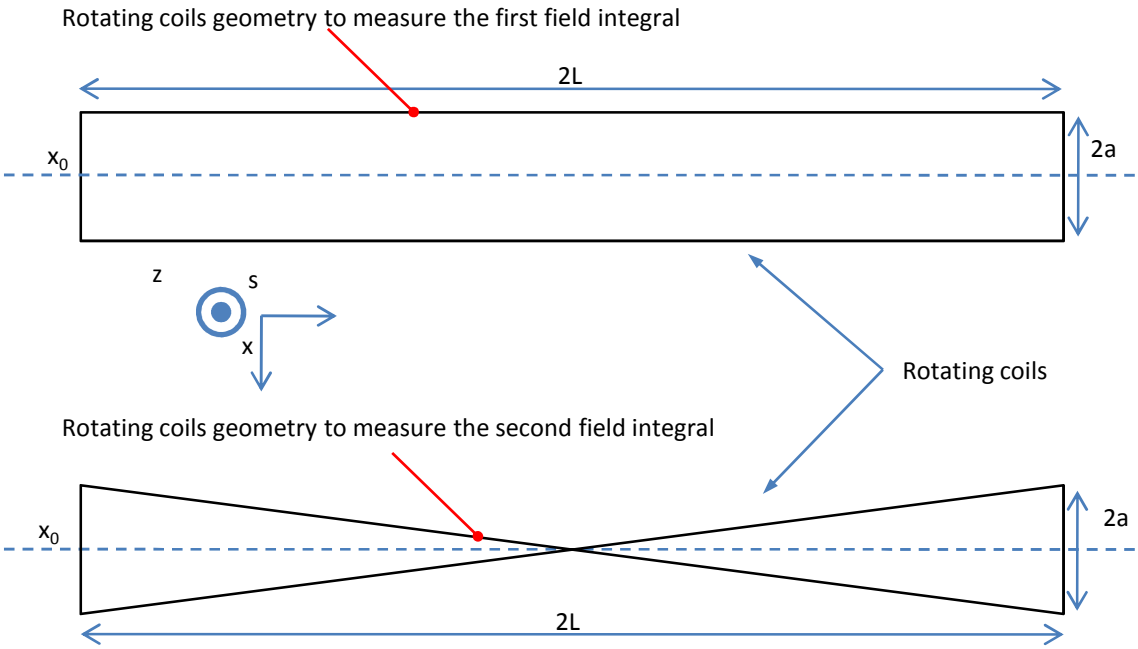

Figure 2.33: Rotating coil geometries used in order to measure the first and second field integral. Coil rotation measures locally vertical and horizontal field integral while a coil translation measures the integral variation.

The rectangular section of the rotating coil intercepts the magnetic flux centred on the position (x_0, z_0). The coil orientation allows the selection of the first field integral component to be measured. When the coil is in the vertical (horizontal) plane, the magnetic flux Φ_x (Φ_z) collected by the coil, is given by:

$$\Phi_x(x_0, z_0) = N \int_{z_0-a}^{z_0+a} \left(\int_{-L}^{L} B_x(x_0, z, s)\, ds \right) dz$$
$$\Phi_z(x_0, z_0) = N \int_{x_0-a}^{x_0+a} \left(\int_{-L}^{L} B_z(x, z_0, s)\, ds \right) dx \qquad (2.93)$$

N is the number of turns and 2a is the width of the coil. In practice the rotating coil length is much longer than the undulator length in order to intercept the entire undulator field produced along the longitudinal direction, including its edge field. At the ESRF the coil is 4m (3-4 mm) long (width). Since the undulator length does not exceed 2 m, one replaces $+L$ $(-L)$ with $+\infty$ (-∞) in equation (2.93). We write the flux intercepted by the coil as follows:

$$\Phi_x(x_0, z_0) = 2aN\langle I_x(x_0, z_0)\rangle_{2a} \qquad \Phi_z(x_0, z_0) = 2aN\langle I_z(x_0, z_0)\rangle_{2a} \qquad (2.94)$$

With:

$$\langle I_x(x_0, z_0)\rangle_{2a} = \frac{1}{2a} \int_{z_0-a}^{z_0+a} I_x(x_0, z)\, dz \qquad \langle I_z(x_0, z_0)\rangle_{2a} = \frac{1}{2a} \int_{x_0-a}^{x_0+a} I_x(x, z_0)\, dx \qquad (2.95)$$

The horizontal (vertical) magnetic flux is proportional to the horizontal (vertical) first field integral component averaged over the coil width.

When the rotating coil is twisted, the magnetic flux which it is intercepted becomes [22]:

$$\begin{aligned}\Phi_x(x_0,z_0) &= 2aN\left(\langle I_x(x_0,z_0)\rangle_{2a} - \frac{1}{L}\langle J_x(x_0,z_0)\rangle_{2a}\right)\\ \Phi_z(x_0,z_0) &= 2aN\left(\langle I_z(x_0,z_0)\rangle_{2a} - \frac{1}{L}\langle J_z(x_0,z_0)\rangle_{2a}\right)\end{aligned} \tag{2.96}$$

It is well known that the magnetic flux variation is measurable whereas the magnetic flux itself is not. As the coil is moved from position 1 to position 2 between the time t_1 and t_2, the variation of the magnetic flux $\Delta\Phi$ is given by the Lentz law:

$$\Delta\Phi = \Phi_2 - \Phi_1 = -\int_{t1}^{t2} V dt \tag{2.97}$$

V is the voltage at the edges of the coil, Φ_1 (Φ_2) is the flux through the coil at position 1 (position 2). The coil is rotated around the position (x_0, z_0) to perform local field integral measurement whereas it is translated in order to measure the variation of the field integral.

Figure 2.34 represents the stretch wire geometry that we use to measure the undulator field integrals. The stretched wire is a closed loop whose return is in a region with a negligible magnetic field. The stretch wire is displaced around (x_0, z_0) in order to intercept the magnetic flux centred on this position. Similarly to the rotating coil geometry, the stretch wire has a sufficient length in order to measure the entire undulator field produced along the longitudinal direction. Consequently we set to $\pm\infty$ the boundaries of the longitudinal integration.

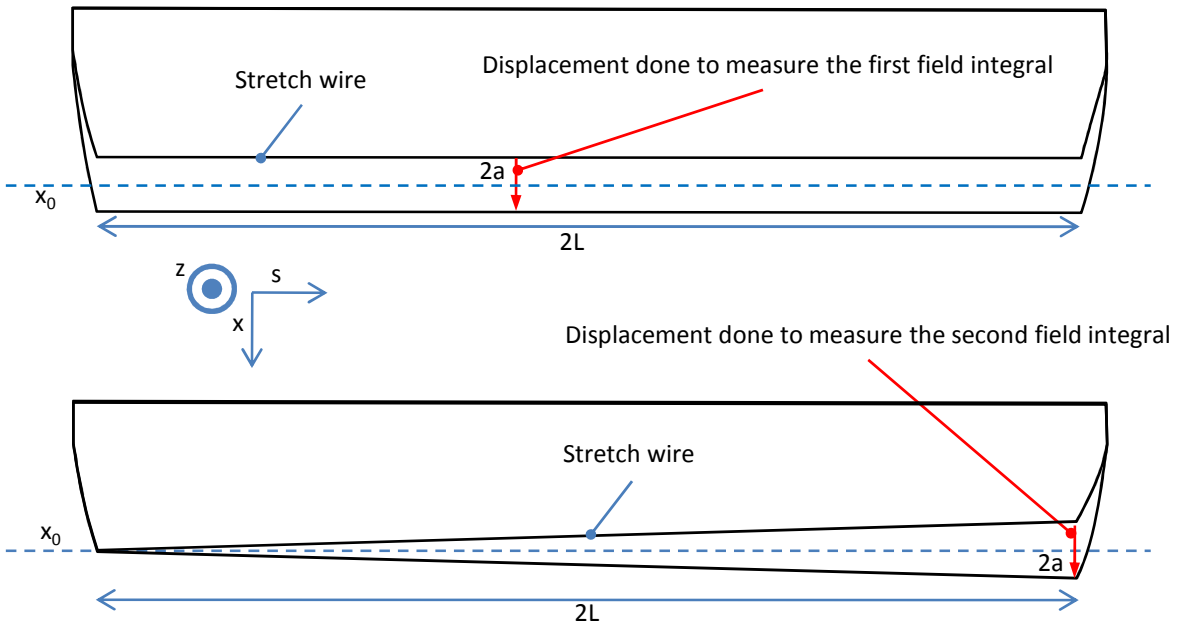

Figure 2.34: Stretch wire displacement used to measure the first and second field integral. The stretch wire displacement measures the component orthogonal to the plane that the stretch wire displacement defines.

Depending on the displacement applied to the extremity of wire, one measures either the first or the second field integral. In order to measure the first field integral, the stretch wire swaps a rectangular area. The direction of the displacement sets the component to be measured; a horizontal

(vertical) translation measures the vertical (horizontal) integral field component. The integrated voltage that corresponds to the displacement $2a$ is then:

$$\int_{t_1}^{t_2} V(t)dt = 2aN\langle I_x(x_0,z_0)\rangle_{2a} \qquad \int_{t_1}^{t_2} V(t)dt = 2aN\langle I_z(x_0,z_0)\rangle_{2a} \tag{2.98}$$

The stretch wire displacement measures directly the local integral field around (x_0, z_0). The stretch wire also measures the double field integral when it swaps a triangular area. To do so, one extremity is moved from $\pm a$ around (x_0, z_0) whereas the other extremity stays at the fixed position (x_0, z_0). The integrated voltage which corresponds to the triangular area is:

$$\begin{aligned}\int_{t_1}^{t_2} V(t)dt &= 2Na\left(I_x(x_0,z_0) - \frac{1}{2L}J_x(x_0,z_0)\right)\\ \int_{t_1}^{t_2} V(t)dt &= 2Na\left(I_z(x_0,z_0) - \frac{1}{2L}J_z(x_0,z_0)\right)\end{aligned} \tag{2.99}$$

The stretch wire is typically displaced over 1 mm to perform field integral measurement. The position error of the stepper motor is usually around 1 µm. The area swept by the stretch wire, is precisely known. Measuring with a similar accuracy the area of the rotating coil is difficult, it is therefore not easy to derive the absolute field integral with a rotating coil. Therefore the rotating coil is best suited to measure magnetic devices with zero field integral such as an undulator; whereas the stretch wire is also used to measure the absolute field integral of bending magnets or quadrupoles for which an accurate absolute measurement is required.

Figure 2.35 represents the field integral of a 32 mm period PPM undulator measured with rotating coil.

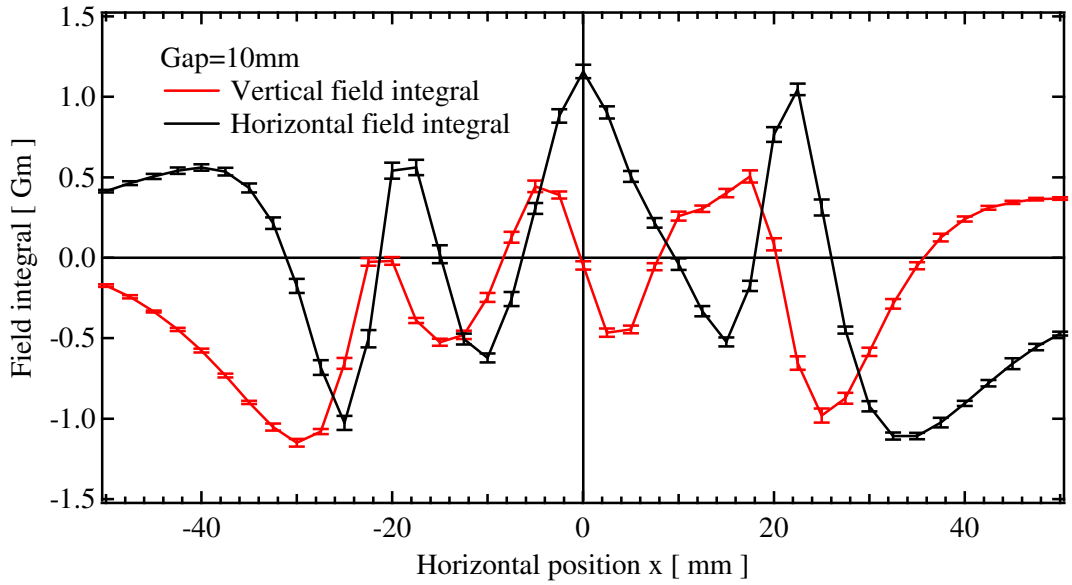

Figure 2.35: Horizontal (black line) and vertical (red line) field integral of a 32 mm period PPM measured with rotating coil before any correction. The undulator gap is closed at 10 mm.

Local field measurement

We compute the RMS phase error from the local measurements of the magnetic field all along the undulator longitudinal axis. The phase error depends on the magnetic field geometry. Thus the probe

position must be known very precisely to accurately map the field geometry. In addition the magnetic measurement needs to be reliable to ensure reproducible phase error measurement. Obviously the sensor used shall be small enough to permit local measurement; the active area of the Hall probes has a 0.23 mm diameter.

Figure 2.36 represents a typical bench used at the ESRF to perform local magnetic measurement [22], [44]. A linear motor drives the probe longitudinally. The linear encoder reads the longitudinal position with 1µm accuracy. The magnetic probe is a semiconductor material such as InAs or GaAs.

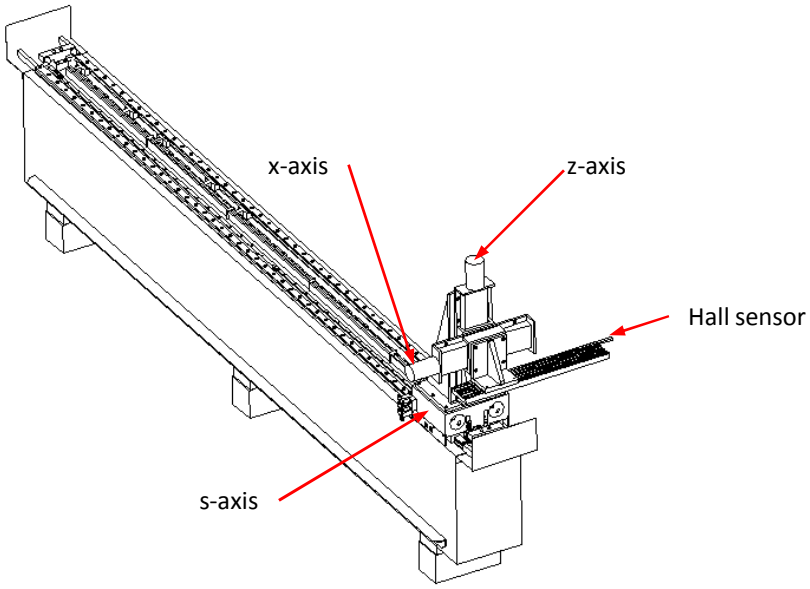

Figure 2.36: Typical Hall probe bench developed at the ESRF.

A permanent current of several mA is driven through the semiconductor. A Hall effect occurs in the semiconductor when it goes through the undulator magnetic field. The voltage V_{Hall} created between the semi conductor extremities is then [44]:

$$V_{Hall} = \rho I\left(\alpha B_z + \gamma B_s B_x + o(B^2)\right) \tag{2.100}$$

Where α is the Hall voltage coefficient and γ the planar Hall effect. These coefficients relate the voltage to the undulator field. The Hall voltage coefficient α is the main Hall contribution. This coefficient is not a constant; it depends mainly on the temperature and the field amplitude. In practice Hall voltage coefficient is calibrated in a uniform magnetic field. The other ones are corrected with the undulator itself [44]. Indeed higher order Hall parameters introduce some artificial harmonics such as even harmonics into the undulator field. Higher order parameters are corrected in order to cancel such harmonics.

A voltmeter records the Hall voltage on-the-fly to shorten the measuring time. With a typical speed of 30 mm/s, a 2 m long undulator is measured in less than 2 min. For undulators with period larger than 20 mm, 1 mm is a typical sampling distance. For smaller period undulators, the sampling distance is lowered to 0.5 mm.

Because of a voltage noise, the Hall probe bench is not suitable for integral measurements. Usually one corrects the local magnetic field measured with the Hall probe bench so that its integral equals integral field measurement. Finally both benches are necessary to perform an accurate magnetic measurement. Figure 2.37 represents the on axis magnetic field along a 32 mm period PPM, it has been measured with the Hall probe bench. The three field components are represented in Figure 2.37. In a perfect planar undulator the horizontal and the longitudinal field would be null along the undulator axis. Magnetic errors, off axis measurement and Hall probe misalignment explain the finite value of both components. The accuracy of Hall probe bench is a few G. Now we will introduce the magnetic corrections which are also called shimming.

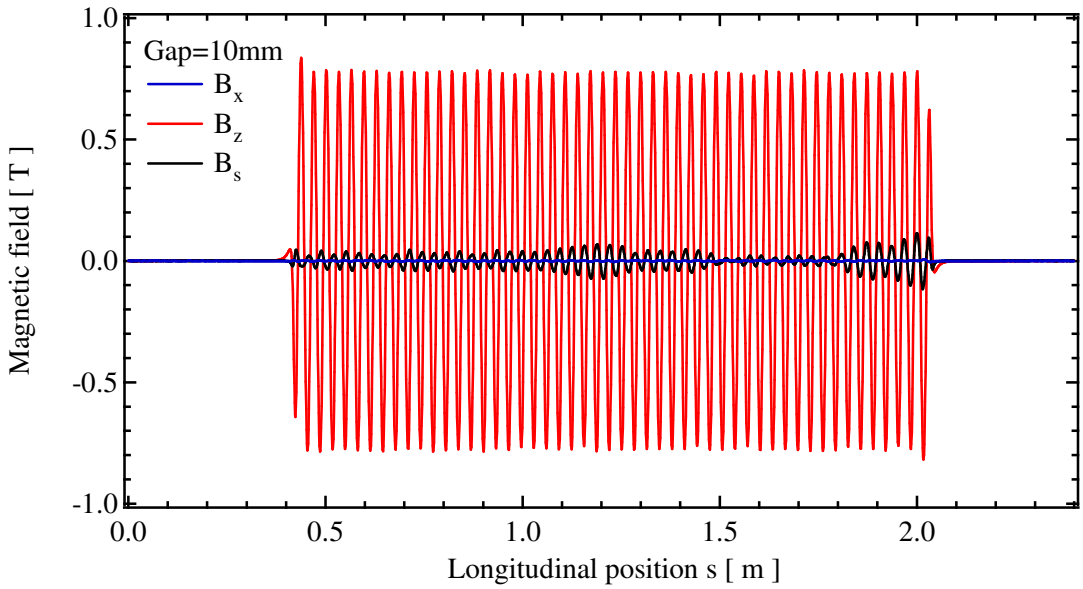

Figure 2.37: On axis magnetic field of a 32 mm period PPM undulator, the gap is closed at 10 mm. The vertical (red curve), horizontal (blue curve) and longitudinal (black) field components are measured.

2.4.5. Magnetic field shimming

The magnetic error correction process is called the shimming. In an undulator, there are two categories of shimming, the multipole and the phase error shimming. The multipole shimming is the process to correct field integral errors. The phase error shimming consists in minimizing errors which cause a finite phase error.

Multipole shimming

The multipole shimming minimizes the vertical and the horizontal variation of the field integral and corrects any multipole component. The correction of the undulator field integral is carried out in two steps. First the multipole shimming is separately applied to each girder. Afterwards girders are brought together to build the undulator. The final stage of the field correction consists then in lowering the interaction field integral. The multipole shimming on each girder takes advantage of the field integral property [22]. The methodology used at the ESRF is inspired by this process. This is detailed in chapter 4.2. Some of the other methodologies used in synchrotron radiation sources will be overviewed.

If one considers each single girder, one could apply the Cauchy integral formula on the closed contour $\mathcal{C}$ represented in Figure 2.38. Knowing the field integral on the contour $\mathcal{C}$ is sufficient to compute the field integral at any point in the surface bounded by the contour $\mathcal{C}$. We consider that the points A and D are located at infinity and the radius of the half circle is also infinite. As a result the field integral is null on the half circle and measuring the field integral along the line A-D is sufficient to compute the field integral at any point z located in the half plane above the line A-D. Finally if $I_z = 0$ over the line AD, both I_x and I_z are null for any point located in the half plane above the line A-D. Since the field integral is already negligible between A-B and C-D, one can limit the horizontal range over which we measure the field integral to the segment B-C. As a conclusion ensuring $I_z = 0$ over the segment B-C, implies a null field integral in the half plane above the line A-D; any multipole content is equal to zero in the half plane.

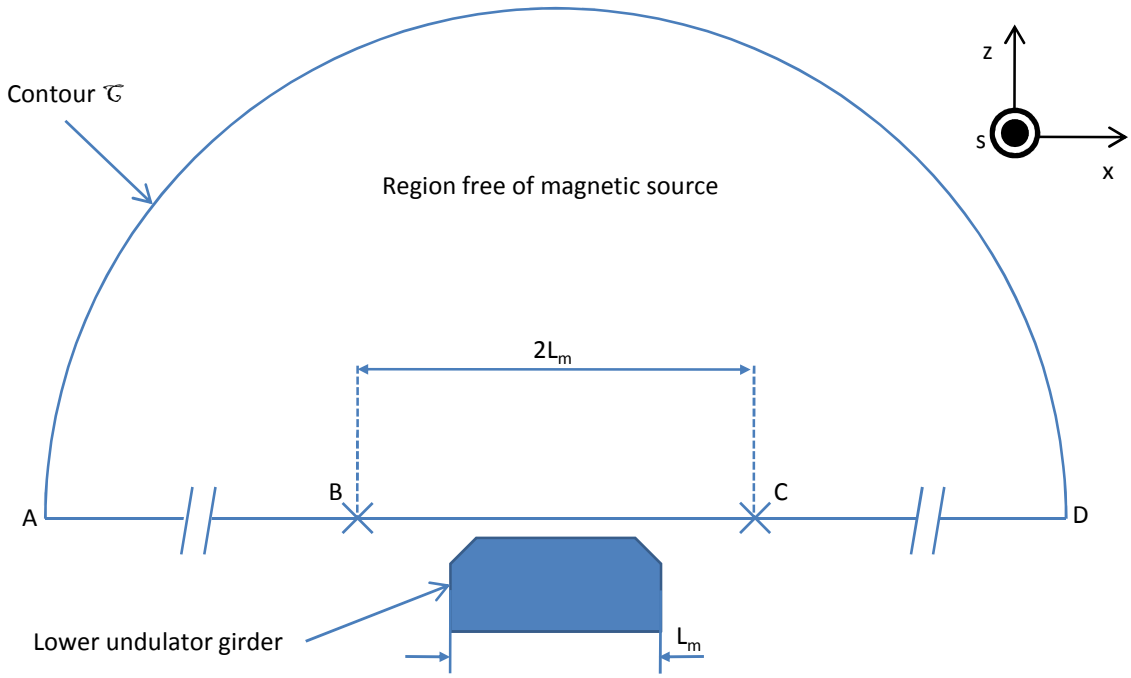

Figure 2.38: Schematic view of the rectangular contour on which the Cauchy integral formula is applied on the field integral which the lower undulator girder produces.

Practically two types of correction are applied to the field integral. One either displaces magnets and poles or one places some thin pieces of iron at the surface of the magnets. Any pole or magnet displacement (rotation or translation) is called a mechanical shim. The thin piece of iron is a magnetic shim. The iron piece is placed in the undulator gap, on the surface of a magnet or a pole. The magnetic flux, which enters the gap, is then partially short-cut. The magnetic shims always reduce the value of the magnetic field [25]. In addition, when several magnetic shims are closed together, their magnetic signatures do not add linearly. For these reasons, one prefers to use the mechanical shim.

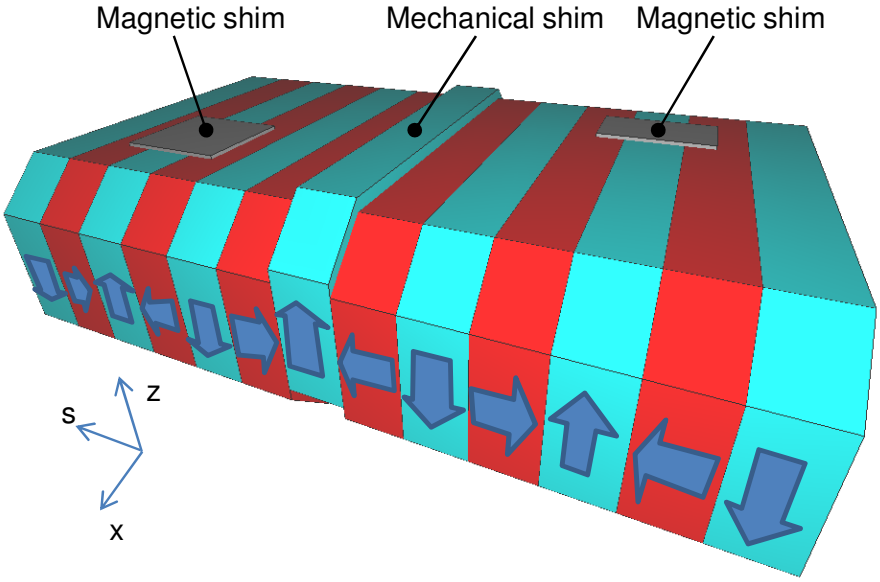

Figure 2.39: Examples of magnetic (thin piece made of iron) and mechanical (magnet displacement) shims applied during a multipole shimming.

Figure 2.40 represents the signature of a mechanical shim. It is observed that a vertical (horizontal) translation of a magnet with vertical magnetization causes a vertical (horizontal) dipole.

The field integral presents some sharp peaks. The rotation of a magnet pole with horizontal magnetization causes a smoother field integral. The dipole generated by the rotation is rather flat.

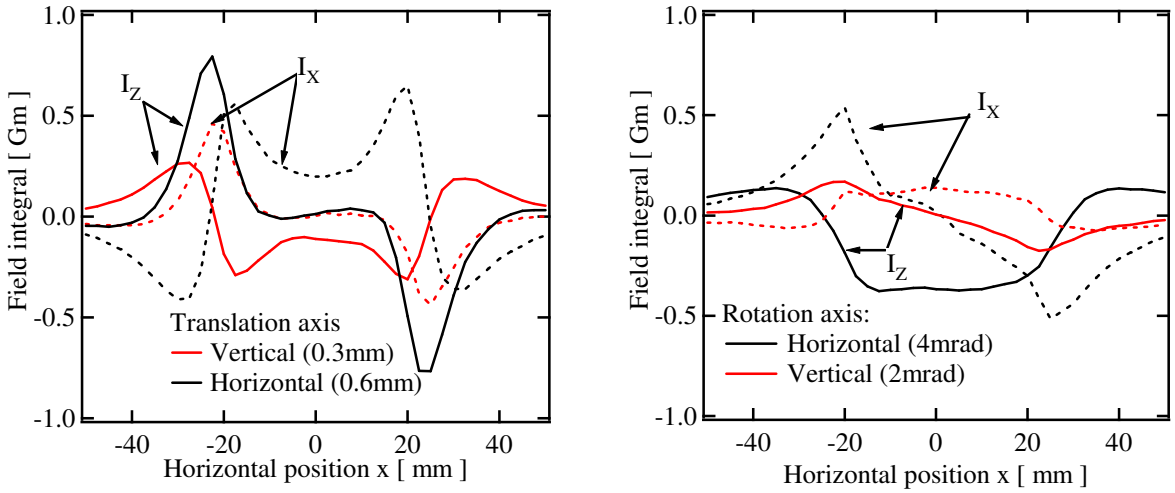

Figure 2.40: Field integral signature of a mechanical shim for a single girder of a PPM with 32 mm period. On the left plot a magnet with vertical magnetization is horizontally (black curve) and vertically translated (red curve). On the right plot a magnet with longitudinal magnetization is rotated with a 2 mrad (4 mrad) angle around the vertical (horizontal) axis. The field integrals are measured with the rotating coil at a vertical distance of 5 mm above the magnets surface.

Figure 2.41 displays the signature of a magnetic shim. The field integral is localized and centred on the shim position. This may be used to correct some localized errors.

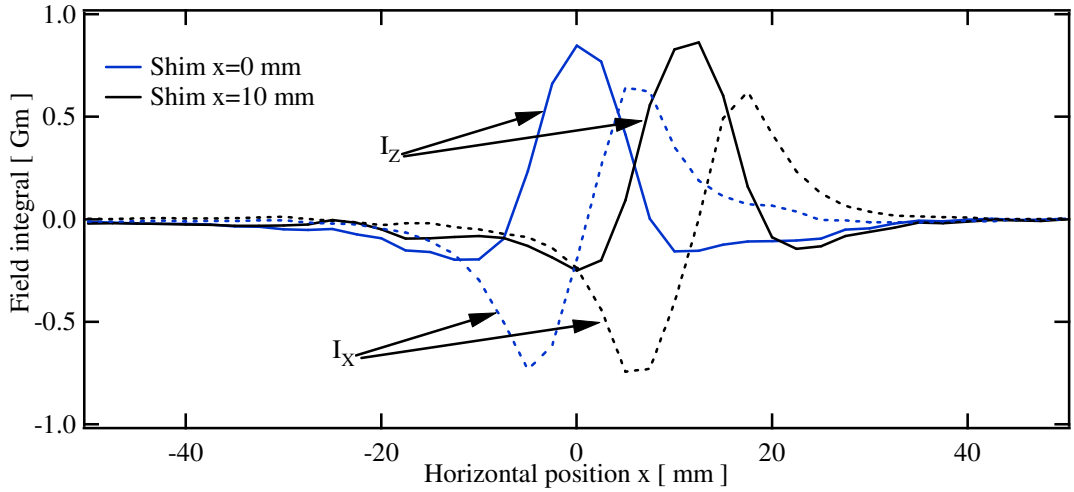

Figure 2.41: Field integral signature of a magnetic shim for a single girder of a PPM with 32 mm period. Magnetic shim is placed on a magnet with vertical magnetization at x=0 mm (blue curves) and x=10 mm (black curves). The shim dimension is L_x=10 mm, L_z=0.3 mm and L_s=16 mm. The field integrals are measured at a vertical distance of 5 mm above the magnets surface.

Phase error shimming

The phase shimming consists of ensuring an π increase of the phase ϕ_i from one undulator period to the next. To do so one delays or advances the electron from one undulator period to the next by increasing or decreasing the magnetic field along the undulator. Magnetic and mechanical shims are then used to decrease or increase locally the peak field. According to (2.76), the local field variation δB_z due to phase shimming should not introduce field integral variation. Indeed any field integral

variation δ_x associated to the local field variation δB_z, would further increase the phase error. As a result in order to perform an efficient shimming, one displaces independently magnets with horizontal magnetization or one displaces simultaneously two magnets with vertical magnetization but with opposite polarity. One may also place magnetic shims along the undulator axis at the surface of magnets with longitudinal magnetization. Magnetic and mechanical phase shimming applied on a PPM undulator are represented in Figure 2.42.

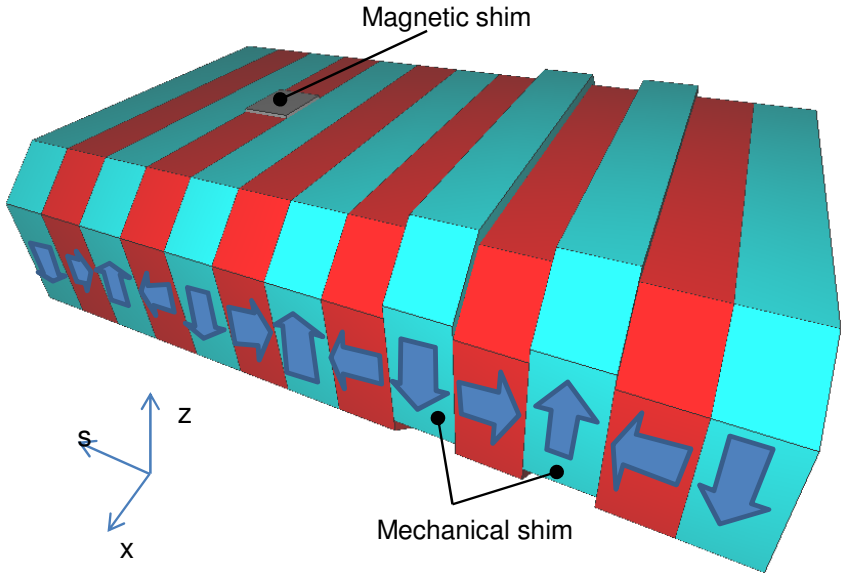

Figure 2.42: Examples of magnetic (thin piece made of iron) and mechanical (magnet displacement) shims applied used to perform phase error shimming.

The signature of a mechanical and a magnetic shim are displayed in Figure 2.43. Similarly to multipole shimming, magnetic shim always reduces the value of the magnetic field and possible interaction between magnetic shims may introduce a non linear effect. Therefore mechanical shims are also preferred during the phase shimming. Magnetic/ mechanical shimming changes locally the field amplitude without changing the undulator field integral.

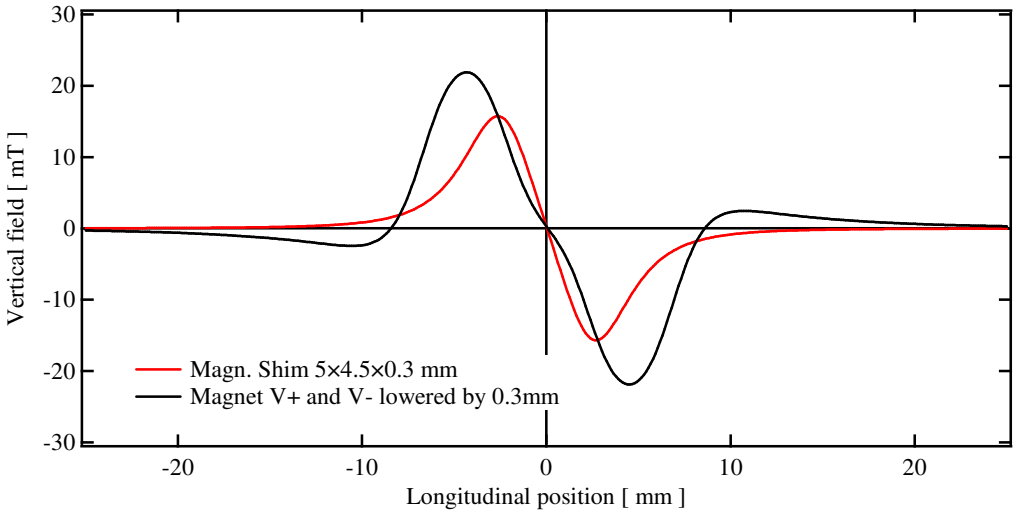

Figure 2.43: Signature of a magnetic (red curve) and a mechanical shim (black curve) on the PPM18 on-axis peak field. The undulator gap is closed at 10 mm. The signatures have been computed with RADIA. The undulator gap is closed at 6 mm.

We have reviewed the fundamental properties of the synchrotron radiation emitted by electrons in undulators and wigglers: electric field, brilliance, spectral angular flux and polarization. It appeared that undulators are a source of more brilliant synchrotron radiation than the wigglers, but the latest ones are still used for dedicated purpose, such as high energy photon production. Nowadays most insertion devices are made using permanent magnets, $Nd_2Fe_{14}B$ or SmCo ($SmCo_5$, Sm_2Co_{17}). Some designing and measurement solutions for these insertion devices have been introduced. Having covered the foundation of the existing technology, we will now focus on a particular insertion device development: the Cryogenic Permanent Magnet Undulator (CPMU). This is a short period high field undulator which aims at producing high energy photons; it may replace advantageously the existing short period high field undulator.

3. Design of a CPMU

This chapter covers the design of a cryogenic permanent magnet undulator (CPMU). It consists of operating an undulator based on $Nd_2Fe_{14}B$ magnets cooled at cryogenic temperature. First we will expand on the interest of producing such a type of insertion device. A CPMU realization underlies the use of a cryogenic system and the development of a magnetic measurement bench compatible with low temperature operation; these points will be discussed. We will review the numerical model built to predict the undulator peak field and field integral at cryogenic performance. This RADIA model is based on experimental measurements of $Nd_2Fe_{14}B$ magnets. The simple thermal model developed to determine the CPMU thermal budget is reviewed. Finally, we will look at the consequences of the cooling on the mechanical structure. At this point we will detail the magnetic errors induced by a thermal gradient along the undulator.

3.1. Need for a CPMU and design consideration

3.1.1. Short period/high field undulator

Scientific users are interested in insertion devices which produce the highest flux and brilliance achievable. According to equation (2.43), the photon energy at the fundamental harmonic of the undulator radiation is inversely proportional to the undulator period as long as the deflection parameter is kept constant. Thus a small period/high field undulator produces high energy photons. This is the major motivation to produce small period/high field undulators. Moreover shortening the undulator period enhances the flux since it also increases the number of periods per unit length. In parallel to ID development, an increase of the beam current from 200 mA to 300 mA is under preparation [45]. This would improve the flux from any device installed at the ESRF. We will first review the present status of short period/high field undulators. The future perspectives in the development of short period/high field undulators will be discussed [46] and the CPMU concept is introduced.

Present status

The technological difficulty is to reduce the period length and to increase the peak field simultaneously. We use smaller magnets to shorten the period length, but at a given gap they produce a lower magnetic field. Closing the gap further is then an immediate solution to compensate for the reduction in period length. Thus the minimum gap achievable is one of the limitation factors. The technological progress made on the vacuum chamber such as the availability of Non Evaporable Getter (NEG) coated chambers has made possible the reduction of the minimum gap from 20 mm down to 10 mm for in air undulator. Another major step in the gap reduction has been made with the development, first in Germany in the 80s [47], [48] and then massively in Japan in the mid 90s, of the in-vacuum undulator [49], [50], [51], [52]. As shown in Figure 3.1, the magnetic assembly is no longer in the air but enclosed in the vacuum chamber wherein the electron beam is stored. With such an undulator, the lowest gap is achieved when closing further the gap reduces the beam lifetime [49].

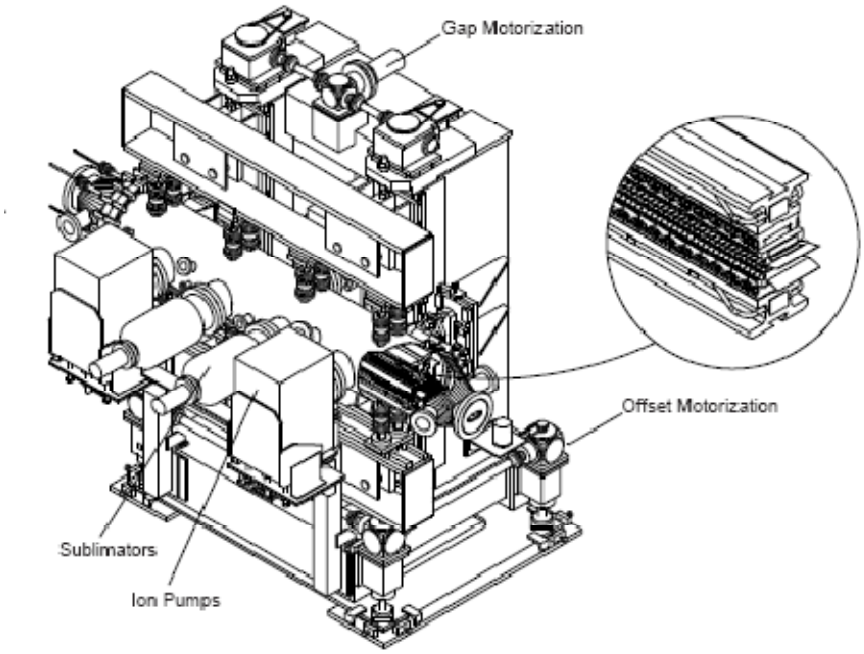

Figure 3.1: In-vacuum undulator. The magnetic assembly is enclosed in the vacuum chamber wherein the electron beam is stored. Picture from ESRF [53].

Many constraints had to be taken into account in order to realize such a device:

- As the electron beam circulates in the storage ring, an image current propagates simultaneously in the opposite direction at the surface of the vacuum chamber. It is necessary to ensure the continuous flow of the current image along the storage ring in order to prevent the electron beam from instabilities [54]. In an in-vacuum undulator the thin Cu-Ni foil is used for this purpose [49]. It consists in a 50 µm thick Cu foil with a 10 µm thick Nickel coating on one face. The Nickel coated side is facing the magnet array and provides an adequate magnetic attraction to keep the foil in position. The uncoated Cu side is facing the electron beam and allows the development of image current with limited heating due to the high conductivity of Cu.

- We should also ensure smooth geometrical variation between the vacuum chamber and the undulator girder in order to avoid instabilities [54]. One then uses the so-called RF fingers to smoothly connect the in vacuum chamber and the girders for any gap value [49], [53]. They are generally made of Copper and are equipped with cooling channel in order to damp the heat brought by the electron beam.

- Precautions have to be taken to guaranty the high vacuum compatibility. The surface of the magnets is Nickel coated to lower the surface desorption rate. Heavy chemical species such as hydrocarbons are avoided. In addition, a residual gas analysis validates the high vacuum compatibility, before any in-vacuum undulator installation. Finally, once the undulator has been installed on the straight section, the magnetic assembly is baked up to 400 K to evaporate and pump the residual water. After baking, the pressure is around or below 10^{-10} mbar.

- Finally, we use magnets with a strong resistance to demagnetization induced by radiation damage since partial magnet demagnetization would degrade the undulator field quality. Indeed, demagnetization has been observed in different synchrotron radiation sources, ESRF [55] and APS [56]. In the specific case of an in-vacuum undulator, two distinctive phenomena might be involved in the demagnetization. Both of them linked to an electron collision, either directly between the electron and the magnet, or between a particle emitted during a former collision between the electron and another piece of the storage ring (RF finger, vacuum chamber and so on).

Several studies have been done about the radiation damage in rare earth magnets [57], [58], [59], [60], [61], [62]. Although the process involved in the demagnetization is not clearly understood, studies point out that:

- Sm_2Co_{17} presents a higher resistance to radiation damage compared to all grades of $Nd_2Fe_{14}B$.
- For any material, the hardness to irradiation increases with the coercive field.

Finally, as far as resistance to radiation damage and hardness at high temperature are concerned, Sm_2Co_{17} is the safest candidate to build in-vacuum undulators at ambient temperature. Moreover for a small ratio gap over period, the HYB design produces a higher peak field than the PPM design. Indeed compared to hybrid technology, the gap of a PPM undulator with the same period has to be reduced by about 1.2 mm to produce the same peak field [63]. For these reasons, at the ESRF, the latest in-vacuum undulator designs are based on hybrid technology with Sm_2Co_{17} magnets. Typically the smallest gap achievable there is 6 mm. However the remanent field is limited to 1.05 T. In addition one should mention that the in-vacuum undulator at SPring-8 uses $Nd_2Fe_{14}B$ magnets with a gap of 8 mm. At SPring-8 they use an additional thermal treatment to enhance magnet resistance to demagnetization [58].

As far as gap reduction is concerned, the in-vacuum undulator is the ultimate ID. In order to further reduce the undulator period, magnetic material with higher remanence is required.

SCU

Superconducting materials are natural candidates to produce small period undulators with a high peak field. A SuperConducting Undulator (SCU) should operate at temperatures below 4 K. As with any superconducting device, great care should be given to the thermal budget to prevent any quench. Although this technology is promising, there are nowadays a number of technological challenges to solve. In particular magnetic measurement benches have to be developed to perform magnetic measurements at such a low temperature. Following the development of the High Temperature SuperConductor (HTSC), a first design using HTSC has been proposed by T. Tanaka [64].

CPMU

$Nd_2Fe_{14}B$ magnetic properties at low temperature open new perspectives in the realization of small period undulators. Indeed, cooling $Nd_2Fe_{14}B$ material increases their intrinsic coercive field so much that their hardness to radiation damage is comparable to Sm_2Co_{17} [65]. Consequently $Nd_2Fe_{14}B$ grades with higher remanence than SmCo are then available for small period undulators. For example, $Nd_2Fe_{14}B$ magnets with remanence above 1.25 T at ambient temperature could be used. Moreover cooling improves the remanence down to a limited temperature where a reversible Spin Reorientation Transition (SRT) occurs [66], as discussed in section 3.2.1. Below this temperature threshold, this reversible effect macroscopically leads to a remanence reduction. This easy axis orientation occurs below 150 K and depends on the composition of the $Nd_2Fe_{14}B$ alloy.

Such a $Nd_2Fe_{14}B$ based in-vacuum undulator operating at cryogenic temperature, typically around 150 K, is called a cryogenic permanent magnet undulator CPMU. A CPMU project was first proposed at SPring-8 [8], [67]. It is a 60 cm long PPM with 15 mm period. The purpose of this device is not for it to be installed in the storage ring. This small undulator is more dedicated to the study of the magnetic performance at cryogenic temperature in laboratory. An alternative project has been proposed at the ESRF [68]. This CPMU is planned to be operated in real conditions, on the synchrotron facility. We review hereafter the ESRF CPMU project.

3.1.2. CPMU technological consideration

The aim of the CPMU project at the ESRF is the full scale realization of a short period high field undulator with cooled $Nd_2Fe_{14}B$ magnets and its installation on a straight section in the ESRF storage ring. The CPMU has to fulfil the same requirements as standard in-vacuum undulators, i.e. high vacuum compatibility and reliable operation. A cryogenic system cools and maintains the magnetic

assembly at cryogenic temperature; it should also be reliable for daily operation. These considerations are detailed in this section.

Selection of $Nd_2Fe_{14}B$ material

Radiation damage on permanent magnets has been studied intensively since 2000 within the framework of collaboration between SPring-8 and the Pohang Accelerator Laboratory [58], [65]. They have investigated the increase of the resistance to radiation damage at cryogenic temperature with different $Nd_2Fe_{14}B$ magnet grades. The magnets used are commercially available products from Hitachi (NEOMAX27VH, NEOMAX35EH and NEOMAX50BH). The coercive field and the remanence of these $Nd_2Fe_{14}B$ magnets, measured at ambient temperature and at 150 K, are displayed in Figure 3.2. Those of other $Nd_2Fe_{14}B$ magnets produced by Hitachi and Vacuumshmelze are also reported and compared.

It has been shown that at 140 K, NEOMAX50BH magnet exhibits a strong resistance to radiation damage, similar to those of Sm_2Co_{17}. At 140 K the coercive field $H_{cj}$is around 3800 kA/m. The authors report also that special treatment such as annealing and magnets stabilization in a reverse field may further increase their resistance. Actually the NEOMAX50BH magnet is one of the grades with the highest remanence and thus with the lowest coercive field at ambient temperature. Finally, as far as radiation damage is concerned, any $Nd_2Fe_{14}B$ grade is suitable for CPMU operation.

So far, Nickel coating and magnetic assembly baking ensure the high vacuum conditioning. Anyway progress has been made at the ESRF since the start of the current work; an in-vacuum undulator working at ambient temperature has been successfully installed without baking [69]. However for a first step, it has been decided to bake the undulator. Therefore $Nd_2Fe_{14}B$ magnets with a coercive field H_{cj} higher than 2000 kA/m are required to avoid demagnetization during baking at 120°C (393 K). $Nd_2Fe_{14}B$ magnets with the highest remanence at ambient temperature exhibit a coercive field clearly below this limit. As a result magnets such as NEOMAX50BH are not suitable for an in-vacuum undulator. As a consequence high vacuum conditioning compatible with high remanence and low coercive field magnet is necessary to take full advantage of the CPMU concept.

For the CPMU project at the ESRF we eventually selected a $Nd_2Fe_{14}B$ grade whose intrinsic coercive field H_{cj} is slightly above 2000 kA/m. The $Nd_2Fe_{14}B$ magnet is a NEOREM product, the 495t magnet; at 300 K the intrinsic coercive field H_{cj} is 2150 kA/m and the remanence is 1.18 T.

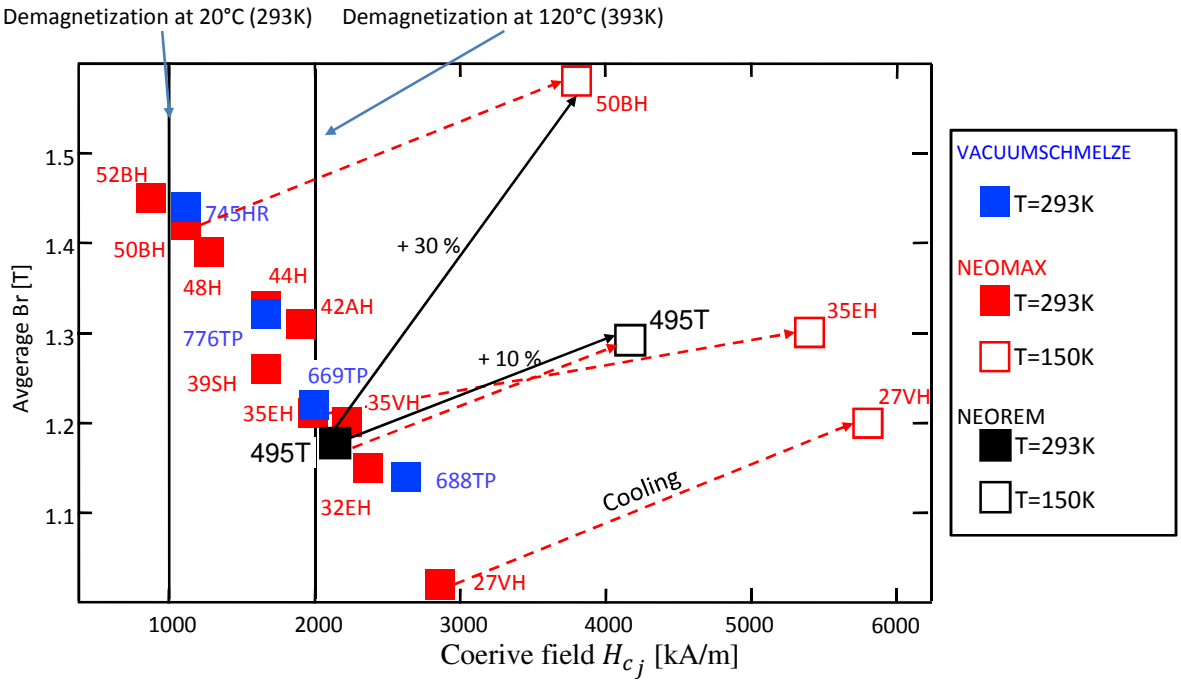

Figure 3.2: Remanence and coercive field of several commercially available $Nd_2Fe_{14}B$ magnet grades produced by Neorem (black cube), Hitachi (red cube) and Vacuumschmelze (blue cube).

HYB18 the CPMU magnetic assembly

The primary purpose of a CPMU is the development of a short period high field undulator by means of an in-vacuum undulator. For such a device the gap is closed down to 6 mm; this leads to a small gap to period ratio. In section 2.4.3 PPM and HYB structure have been compared to this ratio. With a HYB structure, one reaches a higher peak field for a small ratio so this structure is the best candidate to produce a short period high field undulator.

The undulator has been magnetically designed to get a deflection parameter equal to 1.5 at 150 K. This leads to the HYB18 design already presented in section 2.4.3. The geometrical parameters of the HYB18 and the value of the peak field at ambient temperature are summarized in Table 3.1.

Table 3.1: Period, length, dimension of poles and magnets and the peak field at ambient temperature of the HYB18.

Period	Length	Number of periods	Pole dimension (L_x, L_z, L_s)	Magnet dimension (L_x, L_z, L_s)	Peak field at 300 K	K
18 mm	1965 mm	108	(32 mm, 24 mm, 2.8 mm)	(50 mm, 30mm, 6.2 mm)	0.832 T	1.5

As with any undulator, the HYB18 CPMU was assembled, measured and corrected so that its field integrals and RMS phase error sit within the tolerances specified in Table 2.4. However it is planned to operate at cryogenic temperature, the CPMU project therefore involved the development of a magnetic measurement bench compatible with cryogenic operation to measure the field integrals and the phase errors at cryogenic temperature. Moreover the local and integral field measurements at cryogenic temperature would:

- Validate the non linear magnetostatic model built with RADIA. The peak field and field integral measurements would validate the numerical model.

- Validate at cryogenic temperature the correction done at ambient temperature. Indeed one may ask if the shimming done at ambient temperature, is still valid at cryogenic temperature or if any further magnetic errors, growing with decreasing temperature, would need correction at cryogenic temperature.
- Measure the peak field increase at low temperature. Above the SRT temperature, an increase of undulator peak field is expected since the magnet remanence increases while temperature decreases.

In order to figure out the performance one may achieve with such CPMU, one plots in Figure 3.3 the computed spectra through 1 mm × 1 mm slit located at 30 m from the undulators produced by a CPMU undulator based on $Nd_2Fe_{14}B$ magnets with high remanence (B_r = 1.58 T) and a standard in-vacuum undulator; the deflection parameter equals 1.5. The electron beam parameters used for the computation are listed in Table 3.2. The standard in-vacuum undulator is based on Sm_2Co_{17} magnets and is designed with a 20 mm period. The use of $Nd_2Fe_{14}B$ magnets with high remanence allows to decrease the undulator period down to 17 mm. Magnetic designs are based on the hybrid technology with soft iron poles made of low carbon steel. Lowering the undulator period shifts the fundamental harmonic of the X-ray spectrum to higher energy. In order to further reduce the undulator period, one rather uses poles made of Vanadium Permendur since it has a higher saturation magnetization (2.35 T) than low carbon steel (2.1 T).

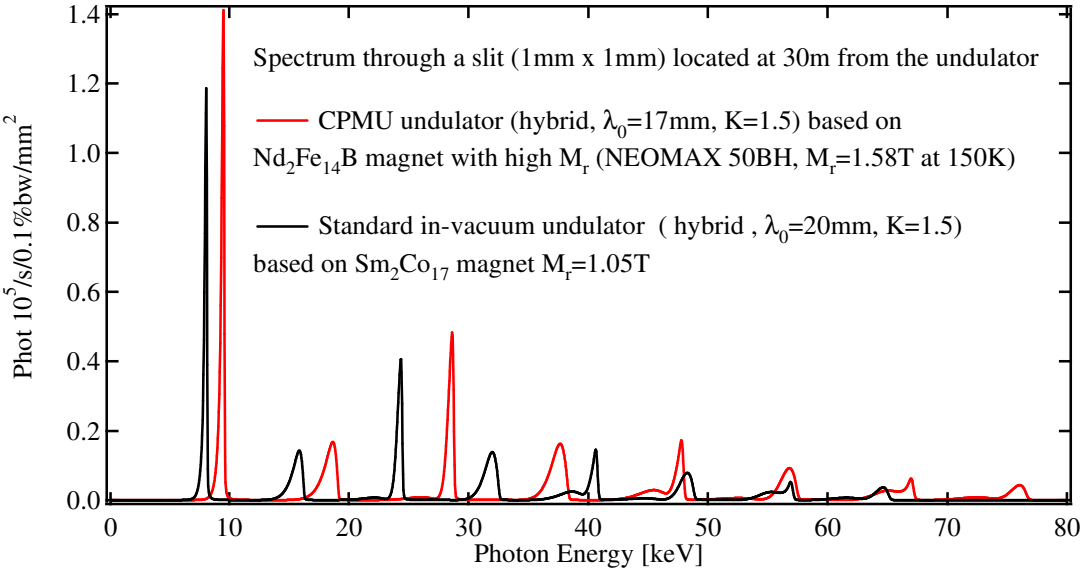

Figure 3.3: Photon flux through a 1 mm × 1 mm slit located at 30 m from a CPMU undulator (red curve) and a standard in-vacuum undulator with Sm_2Co_{17} (black curve). The photon flux is computed with SRW, the characteristics of the electron beam are given in Table 3.2.

Table 3.2: Beam parameters used for the computation of the spectrum through a slim slit.

Beam current [mA]	200
Energy spread	10^{-4}
Horizontal emittance [nm rad]	3.9
Vertical emittance [nm rad]	0.025
Horizontal Beta function [m]	0.5
Vertical beta function [m]	2.73

The cooling system

A cooling system is necessary to cool the CPMU to cryogenic temperature. In addition, the cryogenic system must prevent any temperature gradient along the magnetic assembly as it might induce additional magnetic errors.

The CPMU operates at higher temperature than the SRT which is above 100 K. According to the thermal budget discussed in section 3.3, at temperature higher than 100 K, the thermal budget is kept below 200 W. Extracting such thermal power at this temperature is not a technological issue. Several cooling solutions, namely Gifford-McMahon (GM) cryocooler and circulation cooling system, are already available from companies [70], [71]. In the Gifford-McMahon cryocooler, helium gases enclosed in a volume called the cold finger experiences a thermodynamic cycle, the isobaric-isothermal Ericsson cycle. The cycle is theoretically reversible and the cooling power varies from 5 W to 200 W in the temperature range 30 K-300 K [72]. The heat is extracted locally at the cold finger. If one uses the GM cryocooler to cool the 2 m long undulator, one may need several cryocoolers disposed along the undulator to avoid a temperature gradient along the magnetic assembly. The other cooling technology is based on a circulation of a cryogenic fluid which flows through refrigerant channels. Such a cryogenic system is suitable with long device cooling. Circulation cooling system allows the use of refrigerant channels similar to those used in standard in-vacuum undulators. Only few changes are required on standard in-vacuum refrigerant channels to be compatible with a CPMU operation. Actually such a circulation cooling system has been developed at the ESRF to cool monochromators. More than 20 units are now in daily operation at the ESRF. It has been chosen as the CPMU cooling system. Their main advantages are their low coolant cost and the little needed maintenance. The main drawback is the lack of flexibility. The cooling system temperature is fixed around 80 K. In particular, one couldn't simply connect the refrigerant channels to the cooling system to operate the CPMU at higher temperature than 100 K. It is necessary to control the thermal flux between the magnetic assembly and the cooling system. An additional heating system is also required if one would change the CPMU temperature. The calibration of the thermal flux between magnetic assembly and the cooling system is detailed in sub chapter 3.3.

Figure 3.4 represents schematically the cooling system developed at the ESRF. The cooling system is made of two liquid nitrogen (LN_2) circuits and one heat exchanger between both circuits:

- The inner LN_2 closed loop.
- The LN_2 bath at atmospheric pressure.

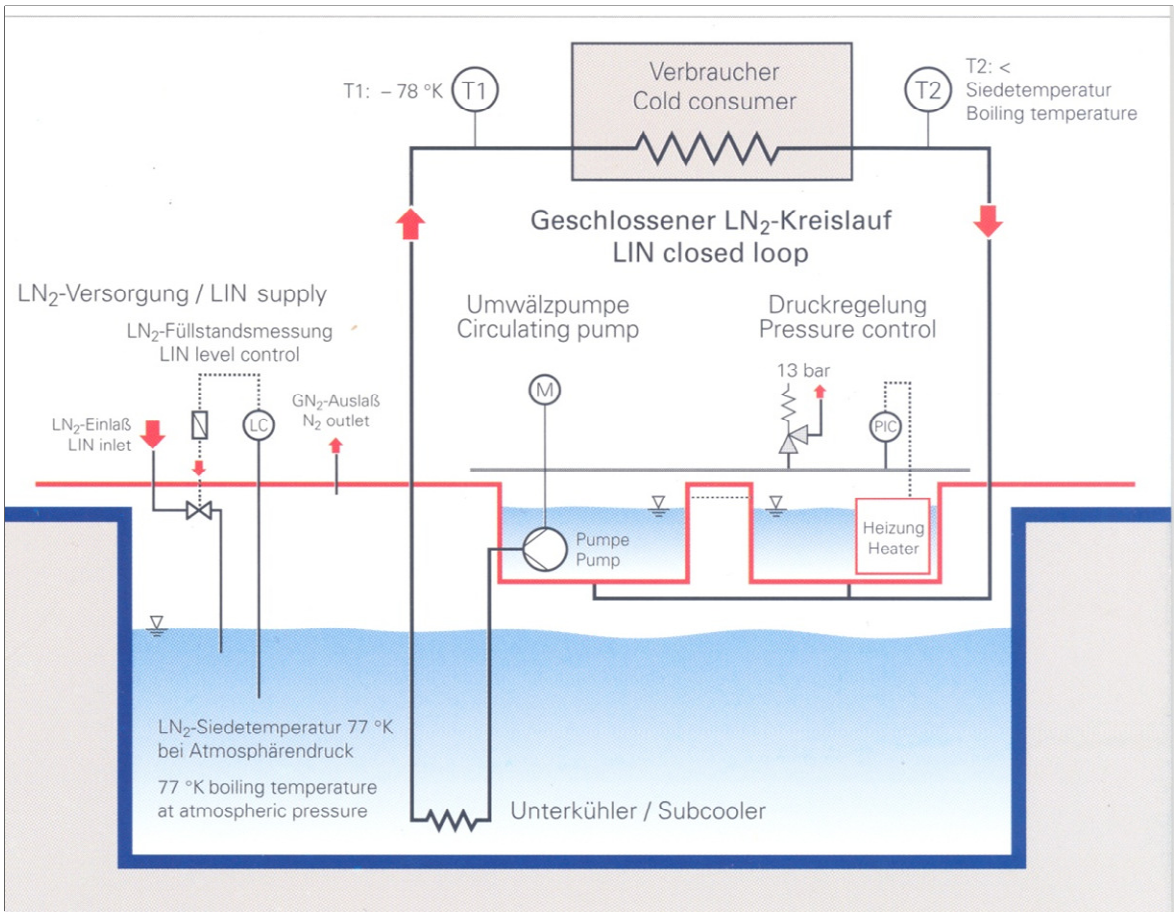

Figure 3.4: Schematic description of the LN_2 cooling system. The cooling is made of two LN_2 circuits, the inner loop and the sub cooler. Picture from MESSER [71].

The inner LN_2 closed loop is connected to the refrigerant channels. The heat is transferred from the magnetic assembly to the LN_2 in the refrigerants channels in order to cool and maintain the magnetic assembly at the temperature T_{cpmu}. T_1 and T_2 are the LN_2 temperature at the CPMU entrance and output. A pump forces the LN_2 circulation in the closed loop. Once the inner loop is full, the LN_2 consumption is very low. In a normal operation, one may need to refill the loop to compensate the possible internal losses.

The LN_2 bath at atmospheric pressure is called the subcooler; the LN_2 is at 77 K in the subcooler. The heat exchanger between LN_2 circuits is immersed in the LN_2 bath. Finally the subcooler sets T_1, the LN_2 temperature in the closed loop at the CPMU entrance around 80 K and absorbs the thermal flux coming from the closed loop. This heat transfer between both circuits consumes some LN_2 in the subcooler. The subcooler is refilled to compensate for this LN_2 consumption.

If one considers dQ/dt the rate of thermal heat that enters in the CPMU, the LN_2 flows through the cooling pipes and transports the thermal power dQ/dt away from the CPMU. The thermal flux absorbed in the refrigerant channels increases the LN_2 temperature from T_1 to T_2. The thermal power is:

$$Q_c = \dot{m} \int_{T_1}^{T_2} C_p dT \tag{3.1}$$

Where $\dot{m}$ is the mass flow and C_p the nitrogen calorific mass. The nitrogen should not boil in the closed loop otherwise it may create vibrations in the CPMU. As the boiling temperature increases with pressure, the liquid is pressurized to keep T_2 below the boiling temperature. The vessel with the pressure control and the heating system set the pressure in the inner loop between 3 bar and 13 bar. At

13 bar the boiling temperature equals 108 K. The mass flow and the pressure in the inner loop limit the maximum cooling power to 2 kW. The maximum cooling power exceeds largely the one required for the CPMU.

3.2. Numerical magnetostatic model of the CPMU

Some magnetization curves of the $Nd_2Fe_{14}B$ magnet dedicated to the CPMU project, i.e. the 495t NEOREM magnet, have been measured at low temperature in order to determine the coercive field and the peak field increase. We have also created with RADIA, a CPMU nonlinear model based on such experimental magnetization curves. This model determines the temperature at which the undulator would produce the highest on axis peak field. The field integrals have also been investigated. Both results will be presented in the following section.

In addition, the $Nd_2Fe_{14}B$ exhibits an easy axis reorientation; it introduces some singularities on the $Nd_2Fe_{14}B$ magnetization curve. First we will introduce them by considering a single crystal. We will then present the magnetization curves measured on real $Nd_2Fe_{14}B$ samples. Finally we will discuss the CPMU numerical model.

3.2.1. Magnetic properties of the $Nd_2Fe_{14}B$ compound

Qualitative description at the microscopic level

The magnetic properties of the $Nd_2Fe_{14}B$ compound result from the contribution of Fe and Nd magnetism [73]. In particular a competition exists between Fe and Nd magnetocrystalline anisotropy [74]. The Fe anisotropy favours the alignment of the Fe moments along the uniaxial crystallographic c-axis of the tetragonal phase (see Figure 2.15). The anisotropy of the Nd ions depends on several Crystalline Electric Field (CEF) terms. The 2nd order terms which are dominant at high temperature then force the alignment of the Nd moments along the c-axis, in accordance with the Fe anisotropy. The 4th order terms favour a canted configuration of the Nd moments with respect to the c-axis. These terms become dominant at low temperature and are at the origin of the SRT occurring at 135 K. below the SRT, the Nd moments depart from the c-axis orientation. The competition between the Fe anisotropy and the Nd-Fe coupling determines the orientation of the Fe moments. The Nd-Fe exchange interaction is largely dominant and the Fe moments are almost aligned with the average Nd moment orientation.

Phenomenological analysis

This section is mainly inspired from the P. Tenaud's PhD thesis [75]. At a macroscopic level, it can be shown that the introduction of the magnetocrystalline potential energy E_{An} is sufficient to schematically describe the $Nd_2Fe_{14}B$ magnetic properties presented above. The energy E_{An} depends only on the global magnetization orientation and is defined as:

$$E_{An}(\theta) = K_1 \sin^2(\theta) + K_2 \sin^4(\theta) \tag{3.2}$$

The anisotropy constants K_1 and K_2 are respectively the 2nd and the 4th order terms, θ is the angle between the magnetization and the c-axis of the tetragonal structure. To this order of approximation, one should note that any rotation of the crystal magnetization around the c-axis keeps the energy E_{An} invariant. The anisotropy constants K_1 and K_2 depend on the crystal temperature [75], as displayed in Figure 3.5.

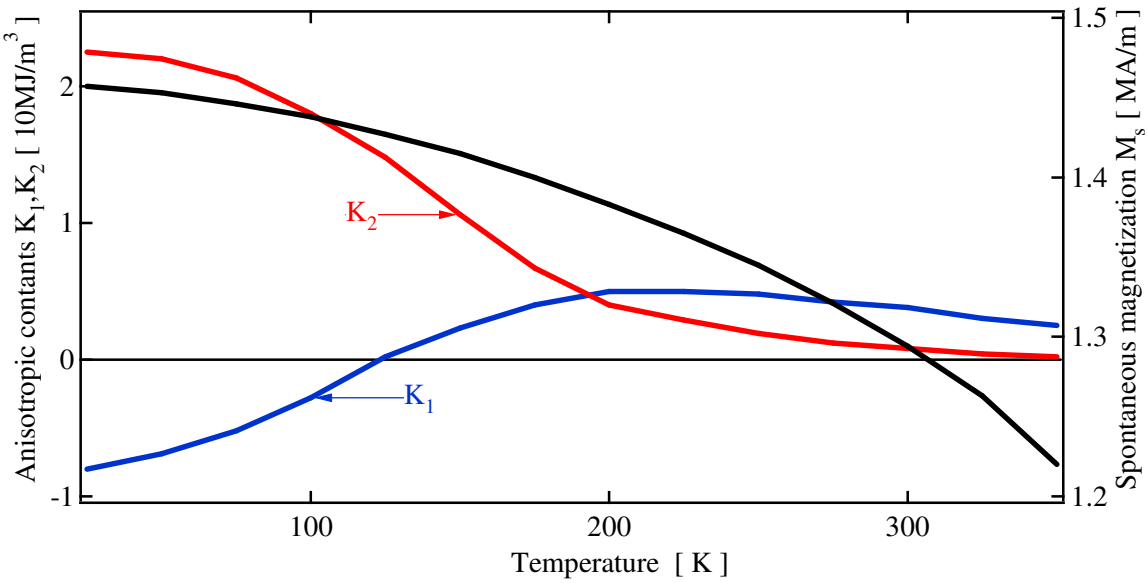

Figure 3.5: Spontaneous magnetization (black curve) and anisotropy constants K_1 (blue curve) and K_2 (red curve) of $Nd_2Fe_{14}B$ crystal. Data sourced in [75].

By definition, the easy magnetization axis minimizes the magneto crystalline energy E_{An}. Thus the easy axis orientation θ_e vanishes $dE_{An}/d\theta$:

$$\frac{d}{d\theta}E_{An} = \sin(2\theta)\,(K_1 + 2K_2\sin^2(\theta)) \tag{3.3}$$

The angle θ_e of the easy axis with respect to the c-axis depends on the value of the anisotropy constants K_1 and K_2. At ambient temperature the anisotropy constants K_1 and K_2 are positive. One can easily deduce from equation (3.3) that $\theta_e = 0$; the easy axis is along c-axis. The $Nd_2Fe_{14}B$ crystal has a strong axial magneto crystalline anisotropy at this temperature.

At low temperature $K_1 < 0$ and $K_2 > 0$, a non null angle θ_e minimizes the equation (3.2); the easy axis makes an angle θ_e with respect to the c-axis. The easy axis departs from the c-axis .Since the rotation of the magnetization around the c-axis keeps the energy constant; the easy axis then describes a cone around the c-axis. One has:

$$\theta_e = \sin^{-1}\left(\sqrt{-\frac{K_1}{2K_2}}\right) \tag{3.4}$$

In this phenomenological approach, the easy axis re-orientates itself as θ_e becomes non null. The SRT then occurs with the cancellation of the K_1 anisotropy constant. In addition, the magnetocrystalline anisotropy provides an energy barrier at the origin of the coercivity. The coercive field $\vec{H}_{c_j}$ is the necessary field to apply in order to reverse the $Nd_2Fe_{14}B$ single crystal magnetization. The coercive field depends on the direction along which one applies the magnetic field. The magnetization curve of a $Nd_2Fe_{14}B$ single crystal is described hereafter.

Theoretical hysteresis cycle for a $Nd_2Fe_{14}B$ single crystal

We will compute the ideal hysteresis cycle of a $Nd_2Fe_{14}B$ single crystal according to the Stoner and Wolfharth model [26]. In this model the mechanism involved in the magnetization reversal is a uniform moment rotation. Although the coercive field obtained with this model is much higher than the ones of real magnets, it can illustrate the perspective of cooling down $Nd_2Fe_{14}B$ magnets and the limitation that the SRT brings. Cooling $Nd_2Fe_{14}B$ magnets largely increases the magnet coercive field whereas the SRT leads to a reduction of the magnetization along the magnet easy axis.

As shown in Figure 3.6, one applies a magnetic field H on the $Nd_2Fe_{14}B$ single crystal; the c-axis and the magnetic field H have an angle θ_u. We note θ_H the angle between the spontaneous magnetization M_s and the magnetic field H. The angle θ between the spontaneous magnetization M_s and the c-axis equals:

$$\theta = \theta_H - \theta_u \tag{3.5}$$

We neglect the dipolar energy and the shape anisotropy of the single crystal. The single crystal energy in the magnetic field H is:

$$E(\theta_H, H) = -\mu_0 M_s H \cos(\theta_H) + K_1 \sin^2(\theta_H - \theta_u) + K_2 \sin^4(\theta_H - \theta_u) \tag{3.6}$$

The first term is the Zeeman energy. This interaction, which couples the magnetic field with the spontaneous magnetization, tends to align the magnetization with the magnetic field. The two last terms express the potential energy of the magneto crystalline anisotropy.

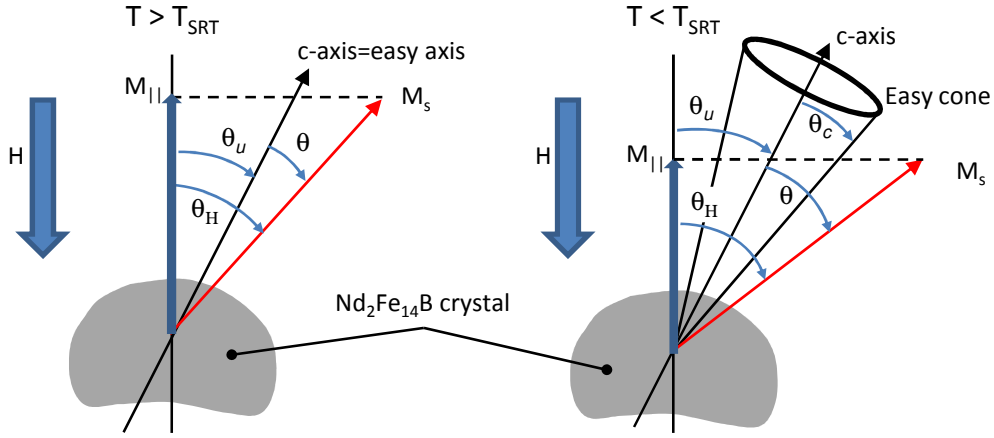

Figure 3.6: The $Nd_2Fe_{14}B$ easy axis is aligned along the c-axis at temperature above the SRT threshold (left plot). Below this threshold the easy axis is distributed along a cone (right plot). The c-axis is the cone axis.

As one applies the magnetic field H on the crystal; its spontaneous magnetization orientates itself with an angle θ_H in order to minimize its energy $E(\theta_H, H)$. The magnetization $M_{||}$ measured along H is:

$$M_{||} = M_s \cos(\theta_H) \tag{3.7}$$

The variation of the $Nd_2Fe_{14}B$ crystal energy $E(\theta_H, H)$ with the magnetization orientation is displayed in Figure 3.7.a), the crystal is at ambient temperature. The magnetization orientation θ_H minimizes the crystal energy $E(\theta_H, H)$. The magnetic field H is applied with an angle of $\pi/18$ with respect to the c-axis; it causes a non null susceptibility. As a result the magnetization orientation θ_H varies with the magnetic field H and the spontaneous magnetization is perfectly aligned with H when $\|\vec{H}\| > \left\|\vec{H}_{c_j}\right\|$.

As H becomes negative, $\theta_H = \pi$ is the stable state. However the magneto crystalline anisotropy provides an energy barrier and the crystal stays in an unstable balance such that $\theta_H < \pi/2$ as long as the magnetic field magnitude is lower than the coercive field magnitude $\|\vec{H}\| < \left\|\vec{H}_{c_j}\right\|$.

The calculated magnetization $M_{||}$ along H at ambient temperature is displayed in Figure 3.7.b). The magnetization curve is rectangular as the magnetic field is applied along the c-axis. Whenever the magnetic field is applied with an angle θ_u, the susceptibility is finite and the magnetization curve is no longer rectangular. The amplitude of the coercive field varies with the angle θ_u.

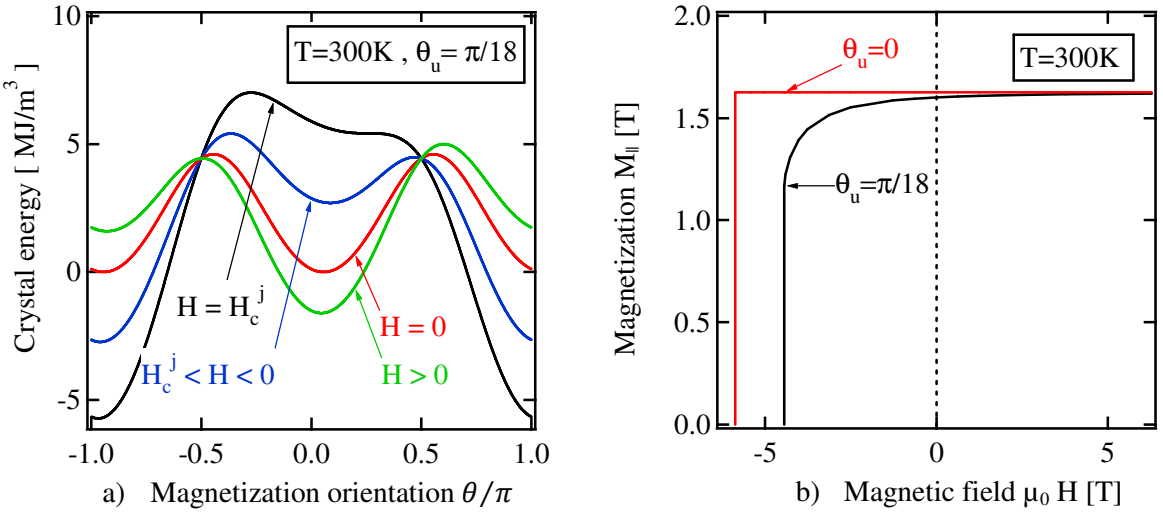

Figure 3.7: The left plot displays the $Nd_2Fe_{14}B$ energy variation with the magnetization orientation at temperature 300 K as we apply a magnetic field H in the crystal vicinity with an angle of π/18 with respect to the c-axis. The magnetization orientation θ_H is numerically computed from equation (3.6). The magnetization $M_{||}$ is displayed in the right plot as the magnetic field is applied along the c axis (red curve). The black curve corresponds to a magnetic field applied with an angle equal to π/18. The magnetization $M_{||}$ is computed using equation (3.7).

At a temperature below the SRT, the easy axis makes an angle θ_e with respect to the c-axis; θ_e is given by equation (3.4). The combination of the Zeeman energy and the magnetocrystalline anisotropy leads to the existence of 4 energy minima. Figure 3.8.a) displays the energy at 25 K, the orientation θ_u is a local maximum.

This small energy bump does not lead to the existence of a coercive process since the magnetization may freely rotate around the c-axis. For instance at $H = 0$, the spontaneous magnetization is oriented along an easy axis. As a result the two angles $\theta_1 = \theta_u - \theta_e$ and $\theta_2 = \theta_u + \theta_e$ minimize the energy; the magnetization "turns" along the easy cone in order to align along $\theta_u - \theta_e$ or $\theta_u + \theta_e$. No energy is needed in order to flip the magnetization from θ_1 to θ_2. In addition a small susceptibility appears since the easy axis and the magnetic field are not collinear.

The balance between θ_1 and θ_2 is broken whenever the magnetic field is applied with a non null angle with the c-axis. The magnetization orientates along the easy axis which minimizes the crystal energy. Thus the magnetization is aligned along θ_1 when the magnetic field is oriented positively along the vertical axis. The magnetization is directed along θ_2 whenever the field is directed towards the negative z.

Figure 3.8.b) displays the magnetization curve at 25 K. No step is observed on the magnetization curve as long as the magnetic field H is applied along the c-axis. As the magnetic field H is applied with and angle θ_u with respect to the c-axis, one observes a drop in the crystal magnetization curve at $H = 0$. This originates from the flip of the magnetization orientation from θ_1 to θ_2. The magnetization jump amounts to:

$$\Delta M = 2M_s \sin(\theta_e) \sin(\theta_c) \tag{3.8}$$

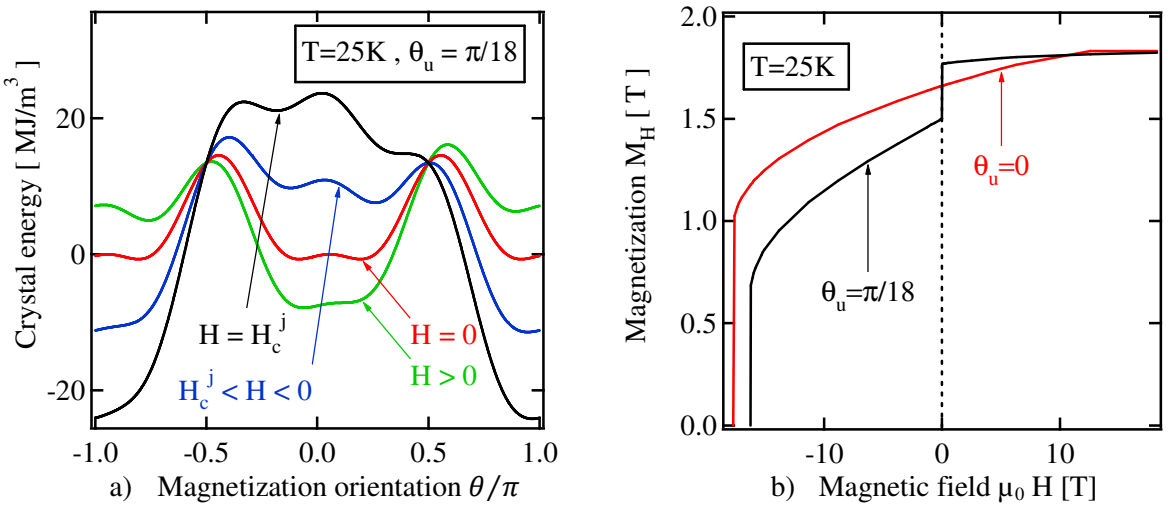

Figure 3.8: The left plot displays the $Nd_2Fe_{14}B$ energy variation with the magnetization orientation at temperature 25 K as we apply a magnetic field H in the crystal vicinity with and angle of π/18 with respect to the c-axis. The magnetization is displayed in the right plot as the magnetic field is applied along the c axis (red curve). The black curve corresponds to a magnetic field applied with an angle equal to π/18.

The perspective and the limit of cooling down $Nd_2Fe_{14}B$ magnets appear clearly in Figure 3.9. Figure 3.9 plots the variation of the coercive field, the spontaneous and the remanent magnetization with the $Nd_2Fe_{14}B$ crystal temperature assuming $\theta_u = 0$. The coercive field and the spontaneous magnetization of the $Nd_2Fe_{14}B$ single crystal increases as the temperature decreases. The calculated value is three times higher at 25 K than at ambient temperature, giving rise at cryogenic temperature to a large resistance to magnetization. However the SRT causes an angle between the c-axis and the easy axis. This leads to the reduction of the remanent magnetization at temperature below the SRT.

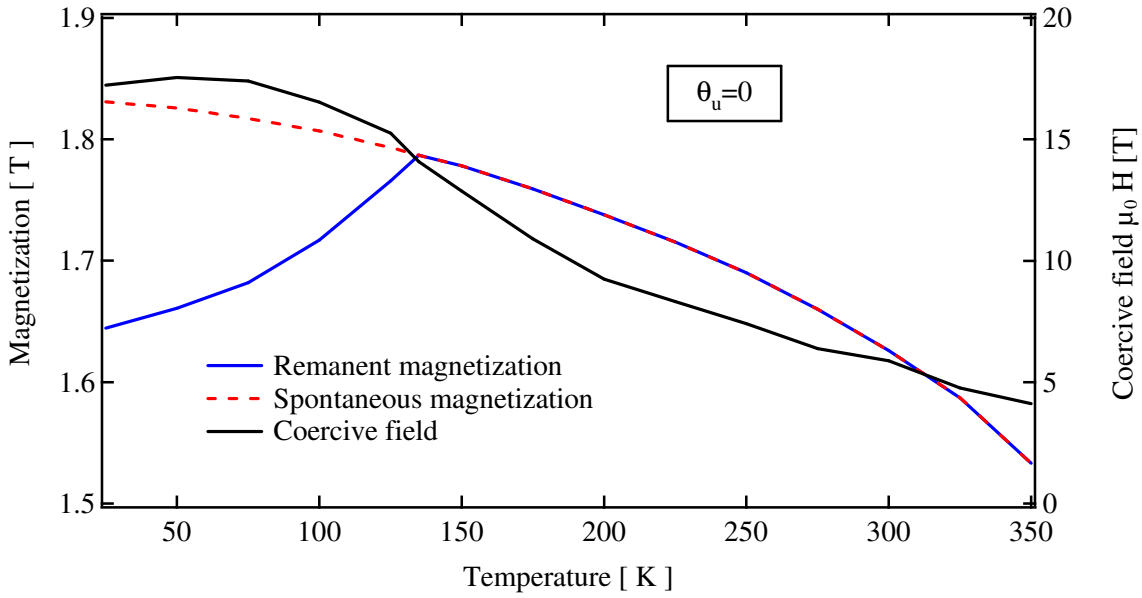

Figure 3.9: Variation with the temperature of the spontaneous magnetization (red dashed curve), the remanent magnetization (blue curve) and the coercive field (black curve) of the $N_2dFe_{14}B$ crystal. The remanent magnetization is computed using equation (3.7). The spontaneous magnetization is sourced in [75].

From crystal to magnet

In the Stoner and Wolfharth model [26], the magnetization reversal mechanism in crystal is a uniform rotation of the spontaneous magnetization. The coercive field is computed from the crystal energy. Actually coercive field of $Nd_2Fe_{14}B$ magnets produced by powder metallurgy is lower than the Stoner and Wolfharth presented before. Defects in magnets reduce the coercive field. The magnetization curves of real $Nd_2Fe_{14}B$ magnets at various temperatures are presented hereafter.

3.2.2. Magnetization curves of 495t NEOREM magnet

First, we will look at the first magnetization curve of the 495t NEOREM magnet. Afterwards, magnetization curves of the 495t NEOREM magnet at low temperature are exposed. Finally one deduces the magnet performance at a low temperature from the experimental magnetization curves. Measured magnetization curves are also used to build a 3D nonlinear model of the CPMU. One needs therefore to measure the magnet magnetization as the magnetic field is parallel and perpendicular to the easy axis in order to get a complete magnet description. Measurements have been carried out at the Louis Néel Laboratory with a 10 T magnetometer [76]. The resolution order of the magnetization measurement is 2.6 µT with an absolute precision of 0.6%. The 10 T magnetometer is presented in Appendix A.

First magnetization curve

Magnetization measurements have been performed on several samples geometries. Some samples with cubic ($4 \times 4 \times 4 mm^3$) and rectangular ($4 \times 4 \times 1 mm^3$) shape have been cut in the core of a demagnetized $Nd_2Fe_{14}B$ block. The samples have been first magnetized at ambient temperature before being cooled at cryogenic temperature; the magnetic field H was applied along the easy axis of the samples and $M_{\parallel}$ is the magnetization measured along the easy axis. Figure 3.10 represents the first magnetization curve at 300 K for both geometries. The coercive field and the remanent field differ slightly between both samples. The sintered magnet manufacturing process results in large non homogeneities in block volume so that one interprets these non homogeneities as being the origin of the differences. One first observes a large initial susceptibility; the wall which separates the different magnetic domains propagates freely. The domains with their magnetization aligned with the applied field H grow rapidly. The propagation of walls and the domain growth are reversible. The magnetization then reaches a first plateau before saturation. Any further variation on the magnetization corresponds to an irreversible process.

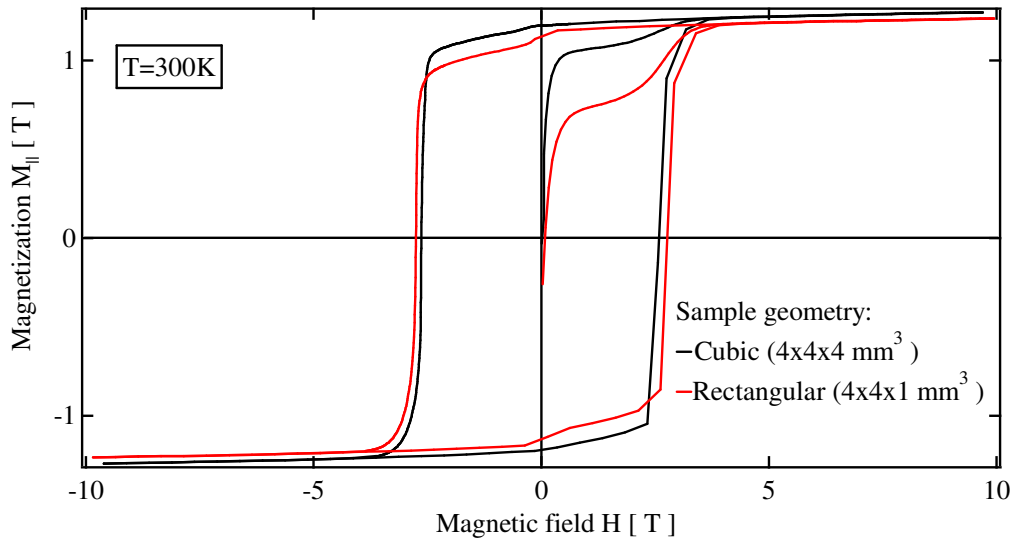

Figure 3.10: First magnetization curve at ambient temperature measured on a cubic (black line) and a rectangular (red line) sample.

One also remarks a magnetization step around $H = 0$. Tenaud and al. showed that this step is an irreversible magnetization loss [75], [77]. It arises from a strong reduction of the coercive field at the sample surface. The coercive field is strongly reduced over a depth ϵ from the surface. The depth corresponds roughly to the grains average diameter. Tenaud approximates magnet as an assembly of α grains in hard magnetic phase with high coercive field $H_{c_{j_H}}$ and $1-\alpha$ grains in soft magnetic phase with low coercive field$H_{c_{j_S}}$. α is the ratio of the hard magnetic phase volume over the total volume. The magnetization M is the sum of the soft and hard magnetic phase magnetization. This soft magnetic phase causes a parasitic step that one would naturally get rid of in order to obtain a correct $Nd_2Fe_{14}B$ magnetization curve. In a reverse magnetic field H such that $H_{c_{j_H}} < H < H_{c_{j_S}}$ and for a hard (soft) magnetic phase whose density equals to α $(1-\alpha)$, the magnetization M is:

$$M = \alpha M_{sat} - (1-\alpha)\, M_{sat} \tag{3.9}$$

M_{sat} is the magnetization measured on the sample as a 10 T magnetic field was applied. The magnetization step ΔM is

$$\Delta M = M - M_{sat} = 2(1-\alpha)M_{sat} \tag{3.10}$$

One should note that real $Nd_2Fe_{14}B$ magnets don't present such a step since magnets are covered with a slim Ni coating during their fabrication in order to protect them from corrosion.

When the sample has a rectangular base which a and h are the two side lengths, the volume ratio α and the magnetization jump $\Delta M/2M_{sat}$ are:

$$\alpha = 1 - \frac{4\epsilon}{a} - \frac{2\epsilon}{h} \qquad\qquad \frac{\Delta M}{2M_{sat}} = \frac{4\epsilon}{a} + \frac{2\epsilon}{h} \tag{3.11}$$

One deduces easily the expression of the volume ratio and the magnetization discontinuity for the cube by replacing h with a in equation (3.11). The main advantage of this model is to simply relate the ratio $\Delta M/2M_{sat}$ to the geometry parameters. It is also feasible to numerically recover the step at ambient temperature with RADIA since RADIA allows the irreversible non linear part of the magnetization curve to be built and to simulate the magnet performance within this area [78]. The magnetization curve of the non linear anisotropic materials may be described in RADIA with:

$$\begin{aligned} M_{\parallel}(H) &= \chi_{\parallel_0}\left(H - H_{c_j}^0\right) + \sum_{i=1}^{3} M_{\parallel_i} \tanh\left(\chi_{\parallel_i}\left(H - H_{c_j}^i\right)/M_{\parallel_i}\right) \\ M_{\perp}(H) &= \chi_{\perp_0} H + \sum_{1}^{3} M_{\perp_i} \tanh\left(\chi_{\perp_i} H / M_{\perp_i}\right) \end{aligned} \tag{3.12}$$

$M_{\parallel}$ $(M_{\perp})$ is the magnetization along (perpendicular to) the easy axis. RADIA gives a non linear description of both magnetizations by mean of hyperbolic tangent functions. The above expression is used to define the parallel magnetization. We focus on this only since the perpendicular magnetization is not necessary to recover the step observed on the measured magnetization curve. The susceptibilities, the coercive fields and the magnetizations used to describe the parallel magnetization of the hard magnetic phase are listed in Table 3.3. These parameters are given for the cubic and the slim sample. They have been tuned so that the hard magnetic phase fits well the measured magnetization curve in the reverse field H such that $H < H_{c_{j_S}}$. To describe the soft magnetic phase in this model we use the parameters of the hard magnetic phase, except the coercive field. In order to rebuild the experimental magnetization curve, one selects the coercive field of the soft magnetic phase and the depth into which one applies the soft magnetic material

Table 3.3: Susceptibilities, coercive fields and magnetization for the cubic and the slim samples. These parameters describe the magnetization parallel to the easy axis.

Hard phase	$\mu_0 H_{c_j}^{i}$ [T]	$\chi_{\parallel_0}$	$M_{\parallel_1}$ [T]	$\chi_{\parallel_1}$	$M_{\parallel_2}$ [T]	$\chi_{\parallel_2}$	$M_{\parallel_3}$ [T]	$\chi_{\parallel_3}$
Cubic sample	2.64	0.017	0.835	10.5	0.2	3.5	0.1	0.10
Slim sample	2.756	0.045	0.795	18.5	0.19	0.8	0.19	0.014

Figure 3.11 displays the magnetization curves built with RADIA. They fit quite well the experimental ones. The thicknesses deduced from the analytical model and used in the RADIA model are listed in Table 3.4. The rectangular sample presents a soft magnetic phase at its surface whose coercive field is twice as small as the cubic one. A longer in air storage and the difficulty of polishing such tiny samples compared to cubic samples might explain such differences.

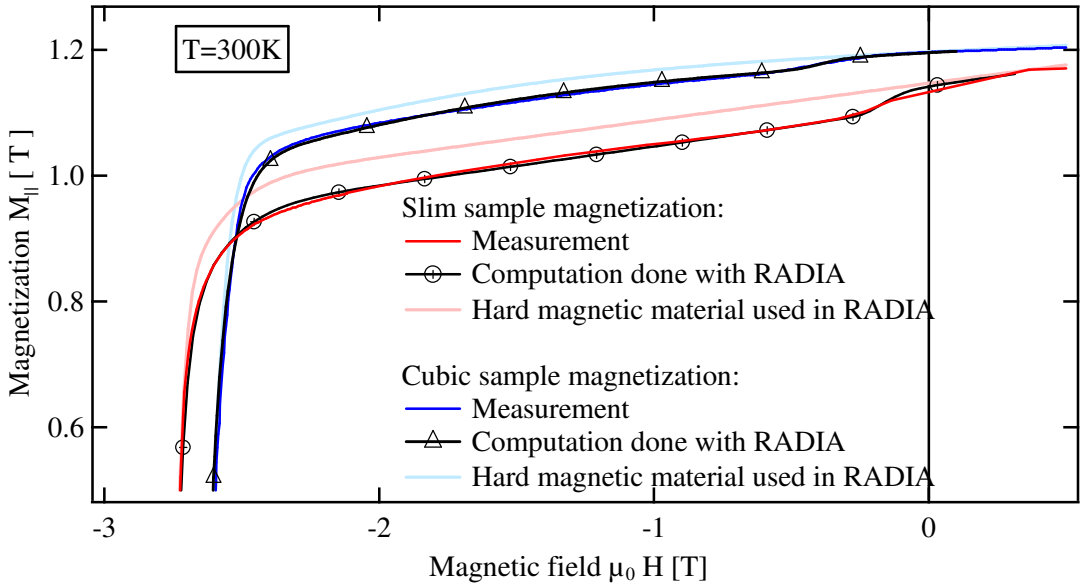

Figure 3.11: Magnetization measured with the 10 T magnetometer and computed with RADIA. The hard magnetic material describing the core of the slim (cubic) sample in RADIA is coloured in light blue (light pink). The thicknesses of the soft magnetic phase in the RADIA model (coercive field, thickness), are listed in Table 3.4.

Table 3.4: Main parameters of the soft magnetic phase at the sample surface.

	Analytical model		RADIA		
Sample geometry	$\Delta M/2M_{sat}$	Thickness [µm]	$\mu_0 H_{c_{j_H}}^{i}$ [T]	$\mu_0 H_{c_{j_S}}^{i}$ [T]	Thickness [µm]
Cubic	0.0072	4.8	-2.64	-0.264	7
Rectangular	0.025	8.4	-2.756	-0.125	

Magnetization curves at low temperature

In the following, we present the magnetization measurement parallel and perpendicular to the easy axis performed at low temperature.

Magnetization has been measured from 80 K to ambient temperature. Measurements on the slim sample are displayed in Figure 3.12. Below 150 K, the coercive field is higher than 5 T. The remanent magnetization increases at low temperature. However below 150 K, the step causes the magnetization curve with highest remanent magnetization to cross the curves with the lowest remanent magnetization in reversed magnetic field. This crossover clearly limits the cooling benefit. At low temperature, this smooth step may arise from the soft magnetic phase and the easy axis reorientation. Indeed within a magnet, grain easy axes are distributed around the macroscopic easy axis so that some easy axes make an angle with the applied magnetic field. As explained in section 3.2.1, this misalignment leads to a step on magnetization curve below the SRT.

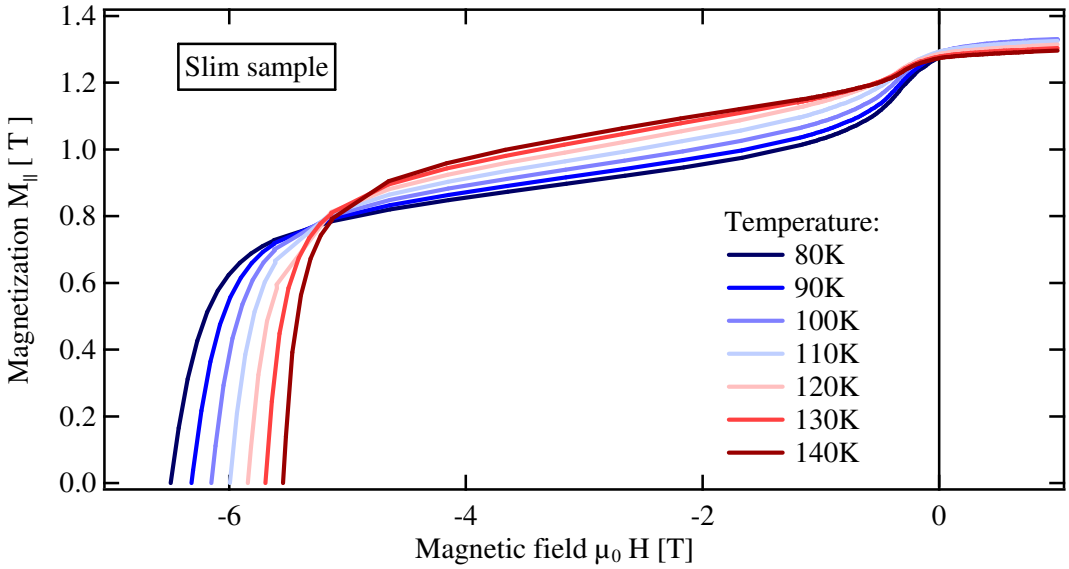

Figure 3.12: Second quadrant of the magnetization measurement measured on the slim sample. The measurements were performed with the 10 T magnetometer between 80 K and 140 K.

Measurements on the cubic sample are presented in Figure 3.13. One observes that the step causes the 495t NEOREM curve at 120 K to cross and to go below the curve at 240 K in a strong negative field, even though the remanent magnetization at 120 K exceeds the one at 240 K.

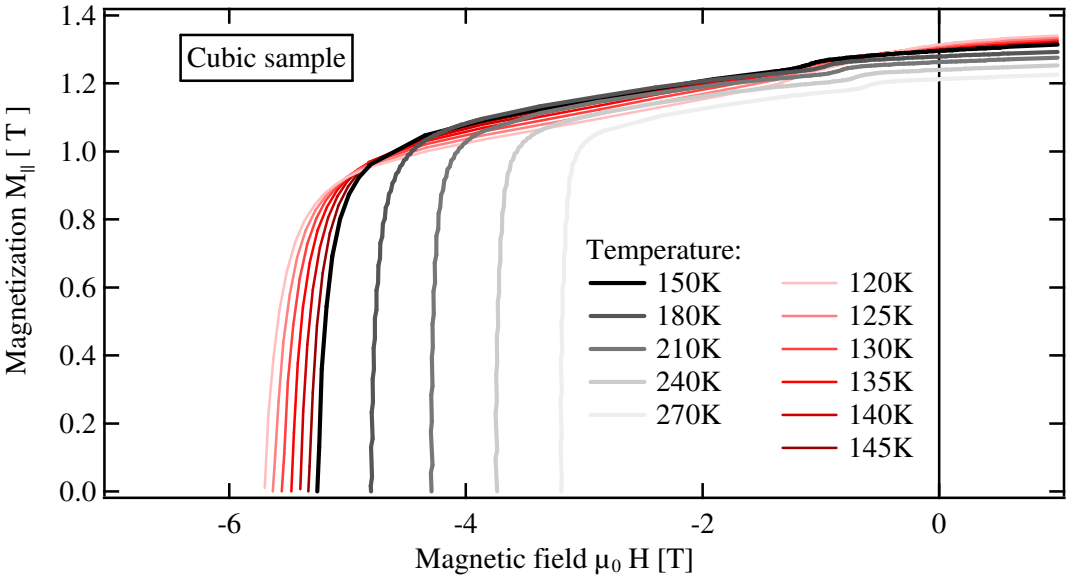

Figure 3.13: Second quadrant of the magnetization curve measured on the cubic sample. The measurements were performed with the 10 T magnetometer between 120 K and 270 K.

The soft magnetic phase spoils the determination of easy axis reorientation. Both steps are mixed together so that it is difficult to distinguish them. The magnetization step is displayed at 120 K and 140 K in Figure 3.14 for the cubic and the slim sample. The SRT transition takes place at a temperature between 120 K and 140 K. Hence the discontinuity observed along the magnetization curves at 140 K arises from the magnetization reversal which occurs at the sample surface. The magnetization jump at 120 K results from the easy axis reorientation and the magnetization reversal. One deduces from the magnetization curves at 140 K that the coercive field magnitude $\left|H_{c_{j_S}}\right|$ is clearly smaller than 1 T as one considers the slim sample. On the other side the soft magnetic phase at the cube sample surface exhibits a coercive field magnitude higher than 1 T. Below the SRT threshold, the easy axis reorientation causes a step on the magnetization curve at low negative field ($|H| < 1$); consequently the two steps overlap in a slim sample while they are still distinguishable in a cube. It then becomes difficult to properly eliminate the step originating from the coercive field reduction from magnetization curves measured on a slim sample. Finally one prefers to use the cubic sample to measure the $Nd_2Fe_{14}B$ magnetization curve at low temperature.

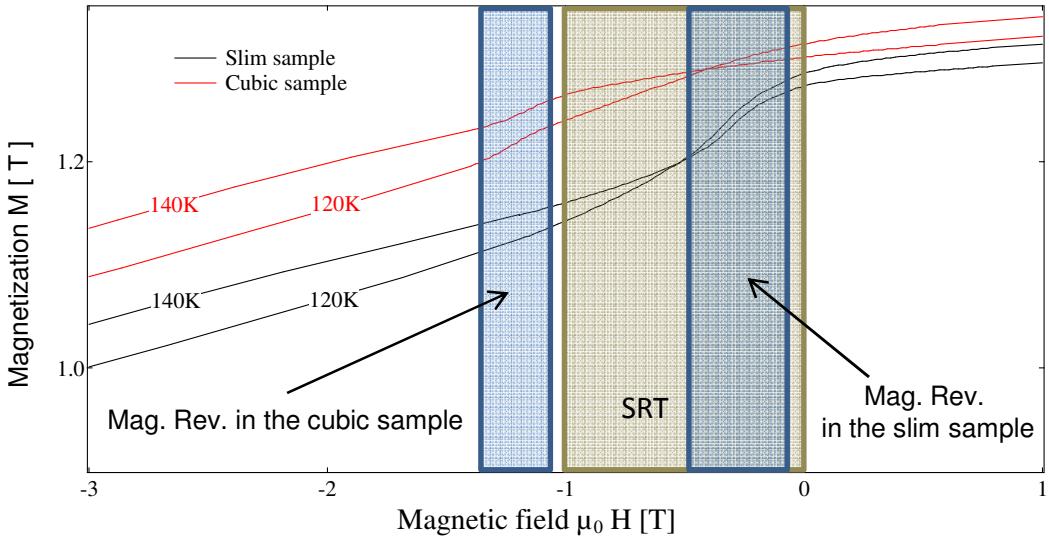

Figure 3.14: Detail of the step at 120 K and 140 K observed on the magnetization curves of the cubic (red) and the slim (black) samples.

The magnetization perpendicular to the easy axis in the case of the cubic sample is displayed in Figure 3.15. The magnetic field is applied perpendicularly to the easy axis in order to measure transverse magnetization curve. The magnetic field required to reverse the magnetic field then largely exceeds the coercive field. Finally the sample doesn't experience a magnetization reversal at its surface; one doesn't observe discontinuities on the transverse magnetization measurement. At ambient temperature the magnetization perpendicular to the easy axis varies linearly with the magnetic field. Lowering the temperature increases the transverse susceptibility. One observes below 150 K non linearity on the transverse magnetization, this phenomenon is also linked to SRT.

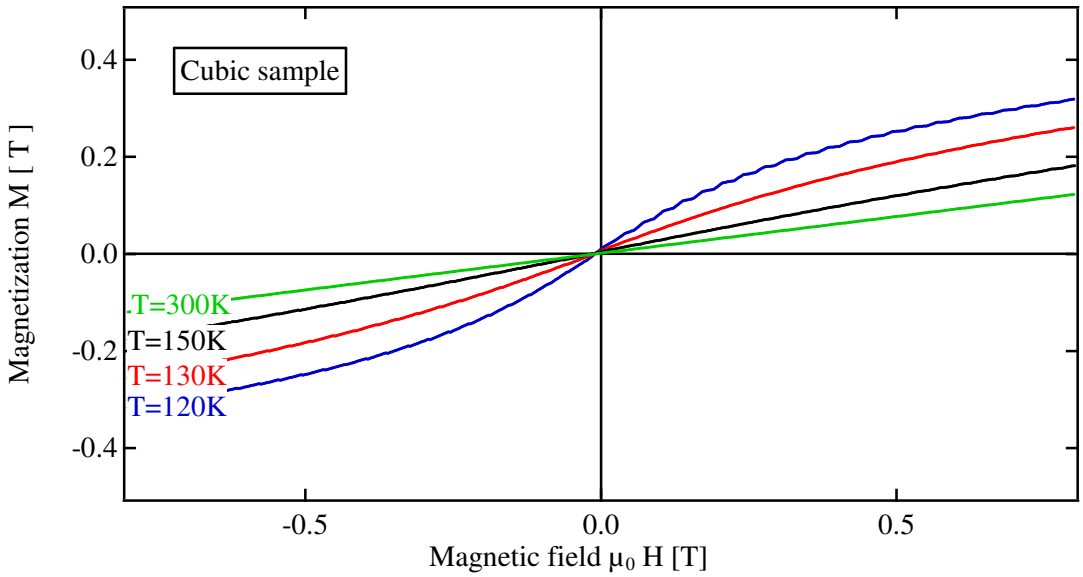

Figure 3.15: Magnetization perpendicular to the easy axis measured on the cubic sample between 120 K and 300 K with the 10 T magnetometer.

Variation of the coercive field and the remanent magnetization with the temperature

The remanence magnetization of the 495t NEOREM magnet varies linearly with the temperature between the ambient temperature and 120 K. It reaches a maximum at 120 K. Figure 3.16 represents the variation of the remanent magnetization with the temperature.

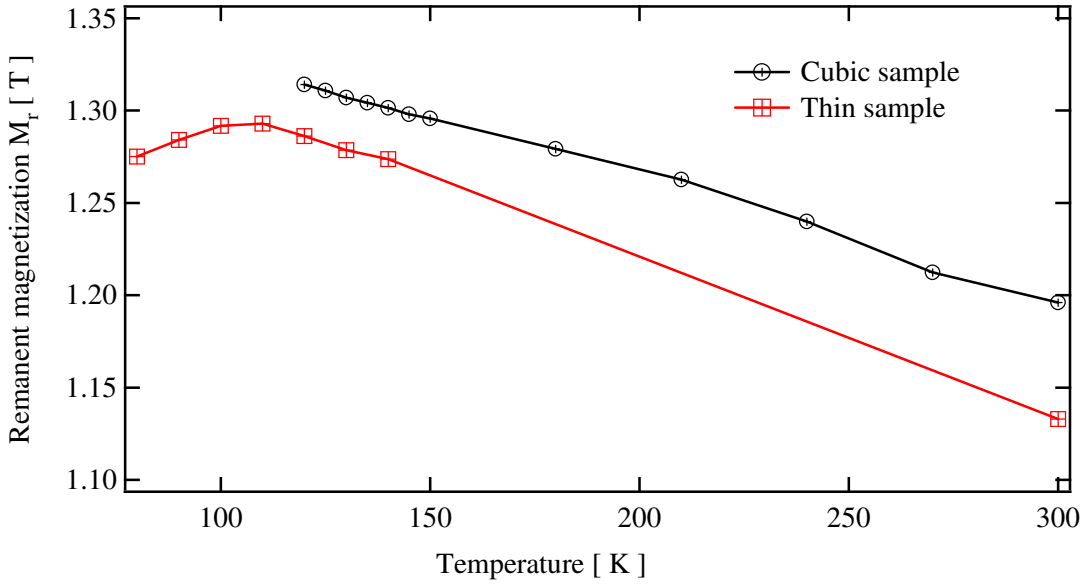

Figure 3.16: Variation of the remanent magnetization with the temperature.

The coercive field is displayed in Figure 3.17. The coercive field decreases linearly with the temperature. Cooling the $Nd_2Fe_{14}B$ magnet down to 150 K nearly doubles the coercive field. Below 150 K the coercive field is larger than 5 T. With such a high coercivity, the $Nd_2Fe_{14}B$ magnet presents a resistance to radiation damage similar to the Sm_2Co_{17} magnet.

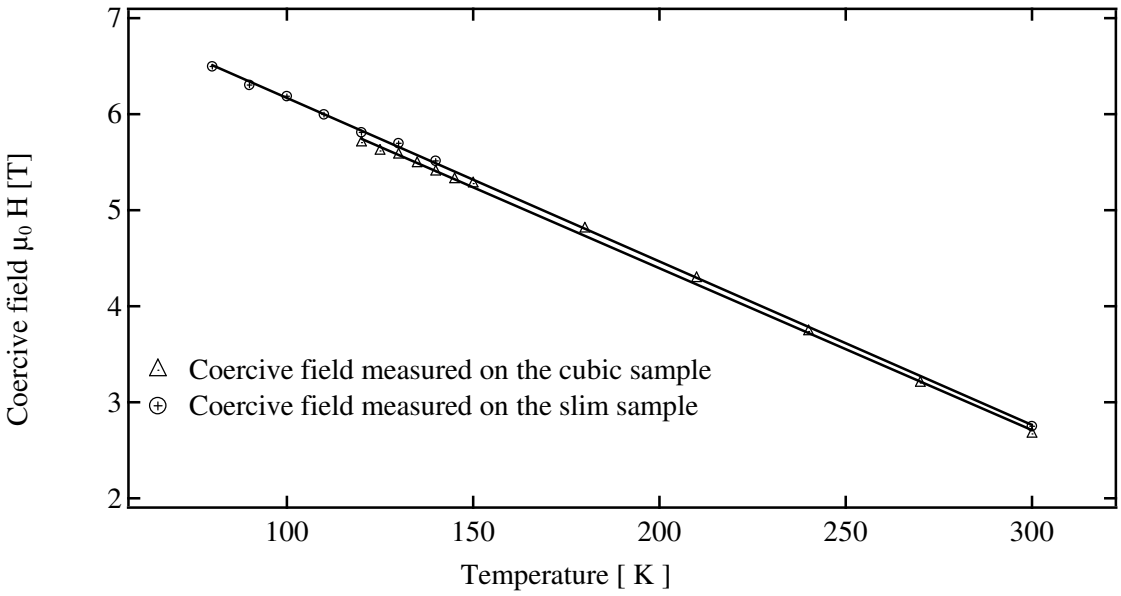

Figure 3.17: Variation of the coercive field with the temperature for the cubic and the slim sample.

3.2.3. $Nd_2Fe_{14}B$ cryogenic undulator

The analysis of Figure 3.14 and Figure 3.15 suggests that we cannot correctly simulated the magnetic field of the $Nd_2Fe_{14}B$ cryogenic undulator using conventional linear anisotropic models. In both directions parallel and perpendicular to the easy axis the material model needs to be non linear. The non linear model is exposed below. However a surface effect spoils the magnetization measurement parallel to the easy axis. The post processing done to correct the measurement is first presented.

Post processing

$Nd_2Fe_{14}B$ is known to be very sensitive to corrosion in air, even at ambient temperature. Thus a special foil covers industrial $Nd_2Fe_{14}B$ magnets in order to protect them from corrosion in air. The samples we use to measure the $Nd_2Fe_{14}B$ magnetization were cut in 495t NEOREM block core. Since no surface treatment was performed on the sample surface, a soft magnetic phase developed at its surface. The magnetization reversal in the soft magnetic phase causes a parasitic step on the 495t NEOREM magnetization curve parallel to the easy axis. One may also consider the magnetization reversal as an anomaly on the parallel susceptibility. The magnetization measured at 240 K is plotted in Figure 3.18. The parallel susceptibility $\chi_{\parallel} = dM_{\parallel}/dH$ is also displayed. The magnetization reversal causes a characteristic bump on the parallel susceptibility.

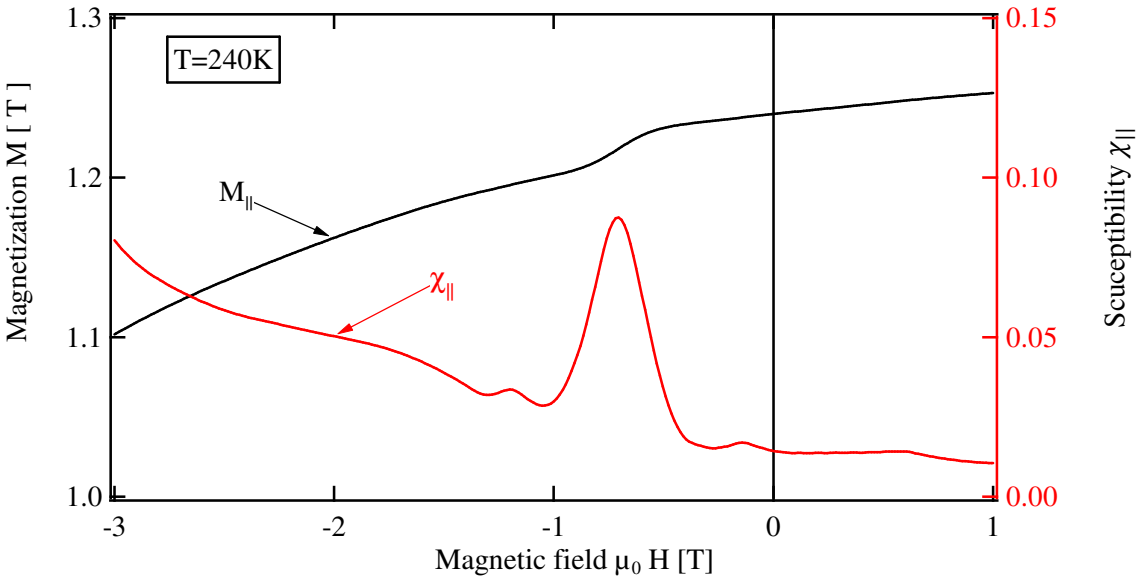

Figure 3.18: Detail of the step observed on the magnetization curve at 240 K and the corresponding bump on the susceptibility.

The processing consists of rebuilding a magnetization curve from a parallel susceptibility $\chi_{\parallel_c}$ free of the local bump. The susceptibility $\chi_{\parallel_c}$ is derived from the experimental measurement in the region away from the parasitic magnetization reversal. In the magnetization reversal region, one approximates then the susceptibility $\chi_{\parallel_c}$ with a linear function. Two different fits $\chi_{\parallel_{c1}}$ and $\chi_{\parallel_{c2}}$, which approximate the susceptibility $\chi_{\parallel_c}$, are displayed in Figure 3.19. The magnetization curves which one builds from the different susceptibilities are also plotted. The difference between both curves is smaller than 50G/0.5mT at any magnetic field H; the proposed correction is quite robust.

All magnetization curves are processed in the same way in order to correct the observed step. They are plotted in Figure 3.20. One uses these curves to describe the 495t NEOREM $Nd_2Fe_{14}B$ magnets within the RADIA CPMU model.

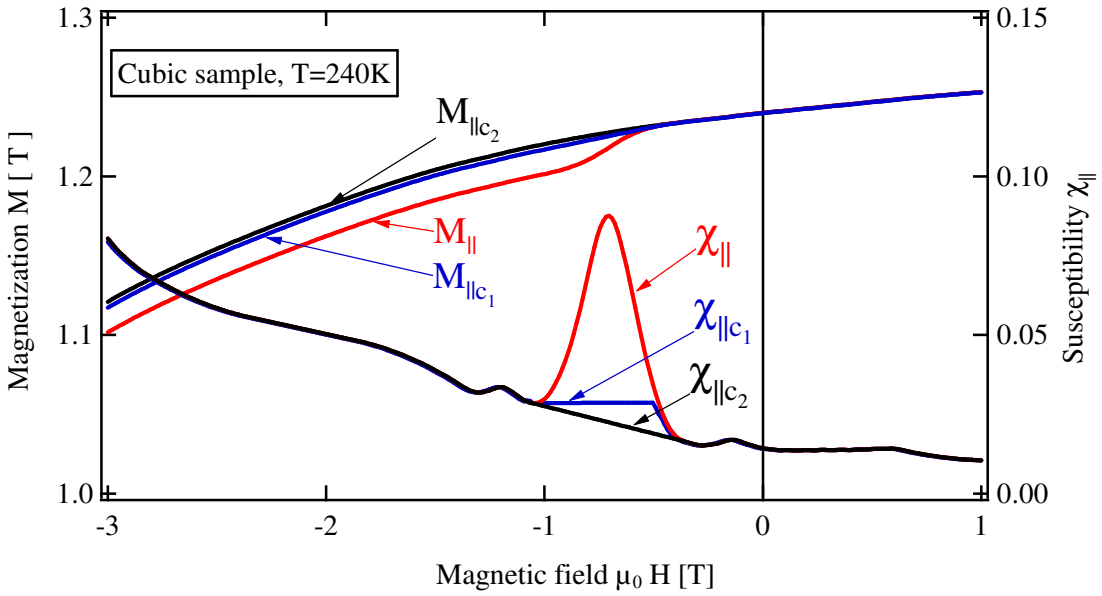

Figure 3.19: Detail of the step correction performed on the experimental magnetization measurement.

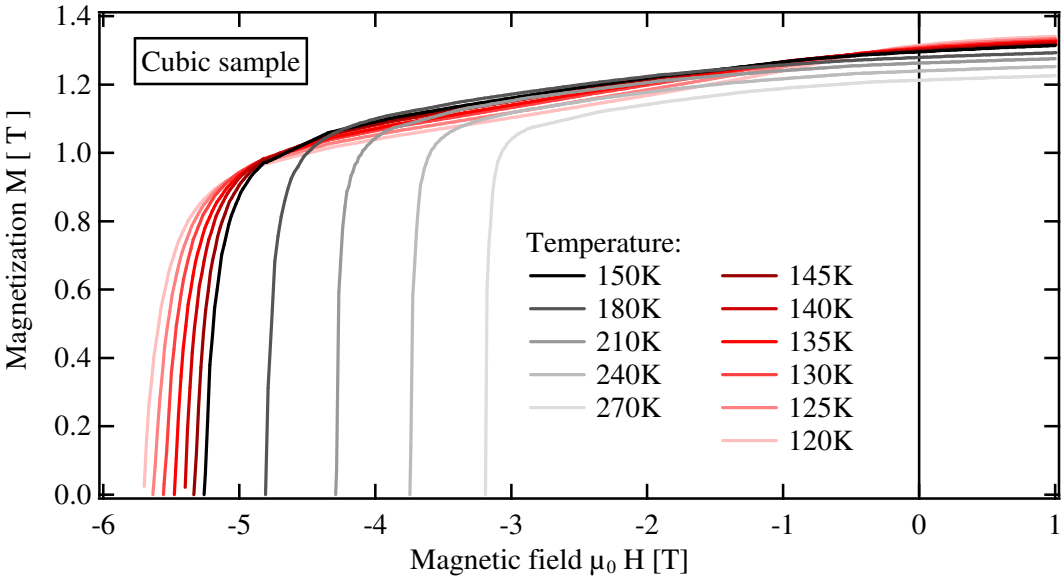

Figure 3.20: Processed magnetization curve. Measurements on the cubic sample have been all corrected with the process detailed above.

HYB18 peak field and field integral

We present hereafter the RADIA model of the hybrid undulator dedicated to the CPMU project at the ESRF. Within the RADIA model, one assumes that the magnetic properties of the pole material are constant at all temperatures. The pole material used is low carbon steel (XC06) with a saturation magnetization of 2.1 T. In this case, 495t NEOREM magnet magnetization curves are used to compute the CPMU magnetic performance at low temperature. The previous section clearly illustrates that conventional linear anisotropic model is not accurate enough to describe $Nd_2Fe_{14}B$ magnets. One uses the powerful feature of RADIA to describe non linear anisotropic materials according to equation (3.12). The fits were limited to -1.9 T to 1.25 T for the magnetic field H in order to get a high level of accuracy on the magnetization. This range includes the working points in the magnet blocks of the undulator.

Figure 3.21 represents the first harmonic magnitude of the HYB18 versus the temperature for a gap of 6 mm. Cooling the 495t NEOREM magnet from ambient temperature down to 150 K increases the HYB18 first harmonic magnitude about 8%. Within a PPM design, the effective peak field increase reaches 9%. However this larger increase doesn't compensate for the PPM lower effective peak field. The CPMU undulator based on hybrid technology produces a higher effective peak field. This peak field is nearly constant between 140 K and 180 K since its variation is lower than 0.1% within this temperature range. Setting the CPMU temperature is not a critical issue; however any temperature gradient along the magnetic assembly should be avoided. This point is discussed in the following section. The first harmonic reaches a maximum at 150 K. This temperature is 30 K above the temperature which maximizes the remanent magnetization. Non linearity in the second quadrant of the magnetization curves explains such difference. Due to the SRT the recoil permeability decreases with temperature.

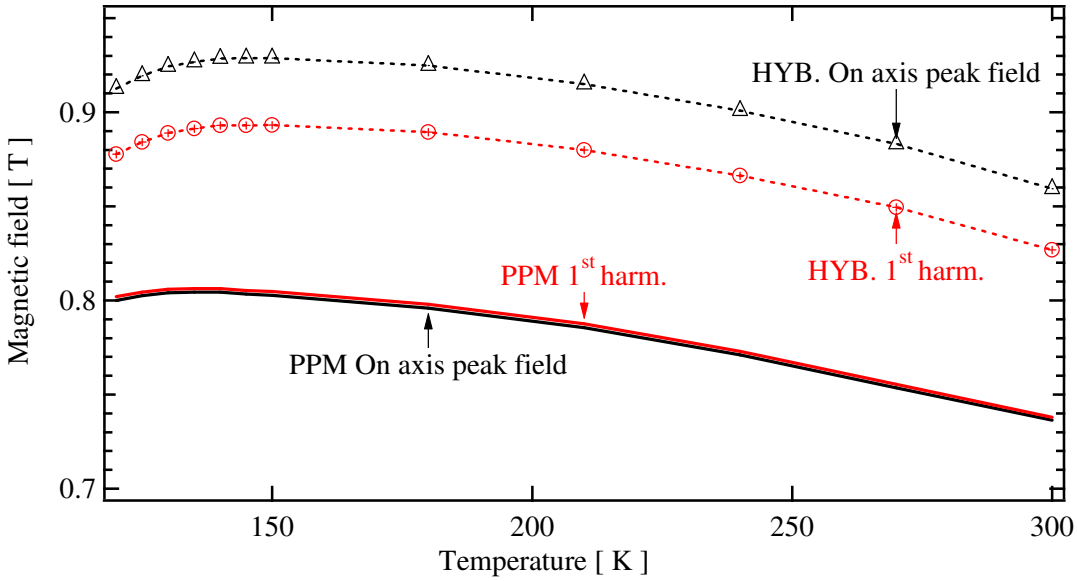

Figure 3.21: HYB18 peak field and first harmonic variation with the temperature. The calculation is done with RADIA for a gap of 6 mm.

The working points (H, M) of a magnet in the HYB18 are represented at 120 K and 150 K in Figure 3.22. They are centred around -1 T. Thus, instead of the remanent magnetization, one would rather use the magnetization close to the magnet working point in an undulator which is -1 T, in order to determine the CPMU temperature. Because of the curve crossover in the second quadrant, this temperature doesn't correspond to the temperature which maximizes the remanent magnetization.

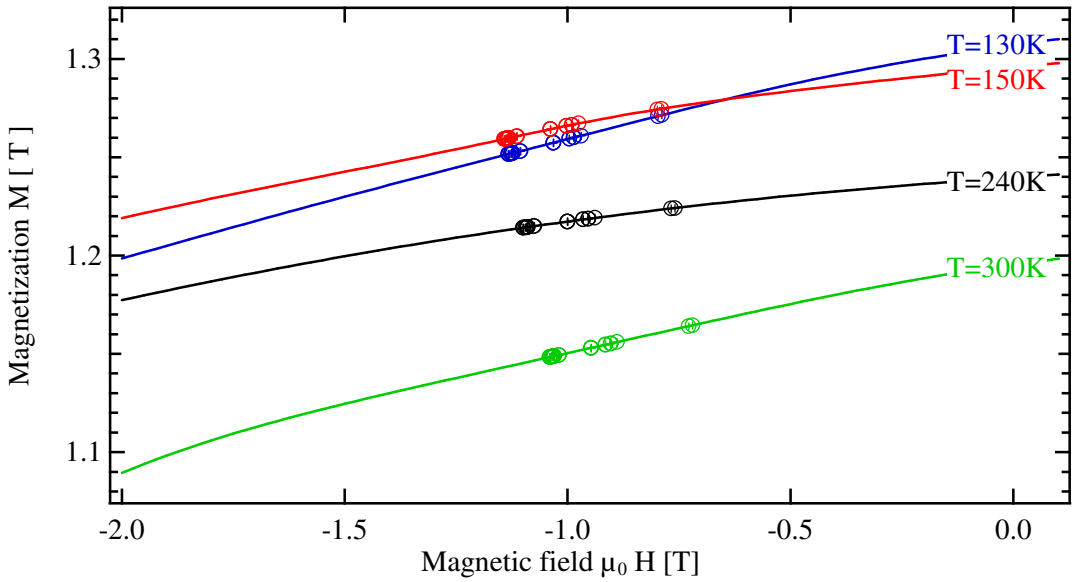

Figure 3.22: Working points, i.e. magnetization and intern magnetic field, of a magnet in the hybrid undulator at various temperatures. The calculation is done with RADIA for a gap of 6 mm.

The field integral has also been investigated. The on-axis vertical field integral variation with the temperature is plotted in Figure 3.23. The field integral decreases with the temperature. This corresponds to the systematic contribution originating from the end field termination. From 300 K to 150 K the increase of the field integral is rather small, typically about 20 Gcm while it becomes important at lower temperature. At 120K the field integral is 60 Gcm. At 150 K, where the CPMU peak field reaches a maximum, the field integral still sits within the limitation listed in Table 2.4.

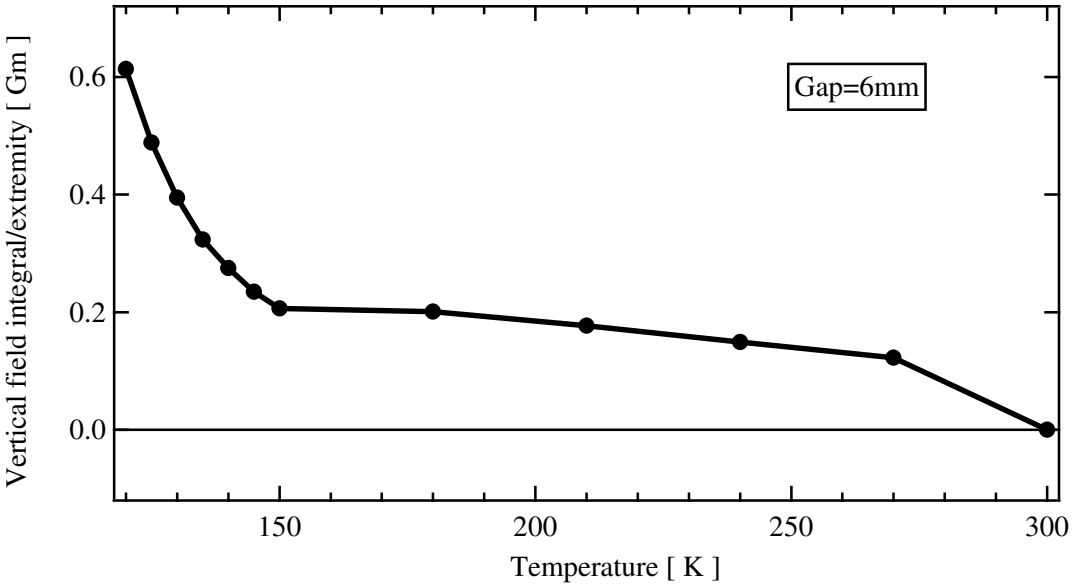

Figure 3.23: Variation of the on-axis vertical field integral with the temperature. The undulator gap is set at 6 mm.

3.3. An approach on thermal analysis of the CPMU

A cooling system at 80 K is used to keep the CPMU temperature constant. Its connection with the CPMU sets the CPMU temperature. In this subchapter, we will describe how we build a CPMU thermal model to calibrate the connection. In the first part we describe the thermal model, the different heating sources and the connection between the cooling system and girders. We compute in the following section the heat transfer from the heating sources with respect to the CPMU temperature. To conclude, we explain how we calibrate the connection as a function of the CPMU temperature.

Figure 3.24 represents schematically the closed loop used to keep the magnetic assembly at a low temperature. A liquid nitrogen closed loop is connected to refrigerant channels fixed on each girder. The magnetic assembly is at cryogenic temperature while its physical environment (mechanical support, vacuum chamber) is at room temperature.

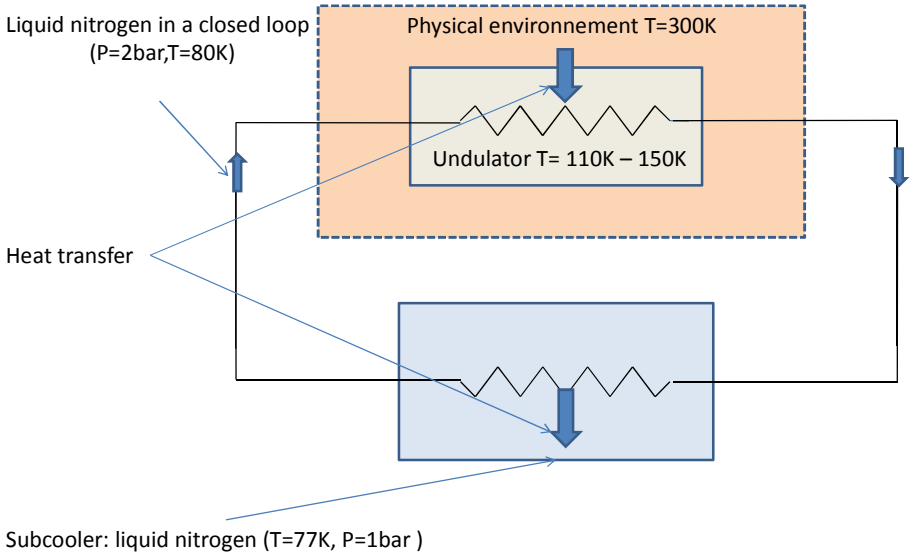

Figure 3.24: Schematic description of the CPMU and its cooling system.

Due to this temperature gradient, thermal flux occurs between the CPMU and its environment. The thermal flux is evacuated by the closed loop and finally transmitted to the sub cooler.

Moreover the nitrogen in the closed loop is at 80 K. Therefore we need to control the thermal contact between the cooling pipes and the magnetic assembly to keep the magnetic assembly around 150 K. We will now define a thermal model in order to:

- Identify the heating sources and the heat transfer modes.
- Calibrate the connection between the magnetic assembly and the cooling system.

3.3.1. Description of the thermal model

Heating sources

Figure 3.25 schematically represents the magnetic assembly and its physical environment. The magnetic assembly is kept under vacuum so that there is no thermal convection between the magnetic assembly and its physical environment. The total thermal flux is the sum of:

- Thermal conduction trough the 20 stems which mechanically connect the girders to the mechanical support. The mechanical support is at room temperature T_e whereas the girders are at cryogenic temperature T_g. Each stem thermally conducts a heat flux ϕ_{st}.
- Thermal radiation between the vacuum chamber and the girders. The vacuum chamber surface is at room temperature T_e whereas the girder surface is at temperature T_g. A heat flux ϕ_{rad} occurs between both surfaces by thermal radiation.

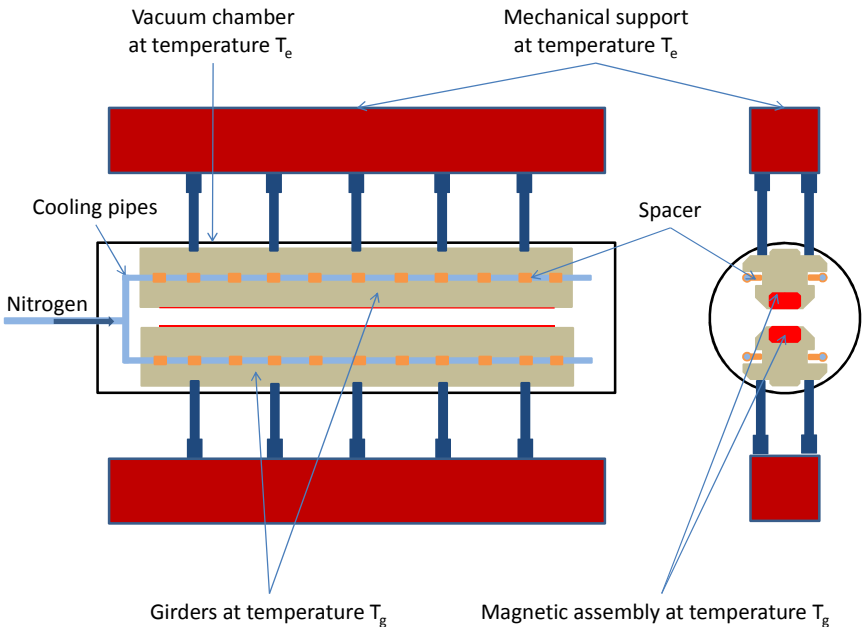

Figure 3.25: Schematic description of the CPMU and its thermal environment.

Girders

The total thermal flux enters the girders and propagates through them. The girders are made of Aluminium which is a good thermal conductor. Thus we assume that the temperature is uniform along the girders. Moreover we neglect the thermal radiation that enters the gap when the undulator is closed at 6 mm. Consequently the magnetic assembly is thermally isolated from the stems and the vacuum chamber. The magnetic assembly is then totally isolated from the heating sources. The magnetic assembly and girders are at the same temperature T_g and the temperature is uniform along the girders.

Spacers

The girders are connected to cooling pipes through which liquid nitrogen flows at 80 K. The nitrogen evacuates the total thermal flux. As shown in Figure 3.25 some thermal resistances (spacers) connect the cooling pipes to the girders. The spacers are placed between the girders and the cooling pipes to ensure:

- The heat transfer to the liquid nitrogen. Each spacer drives the heat flux ϕ_{sp} from the girders to the cooling pipe by conduction. At the spacer-cooling pipe interface, a forced convection transfers the heat flux ϕ_{sp} to the liquid nitrogen.
- The thermal drop from T_g down to 80 K between the girders and the cooling pipes. The spacers are designed to provide the necessary temperature drop.
- A homogenous temperature along the girders. We distribute spacers at regular distance to prevent thermal gradient along the girders.

Electric analogy

We use an electric analogy [79] to schematically represent the thermal model in Figure 3.26. Within this analogy, the temperature is equivalent to an electric potential. The thermal conduction through a material is similar to an electric current through an electrical resistance. Thus the physical environment, girders and cooling pipes are respectively at the potential T_e, T_g and T_s. The potential difference T_e-T_g causes the current ϕ_{st} through the stem. The stem is then a thermal resistance. Similarly, a spacer is a thermal resistance which connects the potentials T_g and T_s. The current through the spacer is ϕ_{sp}. The electric analogy of a radiation heat transfer is more complex. We simply represent the radiation heat transfer as an electric current ϕ_{rad} between the potentials T_e and T_g. In the following section we compute the thermal flux between the potentials T_e and T_g. The thermal flux between the potentials T_g and T_s are computed in section 3.3.2.

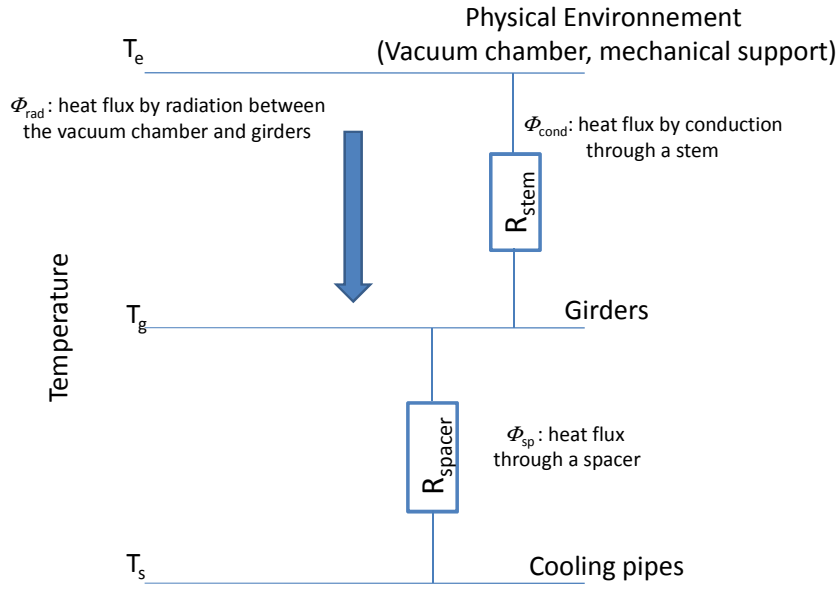

Figure 3.26: Simple electrical analogy of the thermal model.

3.3.2. Heating sources

Conduction through stems

The gradient of temperature between the magnetic assembly and the mechanical support induces a thermal flux in the stems. The Fourier law [79] gives the thermal flux by conduction in the stems:

$$\phi_{st} = -\kappa S \vec{\nabla} T \tag{3.13}$$

ϕ_{st} is the thermal flux, T the temperature, κ the stem thermal conductivity and S the cross section through which thermal flux goes. Actually the material choice is the key parameter to reduce the conduction since the thermal conductivity changes by a factor of 100 from one material to another. The thermal conductivity of 3 typical materials (stainless steel, Aluminium and Copper [80], [81] is plotted in Figure 3.27.

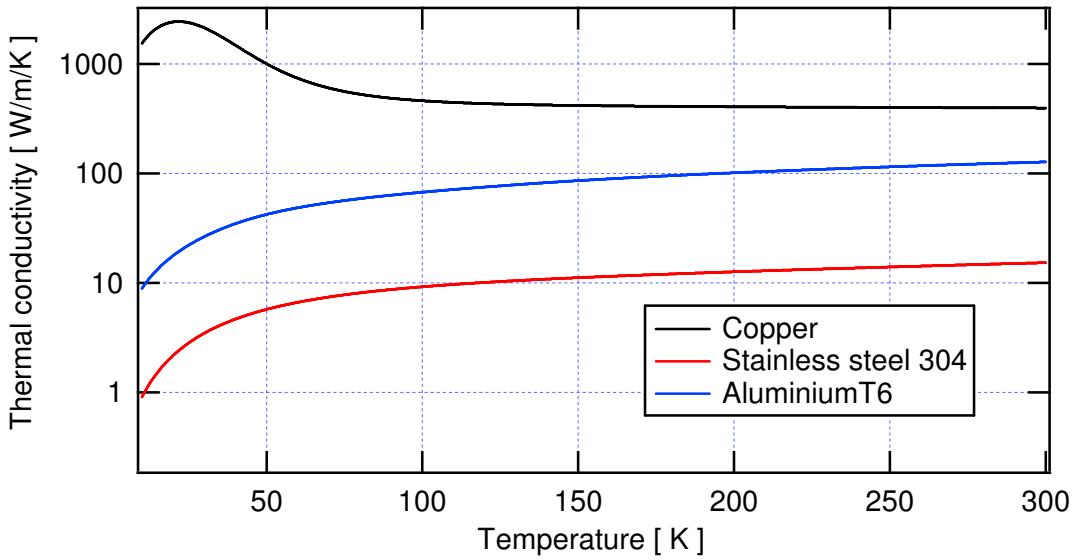

Figure 3.27: Thermal conductivity from 4 K to 300 K for Copper (black), stainless steel (red) and Aluminium (blue).

The material we have chosen for the stems is stainless steel since it has poor thermal conductivity. The real geometry and the simpler geometry used in the thermal model are displayed in Figure 3.28. The thermal model geometry is such that its volume equals the real geometry volume.

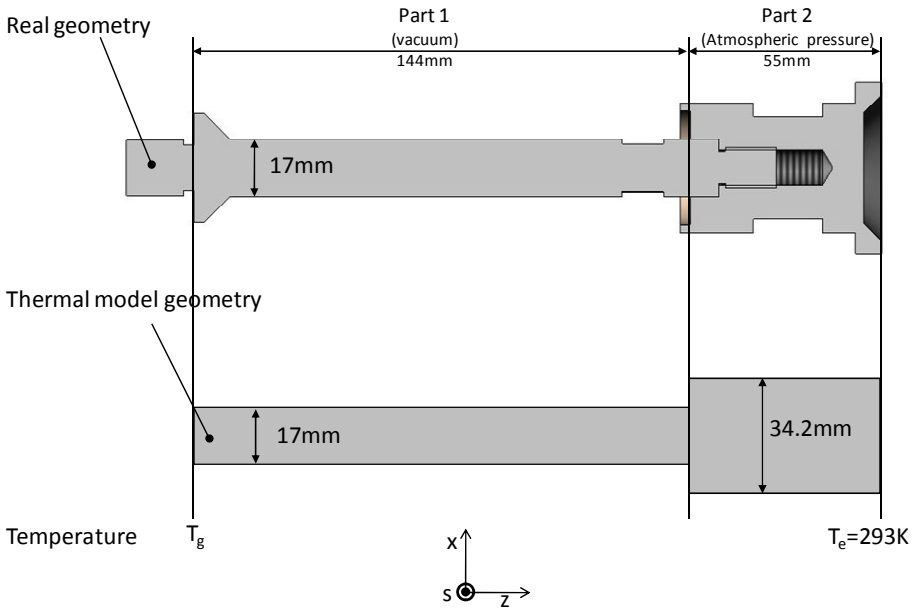

Figure 3.28: Geometry of a real stem and geometry used in the thermal model.

To compute the heat flux through the stems some hypotheses have been made:

- The temperature in the stems depends only on z coordinate.
- The extremity connected to the girder is at the girder temperature T_g.
- The extremity connected to the mechanical support is at T_e=293 K.

Figure 3.29 represents the thermal flux through one stem as a function of the girder temperature. The thermal flux varies almost linearly with the temperature. The thermal flux increases by 25% when the girder temperature decreases from 160 K to 110 K.

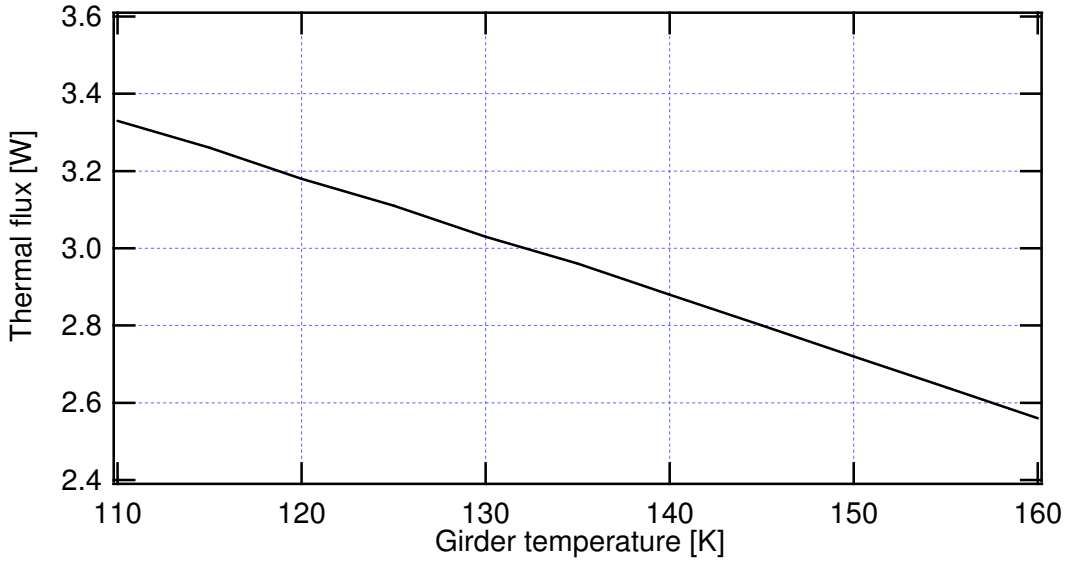

Figure 3.29: Thermal flux through one stem as a function of the girder temperature. One uses equation (3.13) to compute the thermal flux for the geometry plotted in Figure 3.28.

Heat transfer by radiation between the vacuum chamber and girders

The heat transfer by radiation between real surfaces [79] is a complex problem (this heat transfer mode is discussed in Appendix B). We therefore make some assumptions to facilitate its computation. First of all we suppose that the girder and chamber surfaces are grey and diffusive. For such surfaces, the emissivity ε and the temperature completely determine the heat transfer by radiation. In our model, in order to simplify the computation, we assume that both quantities are constant on the surface of the vacuum chamber and the girders.

The cross section of girders, enclosed in the vacuum chamber, is represented in Figure 3.30. The constant temperature on the girder surfaces and the small gap allow us to ignore:

- The radiation of each girder on itself. Girders are not convex so they radiate a certain amount of power on themselves. Since we assume the temperature being uniform on the girders, the radiation of each girder on itself is null.
- The radiation between the two girders. Indeed these are at the same temperature.
- The radiation of the vacuum chamber in the gap. The gap is of around 6 mm. For such a small gap value, only a negligible amount of radiation enters the gap.

Moreover we take the two girders as being one equivalent convex surface at the temperature T_g. The vacuum chamber (girders) is characterized by its surface S_c (S_g), its temperature T_c (T_g) and its emissivity ε_c (ε_c).

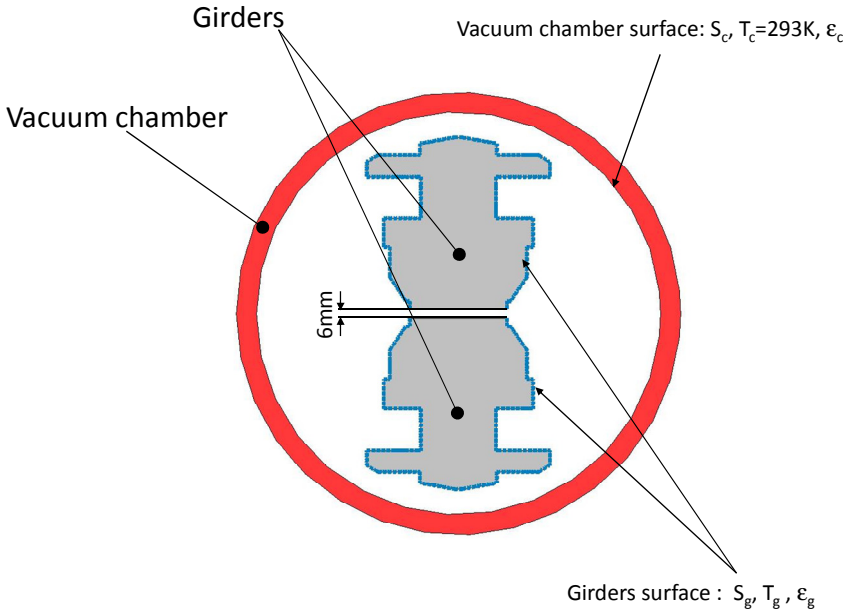

Figure 3.30: Cross section of the undulator. The blue dashed curves represent the surface of the girders used in radiation computation. The gap is closed at 6 mm.

Consequently we only take into consideration the heat transfer between the surface of the girders and the vacuum chamber. The problem is then reduced to a two-surface enclosure, a convex surface enclosed within a concave surface. The magnetic assembly is the convex surface and the vacuum chamber is the concave surface. For such geometry, the thermal flow ϕ_{rad} between S_c and S_g is expressed as [79]:

$$\phi_{rad} = \sigma S_c \frac{T_c^4 - T_g^4}{\frac{1}{\varepsilon_c} + \frac{(1-\varepsilon_g)S_c}{\varepsilon_g S_g}} \tag{3.14}$$

The emissivity is strongly dependent on the nature of the material surface. For instance oxidation increases the emissivity of a metallic surface. As the method of fabrication and the thermal cycling

influence the nature of the surface, it is difficult to determine the emissivity without experimental measurement. Moreover, the girder surfaces involved in the radiation are rather complex and are therefore difficult to determine precisely. Indeed the numerous geometrical non-regularities, such as the magnets support, screws and nuts, increase their surface. To overcome these experimental uncertainties we proceed as follows. As the vacuum chamber is made of stainless steel, we arbitrary set the emissivity of the vacuum chamber at 0.23. This is a typical value for cleaned stainless steel at 300 K [79], [82]. Finally we report surface and emissivity uncertainties to the emissivity of the girders so that it is the only unknown parameter. Aluminium emissivity found in literature is 0.07 at 100 K [79], [82]; because of our approximation we may found a larger value. Figure 3.31 represents the radiated thermal flux as a function of the girder temperature and the emissivity of the girders. The radiated power depends weakly on the magnetic assembly temperature: the variation of the radiated power is about 5% over 50 K. The amount of the radiated power strongly depends on the Aluminium emissivity; it increases by 40% as one doubles its value. The total thermal flux measurement is necessary to determine the girder emissivity.

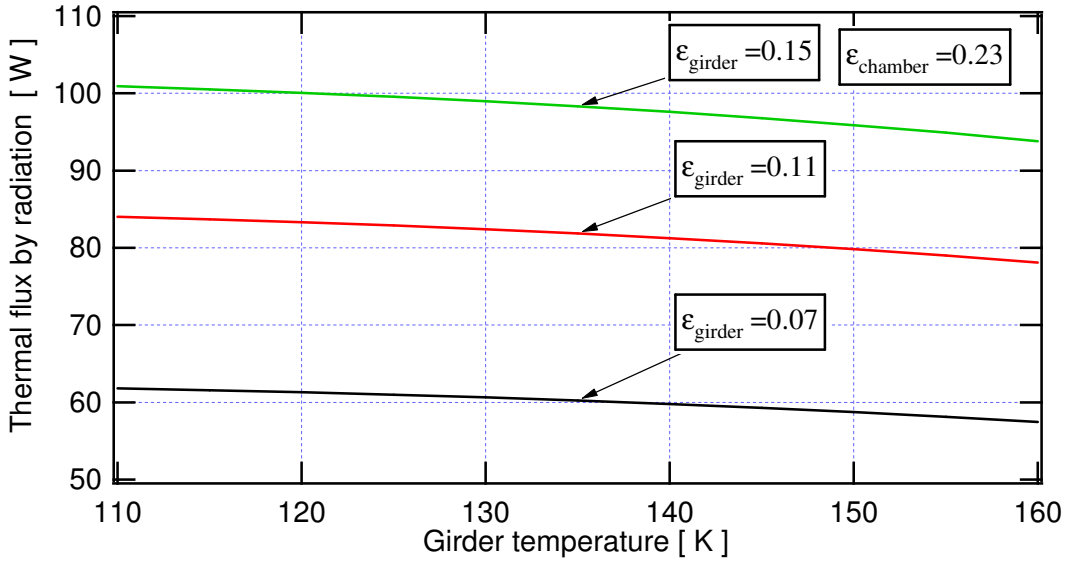

Figure 3.31: Thermal flux by thermal radiation between the magnetic assembly and the chamber as a function of the girder temperature. The chamber is at 293 K. Several girders emissivities have been considered.

Total thermal flux

When the CPMU is cooled at 120 K, we measure a total thermal flux of 150 W, as explained in Appendix C. Inserting this value into the equation (3.14), we calculate a girder emissivity ε_g of 0.11. The girders are mainly made of Aluminium. The experimental emissivity has the same order of magnitude as the theoretical ones. Finally this simple model is good enough to quantify the conduction and the radiation.

Figure 3.32 displays the total thermal flux as a function of the girder temperatures. The total thermal flux is the sum of the conduction through stems and the radiation between the vacuum chamber and the girders. The radiated power is higher than the thermal flux through the stems, although the girders are far off blackbody behaviour (90% of the thermal flux is reflected at the surface of the girders). The conduction mainly contributes to the thermal flux variation with the temperature of the girders.

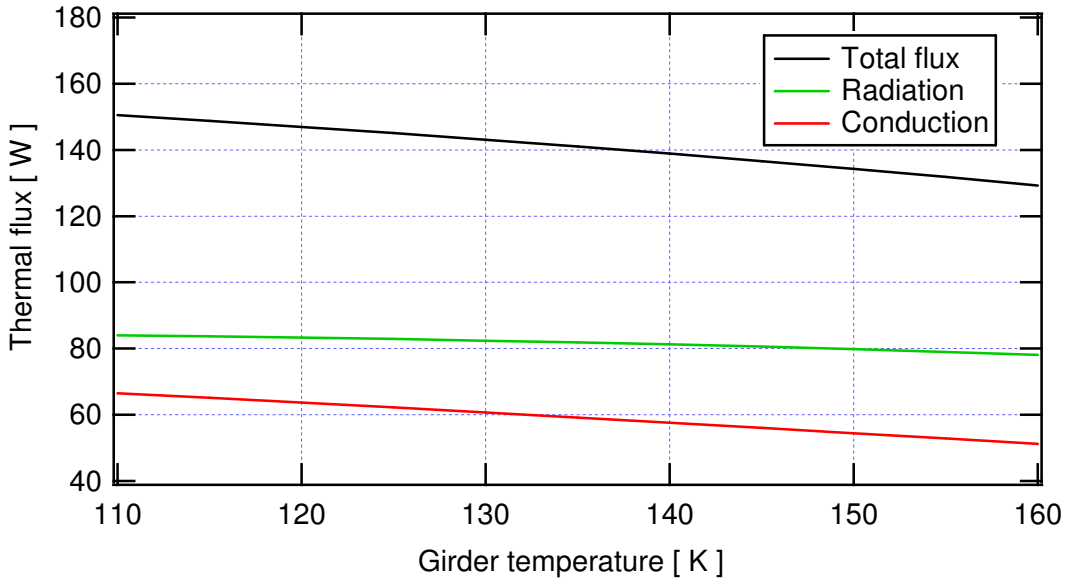

Figure 3.32: Total thermal flux (black), by radiation (green), and conduction (red) as a function of the girder temperature.

The cooling system evacuates the total thermal flux. The cooling system is at a fixed temperature which is lower than the target temperature. Thus the connection between the cooling system and girders has to be calibrated to set the girders at the proper temperature. Thermal resistances (spacers) ensure the connection between the refrigerant channels and girders. We will now discuss their calibration.

3.3.3. Thermal flux through spacers

The spacers drive the total thermal flux from the girders to the refrigerant channels. In this section we discuss the thermal flux ϕ_{sp} through a spacer. This flux determines the number of spacers to be installed in order to keep the girders at an arbitrary temperature. First we will review the heat transfer modes.

Figure 3.33 represents the thermal flux ϕ_{sp} which goes through each spacer. The spacer drives the thermal flux ϕ_{sp} by conduction from the girder to the cooling pipe. At the interface between the spacer and the liquid nitrogen, convection transfers the thermal flux ϕ_{sp} from the spacer to the liquid nitrogen [79].

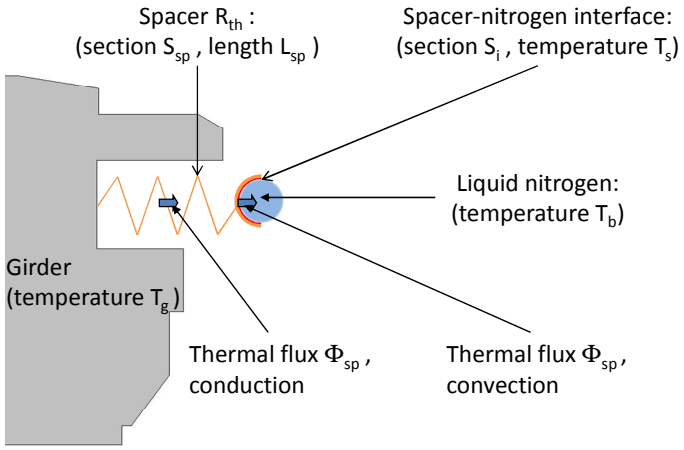

Figure 3.33: Thermal flux through a spacer.

At the interface between the spacer and the liquid nitrogen; we express the thermal flux ϕ_{sp} with the Newton law of cooling:

$$\phi_{sp} = h \cdot S_i \cdot (T_s - T_b) \tag{3.15}$$

h is the convection coefficient, S_i the interface surface, T_s the interface temperature and T_b the liquid nitrogen temperature. Because of the heat transfer, the spacer is not at the liquid nitrogen temperature but at the higher one T_s. The thermal flux by conduction through a spacer ϕ_{sp} is then:

$$\phi_{sp} = \frac{S_{sp}}{L_{sp}} \cdot \int_{T_s}^{T_g} \kappa_{sp}(T) \cdot dT \tag{3.16}$$

κ_{sp} is the spacer thermal conductivity. T_s must be known in order to compute the heat transfer through a spacer. The spacers are made of Copper. The Copper integrated thermal conductivity is displayed in Figure 3.34. The integrated thermal conductivity varies almost linearly with the temperature above 80 K. Thus, between 80 K and 160 K, the thermal conductivity κ_{sp} is nearly constant and then the thermal flux ϕ_{sp} reduces to:

$$\phi_{sp} = \frac{T_g - T_s}{R_{th}} \tag{3.17}$$

With the spacer thermal resistance R_{th} defined as:

$$R_{th} = \frac{L_{sp}}{\kappa_{sp} S_{sp}} \tag{3.18}$$

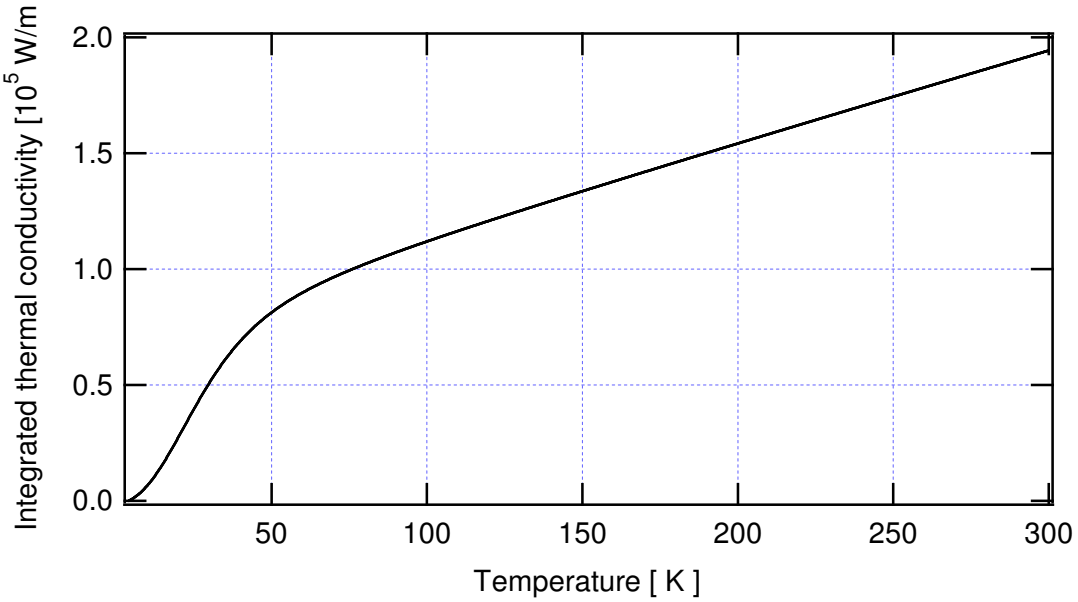

Figure 3.34: Integrated thermal conductivity of Copper as a function of the temperature.

Finally by eliminating T_s from equation (3.15) and (3.17), we express the thermal flux through a spacer as:

$$\phi_{sp} = \frac{1}{R_{eq}} (T_g - T_b) \tag{3.19}$$

With:

$$R_{eq} = R_{th} + \frac{1}{hS_i} \tag{3.20}$$

The thermal flux ϕ_{sp} through a spacer is proportional to the temperature difference between the girder and nitrogen temperature. The total thermal resistance between the nitrogen and the girder, R_{eq} consists of two thermal resistances R_{th} and $1/hS_i$ mounted in series. We will now consider the convection heat transfer at the spacer interface with the liquid nitrogen in order to express $1/hS_i$. The conduction through a spacer will then be studied in order to express the spacer thermal resistance R_{th}.

Convection thermal resistance $1/hS_i$

The determination of the convection thermal resistance requires the investigation of the surface S_i involved in the heat transfer and the convection coefficient h.

The geometry of the spacer fixation to the cooling pipe is displayed in Figure 3.35. Two semi cylindrical shells connect the spacer to the cooling pipe. Four screws squeeze the shells around the cooling pipes. The four screws ensure the thermal contact between the shells. The screws are made of Stainless Steel, a poor thermal conductor material. Therefore, the shells are thermally isolated from each other.

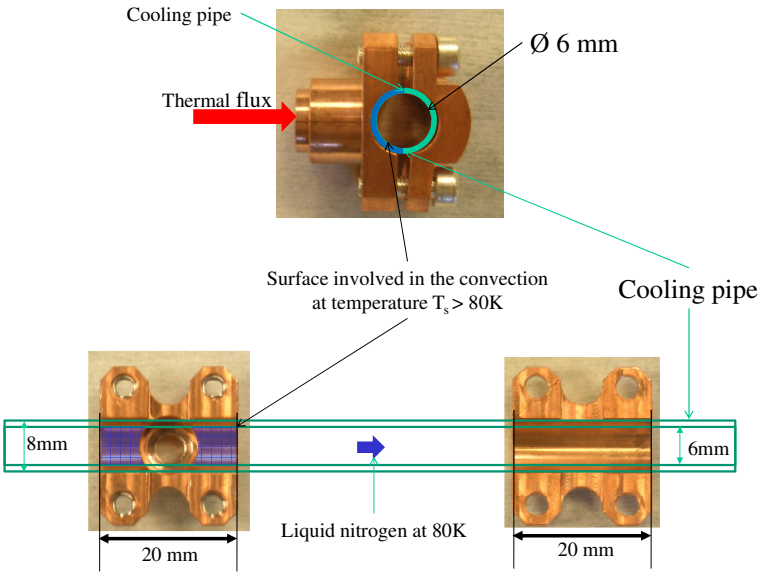

Figure 3.35: Description of the cooling pipe and the spacer fixation.

The thermal flux does not propagate to both shells before being transferred to the cooling pipe. The heat flows from one shell to the cooling pipe whereas the other shell is at Nitrogen temperature. Finally one finds that S_i is almost equal to 100 mm^2.

The convection coefficient h expresses the ability of a fluid to transport energy within a given geometry. Thus this coefficient depends on the cooling pipe geometry and on the nitrogen thermo-physical properties. The cooling pipe is a tube with a circular cross section. This circular cross section has a 6 mm inner diameter D. As described in section 2.1, a pump forces the nitrogen flow through the cooling pipe. Therefore the heat transfer at the interface liquid nitrogen/spacer convection is a forced convection in a circular tube. The resolution of such heat transfer is discussed in Appendix B. For a forced convection in a circular tube, the convection coefficient h is:

$$h = 0.023 \frac{k_f R_{eD}^{4/5} P_r^{2/5}}{D} \tag{3.1}$$

D is the inner tube diameter, k_f the nitrogen thermal conductivity. P_r is the Prandtl number and R_{eD} the Reynolds numbers. They are dimensionless variable and characterize the nitrogen flow in the cooling pipe and the ability of the nitrogen to transport energy.

The Reynolds number R_{eD} is the dimensionless variable which describes the flow. R_{eD} is the ratio of the inertia and viscous forces and is defined as:

$$R_{eD} = \frac{\rho V D}{\mu} \tag{3.21}$$

V is the velocity of the fluid, ρ the mass density and μ the viscosity. In any flow small disturbances exist which can be amplified to produce turbulent conditions. For small Reynolds number, viscous forces are sufficiently large compared to the inertia forces to prevent this amplification. The flow is laminar. But, with increasing Reynolds number, the viscous effects become less significant compared to the effects of inertia, and any small disturbances may be amplified so that transition occurs. The flow is then turbulent.

The Prandtl number is the ratio of the momentum and thermal diffusivity. It measures the relative effectiveness of the momentum and energy transport in the fluid and is defined as:

$$P_r = \frac{c_p \mu}{k_f} \tag{3.22}$$

c_p is the thermal capacity of the fluid. Assuming that the liquid nitrogen is at 80 K in the closed loop; the Prandtl number is almost equal to 2. The Reynolds number characterizes the nitrogen flow and is proportional to the nitrogen flow rate. Figure 3.36 represents the thermal resistance $1/hS_i$ as a function of the flow rate in the closed loop.

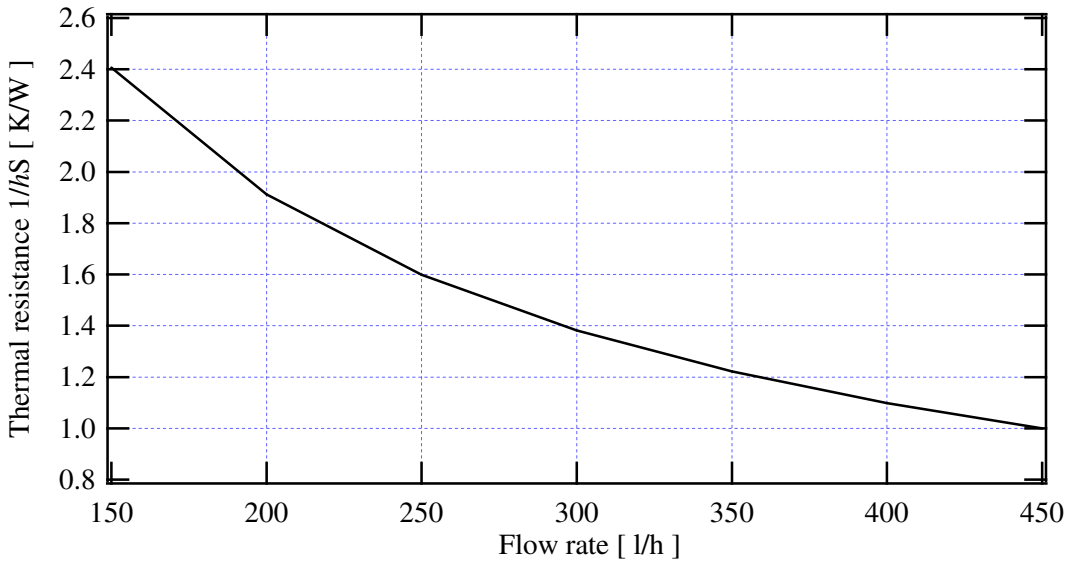

Figure 3.36: Convection thermal resistance as a function of the nitrogen flow rate in the closed loop.

In a typical use; the flow rate being around 350 l/h, the convection thermal resistance reaches a low value, i.e. 1.2 W/K. The temperature difference between the nitrogen and the interface is small, typically a few degrees. Thus the thermal resistance R_{eq} arises mainly from the spacer. We will now discuss its design.

Spacer thermal resistance R_{th}

Spacers drive the thermal flux brought by the heating sources to the cooling pipes. Moreover spacers act as thermal resistances and drop the temperature between the girders and the refrigerant channels from T_g to T_s. We calibrate the thermal resistance of spacers in order to reach the temperature drop between the cooling pipe and the girder. Spacers are designed with high thermal resistance as a temperature drop as high as 70 K is expected. The thermal resistance is proportional to the ratio of the length over the cross section. Thus the spacer might have a small surface compared to its length, in order to achieve a high thermal resistance. However the girders and cooling pipes impose some limits on the spacer design:

- The spacer width couldn't exceed 20 mm in order to be fixed on the girder. However, a large width is necessary to ensure good thermal contact between the spacer and the girder.
- The fixed distance between the cooling pipe and the girder limits the spacer length.

Thus the spacer thickness is the relevant parameter to set thermal resistance. The spacer geometry is shown in Figure 3.37. We assume that the temperature drop is achieved along the slim shim to simplify. We consider that the shell is at temperature T_s. Due to this assumption, the thermal resistance error is below 1%. In addition the use of constant thermal conductivity overestimates the thermal resistance up to 8%. The thermal resistance has the constant value:

$$R_{th} = 15.6 \mp_0^{10\%} K/W \tag{3.23}$$

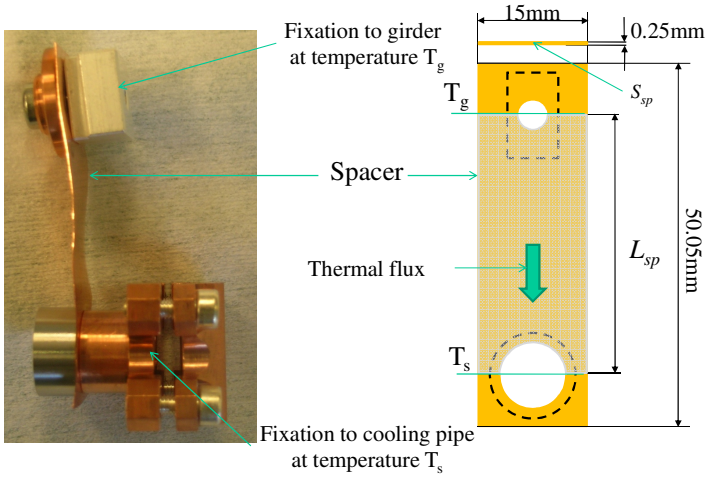

Figure 3.37: Detail of a spacer (Left). The slim Copper piece drops the temperature from T_g to T_s (Right).

Thermal exchange calibration

So far we have computed the thermal flux between the heating source and the magnetic assembly. We have also estimated the flux extracted by a spacer. Finally the number of spacers, needed to maintain the magnetic assembly at temperature T_g, is simply the ratio between the total thermal flux and the flux extracted by a spacer. Figure 3.38 represents for different spacer thickness, the number of spacers to be mounted with respect to the girder temperatures. It appears that the spacer thickness should be tuned depending on the targeted temperature. For instance at 110 K one would prefer to use spacers with a large thickness to avoid the installation of too many spacers. On the other hand at a temperature higher than 160 K, one would rather design spacers with a small thickness. This allows a sufficiently large number of spacers to be kept in order to prevent any temperature gradient along the 2 m long girder. We designed spacers with 0.25 mm thickness. Such a thickness is suitable for temperatures lower than 160 K.

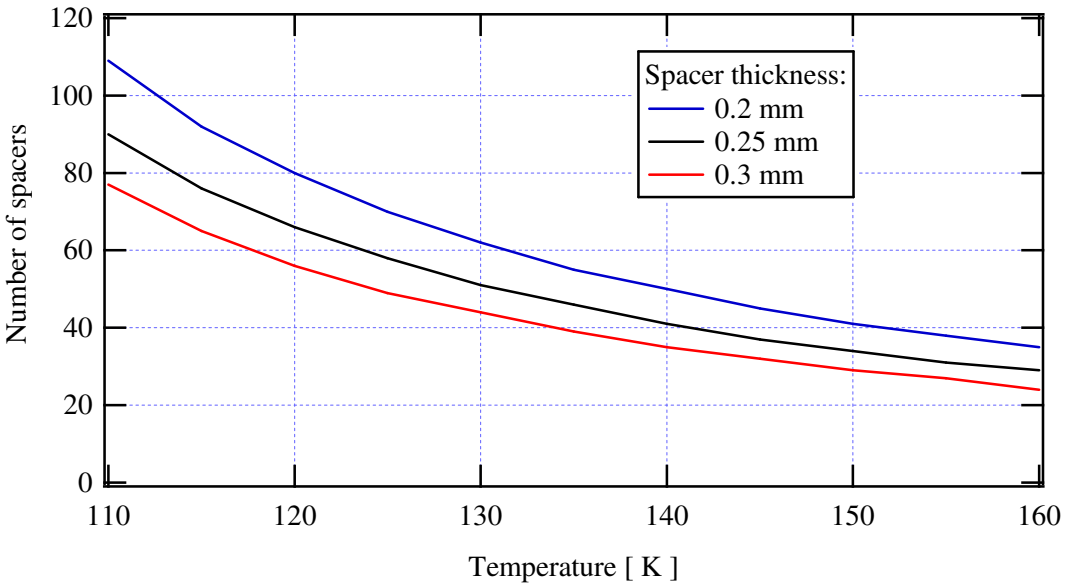

Figure 3.38: Number of spacers to be mounted as a function of the girders temperature. Three different spacer thicknesses are considered.

The total thermal flux fixes the temperature. Thus in order to change the CPMU temperature, one should either change the number of spacers or include a heating system on the girders. A heating system allows the total thermal flux to be changed and consequently the girder temperatures. The experimental set-up includes a heating system which is discussed in section 4.2.

When the magnetic assembly is cooled, thermal flux occurs. A thermal analysis has been done in this sub chapter in order to quantify this thermal flux. A second effect, the mechanical contraction of the cooled assembly occurs as the CPMU is at a low temperature. Indeed the magnetic assembly is partly made of Stainless Steel, soft Iron, and Aluminium. Such materials contract at low temperatures. Therefore we shall now study the mechanical effect due to the low temperature.

3.4. Effects of temperature on the CPMU

In this sub chapter, we describe hereafter the main effects observed on the mechanical structure when it is cooled down to 150 K; the gap opening and the longitudinal contraction. These effects may introduce some magnetic errors as the temperature along the undulator isn't uniform. The CPMU magnetic performance reduction caused by a temperature gradient along the undulator is discussed.

3.4.1. Gap opening at low temperature

The properties of the electromagnetic radiation emitted by a multi GeV electron beam in an ID are deduced from the ID magnetic field. The on axis magnetic field is strongly dependent on the gap as the peak field decays exponentially with the gap. Consequently the gap of the insertion devices is monitored precisely. The motors and coders of the mechanical support succeed in controlling the magnetic gap within 1 µm. However the coders don't read the real gap, i.e. the aperture between the magnetic girders. They read the rotation of the screws which move the girders. The cooled magnetic assembly of the CPMU experiences a mechanical contraction. Finally the gap of the CPMU opens at low temperature because of this contraction. The standard coders are blind to this contraction since no rotation of the screws is attached to this contraction. This section resumes the attempt to compute ab-initio the gap opening of the CPMU. Section 4.2.2 presents the device used to measure the gap opening.

The thermal linear expansion

The gap is defined as the minimum distance between the girders. At ambient temperature, the poles are positioned above the magnets, typically around 50 µm. Thus we define the gap as the distance between the poles of the lower girder and the upper girder. However magnets and poles exhibit different expansion properties at low temperatures. The $Nd_2Fe_{14}B$ crystal tends to expand with decreasing temperature in a direction perpendicular to the magnetization [83], [84]. The magnets are horizontally magnetized then the magnets will expand vertically at low temperature. The poles which are made of soft iron, contract with the decreasing temperature so that there might be a temperature at which they contract below the magnets. Below this temperature the gap should be defined as the distance between the magnets of the lower and the upper girder. Unfortunately there is a lack of experimental data concerning the massive $Nd_2Fe_{14}B$ magnets dilatation at cryogenic temperature. Consequently we keep the gap as the distance between the poles of the lower and the upper girder.

The gap opens at low temperature because of the mechanical contraction of the stems and the magnetic assembly. If we suppose the magnetic assembly to be at temperature T, the gap opening Δg is the sum of the contributions coming from the stems, the girders, the magnet supports and the poles. We can write the gap opening Δg as:

$$\Delta g(T) = 2\left(\Delta l_{stems}(T) + \Delta l_{girder}(T) + \Delta l_{support}(T) + \Delta l_{pole}(T)\right) \tag{3.24}$$

For each contribution the contraction Δl is:

$$\Delta l(T) = \int_0^L \frac{\Delta l}{l}\big(T(u)\big)du \tag{3.25}$$

$\Delta l(T)/l$ is the linear thermal expansion. The thermal linear expansion characterizes the mechanical contraction of materials. The thermal linear expansion of soft iron, stainless steel and Aluminium is displayed as a function of the temperature in Figure 3.39 [85], [86] and [87].

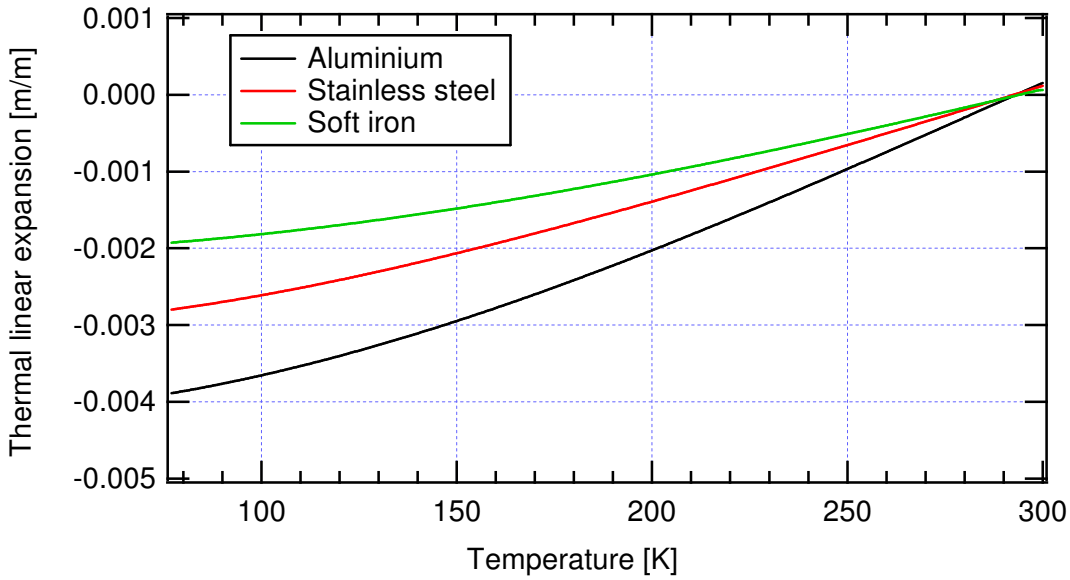

Figure 3.39: Al (black), SS (red) and soft iron (green) thermal linear expansion as a function of temperature.

We assume that the girders, magnets and poles are at uniform temperature T. Thus for these objects, the contraction is simply their thermal linear expansion at temperature T times their length. The temperature gradient between the extremities of a stem is at least 150 K; the assumption of a uniform temperature is not valid for stems. To compute the mechanical contraction of the stems Δl_{stem}, the variation of the thermal linear expansion along a stem should be determined. As the thermal linear

expansion is a function of the temperature, the variation of the temperature along a stem must be computed.

Temperature profile along a stem

We will now consider a simple rod (cross section *A*, length *L* and thermal conductivity κ) at thermal balance whose extremities are at temperatures T_1 and T_2. The temperature is *T* at the position *x*. At the thermal balance, the flux ϕ through the section is conserved along the rod:

$$\phi = \frac{A}{x}\int_{T_1}^{T} \kappa(u)du = \frac{A}{L}\int_{T_1}^{T_2} \kappa(u)du \tag{3.26}$$

The temperature law *x(T)* in the rod is then:

$$x(T) = L\frac{\int_{T_1}^{T} \kappa(u)du}{\int_{T_1}^{T_2} \kappa(u)du} \tag{3.27}$$

In the previous sub chapter, the thermal flux through a stem has been determined as a function of the magnetic assembly temperature. Therefore the thermal profile along the stem can be computed at any magnetic temperature assembly. As shown in Figure 3.28, the geometry of the stems used in the thermal model is made up of two rods with different diameters. The law *x(T)* obtained for a simple rod is applied to each rod in order to compute the stem thermal expansion at temperature *T*.

Finally the contribution to the gap opening of the different parts constituting the magnetic assembly is represented in Figure 3.40. The stems and girders contract more so that almost 75% of the gap opening comes from the thermal expansion of the stems and girders.

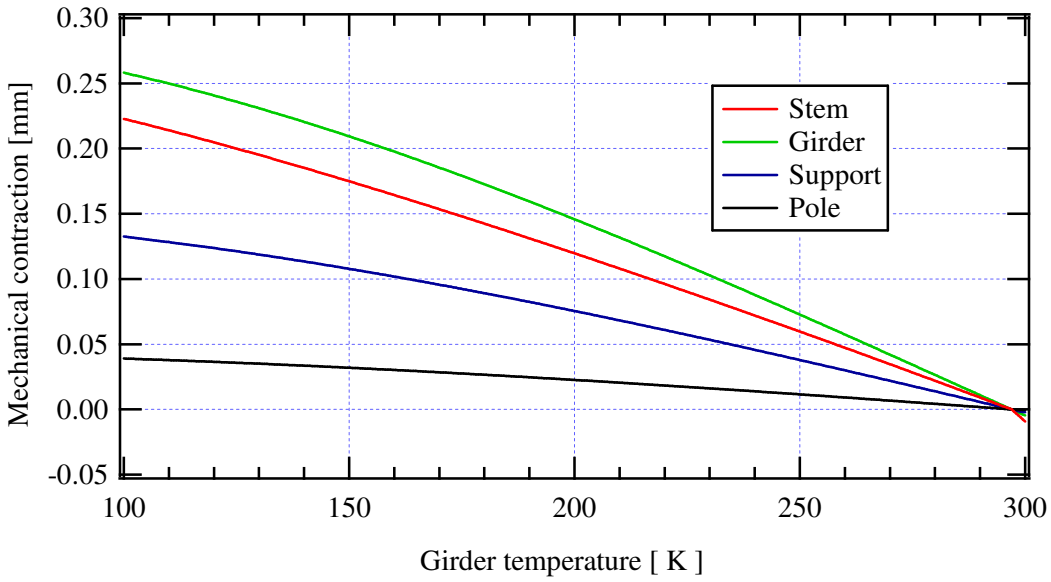

Figure 3.40: Mechanical contractions from 100 K to 300 K of a stem (red), a magnet (black), a pole (blue) and a girder (green).

Finally the gap opening Δg is plotted as a function of the girder temperature in Figure 3.41. The gap opens wider as the temperature decreases. At 150 K the gap is already open about 1 mm.

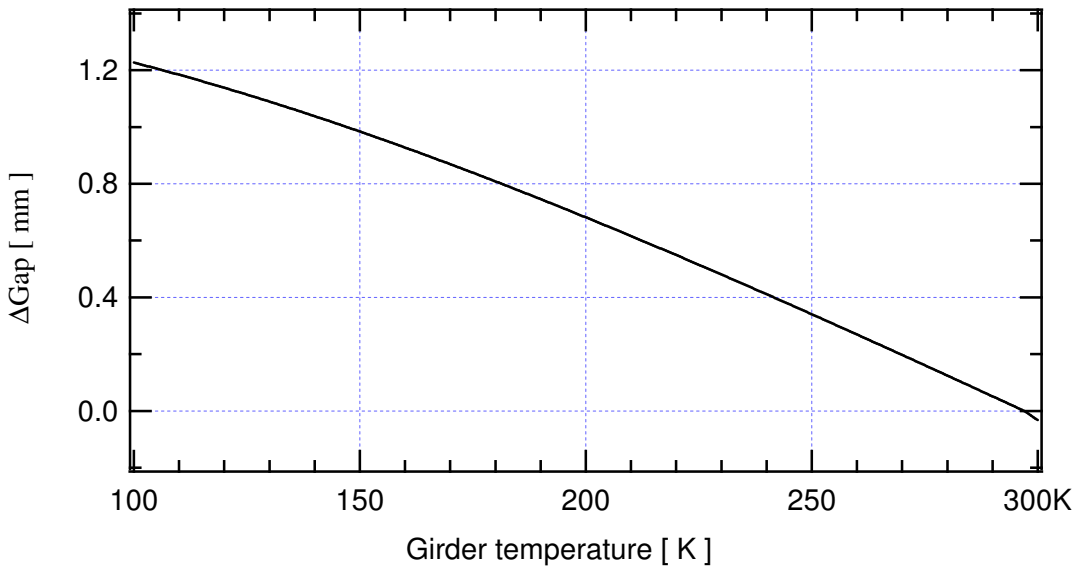

Figure 3.41: Opening of the gap from 100 K to 300 K.

3.4.2. Contraction of the magnetic assembly

The girders are 2 m long and made of Aluminium. They exhibit a strong longitudinal thermal contraction. The magnets, poles as well as the physical environment, such as the mechanical support or the cooling pipe, may have a different temperature and are not made of Aluminium. As a result the magnetic assembly and the physical environment experience a different contraction from that of the girders. We will now present the different solutions to overcome the differential contraction.

Air gaps between magnets and poles

Actually there are residual air gaps between poles and magnets. Typically, these air gaps are within 25-50 µm. During the assembly and correction process of the undulator, they are necessary for the insertion or the removal of magnets in the magnetic assembly. It is therefore necessary to check that the air gap budget per period is compatible with the contraction of the girders in order to avoid longitudinal forces between the girders and the magnetic assembly.

To allow free expansion of the girders the air gaps must be larger than the girders expansion. The air gaps per HYB18 period are represented in Figure 3.42. One may express the condition that δ, the air gap between the magnets and poles, must fulfil per period as follows:

$$\delta \geq \delta_{min} \tag{3.28}$$

With:

$$\delta_{min} = \frac{\lambda_0}{4}\left(\frac{\Delta l}{l}\right)_{Alu} - \frac{L_{sp}}{4}\left(\frac{\Delta l}{l}\right)_{Iron} \tag{3.29}$$

In this expression, we still ignore the magnet expansion. δ_{min} is the minimum air gap and L_{sp} is the longitudinal dimension of the poles. The minimum air gap δ_{min} is displayed in Figure 3.42 as a function of the magnetic assembly temperature.

At any temperature, the minimum air gap δ_{min} is lower than the residual air gap (25-50 µm) necessary to insert or remove the magnets in the magnetic assembly. As a conclusion the air gap is well suited for low temperature operation. In addition the girder expansion completely drives the magnetic assembly contraction. Finally we assimilate the magnetic assembly expansion to the expansion of the girders. In particular we take advantage of this property to determine the temperature of the girders from local magnetic measurement; this principle is detailed in section 5.1.3.

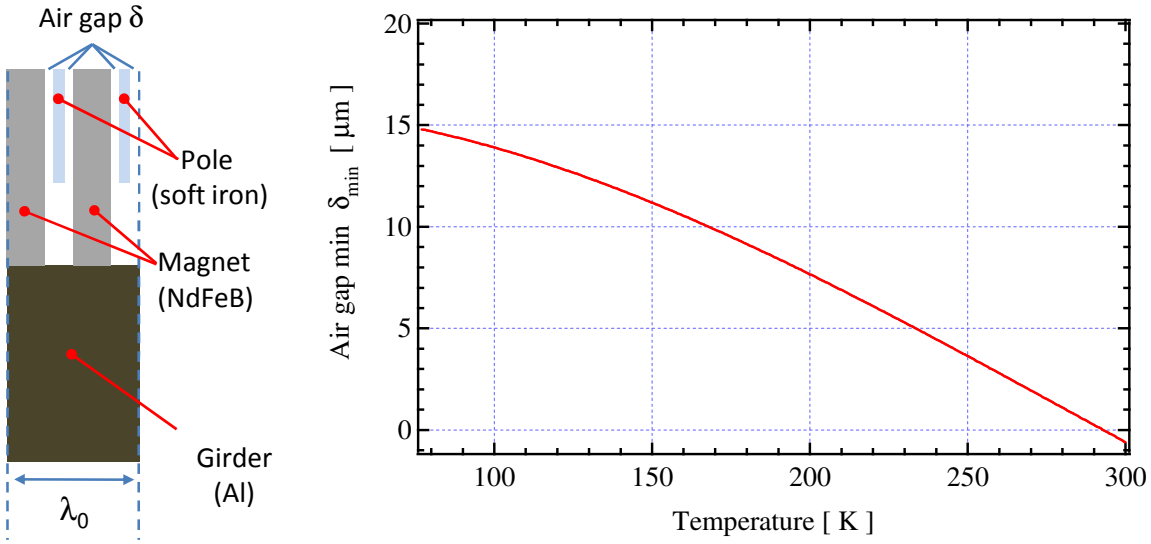

Figure 3.42: Air gaps in the magnetic assembly (left plot) and variation of the air gaps (right plot) with the temperature.

Stem fixation

The CPMU design is based on an in-vacuum undulator. Before its installation in a straight section, any conventional in-vacuum undulator is baked up to 400 K. The baking ensures the high vacuum compatibility. At such a high temperature, the girders expand. Thus stems are mounted on a mobile carriage to allow the magnetic assembly expansion with respect to the mechanical support. The pair of stems located on the middle of each girder is fixed. The others pairs of stems are allowed to move longitudinally during baking. Hence, the stems mounted on the mobile carriage allow the shrinkage of the girders with respect to the mechanical support. Actually the precautions related to baking, are suitable for a low temperature operation.

C-shape spacers

At a steady state the cooling pipes are nearly at liquid nitrogen temperature whereas the girders are typically around 150 K Moreover girders and cooling pipes are made of different materials: Aluminium for the girders and stainless steel for the cooling pipes. The stainless steel exhibits a lower thermal linear expansion than Aluminium so that the thermal linear expansion of the stainless steel at 77 K is nearly the same as that of Aluminium at 150 K. Finally the thermal contractions of the girders at 150 K and the cooling pipes at 77 K are similar.

Nevertheless during the cooling down from 300 K to 150 K, girders and cooling pipes have different thermal transient regimes. As a first approximation, the cooling pipes are always at liquid nitrogen temperature while the temperature of the girders decreases from 300 K to 150 K. During the cooling process, girders and cooling pipes exhibit different thermal contractions. Thus, the spacers allow the cooling pipes to move longitudinally with respect to the girders. The spacer with the slim C-shape ensures this translation. Moreover spacers are fixed rigidly to the girders and cooling pipes to ensure a good thermal contact. Thus the translation is allowed without any thermal contact reduction.

3.4.3. Temperature gradient and CPMU performance

We will analyze hereafter the effect of non uniform temperature along the undulator on the phase error. Qualitatively, any change in the temperature along the undulator locally affects the magnetic gap (thermal expansion) and the magnetic properties of the magnet blocks. Both effects introduce peak field variation and cause an increase of the RMS phase error.

The most significant sources of field quality degradation are a linear and a parabolic temperature distribution centred in the middle of the undulator. Both sources can be combined. They correspond to forced heat flux at the ends of the undulator. A simple model has been used to quantify the impact of temperature variation on the CPMU phase error. We first describe the temperature profile used.

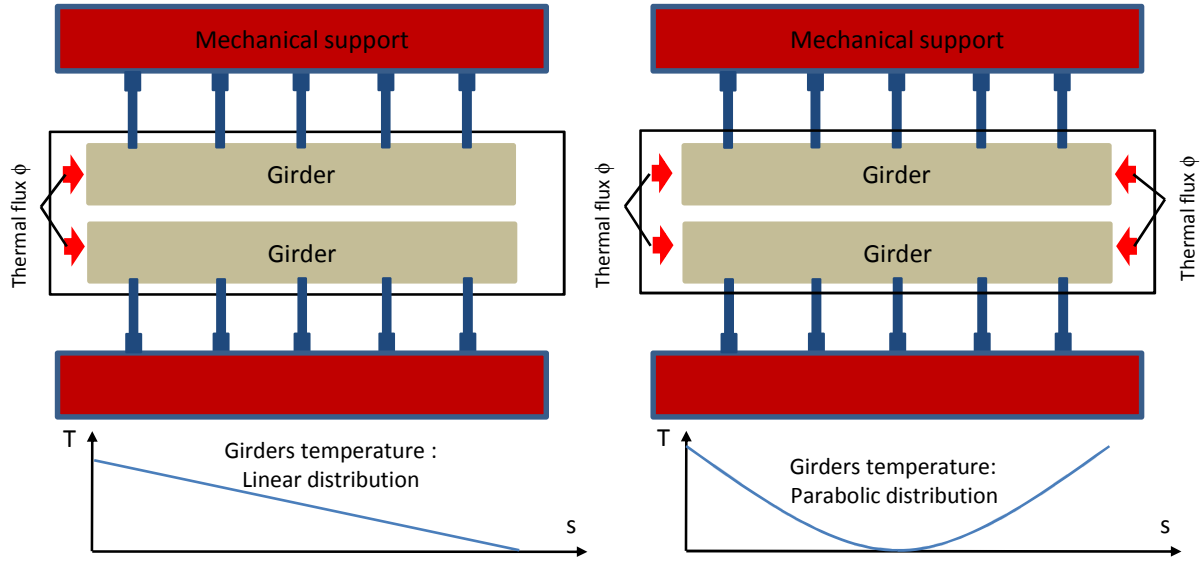

Figure 3.43: Heat flux at the girders extremities and temperature profile.

Temperature profile

We will consider a linear and a parabolic temperature profile along the girders in order to investigate the impact of a temperature variation on the magnetic performance. We write the temperature along the 2 m long girders:

$$T(s) = T_0 + \Delta T \frac{s}{L} \qquad T(s) = T_0 + \Delta T \left(\frac{2s}{L}\right)^2 \qquad -\frac{L}{2} \leq s \leq \frac{L}{2} \tag{3.30}$$

T_0 is the temperature at the origin that we fix at the middle of girders, L is the undulator length and ΔT is the amplitude of the temperature variation along girders. We assume that ΔT varies linearly with the temperature; ΔT is null at ambient temperature and equals 6 K at 120 K. Figure 3.44 represents the variation of ΔT with the temperature.

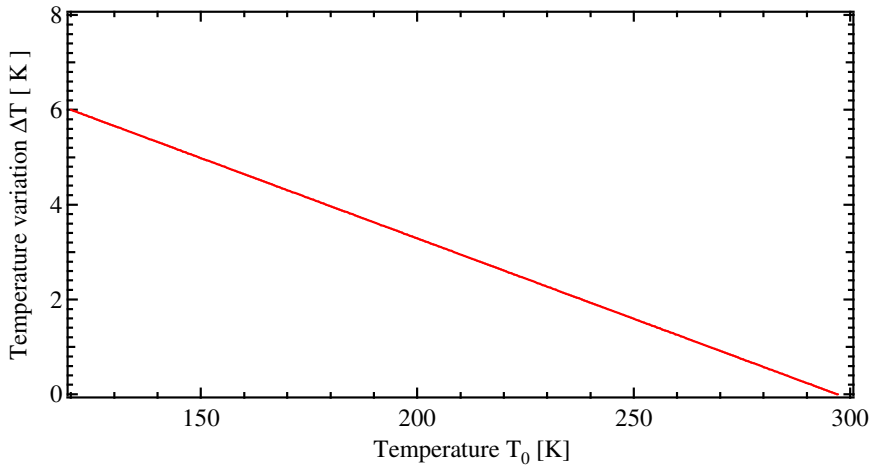

Figure 3.44: Variation of the temperature gradient with temperature T_0.

Model description

One may write the undulator field as a function of the longitudinal position s and the temperature distribution $T(s)$:

$$B_z\big(s,T(s)\big) = B\big(T(s)\big)\sin\left(\frac{2\pi}{\lambda_u}s\right) \tag{3.31}$$

The field amplitude $B\big(T(s)\big)$ depends on the magnet temperature and the gap variation. We determine in section 3.4.1 the gap opening law $\Delta g(T)$. It is displayed in Figure 3.42. The gap deformation along the girders δg is then at the position s:

$$\delta g(s) = \Delta g\big(T(s)\big) - \Delta g(T_0) \tag{3.32}$$

Figure 3.45 represents the peak field and the first harmonic decay with the magnetic gap at ambient temperature. To simplify, we assume that the exponential decay doesn't depend on the temperature so that one writes $B_z(s,T)$:

$$B_z(s,T) = B_{\mathrm{Rad}}\big(T(s)\big)\exp\left(-\frac{\alpha\pi}{\lambda_u}\delta g(s)\right) \tag{3.33}$$

α equals 1.13 or 1.21 as the peak field or the first harmonic is considered. $B_{\mathrm{Rad}}(T)$ corresponds to the peak field or the first harmonic at the temperature T. It has been computed in section 3.2.3 at a 6 mm gap.

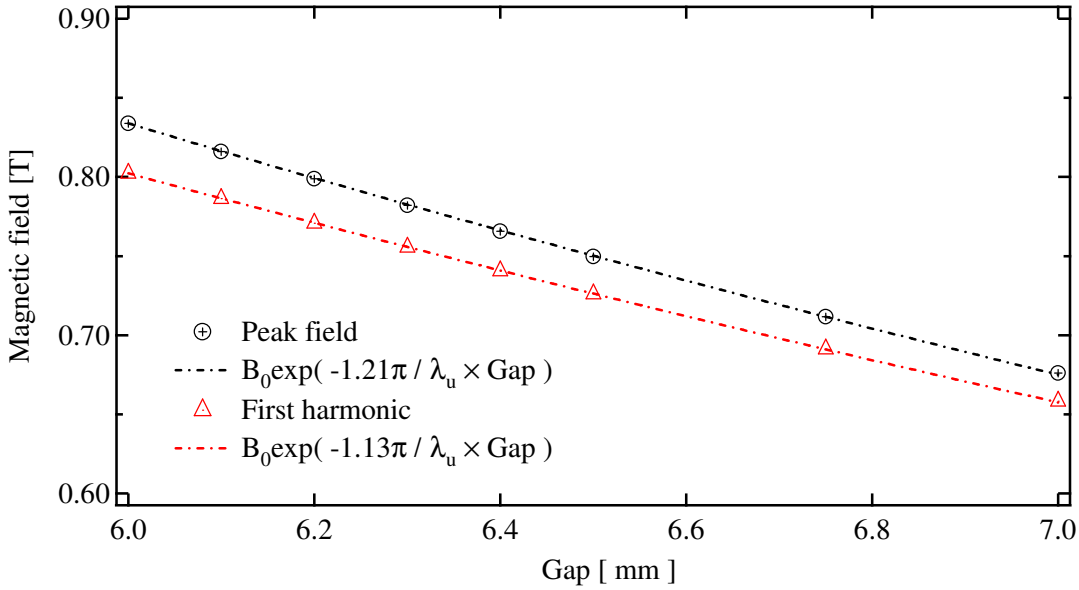

Figure 3.45: Peak field (black circle) and first harmonic (red triangle) decay as a function of the gap. We fit in the simple model with two exponential laws the peak field (black circle) and the first harmonic (red triangle) decays computed with RADIA.

Temperature gradient and peak field variation

The temperature gradient spreads magnet temperature and deforms the gap along the girders. Both effects have an impact on the on axis peak field and introduce a peak field variation ΔB_z:

$$\Delta B_z = \Delta B_z(T_{max}) - \Delta B_z(T_{min}) = \Delta B_z^g + \Delta B_z^m \tag{3.34}$$

With:

$$\Delta B_z^g = B_{\mathrm{Rad}}(T_0)\frac{\alpha\pi}{\lambda_u}\big(\Delta g(T_{max}) - \Delta g(T_{min})\big) \qquad \Delta B_z^m = B_{\mathrm{Rad}}(T_{max}) - B_{\mathrm{Rad}}(T_{min}) \tag{3.35}$$

ΔB_z^g and ΔB_z^m are respectively the peak field variation due to the gap variation and the change in the magnetic properties of magnets.

The peak field variation ΔB_z is displayed with respect to the average temperature in Figure 3.46. The contributions ΔB_z^g and ΔB_z^m are also presented. The gap variation causes a continuous increase of the peak field variation ΔB_z with decreasing temperature and reaches a maximum at around 130 K. The contribution ΔB_z^g defined in (3.35) is positive since a higher temperature means a smaller gap and a higher peak field.

According to the RADIA model, the field amplitude value increases with decreasing temperature from the ambient temperature down to 150 K. In this temperature range, magnets with the lowest temperature produce the highest value of the field amplitude; the contribution ΔB_z^m defined in (3.35) is negative. At lower temperature, the value of the field amplitude decreases with decreasing temperature because of the SRT; the contribution ΔB_z^m is positive. Below 130 K, the amplitude $|\Delta B_z^g|$ is larger than $|\Delta B_z^m|$; the gap variation has more of an impact on the peak field gradient.

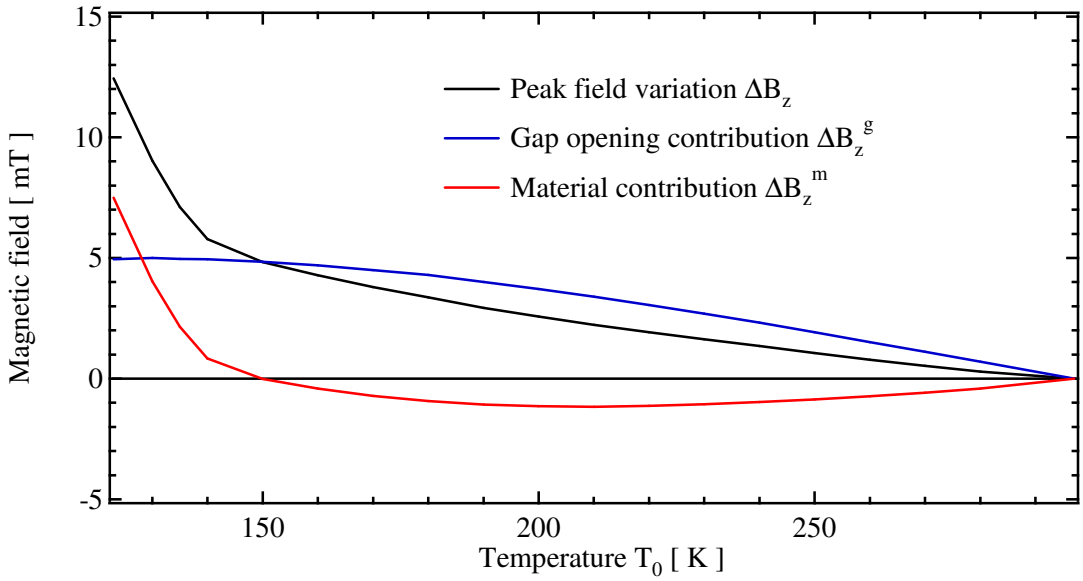

Figure 3.46: The magnet temperature (red curve) and the gap variation (blue curve) contributions to the peak field gradient. We assume a linear temperature distribution along girders.

We also use the simple model described above to investigate the impact on the RMS phase error of a temperature gradient. The results are presented hereafter.

Temperature gradient and RMS phase error

Figure 3.47 represents the RMS phase error variation with respect to the average temperature on the girders. At this time the temperature profile varies linearly along girders. Figure 3.48 represents the RMS phase error variation with respect to the average temperature as the temperature profile is parabolic. The linear temperature distribution induces higher RMS phase error than the parabolic one. However both curves have similar evolutions with the average temperature, whatever the temperature distribution is along the girders. In the following discussion, no distinction is made between the two temperature distributions; we will focus on the average temperature.

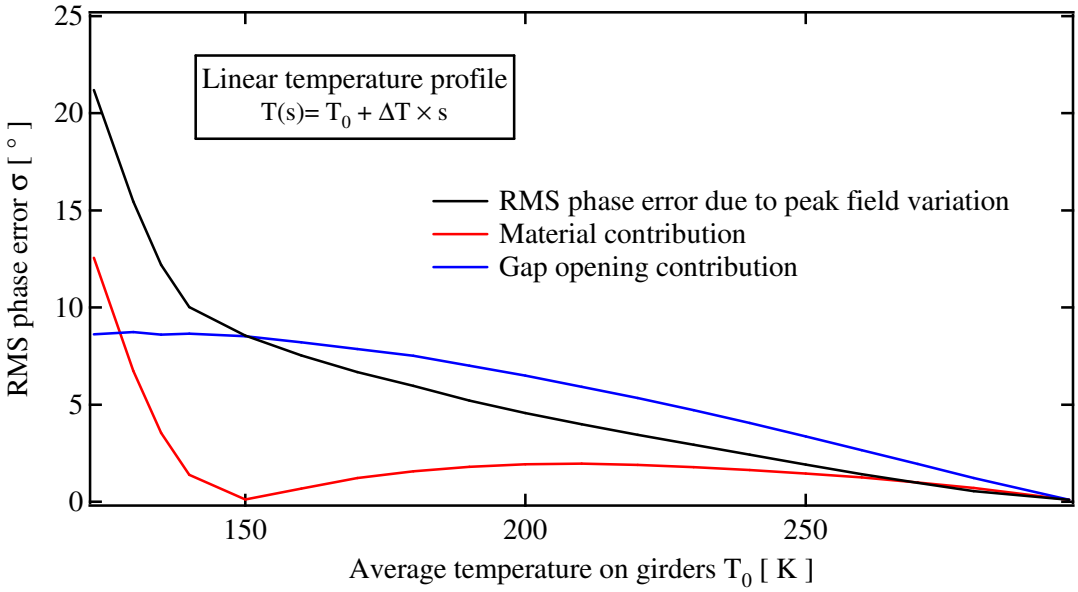

Figure 3.47: Evolution with the average temperature of the undulator RMS phase error (black curve) as the temperature varies linearly along the undulator. The blue (red) curve represents the RMS phase error introduced by the gap deformation (the change of magnet properties). The computation is done with B2E assuming a 6 GeV electron.

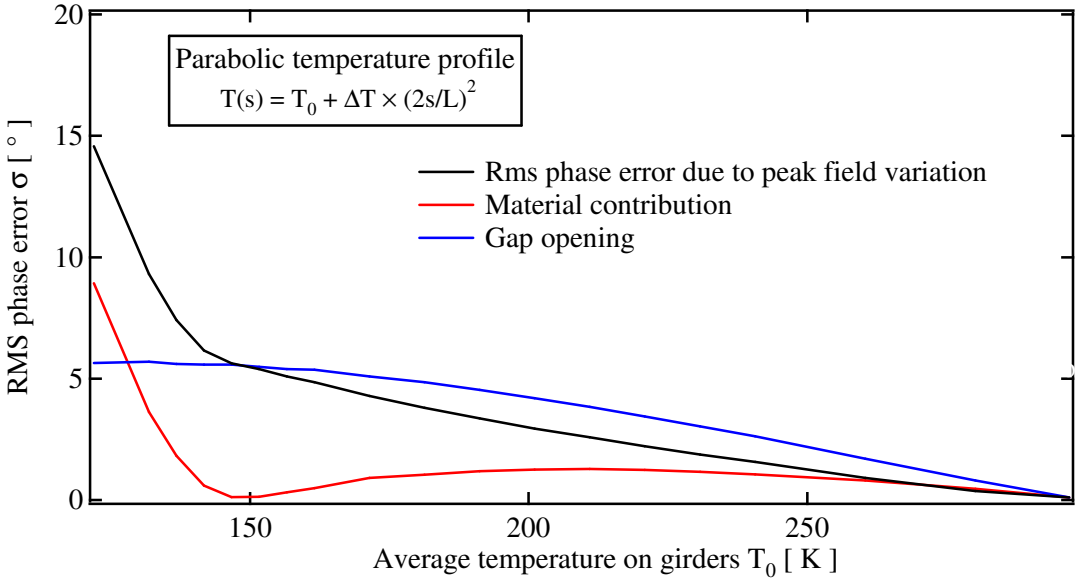

Figure 3.48: Evolution with the average temperature of the undulator RMS phase error (black curve) as the temperature distribution is parabolic. The blue (red) curve represents the RMS phase error introduced by the gap deformation (the change the properties of the magnets). The computation is done with B2E assuming a 6 GeV electron.

The black curves in Figure 3.47 and Figure 3.48 represent the undulator RMS phase error wherein the gap opening and the change of magnetic properties have been taken into account. The undulator RMS phase error isn't simply the sum of the RMS phase errors arising from the contributions ΔB_z^g and ΔB_z^m. Indeed the contributions ΔB_z^g and ΔB_z^m have opposite signs above 150 K while the magnet temperature effect adds to the gap opening deformation below 150 K. This leads to a large increase of the RMS phase error below 150K, the RMS phase error is doubled as the temperature is lowered from 150 K down to 120 K.

As observed in Figure 3.46 the contribution ΔB_z^m cancels at a temperature close to 150 K; the associated RMS phase error reaches its minimum. When the average temperature goes far from this temperature range, the peak field becomes more sensitive to the temperature of the magnets and the RMS phase error increases. Following the RADIA model, the CPMU temperature operation is 150 K. At this temperature, the gap opening is responsible for the increase of the RMS phase error.

To conclude, the main advantage of the CPMU lies in the ability to use $Nd_2Fe_{14}B$ magnets at cryogenic temperature. This low temperature improves the resistance of the magnets to demagnetization, so that we can benefit from their high remanence. The ESRF has a CPMU project: the magnetic assembly is a 2 m long Hybrid undulator with 18 mm period. $Nd_2Fe_{14}B$ material is 495t NEOREM magnet. The chosen cooling system is a liquid nitrogen closed loop. This chapter has covered the design of the CPMU. A numerical model, based on the experimental curves of the 495t NEOREM magnet, has been completed in order to investigate the temperature dependence of the peak field and the field integral. The key learnings are: the peak field is maximal at 150 K and the field integral increases at a lower temperature. A thermal model has also been developed. It calibrates the thermal contact between the cooling system and the magnetic assembly, determines the gap opening and quantifies the impact of a thermal gradient on the RMS phase error. In concrete terms, 32 spacers, with a thermal resistance of 15.6 K/W, are necessary to cool the CPMU at 150 K. At this temperature one expects a gap opening of around 1 mm. The realization of the HYB18, at ambient temperature, is presented in the following chapter.

4. HYB18 assembly and correction at ambient temperature

This chapter covers the assembly and the correction of the HYB18 CPMU undulator. These are performed at room temperature, similarly to other standard undulators produced at the ESRF: the magnet modules are assembled separately on the girder and the ID is corrected at ambient temperature. These corrections are performed so that the electrons emit the most intense radiation as they pass throughout. In addition IDs should not disturb the beam dynamics in the storage ring. We introduced in section 2.3 the field integrals and the phase error; these are the parameters which should be corrected in order to minimize the impact of the magnetic errors on the beam dynamics and on the SR emission. Before discussing the undulator assembling and correction, we first review the different sources or magnetic errors in an undulator.

4.1. Magnetic errors in undulators

We review hereafter the different sources of magnetic errors in undulators. Due to these errors, it is necessary to correct the undulator field.

Before dealing with the potential errors, we should point out the complexity of an undulator which is made up of many different pieces. Figure 4.1 sketches schematically an HYB18 girder.

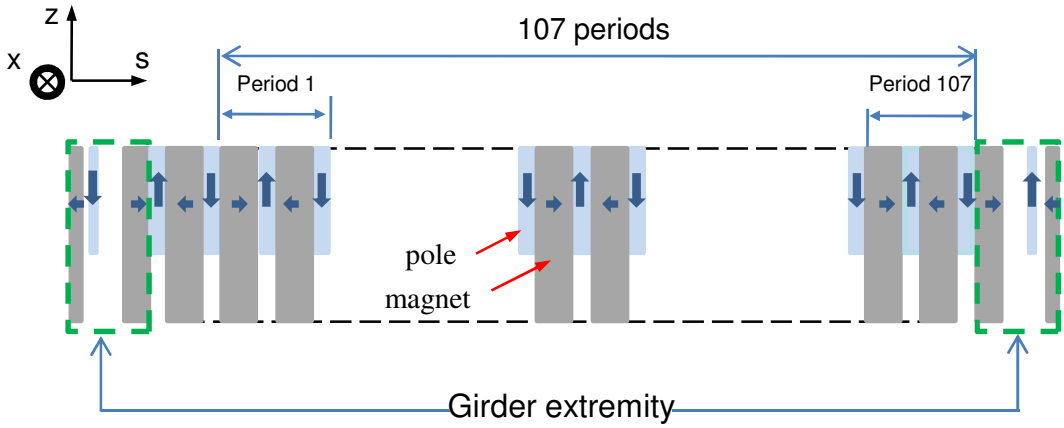

Figure 4.1: Sketch of the HYB18 lower girder. Each girder is made of 215 magnets, 216 poles and its extremities (i.e. 2 magnets A, 2 magnets B and two slim poles as described in section 2.4.3).

Since an undulator is made up of so many pieces, there are many potential sources of errors in the undulator field. Actually these errors can be grouped into two categories, depending on their origin: those which are mechanical and those which are magnetic.

The main mechanical errors are:

- Positioning errors of magnets and poles in the magnetic assembly.
- Geometrical errors of the different mechanical pieces which constitute an undulator: supports of magnets and poles, dimensions of magnets and poles…

The magnetic errors include any magnetization defects in the magnet block. These defects are created during the manufacturing process and are an important source of undulator errors. The most common magnetization defects are [88]:

- Fluctuation of the magnetization value from one magnet to the next among the magnet population.

- Angle between the magnetization direction and the theoretical one.
- Inhomogeneity of the magnetization within a magnet volume.

Insertion device designers impose some constraints on the mechanical pieces and magnet block in order to lower these potential sources of field errors. They are discussed hereafter.

Tolerances and magnet specifications

The mechanical errors are the simplest ones to control. We impose some tolerances on the undulator constituents. These tolerances typically vary from 25 µm to 50 µm. At the ESRF for any kind of undulator, the tolerance for the magnet thickness is fixed at 25 µm. This air gap is necessary to allow the juxtaposition of magnets while assembling, as explained in section 3.4.2. The positioning errors are controlled during the assemble process; for instance a magnet rotation around the vertical axis causes a typical effect which one measures with the integral field bench.

Magnetization fluctuation and angle errors among the magnet population are limited by clear specifications to the manufacturer. Any block out of the spectrum is simply rejected. These specifications rely on the measurement of the three magnetization components (M_x, M_y, M_z). These three components are measured with a Helmholtz coil. The specifications are typically:

- A ±1% maximum variation of the magnetization value from one block to the next.
- A 1° maximum misalignment between the magnetization and the theoretical direction.

These limitations impose a first filtering of the magnets. In practice the manufacturer has to produce more magnets than required in order to ensure a sufficient number of magnets within the range of the specifications. The overproduction sometimes reaches 30%. Figure 4.2 represents the distribution of the angle and the remanence for the 495t NEOREM magnet population dedicated to the HYB18 assembly.

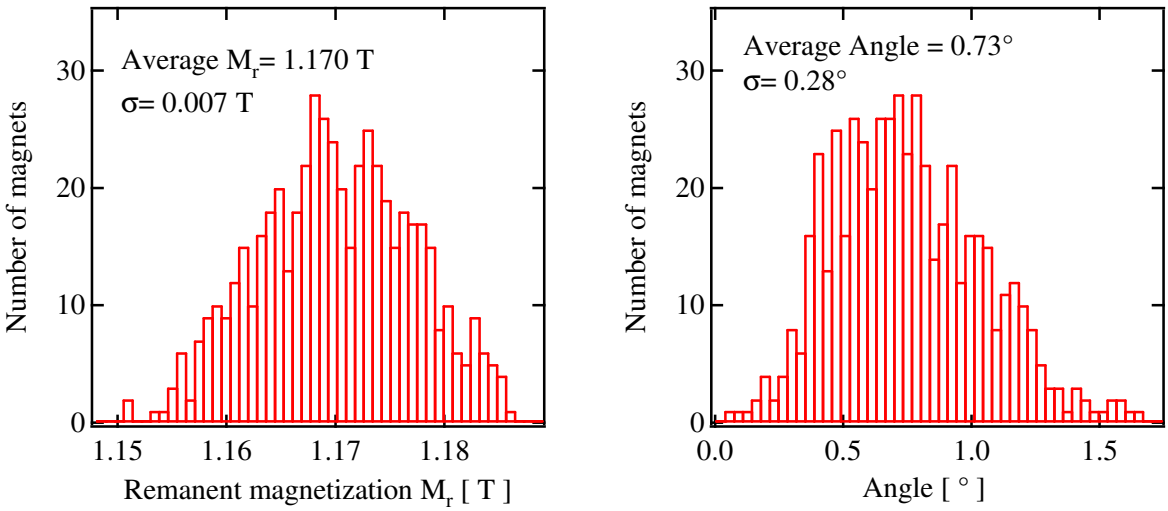

Figure 4.2: Distribution of the remanent magnetization (left plot) over the 495t NEOREM magnet population. The angle (right plot) measures the misalignment of the magnetization orientation with the specified direction.

Then comes another type of error which may cause large magnetization inhomogeneities inside the magnet. The inhomogeneity error is directly linked to the powder metallurgy manufacturing process of the blocks. Magnet powder i.e. $Nd_2Fe_{14}B$ is compacted in a strong magnetic field. This field aligns the $Nd_2Fe_{14}B$ grains along the theoretical magnetization direction. It is easy to see that the magnetization homogeneity depends strongly on the geometry of the applied field and on the magnet size. As far as the magnetic field applied to align the magnet grains is concerned, the smaller the magnet the better the magnetization homogeneity in its volume. Figure 4.3 draws schematically the

typical type of inhomogeneities induced by the disorientation of the grains during the manufacturing process. One generally uses the term North/South asymmetry when considering the magnetization inhomogeneity. The coefficient α_{NS} measures the North/South asymmetry and is defined as:

$$\alpha_{NS} = \frac{B_N - B_S}{2(B_S + B_N)} \tag{4.1}$$

B_N and B_S are the magnetic field components along the s axis. They are measured at a fixed distance from the centre of the magnet north and south faces. At the ESRF the typical distance is 3 mm. Because of inhomogeneities in magnet volume, the magnetic field B_N measured at the centre of its north face may be different from the one B_S measured at the centre of its south face. For the HYB18 the maximum value of the North/South asymmetry authorized is fixed at 0.2.

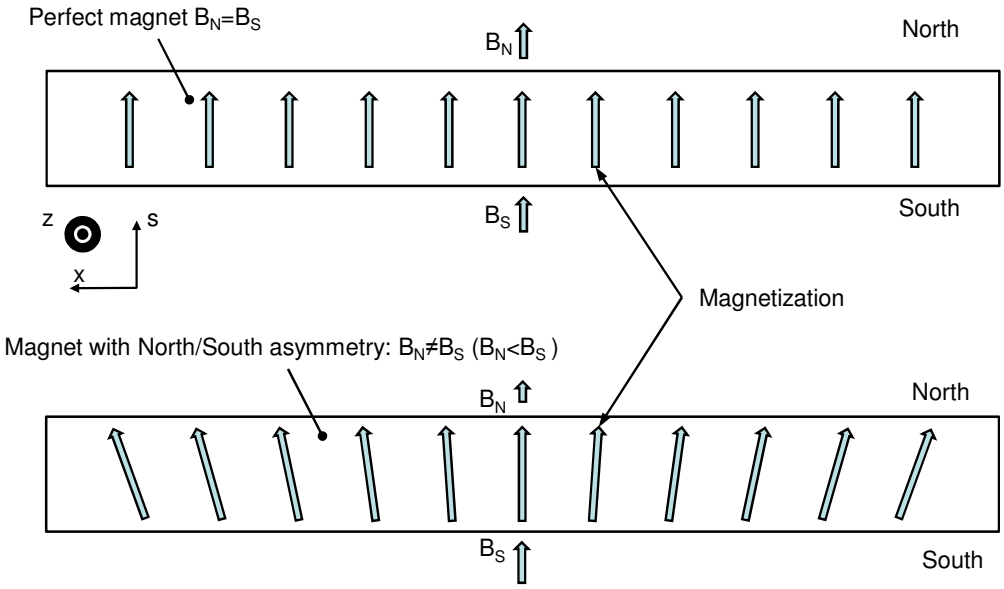

Figure 4.3: Magnetization orientation in a magnet.

All these parameters allow magnet suppliers to deliver high quality magnets for the undulator realization. Nevertheless they are not sufficient to efficiently predict errors in the undulator field. For instance one may assemble undulators according to their North/South asymmetry coefficient α_{NS}. However experience demonstrates that undulators assembled according to this process, present a phase error and field integrals which are out of scope [22]. In other words, an additional characterization of magnet defects is necessary.

Characterization of magnet defects

In the second chapter, we introduced the relevant quantities to measure the impact of undulator field errors on the electron beam dynamics and on the SR, i.e. the field integral and the RMS phase error. It is then obvious that an efficient characterization of magnet defects will rely on these quantities.

At the ESRF the ID girders are mounted one after the other. Thus as long as the ID assembly is not completed, the RMS phase error is meaningless. As a result the first field integral is the figure of merit that has been chosen at the ESRF to assemble the IDs. Each girder of an ID is segmented in elementary arrangements. In order to build up each girder, one pairs the arrangements according to their first field integral.

Figure 4.4 displays a typical magnet arrangement used in a PPM design. In one arrangement, one has exactly the same number of magnets with the magnetization oriented positively and negatively along the vertical axis. The equivalent magnet support for a HYB design is also represented. With such a magnet arrangement, the measured field integral mainly represents the contribution of errors

mentioned above. Field integral benches presented in the first chapter are suitable to measure the field integral generated within a few Gcm accuracy. One measures the field integral $\vec{I}(x,z)$ with the following conditions:

- One measures the field integral at vertical distance $g/2$ from the magnet surface. g is the gap at which one corrects the undulator.
- The integral is measured for -50 mm < x < 50 mm. The horizontal origin is on the magnet symmetry axis.

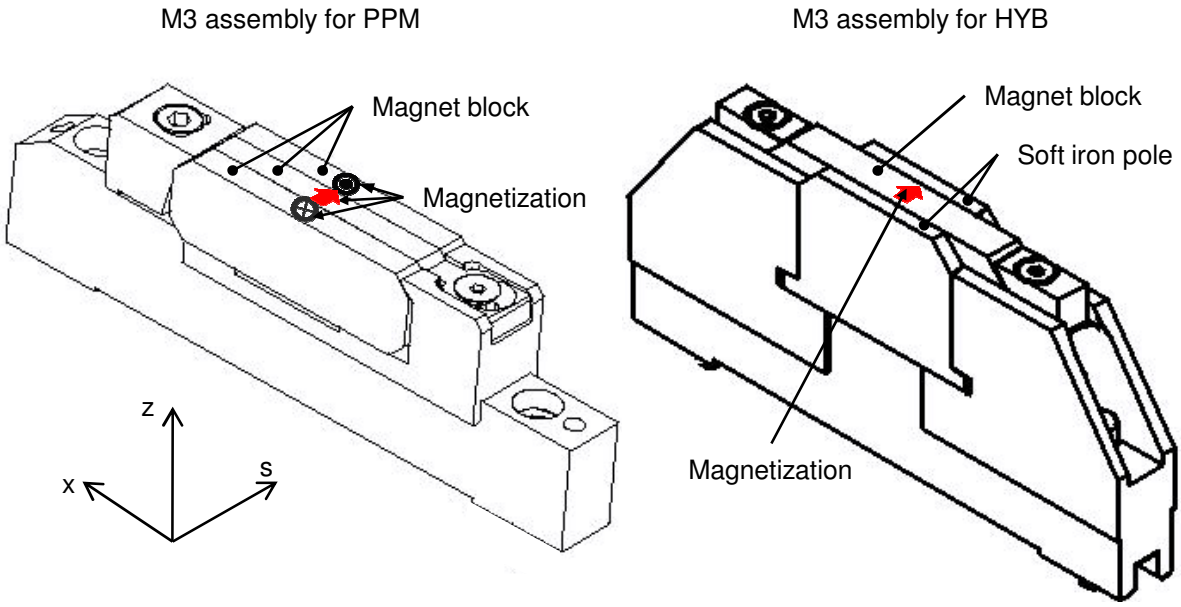

Figure 4.4: Sketch of a M3 assembly for PPM (left) and HYB (right) design. The net field integral of these assemblies results from errors.

In a hybrid undulator, the pole vicinity noticeably changes the field integrals. Figure 4.5 displays the measured field integral of a single magnet with longitudinal magnetization. The measured field integral of the magnet with two adjacent poles (M3 assembly) is also represented. It appears then that measuring the field integral of single magnets is not sufficient to accurately predict the field integral they would produce in a hybrid undulator. Thus it is necessary to measure magnets with adjacent poles to efficiently characterize their impact on the field integral.

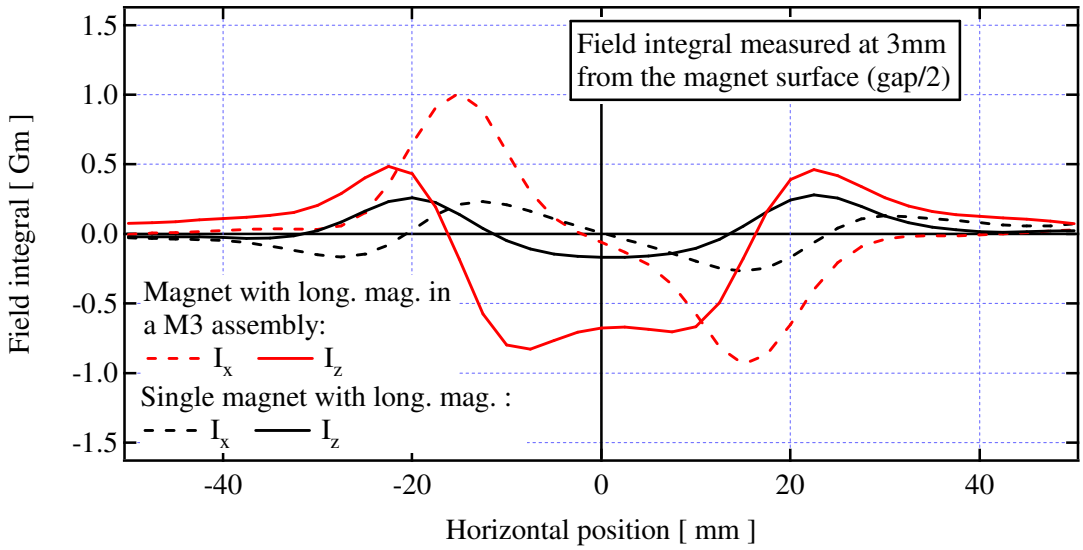

Figure 4.5: Field integral of HYB18 magnet with longitudinal magnetization as it is alone (black line) or in a M3 assembly with 2 soft iron poles (red lines). The field integral has been measured with the rotating coil at 3 mm from the magnet surface.

We compare in Figure 4.6 the field integral which a magnet with magnetic errors in its volume would cause once inserted in a HYB girder and in a M3 assembly. The M3 assembly field integral is very similar to the girder integral. Thus measuring the field integral of a M3 assembly is sufficient to predict the magnet contribution to the total girder field integral. This suggests the possibility to:

- Study a magnet contribution in a hybrid assembly according to its M3 assembly.
- Take a hybrid girder as a sum of M3 assemblies; each M3 assembly would share its 2 poles with the preceding and the following magnet. In particular the periodic part field integral is simply the sum of the field integrals of each M3 assembly.

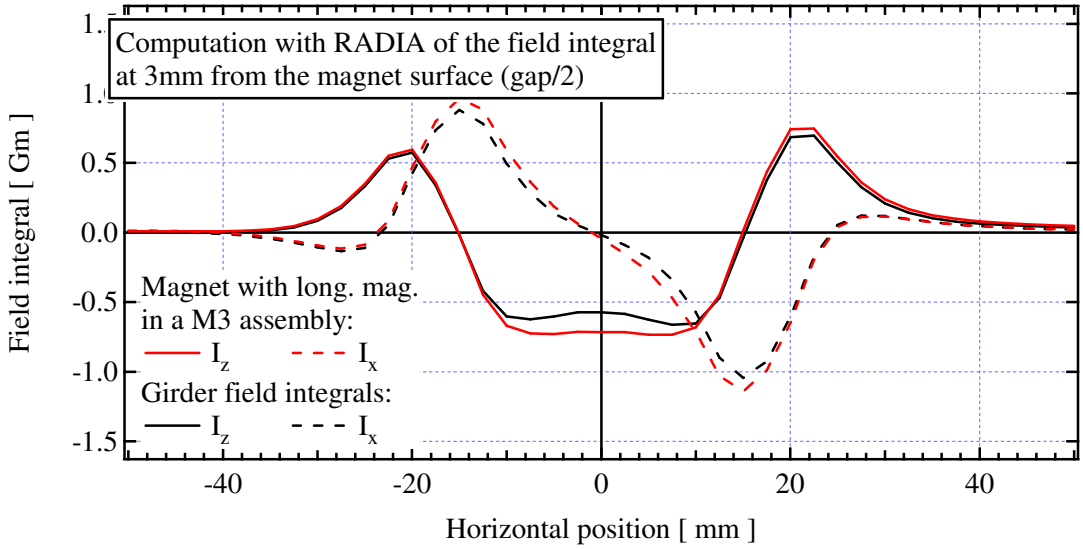

Figure 4.6: Field integral produced by a 495t NEOREM magnet with North/South asymmetry, in a M3 assembly (red lines) and in a complete girder in the vicinity of many poles and perfect magnets (black lines). The computation is done with RADIA.

532 485t NEOREM magnets are available to build the undulator. Each of them has been mounted in an M3 assembly and their field integral has been measured. This in order to predict the field integral

induced in girders. Figure 4.7 represents the on axis vertical field integral of the M3 assemblies with respect to the North/South asymmetry. On axis field integrals are correlated to the North/South asymmetry according to:

$$I_z(x = 0, z = 3) = a + \alpha_{NS} \times b \tag{4.2}$$

With:

$$a = 0.13 \pm 0.01, b = -6.76 \pm 0.08 \tag{4.3}$$

This gives an estimation of the maximum asymmetry required to keep the on axis field integral below a maximum value. For instance in future specification for magnets, one would fix the maximum value of the North/South asymmetry at 0.01 in order to keep the on axis vertical field integral below 0.2 Gm.

Considering the magnetic characterization of the HYB M3 assembly defined in Figure 4.4, one can show that a magnet with a pure North/South asymmetry would produce a field integral invariant for 180° rotations around any of the x, z and s axis. Any magnet rotation in the M3 assembly wouldn't change the sign of the on axis vertical field integral of the M3 assembly. Thus to perform an efficient matching of magnets, it is necessary to have at least a magnet population with α_{NS} values equally distributed around 0. It ensures that each magnet has its own opposite in the population and consequently one may find a magnet in order to compensate another one.

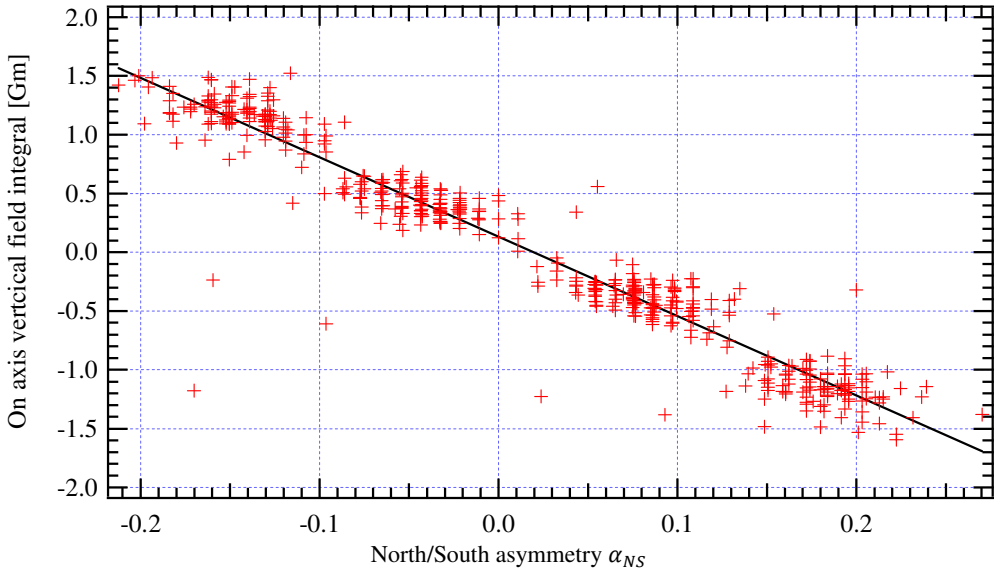

Figure 4.7: On axis vertical field integral of magnet with respect to the North/South asymmetry coefficient. The magnet is in a M3 configuration.

The field integrals of the M3 assemblies are quite large since half of the population have a vertical field integral higher than 1 Gm. We have to remember that the magnetic assembly will have a vertical field integral smaller than 0.2 Gm. Thus, the magnet matching has to be efficient. Hereafter we discuss the assembly process.

4.2. HYB18 assembly

During the ID assembly, girders are mounted one after the other. As discussed in the previous subchapter, the HYB18 girders can be considered as the sum of 215 individual M3 assemblies, each M3 assembly sharing its poles with the preceding and the following one. We pair magnets in each girder according to their M3 field integrals in order to obtain HYB18 girders with the lowest field integral. We explain now how we proceed.

Assembling process of the girders

The periodic part assembling process is schematically sketched in Figure 4.8. It aims at obtaining girders with the lowest first field integral. We measure the field integral of the girders at 3 mm from the magnet surface and between x = -50 mm and x = 50 mm. These are the same conditions as the ones used to measure the M3 assemblies. It is clear that adding a period or 2 M3 is equivalent. We do perform the following steps to assemble the 2 m long HYB18 girder:

- Selection of the first magnet whose M3 assembly has the lowest field integral.
- Building up the periodic part one period after the other.
- Extremities selection once the periodic part mounting is over. One selects two extremities that minimize the residual periodic part field integral.

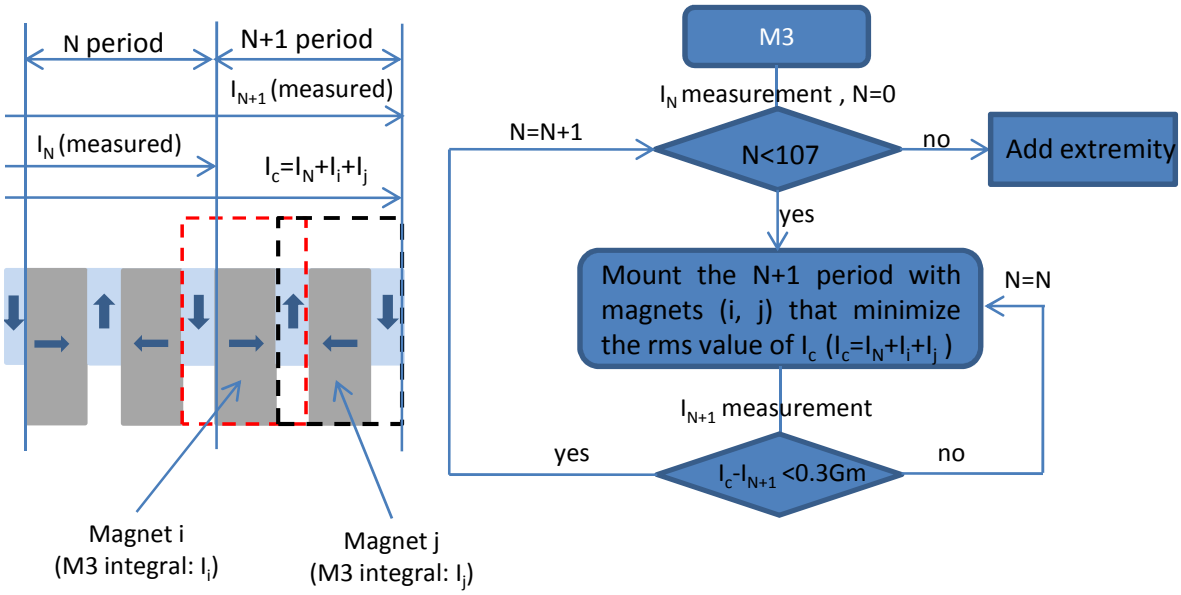

Figure 4.8: Description of the assembling process.

The main operation is the periodic part assembly. The 107 periods are mounted one by one and we measure the field integral to confirm any step. For instance, assuming we have already mounted N periods, I_N is the field integral measured at this stage. We choose two magnets Mi and Mj to build the N+1 period. Magnets Mi and Mj are selected to minimize I_c, the field integral of the girder with N+1 periods. From our previous discussion, one deduces the Mi and Mj contribution to the girder field integral I_c from their M3 field integral measurement. The predicted girder field integral I_c is:

$$I_c = I_N + I_{Mi3} + I_{Mj3} \tag{4.2}$$

I_{Mi3} (I_{Mj3}) is the field integral of the magnet Mi (Mj) in a M3 assembly and I_N the girder field integral with its N periods. In other words we select two magnets for the N+1 period that would best compensate the previous field integral measurement of the girder with the N periods. If the I_{N+1} measurement is too far from the prediction I_c, the N+1 period is dismounted and we select two other magnets for the N+1 period. We consider that the prediction is too far from the measurement whenever the difference between both on axis field integrals is higher than 0.3 Gm. We repeat this operation until we have completed the periodic part assembly. At this point we add the extremities. Figure 4.9 and Figure 4.10 represent the field integral obtained for both girders. The on axis field integral achieved on each girder exceeds the limit fixed in equation (2.62). The upper girder exhibits a characteristic vertical dipole which contributes largely to the undulator vertical field integral. Compared to the lower girder, the upper one has a smoother vertical field integral. One explains the smoother field integral by a better $Nd_2Fe_{14}B$ magnet pairing since it has been the first girder assembled.

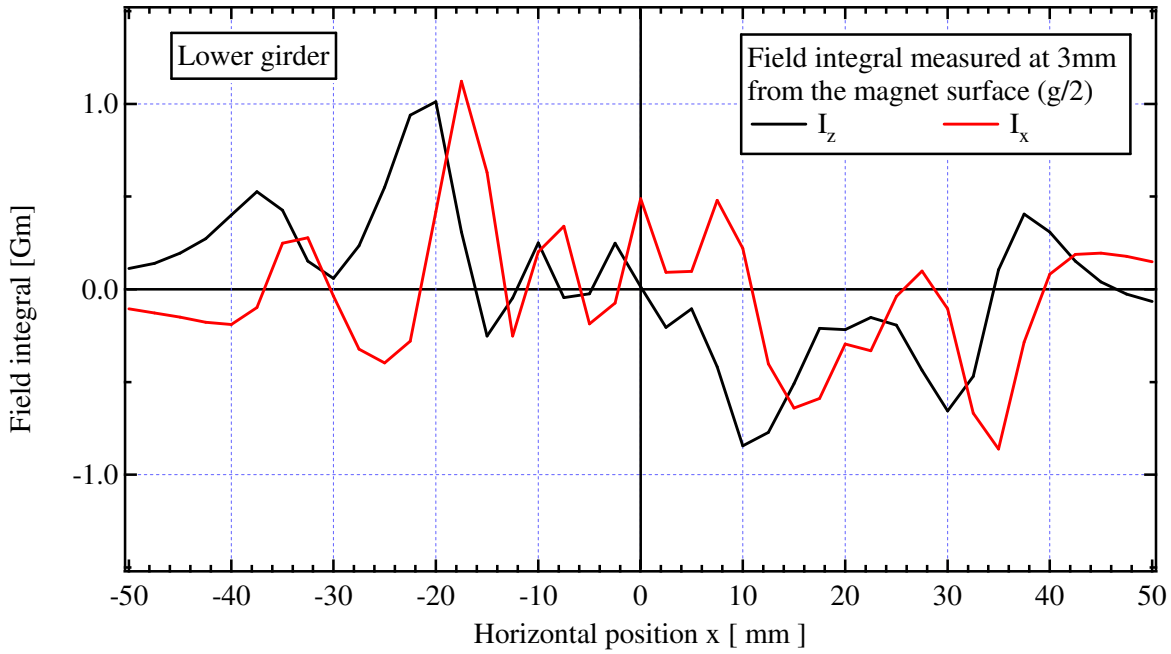

Figure 4.9: Field integral $\vec{I}(I_x, I_z)$ of the lower girder measured at 3 mm from the magnet surface with the rotating coil.

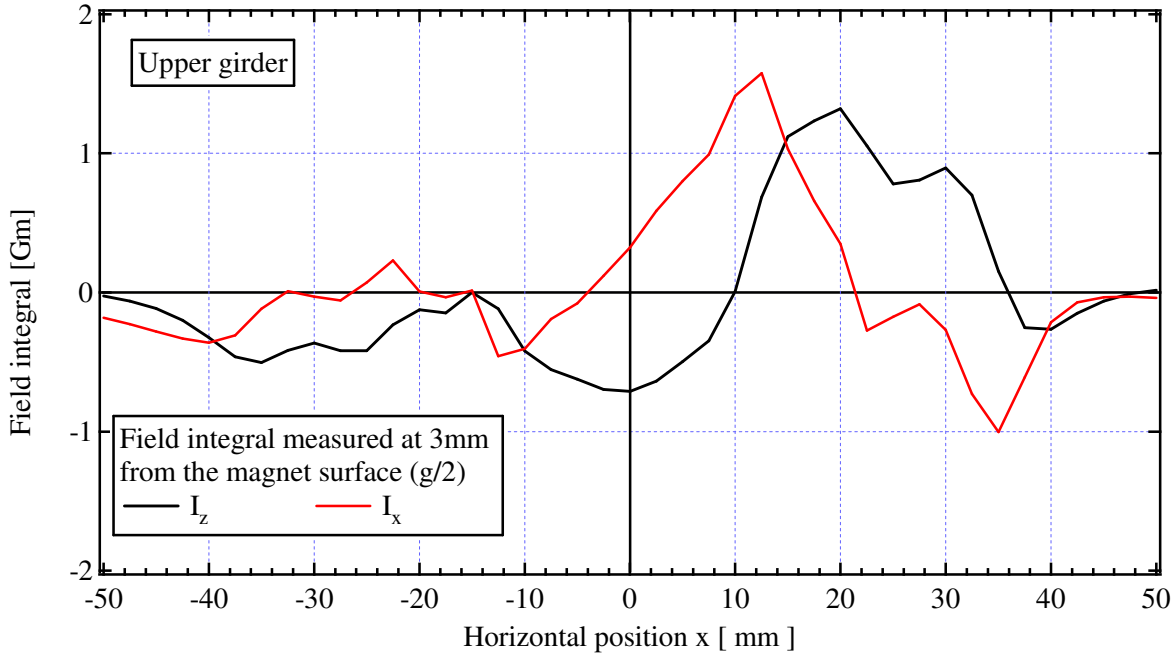

Figure 4.10: Field integral $\vec{I}(I_x, I_z)$ of the upper girder measured at 3 mm from the magnet surface with the rotating coil.

HYB18 initial performance

Once the assembly is completed, the girders are mounted on the mechanical support. Magnetic errors are further corrected to optimize the undulator performance. Figure 4.11 represents the initial undulator vertical I_z. At this point the girders have just been mounted on the undulator mechanical

support. The different contributions to the undulator field integral are also plotted. The interaction between girders causes a small vertical field integral.

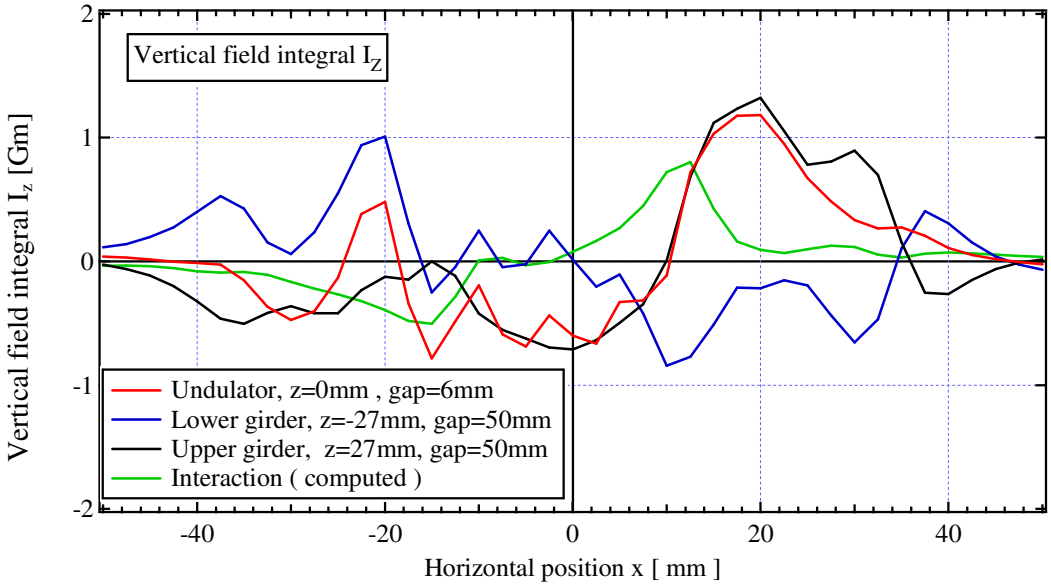

Figure 4.11: Measured vertical field integral of the lower girder (blue curve), the upper girder (black curve) and the undulator (red curve). The interaction (green curve) is computed from these measured integrals. The girder field integrals are measured at 3 mm from the magnet surface, the gap is closed at 6 mm to measure the undulator field integral. Field integrals are measured with the rotating coil at horizontal positions between x = -50 mm and x = 50 mm.

The horizontal field integral of the undulator, the girders and the interaction are displayed in Figure 4.12. The interaction is null on the axis and rapidly grows with horizontal position. The interaction between lower and upper girder causes a horizontal field integral whose peak to peak variation reaches nearly 4 Gm. The interaction contributes largely to the horizontal component of the undulator field integral.

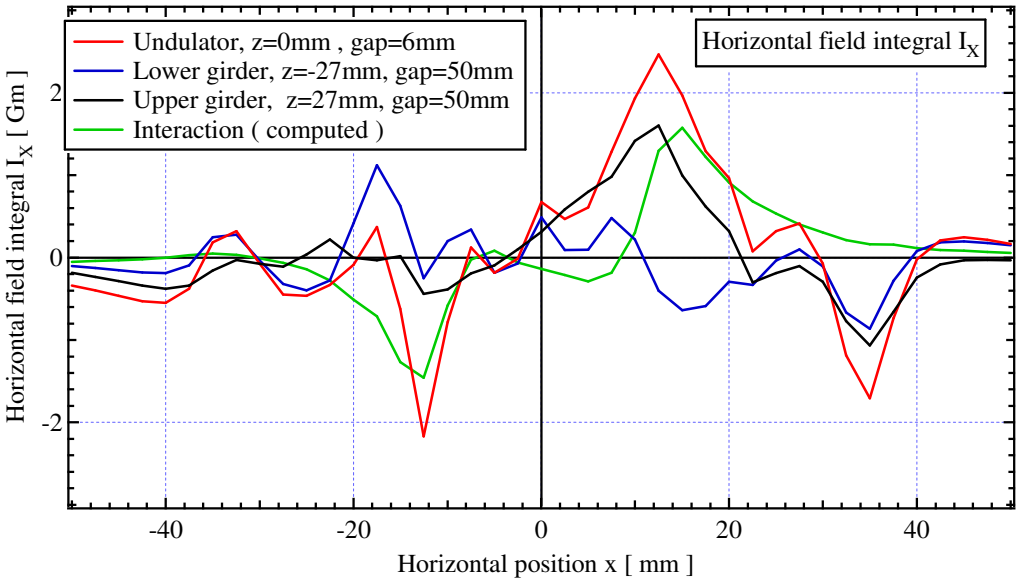

Figure 4.12: Measured horizontal field integral of the lower girder (blue curve), the upper girder (black curve) and the undulator (red curve). The interaction (green curve) is computed from these measured integrals. The girders field integrals are measured at 3 mm from the magnet surface, the gap is closed at 6 mm to measure the undulator field integral. Field integrals are measured with the rotating coil at horizontal positions between x = -50 mm and x = 50 mm.

To sum up, the girders have an acceptable field integral: on the axis, it is lower than 0.5 Gm and off axis the maximum field integral is around 1 Gm. Thus the pairing has been efficient since single magnets have typically field integral of 1 Gm.

With a PPM design, one would have now proceed to multipole shimming in order to lower further the field integral, as explained in section 2.3.1. Whenever we would do this for a hybrid design, we may have an undulator with a large on axis field integral because of the possible interactions between girders. Thus, we check the interactions first in order to take them into account during the correcting stage.

This highlights a limitation to this process for hybrid design. The interaction cannot be forecast at first. We set up each girder independently, and then measure the interaction once the assembly has been done. Due to this unpredictability, SPring-8 has developed another correction scheme, the so called “in situ sorting”. In that case, there is no sorting during the assembly but only once the assembly has been completed [89].

4.3. HYB18 correction

We correct errors in the undulator field in order to keep field integrals below the upper limits given in Table 2.4. Concerning the maximum value of the HYB18 RMS phase error, the HYB18 is dedicated to the ID06, a beamline specialized in instrumentation. Its required energy range has been set up by beamline scientists at between 15 keV and 80 keV. This range is covered by the first three harmonics, meaning that a phase error of 4° would be acceptable. We will now present the ESRF methodology to correct undulator.

4.3.1. ESRF methodology

The undulator field is corrected for a gap value of 6 mm which is the smallest value at which it will be used in the storage ring. Indeed, errors are generally bigger when the gap is the smaller. Thus we correct errors at the smallest possible gap value.

The ESRF process splits the undulator correction into two consecutive steps:

- Correcting the first and second field integrals.
- Correcting the phase error.

These two steps are consecutive but not independent. Indeed correcting the field integrals will impact the phase error. Therefore there would be no point in correcting the phase error first. However a low phase error adds a constraint on the field integral correction: it requires the electrons to be driven in an oscillatory trajectory around their straight direction of motion, as explained in section 2.3.2. The horizontal (vertical) position of electrons in the undulator field is:

$$X(s) = \int_{-\infty}^{s} \theta_x(u)du \qquad Z(s) = \int_{-\infty}^{s} \theta_z(u)du \tag{4.4}$$

Where θ_x (θ_z) is the horizontal (vertical) electron angle along the undulator. It implies the correction of the field integral in such a way that the angles θ_x and θ_z are null all along the undulator. The angles are related to the field integral as follows:

$$\theta_x(s) = \frac{e}{\gamma mc}\int_{-\infty}^{s} B_z(u)du = \frac{e}{\gamma mc} I_z(s) \qquad \theta_z(s) = -\frac{e}{\gamma mc}\int_{-\infty}^{s} B_x(u)du = -\frac{e}{\gamma mc} I_x \tag{4.5}$$

It is clear from equation (4.4) that a straight trajectory implies I_z and I_x to be equal to zero along the undulator. In other words, the integral cannot be corrected only at the entrance and the exit of the undulator, but all along it.

We use local measurements, performed using the Hall probe bench, in order to determine the electron angle or equivalently the field integral along the undulator axis. Figure 4.13 displays the HYB18 on axis magnetic field measured, before any correction.

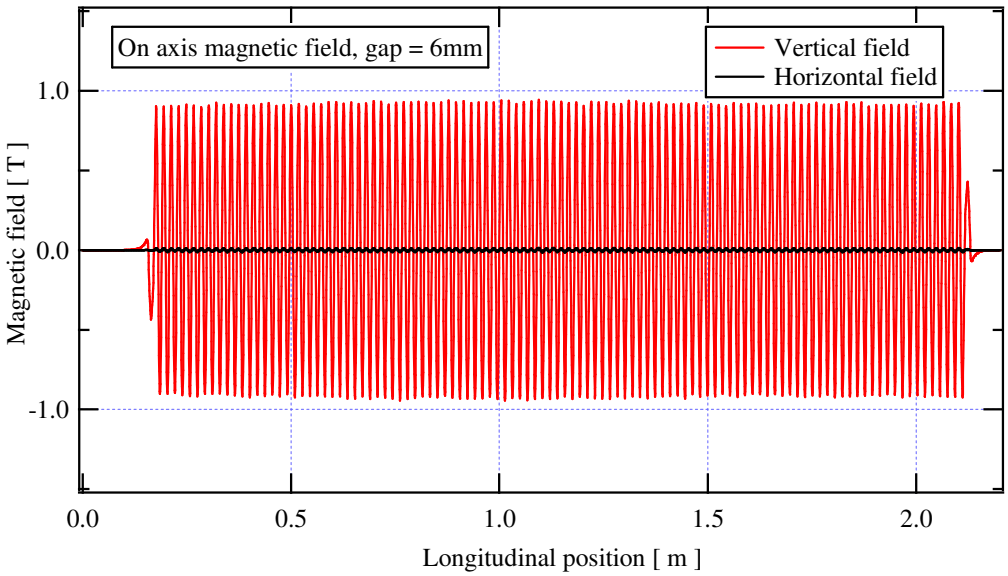

Figure 4.13: On axis vertical (red) and horizontal (black) magnetic field. Measurement performed with the Hall probe bench, the undulator gap is closed at 6 mm.

The angles computed from local measurements for HYB18 before correction, are presented in Figure 4.14. This figure is a way to visually represent the necessary corrections. We observe large peak to peak angular excursions. The integral correction will minimize these peaks and reduce to zero the exit angle, which is similar to obtain a null integral. This tool is a very helpful graphic

representation, in order to determine where the integral field correction should be applied. It is indeed easy to determine, where we have a peak that would overpass a define limit, for instance over 5 µrad.

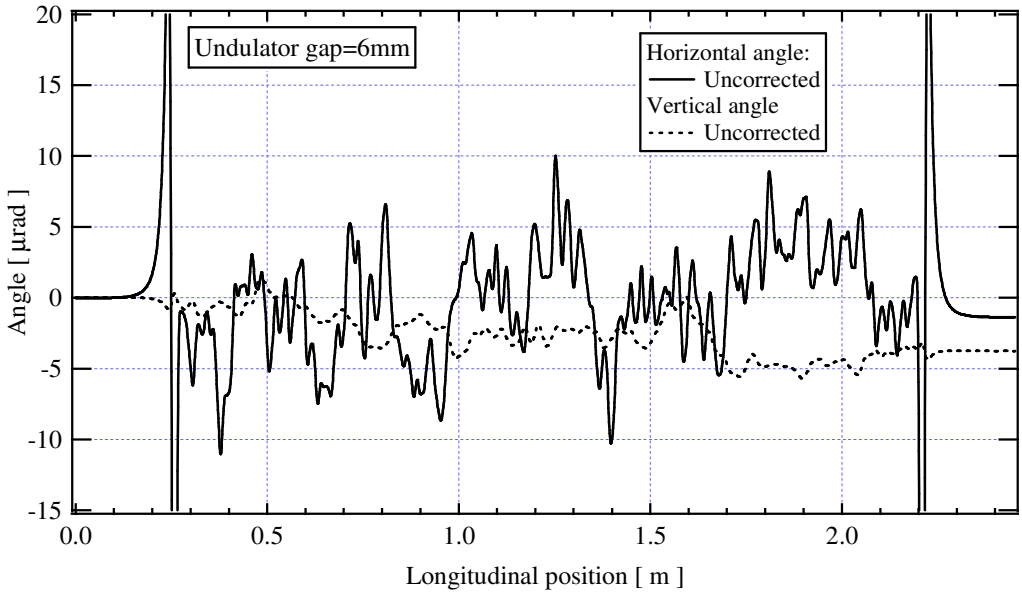

Figure 4.14: Initial vertical (continuous black line) and horizontal (dashed black line) angles of a 6 GeV electron along the undulator before field integral correction. Angles are computed from Hall probe measurement with B2E.

We can stop correcting the integrals:

- When they sit within the limits specified in Table 2.4, at any gap value.
- And when no more angle effect is visible on the phase error.

However a straight electron trajectory is not sufficient to ensure a low phase error, so a specific phase error shimming has to be done afterwards to ensure we reach the target value.

Splitting the process in different steps is a way to focus on a limited number of parameters at a time, and thus aims at keeping things simple and closely linked to the magnetic measurement. On a practical level at the ESRF, technicians in charge of the undulator are responsible for applying the proper actions which efficiently correct the undulator field errors. Obviously it requires an in-depth knowledge of the physical phenomenon.

Alternative approaches to the 2 steps one used at the ESRF exist. They use statistic methodologies of optimization. They assume that correcting an undulator means solving a finite but huge number of settings possibilities. Therefore it is possible to use statistical methods in order to get an efficient and fast computed solution. Some of the stochastic approaches use Monte Carlo techniques [90] and genetic algorithms [91], [92]. However whatever the chosen stochastic methodology is, the ID designer plays a part. He decides on the relative importance of the parameters (horizontal and vertical integrals, trajectories, phase error, and so on) by applying to them weighted correction coefficients. The main advantage is that many parameters can be considered at the same time, which is great for complex structures such as Apple-II [93]. The phase error and integral field can be corrected simultaneously. But the price to pay is the empirical way the parameters are tuned.

We focus now on the specific case of the HYB18 correction at the ESRF, analyzing first the correction of the field integral, and then that of the phase error.

4.3.2. HYB18 field integral correction

As explained before, correcting field integrals means dealing both with the field integral itself and ensuring a straight trajectory. Local measurement is very important at this stage to make sure the electron angle is null all along the undulator.The different possible actions to correct the field integral are:

- Magnet replacements. One may simply find in the unused magnet population, some magnets which are more suitable, so we switch.
- Magnet and pole rotation. Rotate a magnet or a pole produces some typical field integrals. These effects might be used.
- Magnet and pole displacement. One may also displace a magnet or a pole to produce other typical field integrals.

Note that no space for the displacement and rotation of the magnets is planned in the undulator design. We just rely on the geometrical tolerance in order to typically displace magnets over a few tens of microns; the variation of the field integrals is rather low with such displacements. As a result a lot of magnet displacements are necessary to noticeably change the undulator field integral.

Figure 4.15 represents a M3 assembly horizontal translation. The effect is very small, lower than 0.1 Gm. The maximum effect on the vertical integral is observed for x = ±22 mm close to the magnet chamfers. It indicates that the field integral is mainly impacted by the magnet.

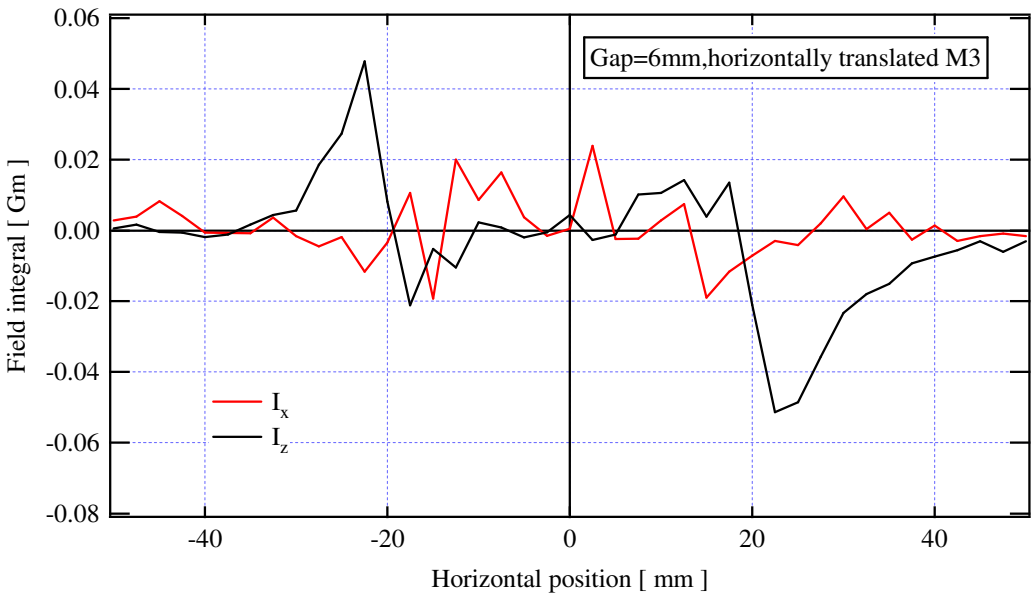

Figure 4.15: Effect of a M3 assembly horizontal translation (50 µm) on the field integral HYB18. The measurement is performed with the rotating coil and the undulator gap is closed at 6mm.

Figure 4.16 represents the field integral variation due to magnet rotation. The variation here is larger than the one due to translation. In addition the on axis field integral variation is non null. Therefore this kind of displacement may be used to correct on axis errors. Once again we observe an effect of the magnet, since the field integral variation extends horizontally over a distance similar to the magnet width.

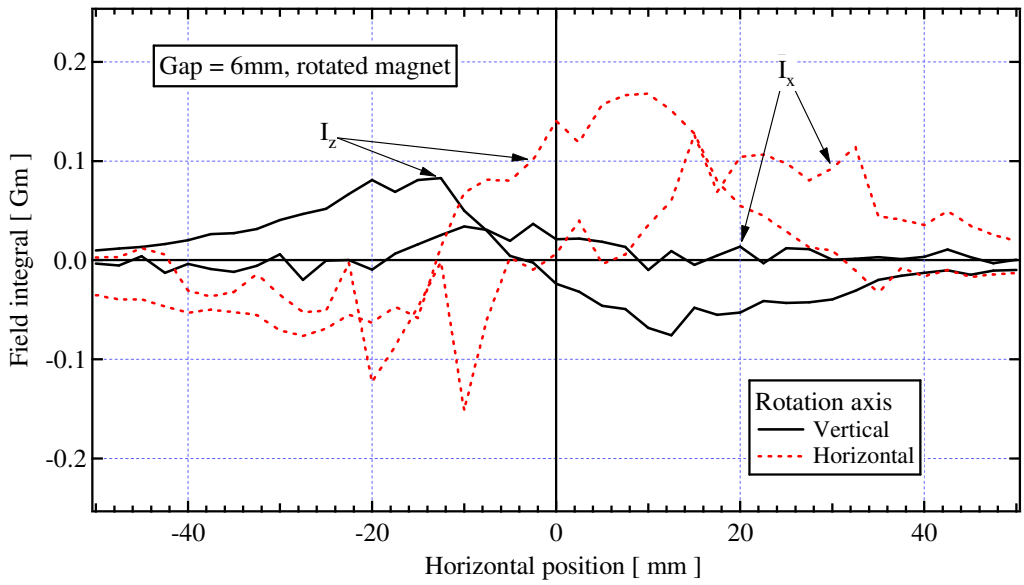

Figure 4.16: Effect of magnet rotation around the vertical axis (black line) and the horizontal axis (red dotted curve) on the HYB18. The order of magnitude of the rotation angle is a few thousandth of mrad.

Figure 4.17 shows the pole translation effects. A vertical (horizontal) translation causes a vertical (horizontal) dipole. Compared to a vertical translation, a horizontal translation only produces a small dipole. This method is more efficient than the others since here we have stronger horizontal and vertical field integrals. However the impact is localized (±20 mm), thus we cannot use it to correct integrals at large horizontal position. In addition, since poles are not directly accessible, this process first requires an M3 assembly to be removed from the undulator, and then to move the pole. Thus, compared to magnet displacement, such a process is much more time consuming.

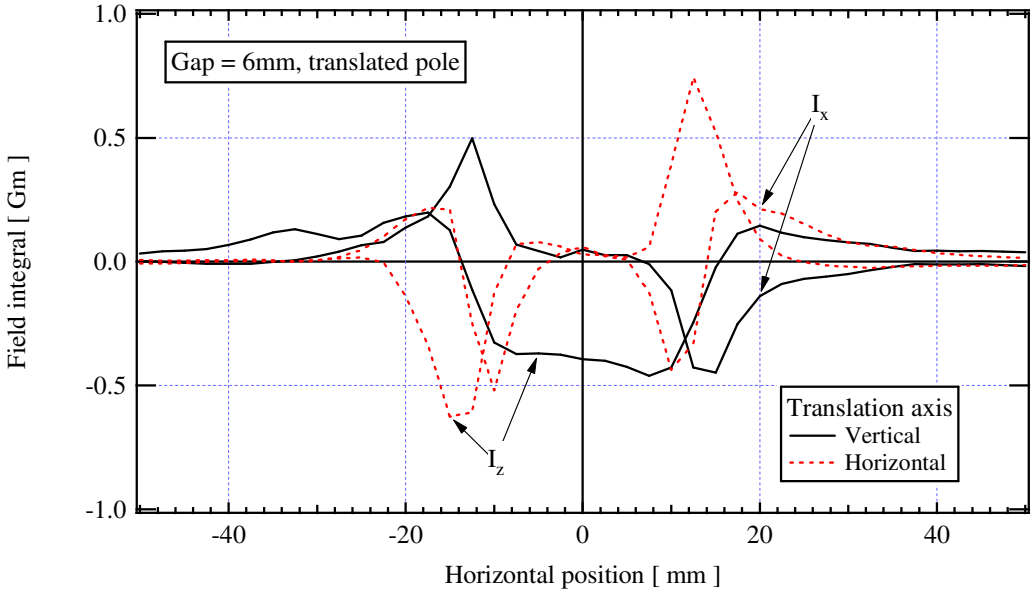

Figure 4.17: Effect of a vertical (black curve) and a horizontal (red dotted curve) pole translation on the HYB18.

Compared with the preceding results it appears that the pole shimming allows a stronger but more localized correction than the translation or rotation of magnets. Magnet shimming cannot be used to correct localized errors and would be limited to correct integral offset for instance. It should be noticed

that whatever would be the envisioned process (magnet or pole shimming), the on axis horizontal field induced is always small. Consequently it is very hard to correct the horizontal dipole.

We have presented the methods to correct the field integral. We will now deal with the angle correction all along the undulator. An efficient way to do this without impacting the total integral value consists of switching 2 magnets within the assembly (process so called swap). Any swap permits to reallocate the defaults within the undulator, and thus changes the angle within it, without impacting the total integral value. In particular, a proper pair of magnets selection corrects the angle offset and locally centres the angle. A swap example is shown in Figure 4.18.

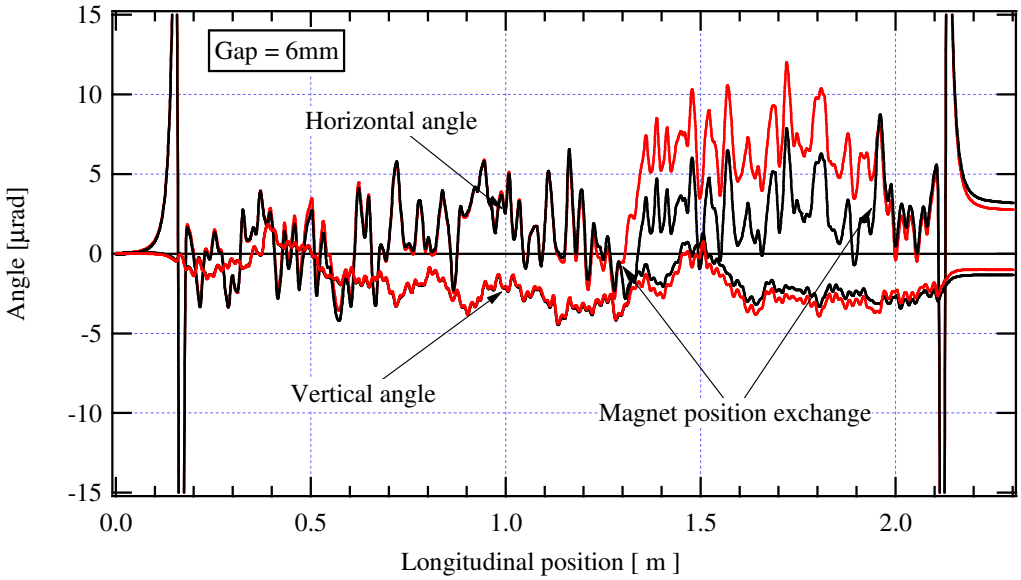

Figure 4.18: Effect of the magnet position exchange on the electron angle. The angle is computed with B2E from the Hall probe bench measurement. The HYB18 gap is closed 6 mm.

A combination of all of these processes has been used in order to correct the field integral and to ensure a null electron angle along the undulator field. More than 90 operations have been necessary to correct the field integral and to straighten electron trajectory. They are listed in Table 4.1. 54 swaps have been performed. The replacement of the magnets was inefficient. Only 2 out of the 430 magnets in the HYB18 have been replaced.

Table 4.1: Main operations performed on magnets and poles to correct HYB18 field integral.

Magnet rotation	Swapping	Magnet translation	Magnet replacement	Pole translation
17	54	9	2	14

The initial and the final field integrals are displayed in Figure 4.19. After corrections we succeeded in correcting the HYB18 on axis field integral. It also presents a smoother variation with the horizontal position around the undulator axis. However off axis, one still observes a large peak field integral.

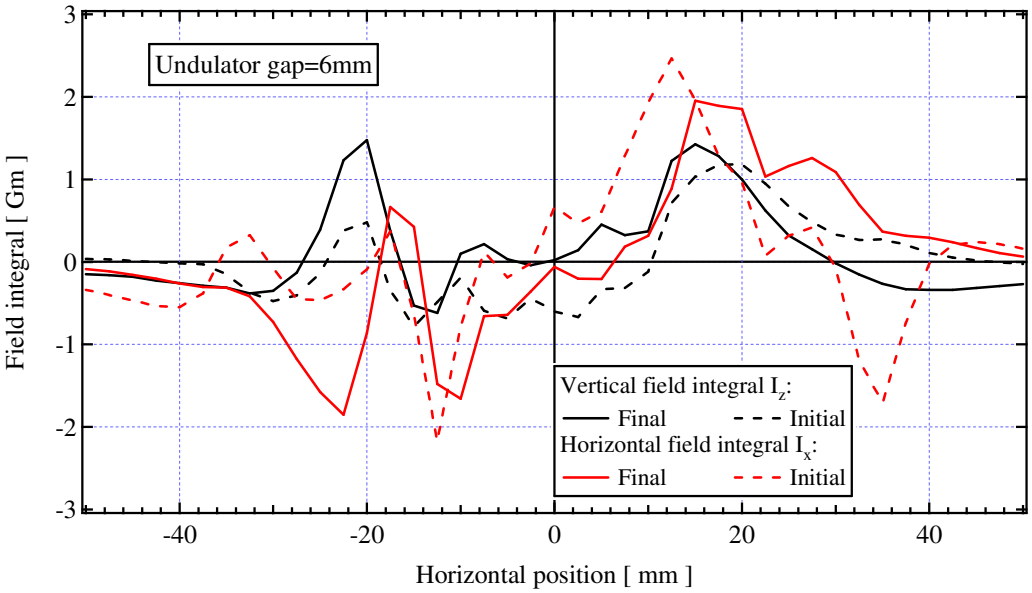

Figure 4.19: Undulator field integrals before (dashed lines) and after (continuous lines) magnetic correction. Vertical (black) and horizontal (red) field integrals are represented. The undulator gap is open at 6 mm.

We correct the undulator field to ensure a low variation of the field integrals with the undulator gap. Figure 4.20 displays the first and the second on axis field integrals as a function of the undulator gap. Because of the electron beam lifetime and the diameter of the vacuum chamber, the gap of an in-vacuum undulator can only be set in this range in a normal operation at the ESRF. The variation of the first horizontal (vertical) field integral and the second horizontal (vertical) field integral is respectively kept below 0.1 Gm (0.2 Gm) and 0.5 Gm^2 (0.2 Gm^2). Except for the second horizontal field integral, all field integrals sit in the limitation specified in Table 2.4.

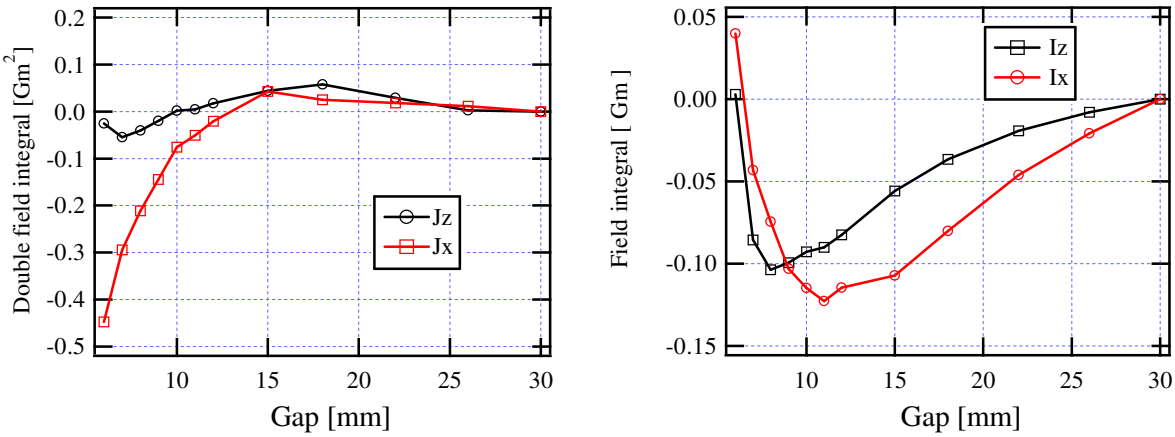

Figure 4.20: First (right plot) and second (left plot) field integral variation with the undulator gap. The field integrals are arbitrary set to 0 as the gap is open at 30 mm.

The correction of the field integral is now completed. The angle of a 6 GeV electron angle in the HYB18 undulator field after correction is displayed in Figure 4.21. The angle is centred around 0 to minimize the angle effect on the phase error. The peak field value is now limited to ± 5 µrad which is above the ESRF standard (±2 µrad). Lowering the electron angle further in the undulator field is difficult. We may assume that the shape of the peaks seen on the electron angle (thin and sharp) comes from the large integral of the magnets themselves, due to strong North/South asymmetry. These angle defaults induce phase error. Whenever the achievable RMS phase error ends up being outside the

specified requirement, a deeper angle correction will then be required. To do so one may move the poles.

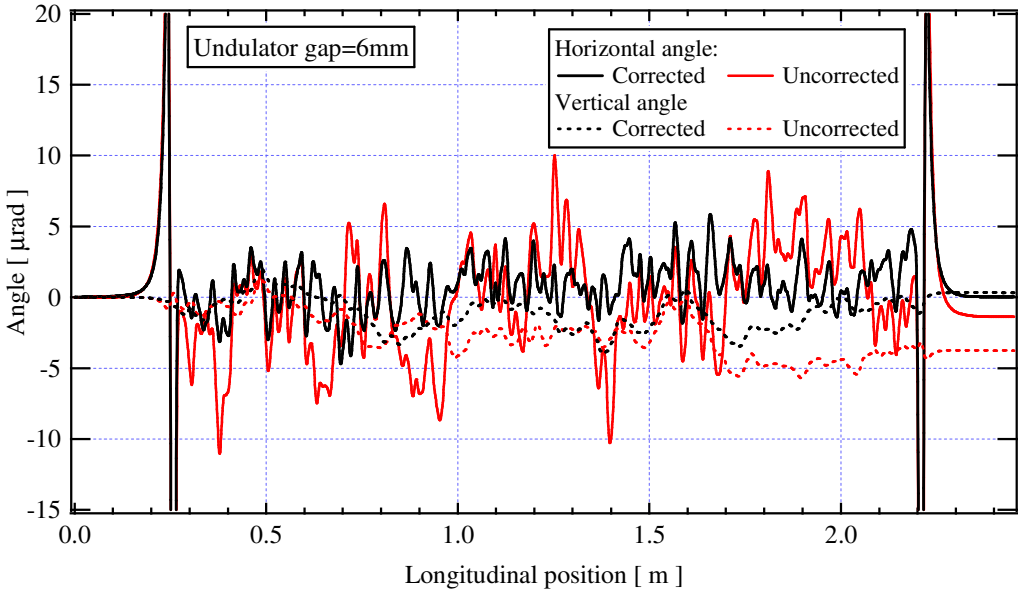

Figure 4.21: Horizontal (continuous black line) and vertical (dashed black line) angles of a 6 GeV electron along the undulator after magnetic correction. The initial vertical (black dashed line) and horizontal (red continuous line) angles are also represented. The angles are computed with B2E from Hall probe bench measurement.

Even though the angle presents some peaks, the electron trajectory is nearly straight, as shown in Figure 4.22. After correction, it is kept below ±2 µm. With such a field integral and angle, we can go to the next stage, correcting the phase error.

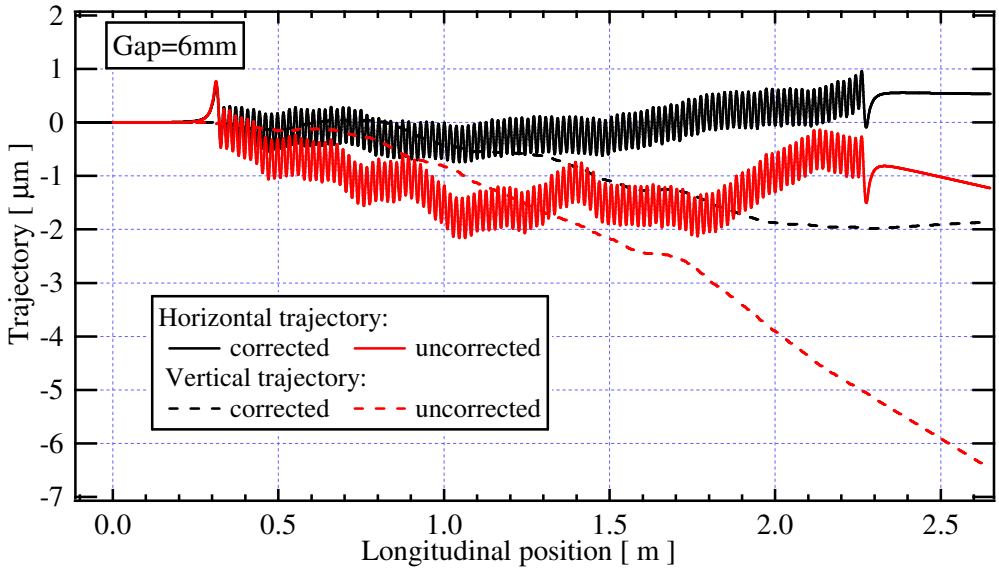

Figure 4.22: 6 GeV horizontal (continuous black line) and vertical (dashed black line) electron trajectories in the corrected undulator field. Horizontal (continuous red line) and vertical (dashed red lines) trajectories in the uncorrected field are displayed. The trajectories are computed with B2E from Hall probe bench measurement. The gap is closed at 6 mm.

4.3.3. RMS Phase error correction

Besides field integral correction, one minimizes the RMS phase error to optimize the HYB18 radiation intensity. The phase shimming consists of increasing or decreasing the on axis peak field locally. This peak field variation delays or advances the electron during its travel and so forth delays or advances locally the electric field emission. A proper tuning of the peak field advance allows the RMS phase error to be minimized.

The RMS phase error is a statistical parameter. One takes advantage of its statistical nature to perform an efficient phase shimming. Each error has a statistical weight on the phase error. Thus one corrects the errors relatively to their weights, correcting in priority the ones having the heaviest weight. Typically these are linked to a gap deformation such as a taper. Thus we first check girder parallelism to make sure we have a constant field within the undulator. In practice, this stage is so important and so closely linked to the nature of the undulator itself (producing a periodic field with constant amplitude) that it is performed at a very early stage, right after mounting the girders on the mechanical support.

To do so, we insert some thin pieces between the mechanical support and the magnetic assembly. These aim at cancelling the gap deformation. A proper tune of size of the pieces is done to obtain parallel girders. The thickness of the thin foil varies from 10 µm to 70 µm. Figure 4.23 represents the phase error before and after the shimming the girders. The large initial phase error arises from the uncorrected parallelism between the girders after the first full assembly. Flattening the gap divides the RMS phase error by 3.

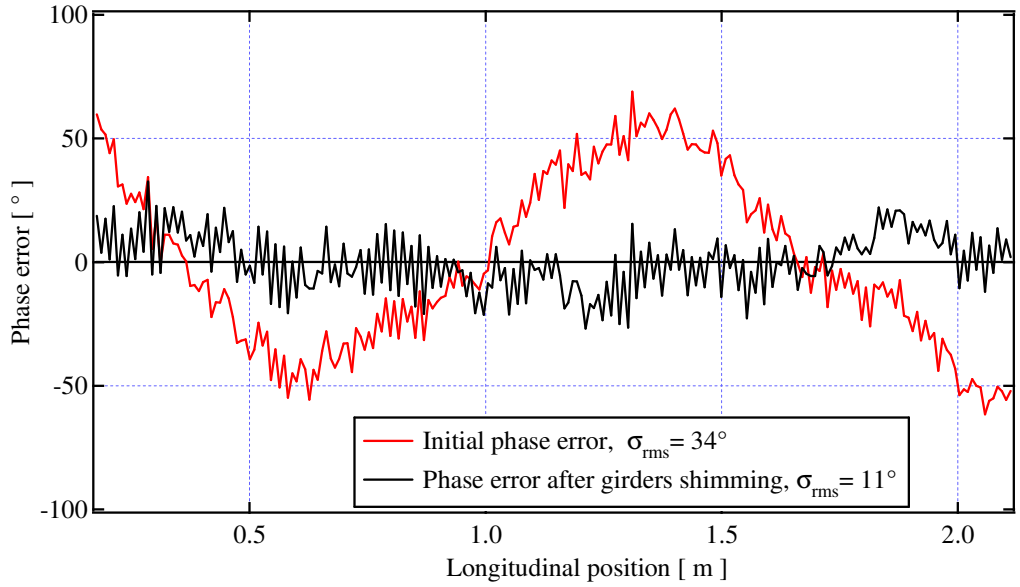

Figure 4.23: Phase error along the undulator before and after the girder shimming. The phase error is computed with B2E from Hall probe bench measurement, the gap is open at 6 mm.

Once we have a good parallelism between girders, the next step in the phase shimming is the correction of the local field errors. This process is actually performed, right after the field integral correction. Local variations are obtained by performing local peak field correction, targeting to lower the phase error. The constraint of this local peak field tuning is to keep the field integral constant. Indeed, a change in the field integral would introduce angle errors in the trajectory, and finally would increase the phase error in the subsequent periods. Therefore, depending on the desired effect, we move up or down two successive poles, vertically and simultaneously; making sure we keep the same proportion for both of them. The easiest way to do so is to displace a M3 assembly since it holds two poles. Figure 4.24 displays an example of two M3 vertical displacements.

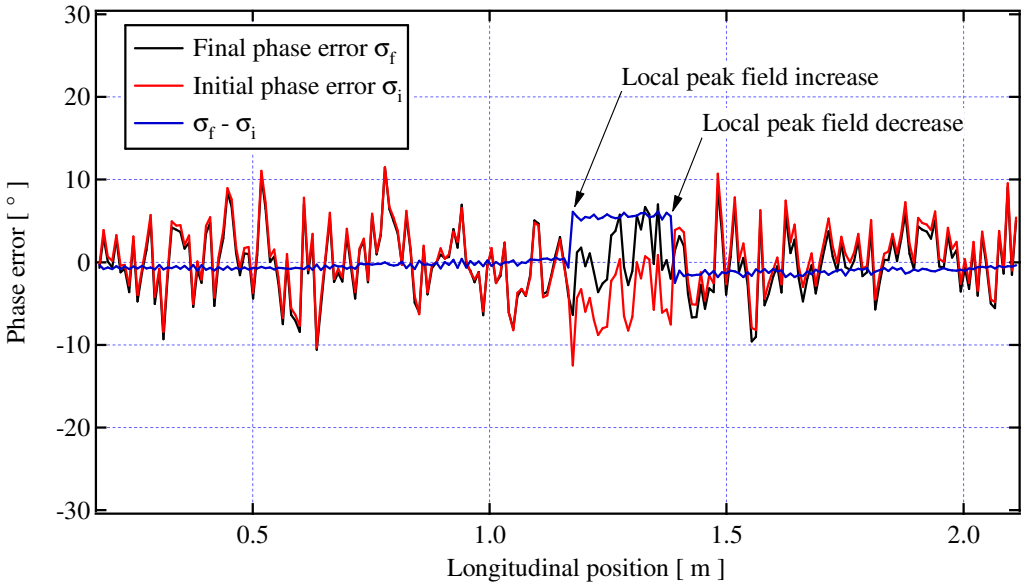

Figure 4.24: Effect on the local peak field variation on the phase error. The phase error is computed with B2E from Hall probe bench measurement, the gap is open at 6 mm.

We repeat such operations on chosen identified errors, regarding to their weight on the total error. In practice, for the HYB18, we move up and down 15 M3 with a vertical displacement varying from 5/100 mm to 2/10 mm. Figure 4.25 compares the final phase error to the initial one. After correction the RMS phase error is 4°.

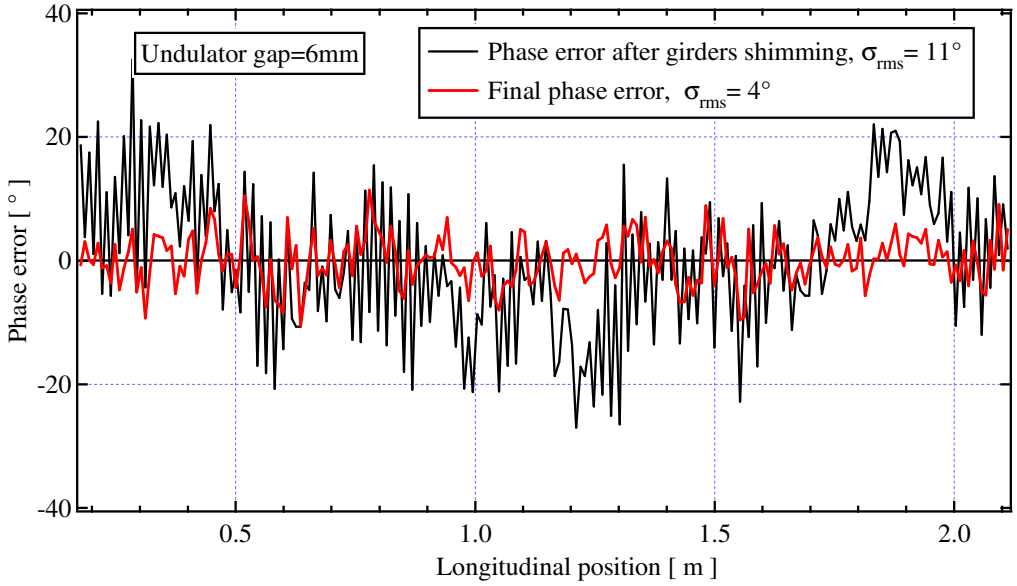

Figure 4.25: Phase error along the undulator before and after correction.

As one varies the undulator gap in order to change the photon energy, one may optimize the undulator radiation at any gap value. This implies keeping the RMS phase error small at any gap value. Figure 4.26 represents the RMS phase error decrease with the gap.

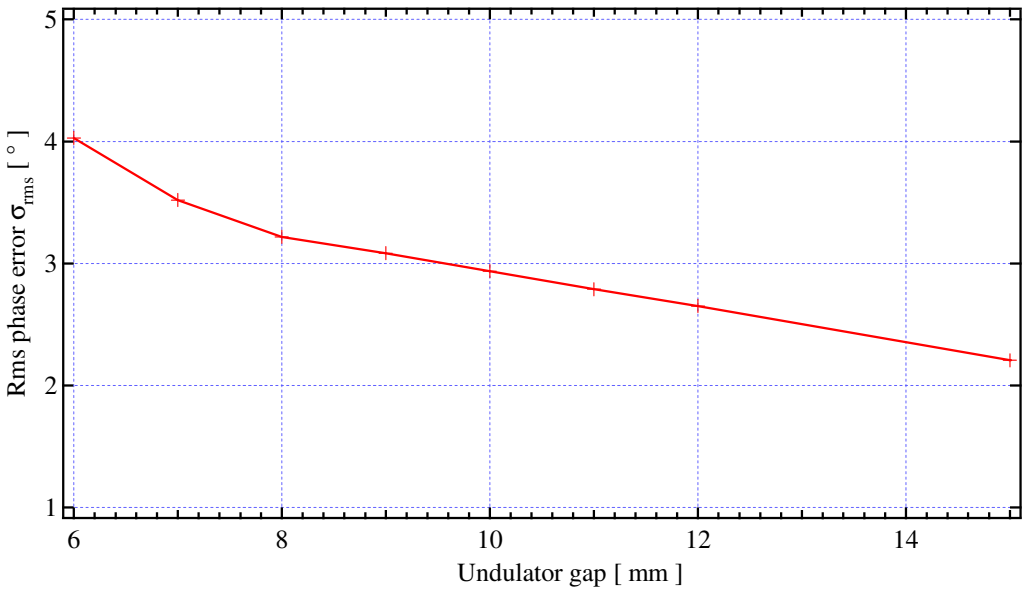

Figure 4.26: Variation of the RMS phase error with the undulator gap.

We succeed in lowering the final RMS error to 4°, as required for final use. However a 4° error is behind the usual ESRF standard RMS phase error, which lies between 2° and 3°. We interpret this larger error as an angle effect which has been detailed in the precedent subsection. Therefore we would have to proceed again to the correction of the integral all along the undulator to lower the angle excursion of electron around ± 2 µrad.

This illustrates the fact that the separation of the field integral and the phase shimming correction processes is a tool which limits the number of parameters we focus on at once and is not a rigid rule. In practice one should be flexible and go back and forth between the two processes in order to optimize the undulator correction.

In the above chapter, we presented the realization of the CPMU magnet assembly, at ambient temperature. The first step was to measure the field integral of the magnets, in order to identify their magnetic error. Their measured field integral is correlated to their North/South asymmetry. Then we used the ESRF methodology to realize HYB18. This first requires assembling girders with the smallest field integral, and then the corrections at the minimum gap. After corrections, the integral field sits almost within the tolerance specifications and the RMS phase error is 4°. The HYB18 measurements presented above were performed at room temperature. The next step is now to analyse the HYB18 performance at cryogenic temperature, which is done in the following chapter.

5. HYB18 performance at cryogenic temperature

We present now the HYB18 performance at cryogenic temperature. This evaluation has two main goals: first, to validate that the CPMU magnetic field increases at cryogenic temperature and secondly to check if the CPMU might be corrected at ambient temperature, just like any standard undulator. To proceed, we first need to develop a magnetic measurement bench compatible with low temperature operation. Then we present the performed magnetic measurements.

5.1. In vacuum measurement bench

The magnetic characterization of the undulator at cryogenic temperature requires the use of a dedicated measuring system. The undulator must be measured in vacuum with residual pressure lower than 10^{-5} mbar in order to avoid heat transfer by convection between the vacuum chamber and the girders. The complete measuring bench must allow local field measurement using Hall probe and field integral measurement as well. The strategy adopted for the design of the measuring bench relies on the following concepts:

- No motorization inside the vacuum. Indeed, the use of electrical motorization in the vacuum requires specific motors. Whenever they are available from manufacturers, these components are in any case very expensive.
- Use of laser interferometer for accurate position recording. The laser beam is transmitted inside the vacuum chamber through quartz windows. The source and the associated electronic part are therefore located outside, allowing better accessibility.
- Fast measurement. Any sensor placed under vacuum, in the vicinity of a cold body progressively cools down due to thermal radiation losses. Hall sensors exhibit a large dependence on temperature because of the Hall sensitivity. Therefore it is crucial to limit the measuring time.

The magnetic measurement bench is not only used to perform magnetic measurement, but also to measure the undulator gap and determine the temperature profile along girders. This original use of the bench is presented hereafter. The measuring bench is shown in Figure 5.1.

The magnetic assembly has also been instrumented with standard cryogenic instrumentation: a heating system, thermocouples and platinum probes. This instrumentation is implemented to find out experimentally the target temperature of the CPMU, as described in Appendix E. We typically use the heating system to set the magnetic assembly temperature from 120 K to 180 K.

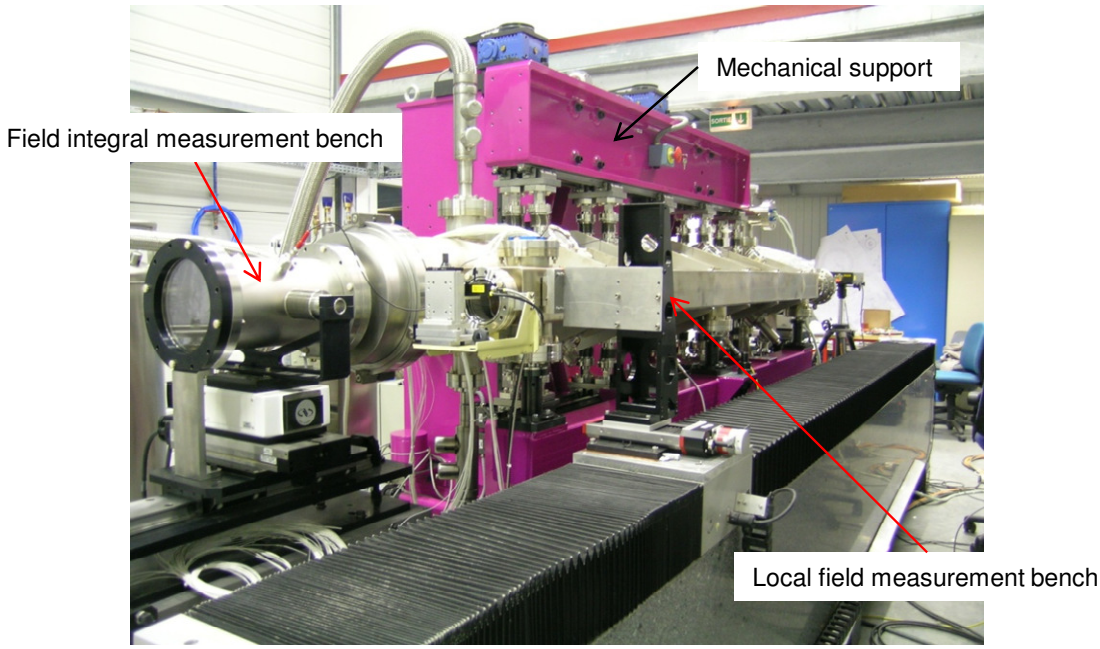

Figure 5.1: In-vacuum field integral and local field measurement bench. Both devices are enclosed in a vacuum chamber.

5.1.1. Field integral bench measurement

Besides field integral measurement, the in-vacuum field integral bench has been designed to perform the gap measurement. The stretch wire geometry has been chosen for this purpose since using a stretch wire is easiest for an in-vacuum operation. Indeed the rotating coil implies both rotation and translation whereas stretch wire only implies translation.

Bench description

Figure 5.2 represents the in-vacuum stretch wire bench. The stretched wire is enclosed in the vacuum chamber together with the magnetic assembly while the return wire is located in air. The translation motors are outside the vacuum chamber for a simple operation. An axis transmits the motor movement to the wire. Bellows limit the wire displacement, the vertical course is then 9 mm and the horizontal course is 35 mm. The weights shown in Figure 5.2 ensure the wire tension.

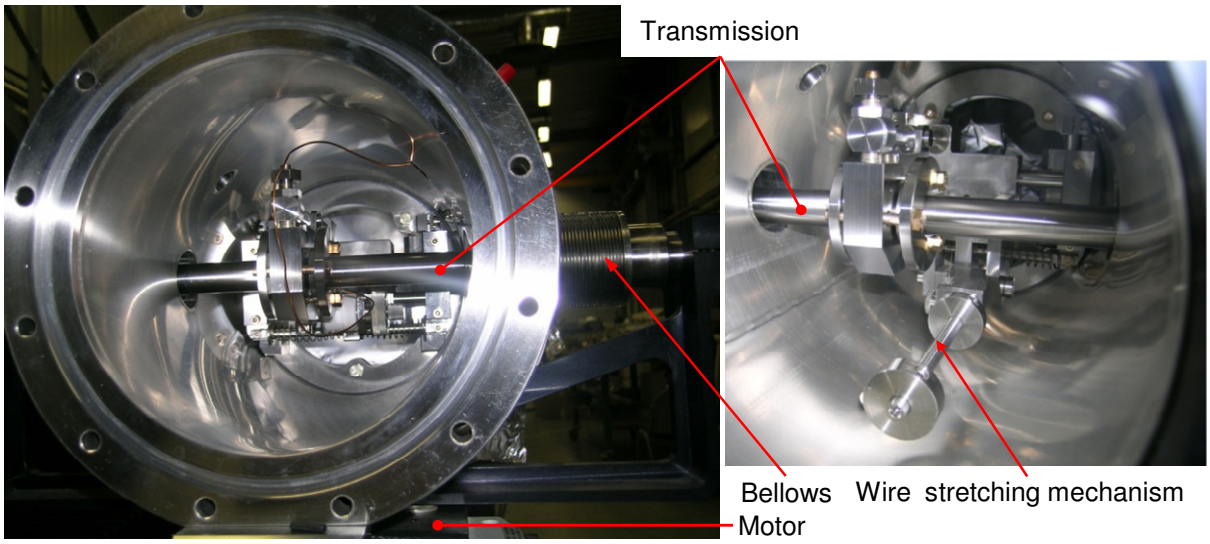

Figure 5.2: Detail of the in-vacuum stretch wire bench.

5.1.2. Local field measurement bench

We use a Hall probe bench to perform local magnetic field measurement since there is nowadays no other mature alternative technology. The bench has been designed to perform "on the fly" magnetic measurement. Actually this has been the critical issue of the in-vacuum magnetic measurement bench realization. The main parameters of the ESRF in-vacuum bench are listed in Table 5.1.

Table 5.1: Parameters of the ESRF in-vacuum Hall probe bench.

Hall probe velocity [mm/s]	≤30
Displacement length [m]	2.75
Reproducibility on the peak field measurement	$1.4\ 10^{-4}$
Reproducibility on the RMS phase error computation [°]	0.03

Hall probe motorization

Figure 5.3 presents schematically the in-vacuum Hall probe bench. It makes "on the fly" magnetic measurement possible just as with the "in-air" Hall probe bench. The Hall probe is enclosed in the vacuum chamber and is fixed on a mobile carriage which is guided along a rail with a ball bearing. We use a simple magnetic transmission between the Hall probe carriage and the motorization located in-air in order to drive the Hall probe carriage along the rail. We use the same motorization as for an in air Hall probe bench. The motorization ensures the Hall probe displacement with a maximum velocity of 30 mm/s over the length of the rail (2.75 m).

To enclose the rail and the Hall probe carriage in the vacuum together with the magnetic assembly, a vacuum chamber dedicated to the in-vacuum bench has been manufactured. The chamber is 3 mm thick and is made of non magnetic stainless steel. The vacuum chamber has been designed with two volumes:

- A large volume where the undulator is enclosed. This volume is similar to standard in-vacuum undulator chamber in order to perform magnetic measurement in a thermal environment similar to the one encountered in normal operation with the standard chamber.
- An additional small volume where the rail and the Hall probe carriage are enclosed.

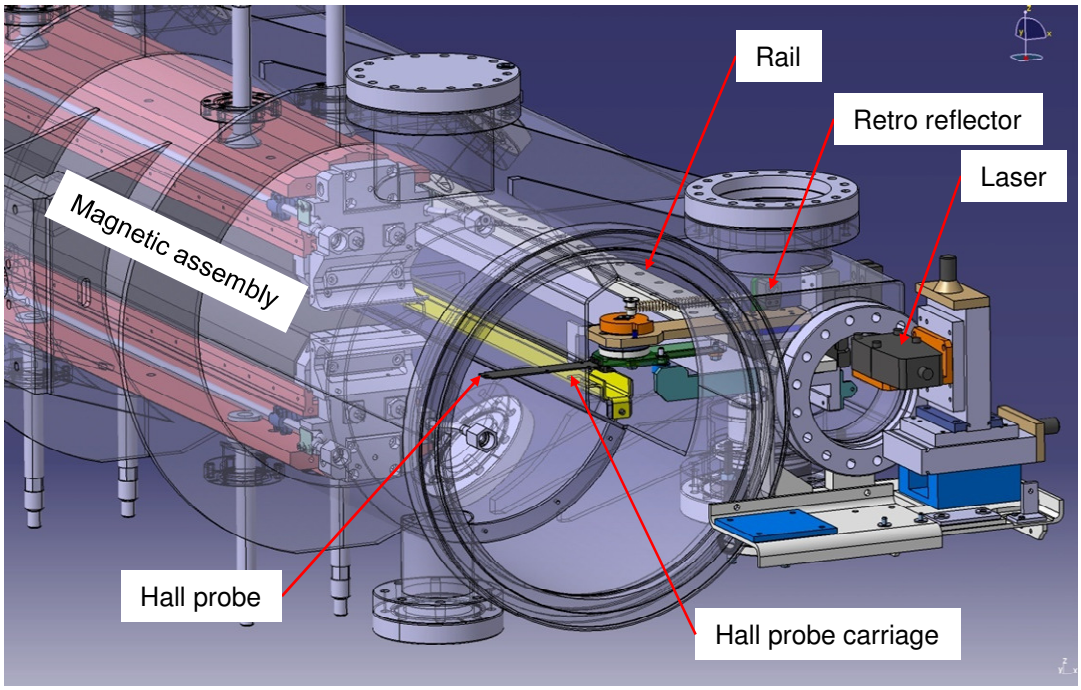

Figure 5.3: Detail of the in-vacuum Hall probe bench.

The motorization is made up of a stepper motor and a 3.8 m long screw. The motor rotates the high precision screw. This rotation displaces an in air chariot on which a magnetic assembly is fixed. A similar magnetic assembly is fixed on the Hall probe carriage enclosed in vacuum in order to get an attractive force between both carriages. The magnetic assembly fixed on carriages is a series of 2 M3 assemblies from an old 23 mm period PPM undulator. The sequence of 2 M3 assemblies fixed on the Hall probe carriage is shown in Figure 5.4.

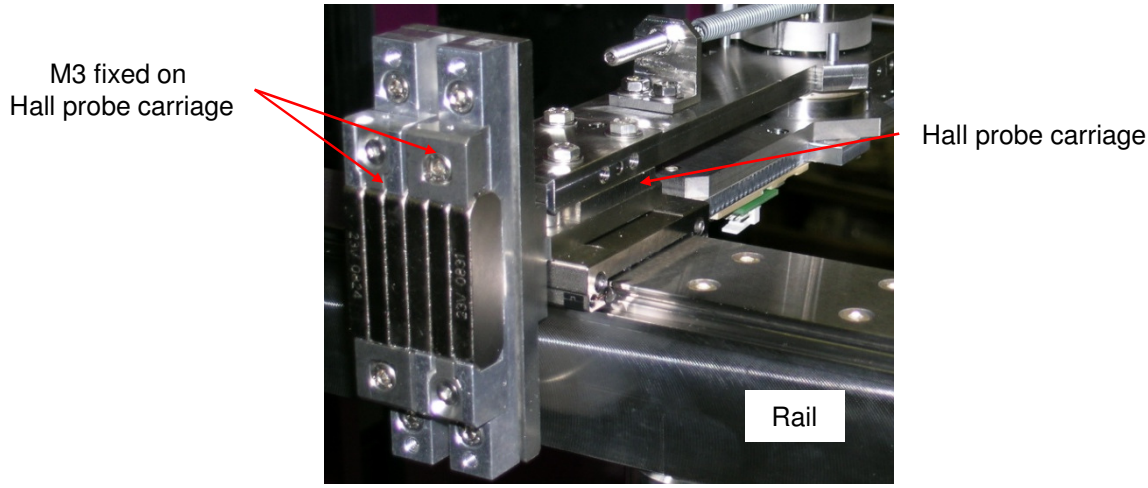

Figure 5.4: Detail of the M3 assemblies fixed on the Hall probe carriage.

The force between the series of M3 assemblies fixed on each carriage is displayed in Figure 5.5. As the carriages face each other, the force between the M3 assemblies is purely horizontal. Because of the non flatness of the vacuum chamber surface, typically, the gap between carriages cannot be reduced further than 10 mm. With such a gap value, the drawing force between the carriages reaches about ten kilograms which is sufficient.

When the carriages are longitudinally shifted, a pulling force appears between the M3 assemblies fixed on each carriage. This pulling force tends to cancel the position shift and drags the Hall probe carriage. As a result, the pulling force drives the Hall probe carriage in an oscillatory motion around

the longitudinal position of the motorized carriage when one moves the motorized carriage. The oscillation amplitude is typically a few microns. With such a small oscillation amplitude, the magnetic assembly is similar to a spring whose strength is 26 N/mm. Because of the friction between the ball bearing and the rail, the oscillatory motion is damped.

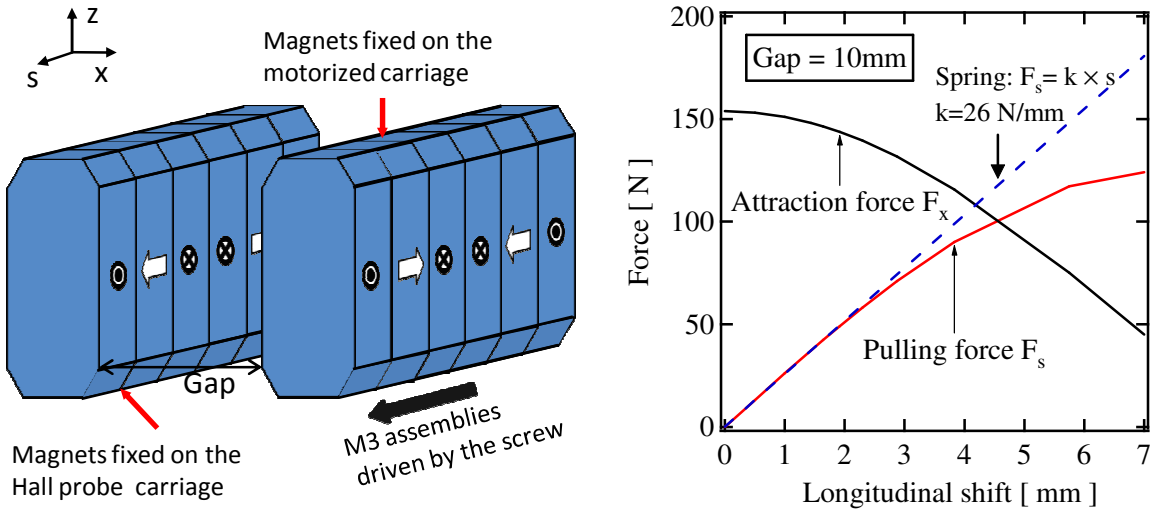

Figure 5.5: Schematic representation of the M3 assemblies fixed on carriages (left plot) and forces (right plot) between M3 assemblies. The gap between M3 assemblies is set at 10 mm. The force computation has been performed with RADIA.

Longitudinal position readings

The transmission between the carriages is not rigid. Consequently the Hall probe carriage might oscillate around the in air carriage fixed on the screw. As a result, reading the position of the in air carriage is not an accurate measurement of the Hall probe position. One then installs a Laser system directly onto the Hall probe carriage.

It has been chosen to use a Michelson interferometer from Renishaw, in order to measure the longitudinal position of the Hall probe carriage. The Michelson interferometer is made of a laser and a retro reflector. The reflector, shown in Figure 5.6, is fixed on the Hall probe carriage. The laser interferometer is presented in Appendix D.

The reflector mirror is located at 27 cm from the Hall sensors. The distance between the reflector and the Hall sensor gives rise to a large lever arm. Consequently, the Hall probe sensor position may differ slightly from the reflector position due to the lever arm and the rail deflection. Finally it is necessary to take into account the rail deflection in order to obtain an accurate measurement of the Hall sensor position.

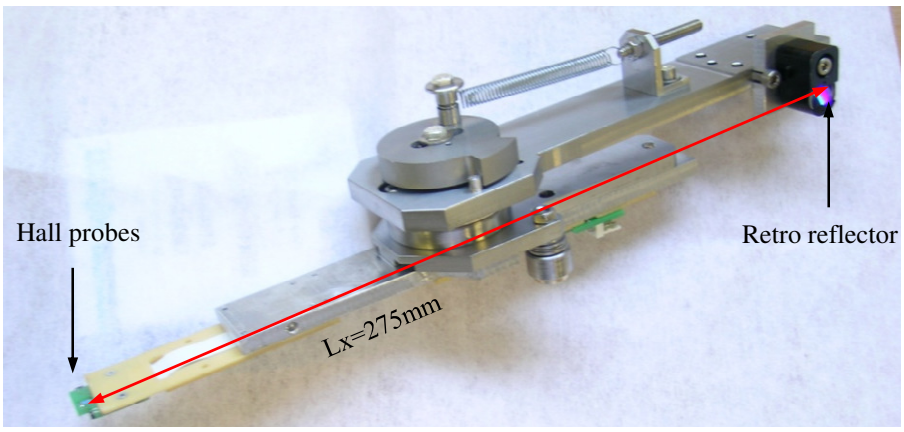

Figure 5.6: Detail of the Hall probe carriage.

Three angles characterize the rail deflection: the yaw θ, the rolling ψ and the pitch φ. The yaw θ is the rotation angle around the vertical axis, the rolling ψ around the horizontal axis and the pitch φ around the longitudinal axis. They are represented in Figure 5.7. The rail deflection causes positioning errors along the three axes so that one would theoretically measure these three angles to recover the Hall probe position properly. However we ignore the small horizontal position errors since we measure the planar undulator field along its axis. Indeed the planar undulator field is independent from the horizontal position around its longitudinal axis.

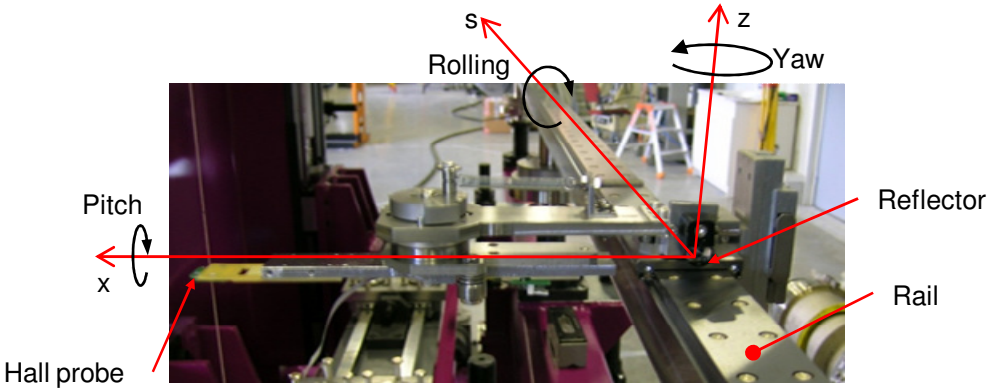

Figure 5.7: The yaw, the pitch and the rolling are the three angles which fully characterize the rail deflection.

In the small angle approximation, the differences between the reflector and the Hall probe positions are related to the rail deflection and the lever as follows:

$$\begin{aligned} ds &= s_{Hall} - s = L_x \cdot \theta(s) \\ dz &= z_{Hall} - z = L_x \cdot \varphi(s) \end{aligned} \tag{5.1}$$

ds and dz are respectively the longitudinal and the vertical position difference between the Hall probe position (z_{Hall}, s_{Hall}) and the reflector position (z, s). The position delay (dz, ds) has been measured with the ML10 interferometer when the Hall probe carriage is moved along the rail. The ML10 laser and the experimental setup are presented in Appendix D. Figure 5.8 presents the position delay (dz, ds) along the rail; dz is also called the vertical straightness.

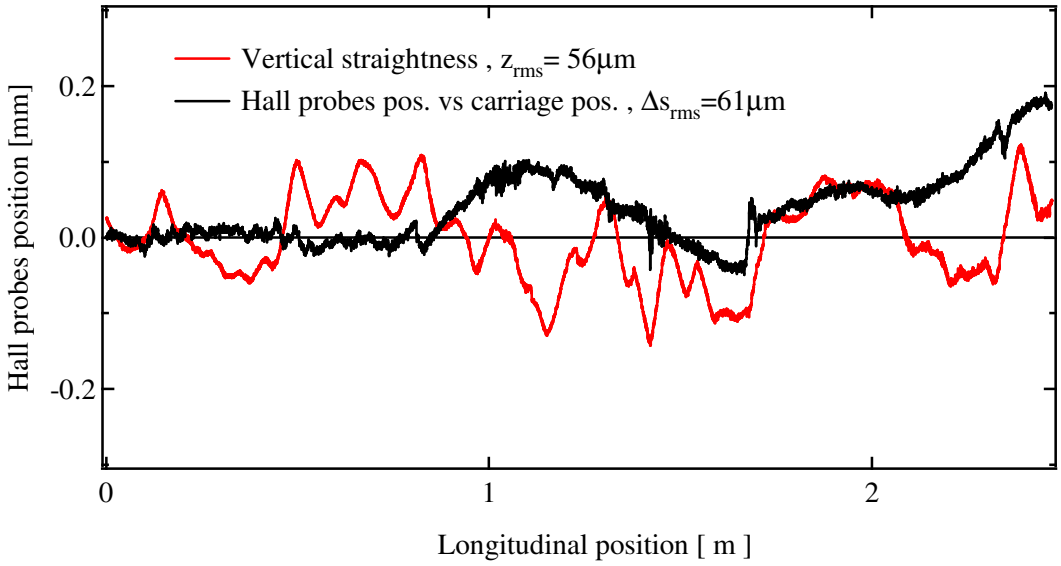

Figure 5.8: Vertical straightness dz and longitudinal delay ds of the Hall sensor along the rail. They have been measured with the ML10 Laser.

The vertical straightness dz and the longitudinal delay ds introduce artificial errors in the measured magnetic field. Because of the vertical straightness, one measures the off axis magnetic field. One relates the measured field B_m to the on axis field B_o as follows:

$$B_m = B_o\,(\mathrm{s})\cosh\left(\frac{2\pi a}{\lambda_0}\,dz(s)\right) \tag{5.2}$$

Where a is a coefficient which depends on the undulator period λ_0, on the gap and on the materials. In practice one uses RADIA to determine a numerically. The off axis magnetic field is larger than the on axis field. The longitudinal delay ds destroys the field periodicity. As the retro reflector is at the position s, the Hall sensor is at the position $s + ds$. The measured field B_m becomes:

$$B_m(s) = B_o(s + ds) \tag{5.3}$$

Figure 5.9 compares the different phase errors as the magnetic field of a perfect undulator is deformed according to equation (5.2) and (5.3). The longitudinal delay ds causes clearly stronger magnetic errors on the measured field than the vertical straightness since it increases the RMS phase error by more than 2° while the vertical straightness keeps it below 0.5°. Thus the vertical straightness is ignored during the measurement.

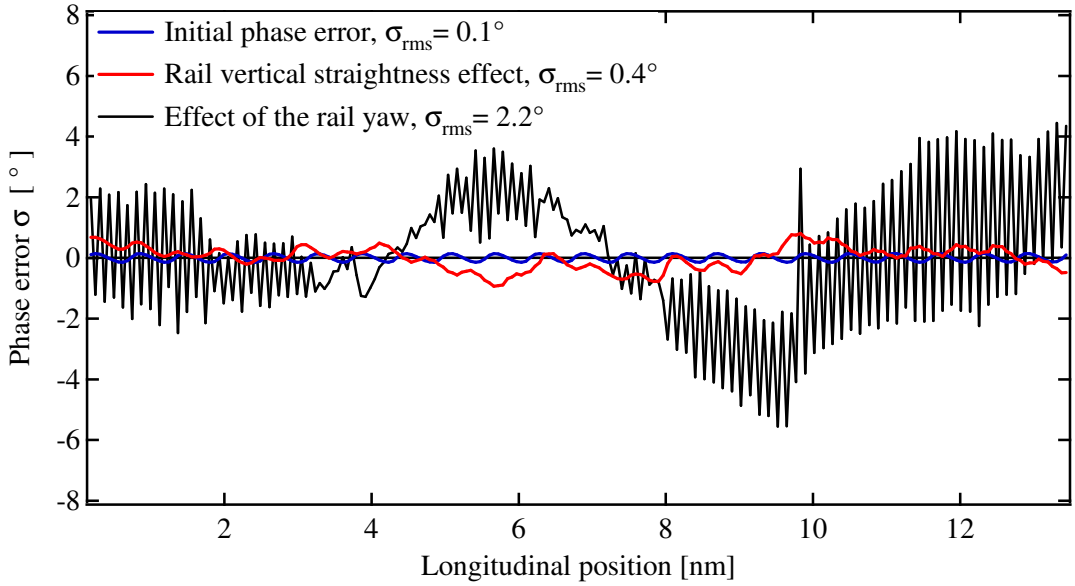

Figure 5.9: Impact of the rail vertical straightness and longitudinal position errors on the phase error. The phase errors are computed with B2E assuming a 2 m long undulator with $\lambda_0 = 18\,mm$, $N = 108, B_0 = 0.82\,T, a = 1.13$.

Hall sensor temperature

The Hall probe is calibrated in air and at room temperature whereas in the in-vacuum bench, it is enclosed in the vacuum chamber, in vicinity to the magnetic assembly at cryogenic temperature. Thus the Hall probe experiences a thermal environment different to the one where it has been calibrated. In addition during local field measurements, the Hall probe is positioned only a few mm away from the surface of the magnets cooled at cryogenic temperature. Heat transfer occurs between the Hall probe and the magnetic assembly during the local magnetic field measurement. As a result the Hall probe temperature decreases during a measurement.

It is known that the voltage V_{Hall} measured on the extremities of the Hall sensors depends on the temperature. For instance, the Hall sensor used at the ESRF is the GH700 from the manufacturer BELL. It holds a theoretical Hall voltage coefficient variation of 0.07 %/C. This value is given from

263 K to 350 K with a 1 mA control current. Consequently is it necessary to determine the Hall probe temperature in order to:

- Ensure that the temperature of the Hall probe enclosed in the vacuum chamber is close to the one at which the calibration is done.
- Determine the variation of the Hall voltage coefficient during an "on the fly" measurement.

The Hall probe is equipped with platinum probe (PT100) as detailed in Figure 5.10; it is an absolute thermal probe the precision of which is 0.1 K. As the Hall probe is enclosed in the vacuum chamber, the PT100 and the Hall probe experience different thermal budgets and therefore the Hall probe temperature differs noticeably from the PT100 one. As a result the PT100 cannot be used to measure the Hall probe temperature during an "on the fly" magnetic measurement.

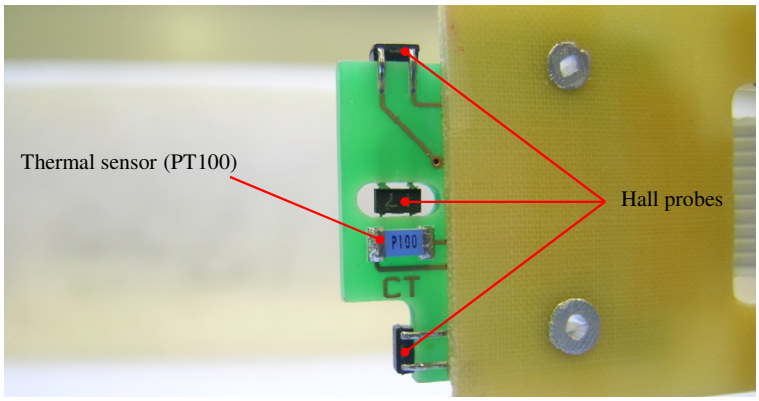

Figure 5.10: Detail of the ESRF Hall probe. It is made of 3 Hall sensors and one PT100. The upper Hall sensor measures the magnetic field along the longitudinal axis, the middle one the vertical field component and the lower one the horizontal component.

In fact the PT100 is used to calibrate the Hall probe resistance without control current. The calibration is carried out in a thermally controlled atmosphere, basically a furnace. We use the furnace to monitor the Hall probe temperatures and one simply measures the Hall probe resistance at different temperatures measured with the PT100. An experimental linear law has been determined in the temperature range 15 °C to 50 °C:

$$R(T) = a + bT \tag{5.4}$$

With:

$$a = 2040 \pm 0.3\ \Omega \qquad b = 3.745 \pm 0.009\ \Omega/°\mathrm{C} \tag{5.5}$$

Once the Hall probe is enclosed in the vacuum chamber, the measurement of the Hall probe resistance determines its internal temperature. Figure 5.11 represents the Hall voltage variation with time as one brings the Hall probe to a fixed position within the undulator gap. The Hall probe temperature decreases from 38 °C to 35 °C in 80 s. As a comparison, one measures a resistance of 2190 Ω on the standard Hall probe bench in the ID laboratory. This resistance corresponds to an internal temperature of 40 °C. Thus the Hall probe enclosed in the vacuum chamber is at a similar temperature as in air. The vicinity of the magnetic assembly causes a linear drift of the Hall voltage during local field measurement.

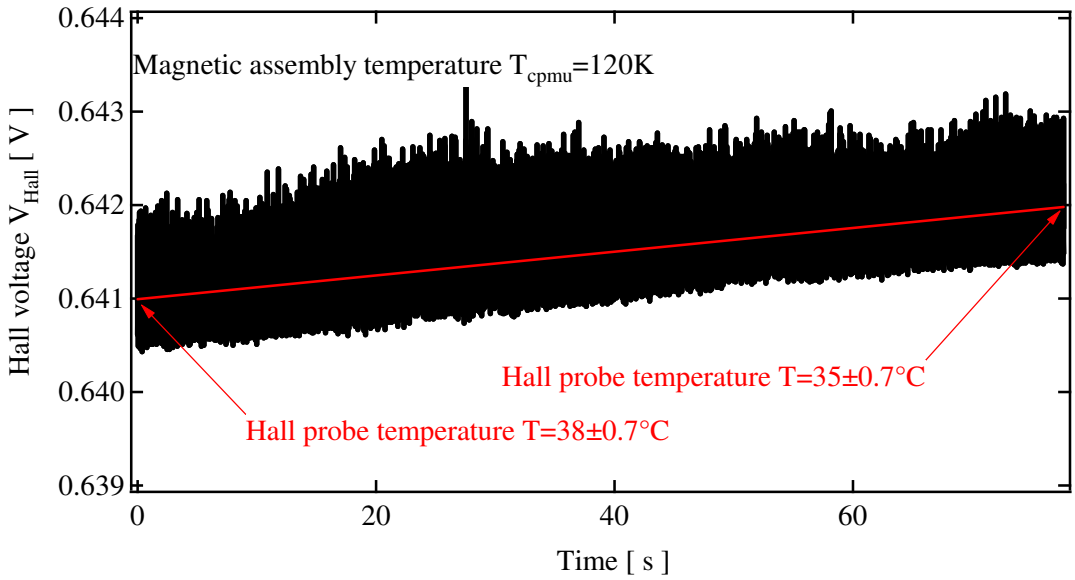

Figure 5.11: Drift of the Hall voltage with the temperature. The Hall probe is enclosed in the vacuum chamber. The Hall probe is kept out of the magnetic assembly gap and is suddenly brought to a fixed position within the undulator gap. One then records the Hall voltage drift. The Hall probe control current is 5 mA and the gap is closed at 6 mm.

Each time we perform an "on the fly" measurement, one records the Hall probe resistance as it enters and leaves the undulator gap. One applies then a linear correction on the measured Hall voltages. Similarly to Figure 5.11, one typically observes a 3 °C temperature decrease during an "on the fly" measurement.

We have studied the impact of the temperature on the Hall probe. We will now analyze the thermo-mechanical effect on the undulator.

5.1.3. Thermal contraction diagnose system

At cryogenic temperature, the CPMU experiences a thermo-mechanical contraction so that it shortens the undulator period and opens the magnetic gap. One uses the in-vacuum bench in order to measure these two contractions. The in-vacuum bench then becomes an original diagnostic system to measure the CPMU temperature and the gap opening at low temperature. This unusual use of the in-vacuum bench is presented hereafter.

Vertical contraction and gap monitoring

As the magnetic assembly is at cryogenic temperature, it experiences a thermo-mechanical contraction. One interprets the contraction in the vertical direction as a magnetic gap opening. This opening depends on the magnetic assembly temperature. Unfortunately it is not measurable with the standard gap monitoring, a special device is therefore necessary.

It has been decided to take advantage of the stretch wire bench, in order to measure the undulator gap. The principle of the gap measurement with the wire is quite simple; it is schematically described in Figure 3.38. One reads the Ohm resistance between the wire and probes fixed on each girder. When there is a contact between the wire and a probe, the resistance is null, otherwise the resistance is infinite. Finally in order to measure a gap, one simply measures the positions at which the wire is in contact with probes installed on the upper and lower girder.

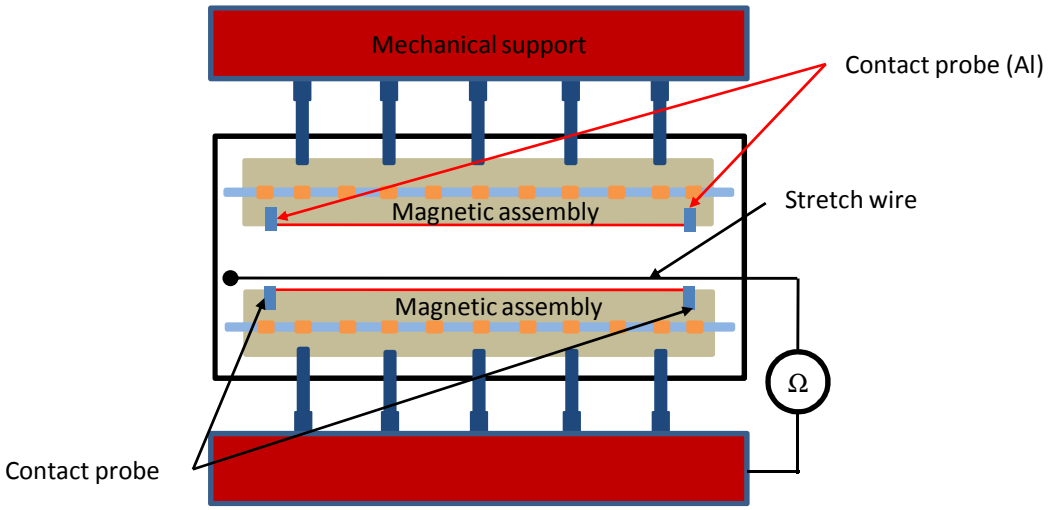

Figure 5.12: Location of the contact probes used to measure the gap.

A contact probe is displayed in Figure 5.13. The contact probes are made of Aluminium and are fixed on girders and therefore are also cooled at cryogenic temperature. Consequently they also experience a thermal contraction. Since poles and probes are made of different materials, they experience different thermal contractions. One easily deduces from Figure 5.13 that the differential thermal contraction between the Aluminium probes and poles, δl is:

$$\delta l = L_{zp}\left(\left(\frac{\Delta l}{l}\right)_{Fe} - \left(\frac{\Delta l}{l}\right)_{Al}\right) \tag{5.6}$$

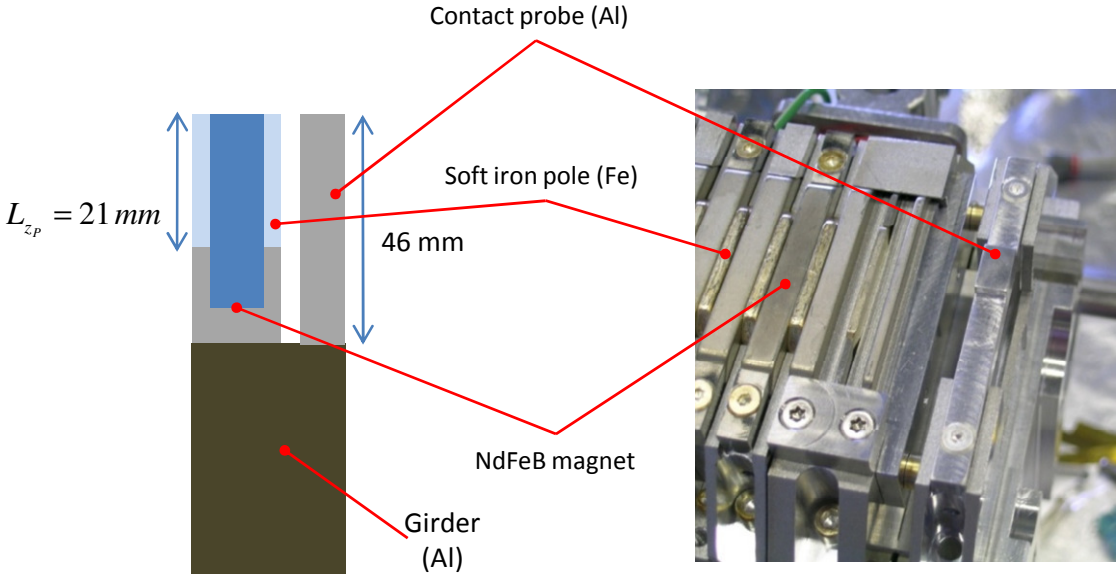

Figure 5.13: Detail of a contact probe used to measure the gap.

The amplitude of the thermal linear expansion of Aluminium is larger that of soft Iron and thus the probes contract more than the poles do. Finally at low temperature one measures with the probes, a larger distance than the gap defined by poles. Figure 5.14 represents the differential thermal contraction between the Aluminium probes and poles as a function of the magnetic assembly temperature. The differential thermal contraction increases as the temperature lowers. At 150 K the differential thermal contraction is as high as 60 µm, it is not negligible. The gap measured with the Aluminium probes is then corrected in order to take into account the differential contraction between Iron and Aluminium.

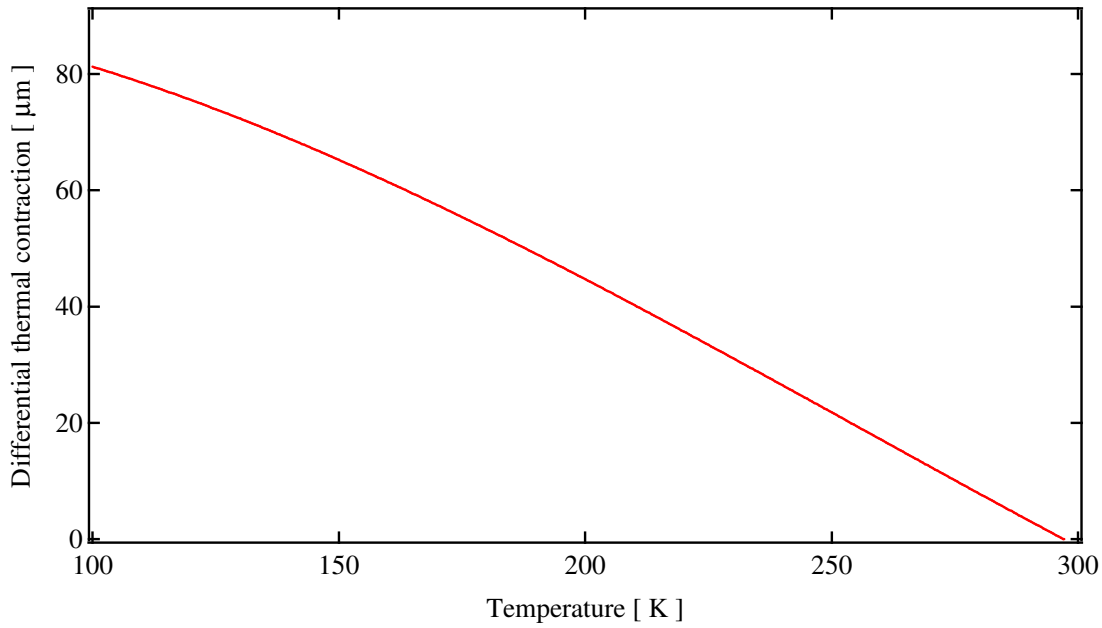

Figure 5.14: Differential contraction between Aluminium probes and the soft Iron poles computed from equation (5.6).

At cryogenic temperature, we use the calculated curve of the gap opening in order to take into account the thermal expansion. We simply measure with the stretch wire, the gap at different temperatures in order to validate the calculated curve. Figure 3.41 compares the calculated gap opening to the measured ones. The calculated curve fits the measured values quite well. This validates the use of the calculated curve to properly set the gap at cryogenic temperature.

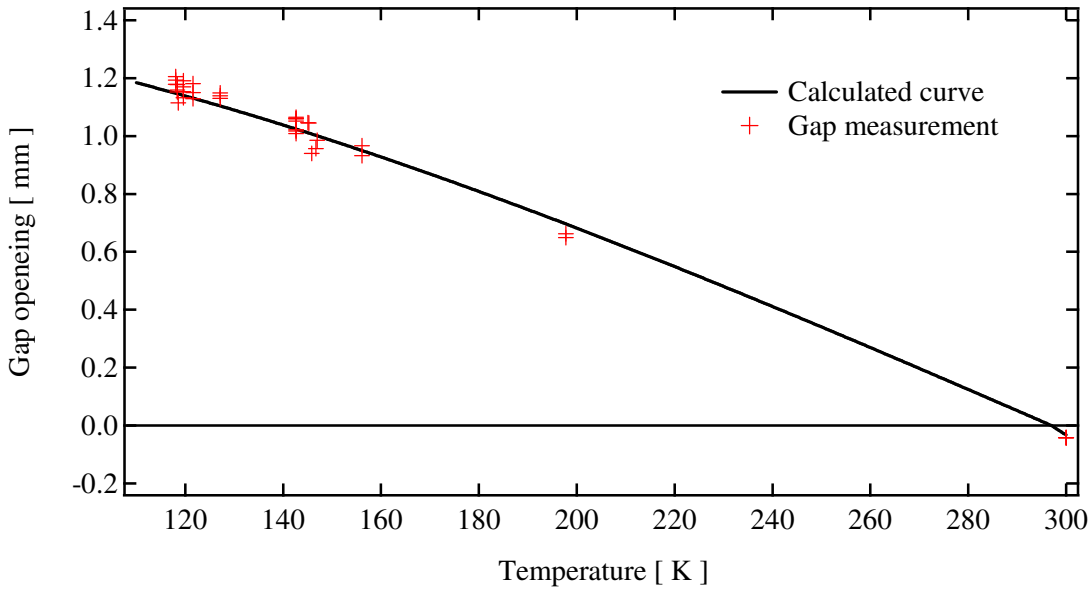

Figure 5.15: Comparison of the calculated gap opening (black line) to measured values (red cross).

Longitudinal contraction and temperature measurement

Besides the gap opening, the thermo-mechanical contraction also shortens the undulator length. Naturally the undulator shortening leads to the contraction of the magnetic field period. Indeed we use this contraction to determine the temperature along girders. The magnetic field period contraction is simply deduced from the Hall probe bench measurement.

The magnetic field period λ_0 shortens as one cools the magnetic assembly at the cryogenic temperature T. We define a thermal period expansion $\frac{\Delta\lambda_0}{\lambda_0}$ in a similar way to the thermal linear expansion $\frac{\Delta l}{l}$, as follows:

$$\frac{\Delta\lambda_0}{\lambda_0}(T) = \frac{\lambda_0(T) - \lambda_0(T = 293K)}{\lambda_0(T = 293K)} \tag{5.7}$$

$\lambda_0(T)$ is the magnetic field period at the temperature T. $\lambda_0(T)$ is measured with the Hall probe bench and thus one deduces from local field measurement the coefficient $\frac{\Delta\lambda_0}{\lambda_0}$.

We concluded in section 3.4.2 that the thermal contraction of Aluminium girders drives the undulator period shortening. Thus we identify the field period contraction $\frac{\Delta\lambda_0}{\lambda_0}(T)$ to the Aluminium thermal linear expansion $\frac{\Delta l}{l}(T)$, one has then:

$$\frac{\Delta\lambda_0}{\lambda_0}(T) = \frac{\Delta l}{l}(T) \tag{5.8}$$

In other words, the determination of $\frac{\Delta\lambda_0}{\lambda_0}$ with the Hall probe bench is a direct measurement of the Aluminium thermal linear expansion $\frac{\Delta l}{l}$. Finally we identify from the theoretical thermal linear expansion $\frac{\Delta l}{l}$, the temperature T at which one would have the measured value $\frac{\Delta\lambda_0}{\lambda_0}$. The Aluminium thermal linear expansion is displayed in Figure 3.39. We will now present the determination of $\frac{\Delta\lambda_0}{\lambda_0}$ from the Hall probe bench measurement.

Figure 5.16 shows the undulator field measured as the magnetic assembly is at ambient temperature and has been cooled at 150 K. The field period shortening appears clearly on the local field measurement. One observes on Figure 5.16 that the position s_f of the peak field at the middle of the undulator field is fixed whatever the magnetic assembly temperature. It is due to the rigid fixation of the girders to the mechanical support at this position. Thermal contraction shrinks the magnetic assembly towards the position s_f.

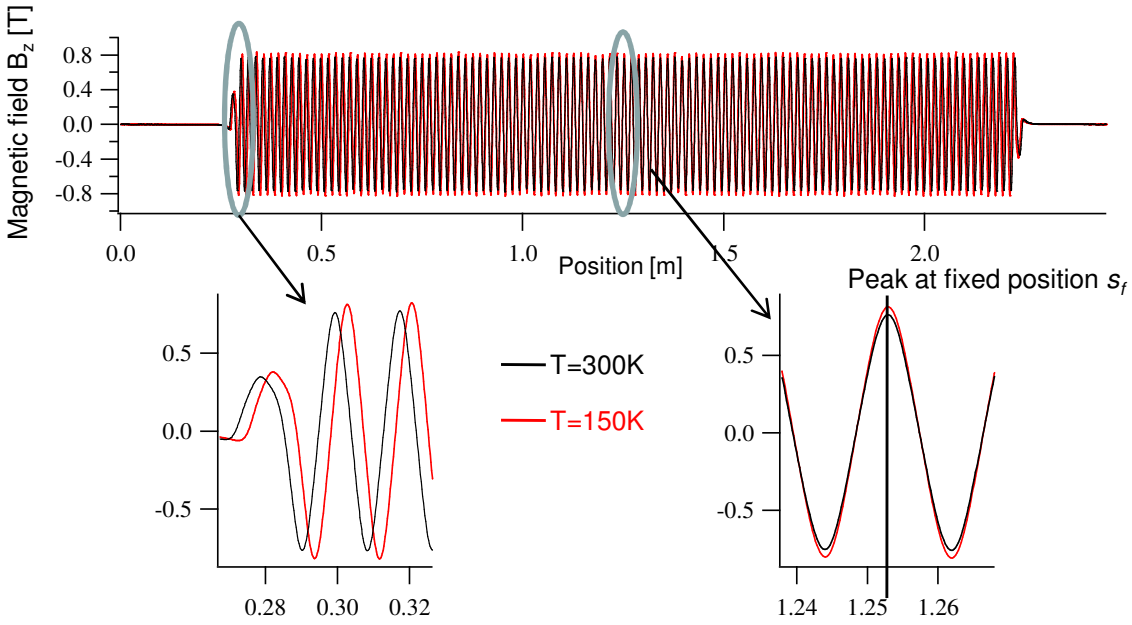

Figure 5.16: Undulator magnetic field measured at 150 K (red) and 300 K (black) with the in-vacuum Hall probe bench. The undulator gap is 6 mm.

We note $s_j(T)$ the j^{th} peak field position of the magnetic field measured at the cryogenic temperature T and s_j^0 its initial position as the magnetic field is at ambient temperature. The longitudinal contraction dl_j, that the j^{th} peak field experiences at the temperature T, is related to $\frac{\Delta\lambda_0}{\lambda_0}$ the thermal period expansion as follows:

$$dl_j = s_j(T) - s_j^0 = \frac{\Delta\lambda_0}{\lambda_0}(T)\left(s_j^0 - s_f\right) \tag{5.9}$$

Finally the thermal period expansion is simply:

$$\frac{\Delta\lambda_0}{\lambda_0}(T) = \frac{dl_j}{ds_j^0} \tag{5.10}$$

Figure 5.17 displays the longitudinal contraction dl_j at 150 K with respect to the initial position s_j^0. Assuming a linear fit, the thermal period expansion $\frac{\Delta\lambda_0}{\lambda_0}$ equals -3.54 10^{-3} ± 3 10^{-6}. If we identify the thermal period expansion to the Aluminium thermal expansion, we deduce a temperature on girders of 117 K. This is close to the temperature of 118 K measured by the PT100 installed on the girders.

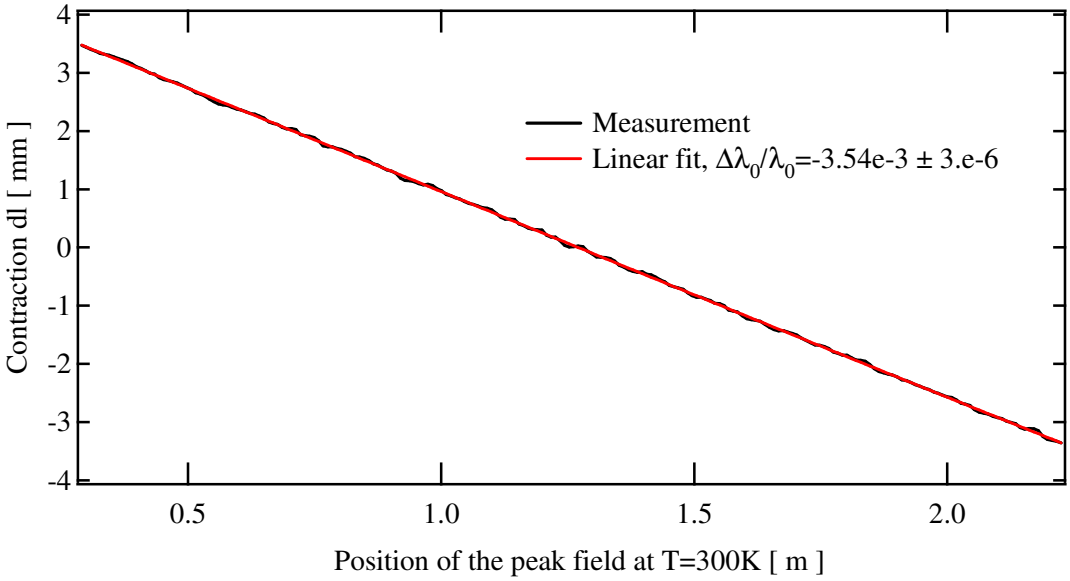

Figure 5.17: Longitudinal contraction of magnetic field as the temperature measured with thermal sensor (PT100) is 118 K. It is computed with B2E from the local field measurement.

One may fit the longitudinal contraction dl_j with a polynomial function in order to take into account non linearity:

$$dl_j = \sum_{i=0}^{n} a_i\left(s_j^0 - s_f\right)^i \tag{5.11}$$

A temperature gradient would cause such non linearity. According to equation (5.10), one simply derives the polynomial function to build the thermal period expansion $\frac{\Delta\lambda_0}{\lambda_0}(s_j)$ along girders. Finally one determines a temperature distribution $T(s_j)$, from the identification of $\frac{\Delta\lambda_0}{\lambda_0}(s_j)$ to the thermal linear expansion $\frac{\Delta l}{l}$.

A temperature gradient also affects the gap locally and the magnetic properties of the magnets and therefore causes a peak field variation along the undulator. We detailed in section 3.4.3 a simple model which correlates the peak field variation to the temperature gradient. The information provided by the peak field variation is independent from the thermal period expansion $\frac{\Delta\lambda_0}{\lambda_0}$. Both measurements of the peak field variations can be compared.

Figure 5.18 presents a temperature profile computed from the thermal linear expansion distribution. The contraction is fitted with a polynomial function whose order is n = 3, it provides a parabolic temperature profile. We observe on the peak field variation a similar parabolic shape. In addition below 150 K, the peak field increases with the temperature according to the RADIA model described in section 3.4.3. We observe on the graph that the field increases with the temperature in accordance with the RADIA model. This allows us to conclude that the temperature profile is well correlated with the peak field variation.

Additionally we also report in Figure 5.18, the temperatures measured with PT100 fixed on the magnetic assembly. The PT100 measurements correspond quite well to the temperature profile computed from magnetic measurements.

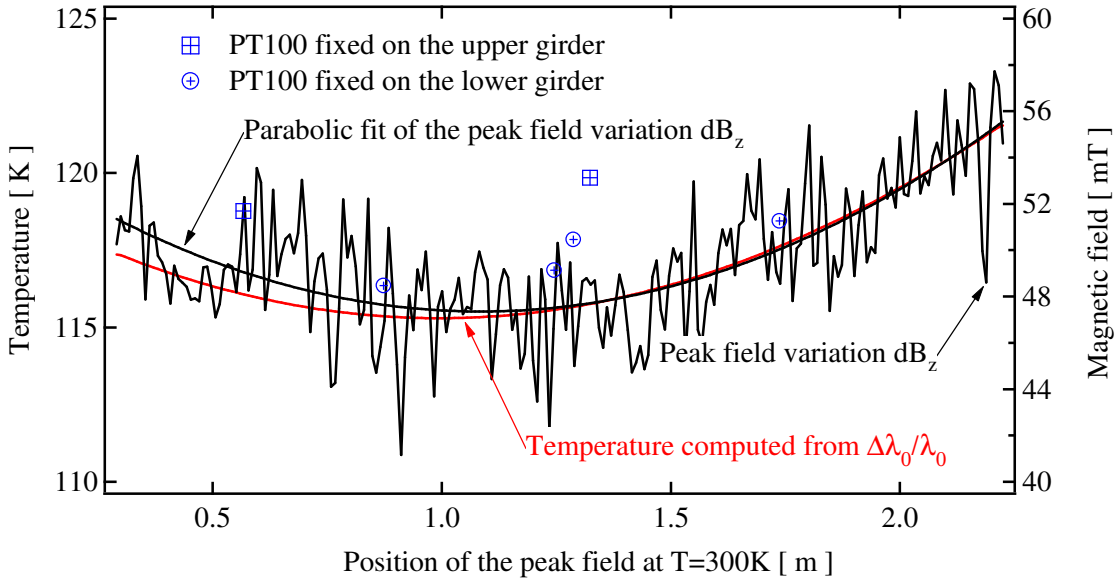

Figure 5.18: Temperature profile (red line) computed from the contraction of the magnetic field and measured peak field variation (black line).

As a conclusion we use the Hall probe bench as a convenient thermal diagnostic system. It doesn't require additional instrumentation on the magnetic assembly. Performing a similar measurement with standard thermal instrumentation involves the installation of a large number of thermal sensors.

5.2. HYB18 measurement at cryogenic temperature

We present below some measurements performed in July 2007. The temperature cycle performed by the magnetic assembly is first discussed. Then we review the magnetic measurements done at low temperature. Both field integrals and local field measurements are presented.

5.2.1. HYB18 cooling

The magnetic assembly was cooled from the 2th to the 15th of July. A total of 64 spacers were fixed between the cooling pipes and girders to cool the magnetic assembly at 120 K. The magnetic assembly temperature was cycled between 120 K and ambient temperature in order to determine the optimal

temperature. We present hereafter the temperature cycle performed by the magnetic assembly. The temperature gradient observed along the girders, is also discussed.

Temperature cycle

The temperature variation measured with a PT100 fixed on the lower girder is displayed in Figure 5.19. Initially the cooling system and the magnetic assembly are at ambient temperature. During the first hours of cooling, liquid nitrogen at 77 K is used to fill the sub cooler and the inner loop. At this stage the sub cooler bath can't maintain the nitrogen circulating in the inner loop in a liquid phase. Since the gaseous nitrogen may damage the LN_2 pump, the inner loop is kept open during the first hours and the pump operates at a low frequency, typically below 25 Hz. As soon as the LN_2 in the inner loop stays in a liquid phase, the inner loop is closed and the pump frequency is increased up to 50 Hz.

After 2 days, the magnetic assembly reaches its thermal steady state. The temperature measured on PT100 is 117 K. One turns on the heating system in order to increase the magnetic assembly temperature up to 150 K. A current of several amperes in the thermofoils is necessary to heat the undulator up to 150 K. Finally to warm the magnetic assembly from cryogenic temperature to ambient temperature, we simply stop the nitrogen circulation throughout the inner loop and open the inner loop to avoid pressure increase. More than 3 days are needed to warm the magnetic assembly at ambient temperature.

The thermal time constant, which drives the thermal transient regime, exceeds several hours while "on the fly" magnetic measurement takes less than 3 minutes. Consequently one may consider the temperature to be constant during any "on the fly" magnetic measurement.

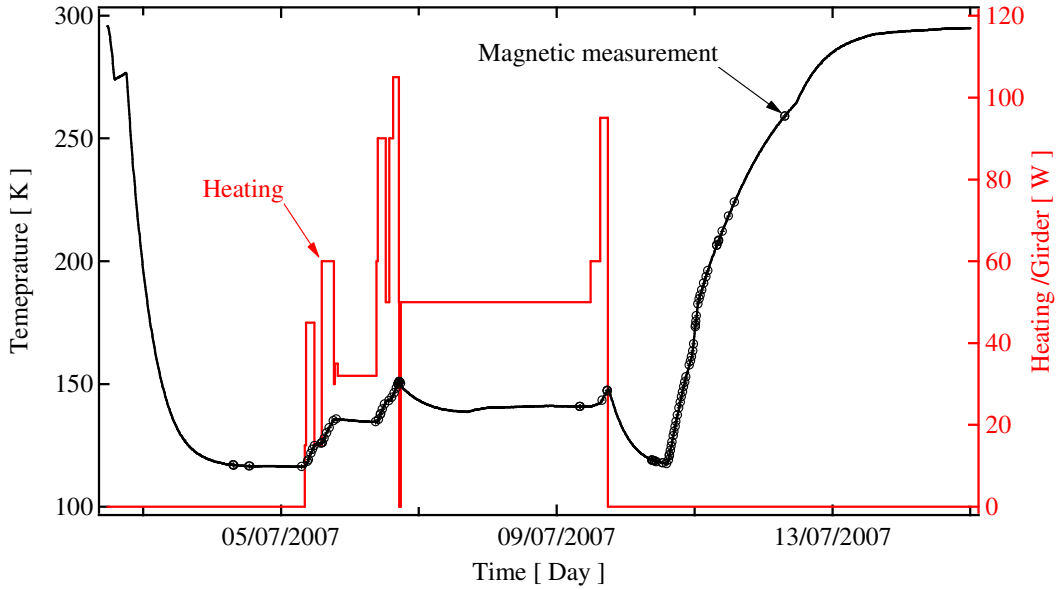

Figure 5.19: Temperature measured with a thermal sensor (PT100) installed on a magnet support at the lower girder. Markers represent the time at which magnetic measurements have been performed.

Temperature gradient along girders

The thermal steady state occurs at 117 K, this temperature is slightly lower than expected. This small difference arises from the Copper blocks fixed on each girder extremity. As shown in Figure 5.20, they are also connected to the cooling pipes and act therefore as additional spacers, lowering the temperature.

It was decided to install these Copper blocks in order to be the closest to real thermal conditions encountered in the storage ring without the electron beam. One should also notice that in the storage

ring one will install thin Cu-Ni foil at the magnet surface and RF fingers to prevent the beam from instabilities, as detailed in the section 3.1.1. The Copper blocks ensure:

- A firm electrical connection between a 60 µm thick Cu-Ni foil installed on the magnet surface and flexible transitions (RF fingers). RF fingers are mounted between the Copper block and vacuum chambers on both sides of the in-vacuum undulator.
- A permanent stretching of the Cu-Ni foil, by means of a spring loaded system, in order to compensate for the differential thermal expansion between the Aluminium girder and the foil.
- A dump of the thermal flux coming from the RF fingers which would enter the magnetic assembly. Because of the geometry of the RF fingers, some electromagnetic modes might be excited locally. This leads to localised heating of the RF fingers. The connection to the cooling pipe ensures the evacuation of this heat.

However the thin Cu-Ni foils are not compatible with the gap measurement and are therefore not used during the magnetic measurement session.

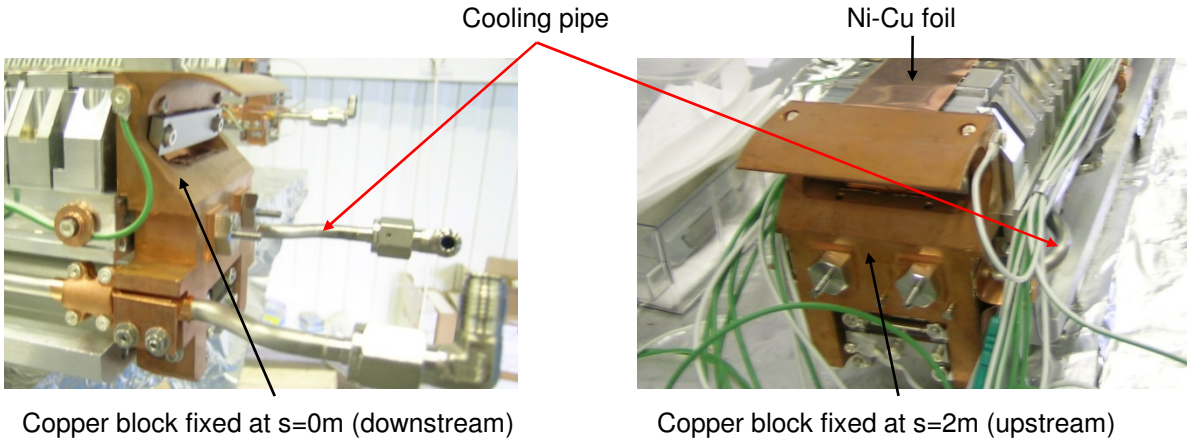

Figure 5.20: Copper blocks fixed at extremities of the girders. The blocks ensure the tension of a thin Cu-Ni foil.

The Copper blocks fixed on the upstream extremity have a poorer thermal connection with the cooling pipes than that on the downstream extremity of the girders. It gives rise to a thermal flux which propagates through the girders and causes a non uniform temperature along the girders.

We determine the temperature distribution along the girders from the local magnetic measurement following the method presented in section 5.1.3. The obtained temperature distributions are parabolic and are similar to the one displayed in Figure 5.18. For each temperature distribution, we note ΔT the temperature difference between T_{max} and T_{min} the maximum and the minimum temperature on girders. ΔT is the amplitude of the temperature variation along HYB18 girders, it depends on the temperature of the girders. Figure 5.21 represents ΔT the variation with the average temperature. The thermofoils used to heat the girders are fixed at the girder extremities. The heating on the girder extremities naturally enhances the observed parabolic temperature distribution, giving rise to a larger temperature difference ΔT. As a result it is preferable to stop the LN_2 flow in the inner loop in order to increase the magnetic assembly temperature.

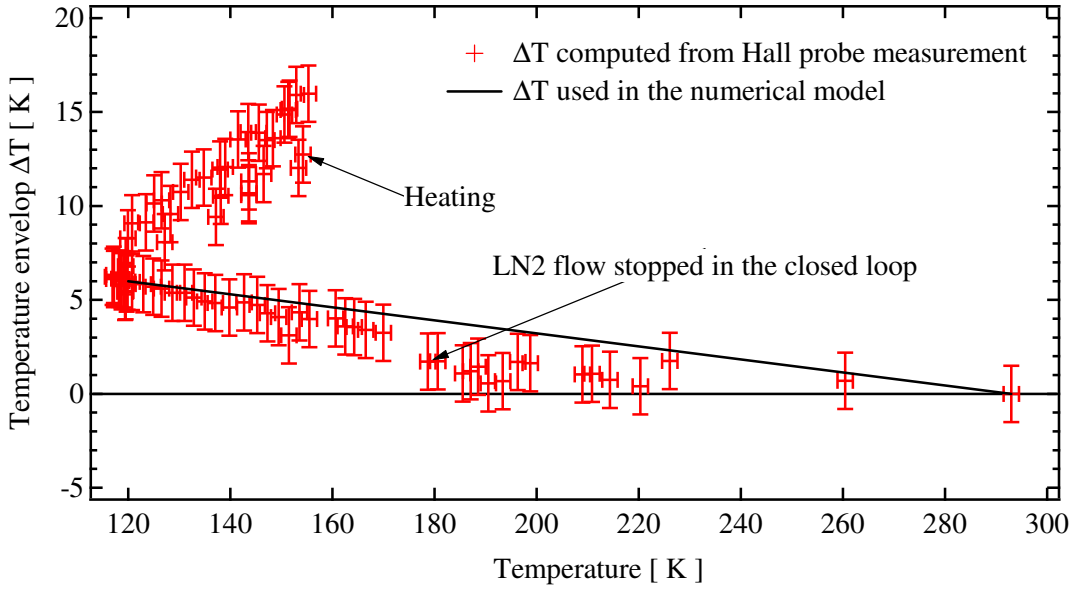

Figure 5.21: Amplitude variation of the temperature distribution (red cross) with respect to the magnetic assembly temperature. The temperature and the amplitude ΔT are computed from the Hall probe bench measurement. The black line represents the amplitude ΔT used in the numerical model describing the impact of the temperature variation on the RMS phase error.

5.2.2. Measurements of the HYB18 field integrals at cryogenic temperature

The main interest of the magnetic assembly cooling is the large increase in the magnet coercive field H_c^j. Another noticeable effect is the increase of the magnet remanence and susceptibility at cryogenic temperature. This effect is expected to increase the field integral at low temperature. Field integral measurements are performed to validate the RADIA model. Since the HYB18 is operated at cryogenic temperature in the storage ring, its field integrals at these temperatures must satisfy equation (2.62). We present hereafter the measurement of the field integrals.

Field integral measurement

Undulators are designed at the ESRF with antisymmetrical extremities. This ensures a null first field integral even though each extremity exhibits a net and large first field integral. Figure 5.22 displays the undulator vertical field integral measured at ambient temperature and at 150 K. The measurement at ambient temperature has been performed with the standard ESRF rotating coil before mounting the girders in the vacuum chamber. Actually it was the first time ever that an undulator at the ESRF has been measured after dismounting and remounting the magnetic assembly. One observes only small differences (17 Gcm) between both measurements. Indeed the antisymmetrical undulator design ensures a constant field integral.

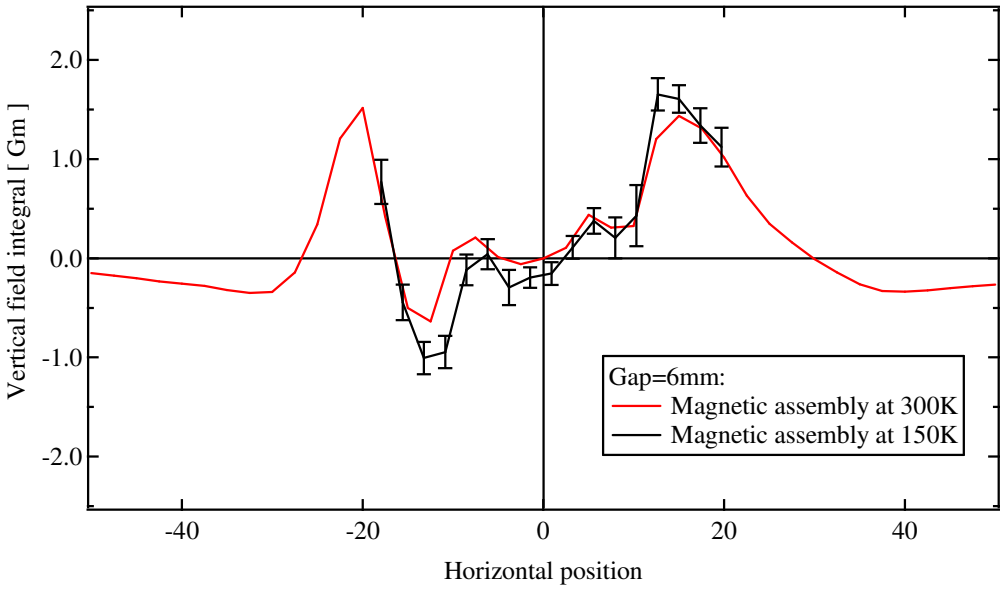

Figure 5.22: Undulator vertical field integral at 300 K (black curve) and at 150 K (red curve). The measurement performed at 300 K (150 K) has been done with the rotating coil (stretch wire).

Field integral per extremity

In an antisymmetrical undulator design, the field integral per extremity cannot simply be determined from the measurement of the undulator first field integral. However the antisymmetric undulator design gives rise to a systematic double field integral as the first field integral per extremity doesn't vanish. Thus in order to determine the field integral per extremity, one must measure the second field integral instead of measuring its first field integral.

Figure 5.23 displays the trajectories experienced by an electron as it goes throughout the magnetic assembly at ambient temperature and at 120 K. The HYB18 has been corrected at ambient temperature and almost produces a null first field integral; the trajectory is straight at ambient temperature. At 120 K below the SRT, the extremities are no longer optimized and produce a net field integral. This causes the angle observed on the electron trajectory. The other undulator extremity exhibits the same net field integral but with the opposite sign. Thus it corrects the first kick angle and the electron leaves the undulator with no angle but with a trajectory offset.

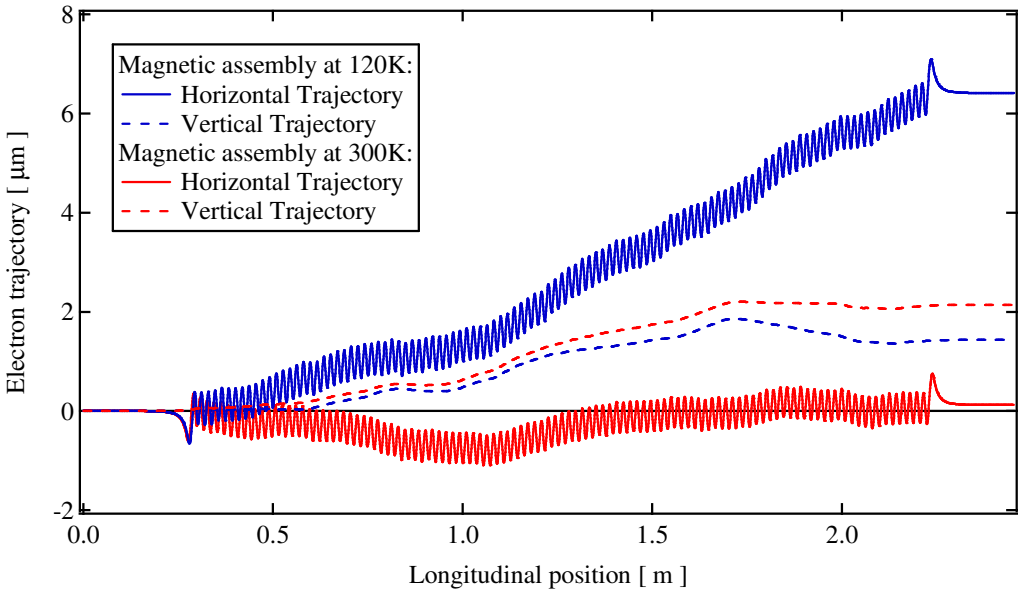

Figure 5.23: Horizontal electron trajectory in the undulator cooled at 120 K and 300 K. It is computed with B2E from the HYB18 local field measurement. The HYB18 gap is 6 mm, the electron energy is 6 GeV.

The first vertical field integral per extremity I_z^e completely determines the undulator double field integral. The relation between the two quantities is simply:

$$J_z = I_z^e \, L \tag{5.12}$$

L is the magnetic assembly length and J_z the second field integral measured with the stretch wire bench. Figure 5.24 shows the variation with the temperature of the first field integral per extremity I_z^e. The measurement corresponds well to the predicted value; the field integral decreases with temperature. However slight differences occur:

- The vertical field integral already increases as the temperature varies from 300 K to 150 K; its value increases from 0 Gm at ambient temperature to 0.2 Gm at 150 K.
- The break slope observed on the predicted field integral at 150 K is shifted to a lower temperature of around 130 K.

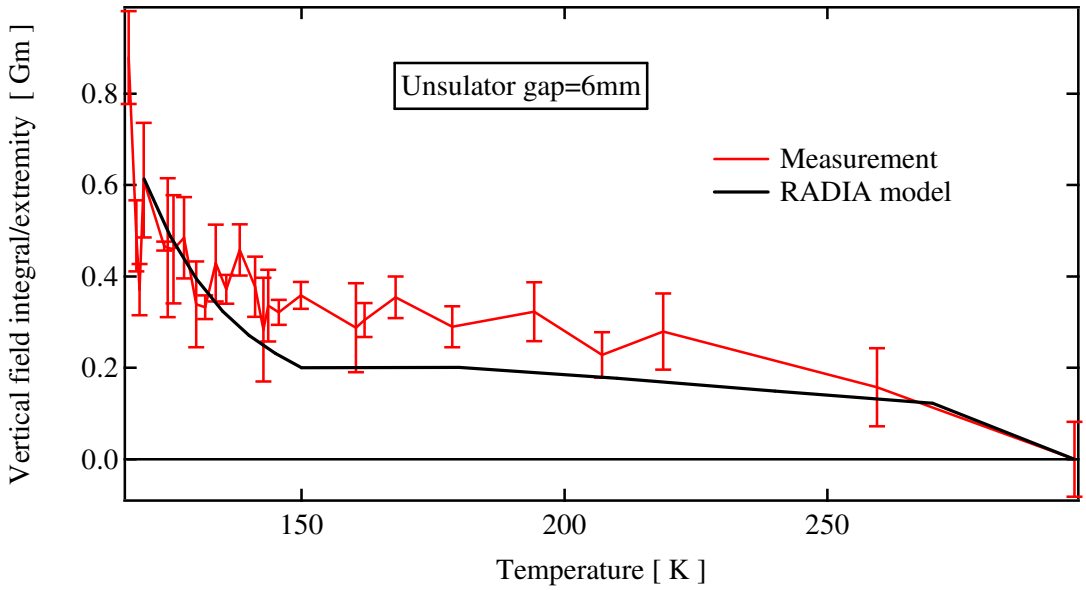

Figure 5.24: Vertical field integral per extremity as a function of the magnetic assembly temperature. The undulator gap is 6 mm.

5.2.3. HYB18 local field measurement

In this section we focus on the local field measurement. Hall probe bench measurements have been performed in order to determine experimentally the HYB18 peak field increase at cryogenic temperature. However the temperature is not uniform along the girders, it introduces some magnetic errors which further increase the RMS phase error. Finally we compare the HY18 radiation flux collected through a slit when the HYB18 is at ambient temperature or at cryogenic temperature. For the ESRF user, this quantity is of primary interest.

Peak field measurement

Figure 5.25 displays the on axis peak field variation with the temperature. The theoretical values are also reported. We notice that the curves have a very similar shape, but one observes an offset between the two of them, the RADIA model peak field being the highest one. The source of this offset lies in the remanence difference between the RADIA sample magnet and HYB18 actual ones. On the one hand we measured at ambient temperature, a remanence of 1.2 T on the particular 64 mm^3 magnet sample dedicated to the RADIA model. On the other hand the average remanence of the magnet population used for the HYB18 calculation is lower, close to 1.17 T. As a consequence the RADIA model overestimates the achievable field.

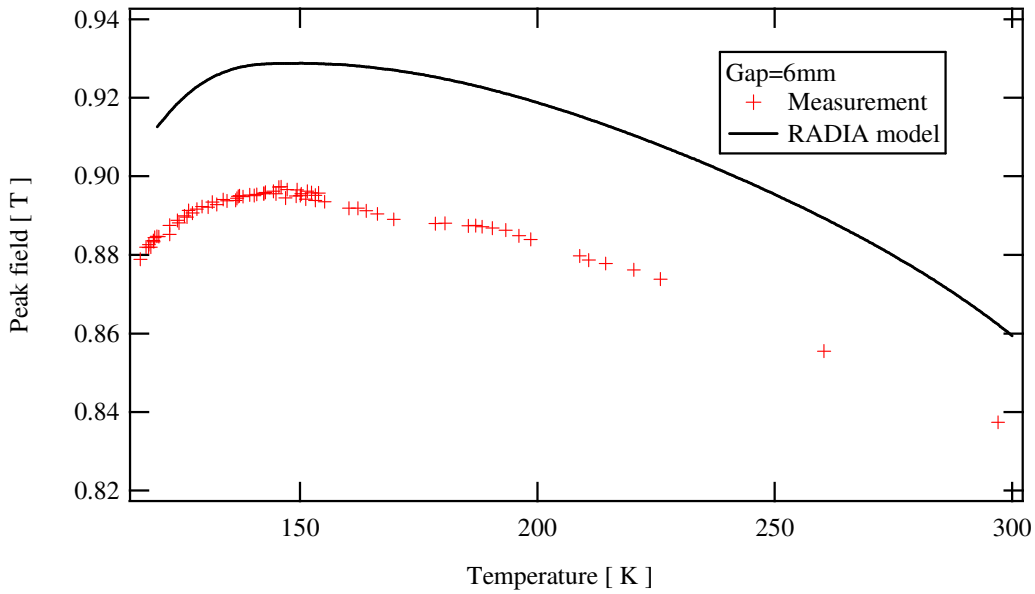

Figure 5.25: Variation of the predicted (black) and measured (red) peak field between 120 K and 300 K.

With an exception being made of the offset due to the remanence difference, the experimental peak field and theoretical curve fit well. One measures the highest peak field at around 150 K; this confirms experimentally that the CPMU temperature is largely above the temperature which maximizes the magnet remanence. The experimental peak field is also nearly constant between 140 K and 180 K; its variation is lower than 0.1 % within this temperature.

To sum up, magnetization curves at low temperature are reliable data to design numerically a CPMU. In addition around the temperature which maximizes the peak field, the variation of the peak field with the temperature is far below 1%. Thus the selection of the CPMU temperature is quite flexible as far as the magnet temperature is concerned.

RMS phase error

After magnetic correction done at ambient temperature, the HYB18 residual magnetic errors give rise to a 4° RMS phase error at ambient temperature. At cryogenic temperature, one expects to keep the RMS phase error at around 4°. However the temperature distribution is not uniform along the HYB18 girders, when the magnetic assembly is cooled at cryogenic temperature. It introduces particular magnetic errors which add to the residual ones. Consequently the RMS phase error increases at cryogenic temperature.

The main source of residual errors at 300 K arises from inhomogeneities in the magnets. We may consider that the magnetic errors induced by temperature are independent of the residual ones at 300 K. Finally following the statistical definition of the RMS phase error, it is reasonable to assume:

$$\sigma(T) = \sqrt{{\sigma_R}^2 + \left(\sigma_{th}(T)\right)^2} \tag{5.13}$$

$\sigma(T)$ is the RMS phase error at the temperature T, σ_R the RMS phase error arising from the residual errors at 300 K. We note $\sigma_{th}(T)$ the RMS phase error induced by the temperature variation along girders.

Figure 5.26 displays the RMS phase error computed from the Hall probe bench measurement. The RMS phase error computed from the equation (5.13) is also displayed. We perform the RMS phase error computation assuming a parabolic temperature distribution since it is strongly suggested by the Hall probe bench measurements. The amplitude variation ΔT of the temperature distribution is the one

introduced in the numerical model; ΔT varies linearly from 0 to 6 K between 120 K and 300 K. We use the field amplitude computed with RADIA in the numerical model.

We have explained in the section 3.4.3 that the phase error $\sigma_{th}(T)$ has two contributions: the gap opening and change of the magnetic properties along girders. We also mentioned that below 150 K, the dominant effect is the material contribution. In addition, it has been observed previously that the RADIA model is slightly biased by a sample with higher remanence. Consequently one may assume that, below 150 K, the field overestimation of the RADIA model has more impact on $\sigma_{th}(T)$, causing a larger deviation between the experimental RMS phase error and the model one.

All together the Hall probe bench measurement confirms the impact of the thermal gradient on the RMS phase error. Above 150 K the gap variation induced by the thermal gradient, governs the phase error while the changes in the magnetic properties dominate the RMS phase error at temperature below 150 K. In addition the gap variation and the changes of the magnetic properties compensate for each other above 150 K whereas they cumulate at lower temperatures.

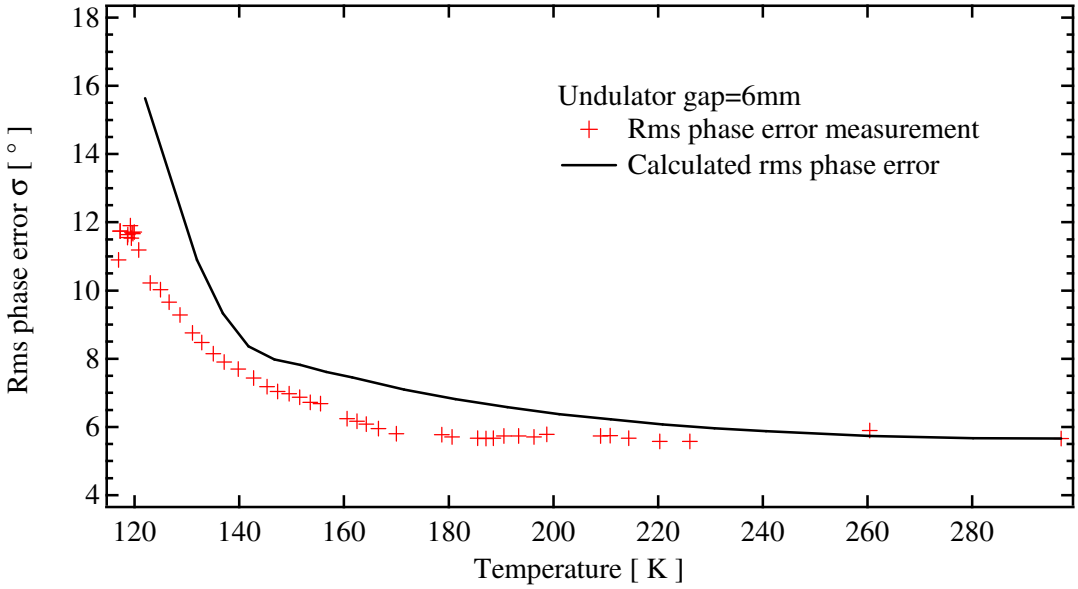

Figure 5.26: Variation with the temperature of the RMS phase errors computed from numerical model (black line) and from the Hall probe bench measurements (red markers).

Spectrum through a slit

In order to clearly illustrate the gain of the HYB18 cooling, we compute the photon flux which an observer located at 30 m from the HYB18 would collect trough a 1 mm × 1 mm slit, when the HYB18 is at ambient temperature or cooled at 150 K. The spectra are displayed in Figure 5.27. The electron beam parameters used for the computation are listed in Table 5.2. Because of the large RMS phase error at 293 K and 150 K, the 7th harmonic is the highest harmonic observable on the HYB18 spectrum. When the HYB18 is at 150 K, one observes an increase of the photon flux and a shift to low energy of the photon energy, the spectrum shift being the most remarkable. The shift of the fundamental photon energy is 650 eV and the flux increase is about 3.5 %. Both effects are due to the HYB18 field amplitude increase at cryogenic temperature.

Table 5.2: Beam parameters used for the computation of the spectrum through a slim slit.

Beam current [mA]	200
Energy spread	10^{-4}
Horizontal emittance [nm rad]	4
Vertical emittance [nm rad]	0.025
Horizontal Beta function [m]	35.2
Vertical beta function [m]	2.52

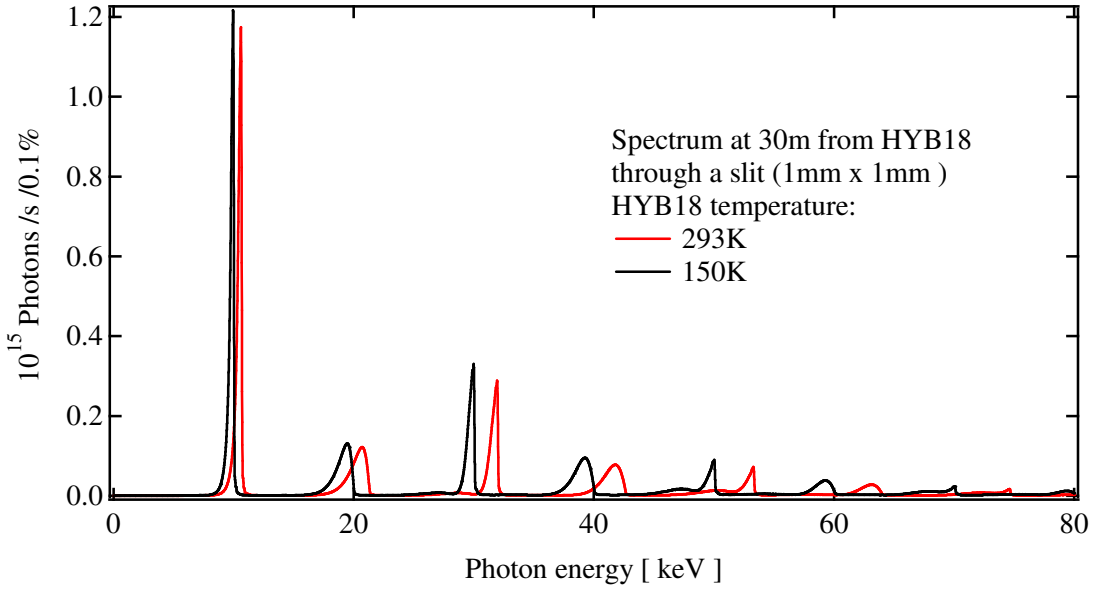

Figure 5.27: Spectrum through a rectangular slit ($1mm \times 1mm$) located at 30 m from the HYB18 as the magnetic assembly is at 150 K (black line) and at ambient temperature (red line). The electron beam parameters used for the computation are listed in Table 5.2.

The purpose of this chapter was on the one hand to validate the CPMU magnetic model, and on the other hand to ensure that the corrections, made at ambient temperature, are still valid at low temperatures. To do so, we measure the temperature dependence of the peak field and of the first field integral per extremity, for a temperature between 120 K and 300 K. First of all we build an in vacuum magnetic measurement bench (stretch wire and Hall probe) to make measurements possible at such a low temperature. Then the in-vacuum undulator is cooled down to 120 K. Experimental magnetic measurements confirm the numerical model predictions: the field is maximal at 150 K, and the field integral per extremity increases below 150 K. The computation of the phase error validates the corrections carried out at ambient temperature: no additional error is observed on the phase error, except for a thermal gradient along the girders.

6. Conclusion

In 2004, T. Hara proposed a CPMU concept, consisting of a PPM undulator using $Nd_2Fe_{14}B$ magnets cooled with Liquid Nitrogen at around 150 K. This raised two main questions: what would the magnetic performance of such an undulator be? Is it technologically feasible to cool down an undulator which is several meters long without introducing errors in the undulator field? In order to answer these issues, a 2 m long CPMU was proposed at the ESRF. This piece of work covers the design of the CPMU, the assembly and the performance evaluation of this device.

Firstly a RADIA numerical model was developed in order to predict the peak field and the field integral dependence to temperature; this gave us the optimum temperature to operate. A 2 m long Hybrid undulator with 18 mm period was then assembled and corrected, at ambient temperature. Next, the CPMU was cooled to 150 K, using a closed liquid nitrogen loop. To evaluate its performance, we created an in vacuum magnetic measurement bench, capable of operating at cryogenic temperatures. This bench is unique since it allies both local field and field integral magnetic measurements. Finally we compared these results with the RADIA model computations.

The in-vacuum bench developed at the ESRF has been successfully operated to perform magnetic measurements from 120 K to ambient temperature. Both local field and field integrals validate the numerical magnetic model. The HYB18 peak field reaches its maximum value 30 K above the temperature at which the $Nd_2Fe_{14}B$ magnets maximize their remanent magnetization. In addition the field integral per HYB18 extremity increases at temperature below 150 K. The spin reorientation transition causes an increase of the $Nd_2Fe_{14}B$ magnet susceptibility. This is directly at the origin of the HYB18 field integral increase and the temperature shift between the maximum of the $Nd_2Fe_{14}B$ magnet remanent magnetization and the HYB18 peak field. One also observes that the HYB18 peak field is fairly constant between 140 K and 180 K, in accordance with the RADIA model. Finally in agreement with the RADIA model, the target temperature chosen to operate the HYB18 is 150 K.

It has been observed that the RMS phase error increases as the temperature decreases. The growth of the RMS phase error is smooth between 300 K and 150 K. One measures a 1° increase of the RMS phase error, as the HYB18 is cooled down 150K. At a lower temperature the growth is exponential. Such an increase in the RMS phase error is evidence of additional magnet errors at low temperatures. It has been determined, from a model based on the RADIA calculation and on the thermal model, that the additional magnetic errors, measured at cryogenic temperature, are all related to the non uniform temperature along girders. The temperature variation has a localised effect on the magnetic gap and the magnetic properties of the magnet blocks. The total RMS phase error then becomes the quadratic sum of the residual RMS phase error at room temperature with the RMS phase error induced by temperature variation. At a temperature in excess of 150 K, the undulator field error due to the gap deformation and the variation of the magnet block properties compensate themselves, leading to a small RMS phase error increase. At lower temperatures both effects add to each other, leading to a large increase in the RMS phase error.

The CPMU was successfully installed in the ID6 straight section of the ESRF storage ring in January 2008 [94]. This is pioneer work since it is the first CPMU ever installed on a synchrotron radiation light source. Without the beam, the undulator temperature is 143 K. During the first month of operation, the dependence of the undulator with the beam filling pattern was investigated. In the worst filling pattern (16 bunches, 90 mA), the average temperature reaches 180 K. A thermal flux of 80 W is estimated from this temperature increase. This is about twice the expected thermal value. The temperature distribution along the undulator indicates a uniform heat deposition along the magnetic

assembly. Possible High Order Modes (HOM) in the undulator tank would explain such uniform heat deposition.

Progress on an unbaked in-vacuum undulator has been made [69]; an unbaked in-vacuum undulator is currently in operation in the ID15 straight section of the ESRF. At the re-start of the machine, an increase of the vacuum pressure was observed, when the first beam was injected. The pressure range was 10^{-6} mbar with 60 mA stored in the machine. However the photon beam conditioned the unbaked undulator so that a few days later, the experimental beamline was able to use the photon beam.

The pioneering work on CPMU performed at the ESRF strongly indicates the technological accessibility of the CPMU using $Nd_2Fe_{14}B$ magnets with high remanence ($B_r > 1.2$ T). From the results quoted above, we may point out the requirements which should be met for the construction of the CPMU undulator with low phase error (<2°). Evidently, it is necessary to build an undulator with small RMS phase error (<2°) at ambient temperature. The development of magnets with low error is of primary interest for such devices [88]. Then, at a low temperature, any temperature gradient should be avoided to maintain the RMS phase error. This implies thermally isolating the CPMU; thus a proper design of the extremity is fundamental to prevent the flux coming from the RF fingers from propagating in the magnetic assembly.

Finally, it is believed that, the CPMU would be widely developed in the near future, especially in the numerous medium scale synchrotron radiation facilities (E< 3 GeV) such as SOLEIL [95], DIAMOND, NSLS-II, ALBA and so on. Indeed such a low period/high field undulator opens up the way for the operation of X-ray beamlines in these facilities.

7. Reference

1. **Lienard, A.** Champ électrique et magnétique produit par une charge électrique concentrée en un point et animée d'un mouvement quelconque. *L'éclairage électrique.* 1898, 16, p. 5.

2. **Elder, F. R., Gurewitsch, A. M.; Langmuir, V. R., and Pollock, H.C.** A 70-Mev Synchrotron. *J. Appl. Phys.* 1947, 18, p. 810.

3. **Elder, F. R., Gurewitsch, A. M., Langmuir, V. R., and Pollock, H. C.** Radiation from Electrons in a Synchrotron. *Phys. Rev.* 1947, Vol. 11, 71, pp. 829-830.

4. **Codling, K.** Atomic and Molecular Physics Using Synchrotron Radiation—the Early Years. *J. Synch. Rad.* 1997, Vol. 4, 6, p. 316.

5. Location of the synhroton sources are listed at the ALS website. See: http://www-als.lbl.gov/als/synchrotron_sources.html.

6. **Motz, H.** Applications of the Radiation from Fast Electron Beams. *J. Appl. Phys.* May 1951, pp. 527-535.

7. **Motz, H., Thon, W. and Whitehurst, R.N.** Experiments on Radiation by Fast Electron Beams. *J. Appl. Phys.* July 1953, pp. 826-833.

8. **Hara, T., Tanaka, T., Kitamura, H., Bizen, T., Maréchal, X.M., Seike, T., Kohda, T., and Matsuura, Y.** cryogenic permanent magnet undulators. *Phys. Rev. Spe. Top. Acc. Beams, Vol 7.* 2004, p. 050702.

9. **Jackson, J.D.** *Classical electrodynamics.* John Wiley and sons, 1962.

10. **Marechal, X. M.** *Contrôle de la polarisation de l'émission synchrotron générée par des éléments d'insertion magnétiques périodiques.* PhD, Université Joseph Fourier : Grenoble, France, 1992.

11. **Huard, S.** *Polarisation de la lumière.* Paris : Masson, 1993.

12. **Kim, K. J.** Brightness, coherence and propagation characteristics of synchrotron radiation. *Nucl. Ins. Meth. Phys. Res.* Elsevier Science Publishers, 1986, Vol. A, 246.

13. **Kim, K. J.** Characteristics of synchrotron radiation. *American accelerator school* . 1986.

14. **Elleaume, P.** Generalities on the synchrotron radiation.Chapter 2 in *Undulators, wigglers and their applications,* edited by H. Onuki and P. Elleaume.. London : Taylor & Francis, 2003, p. 38.

15. **Farvacque, L.** Beam dynamics. Chapter 1 in *Undulators, wigglers and their applications,* edited by H. Onuki and P. Elleaume.. London : Taylor & Francis, 2003.

16. **Edwards, D. A. and J., Syphers M.** *An introduction to the physics of high energy accelerators.* New York : John Wiley and Sons, 1993.

17. **Elleaume, P.** Undulator radiation. Chapter 3 in *Undulators, wigglers and their applications,* edited by H. Onuki and P. Elleaume. London : Francis & Taylor, 2003, P 69.

18. **Walker, R. P.** Bending magnet and wiggler radiation. Chapter 4 in *Undulators, wigglers and their applications,* edited by H. Onuki and P. Elleaume. London : Francis & Taylor, 2003, p 108.

19. **Walker, R. P.** Insertions devices: undulators and wigglers. in *CERN accelerator school on synchrotron radiation and free electrons laser,* edited by S. Turner. Genève : CERN, 1998, p. 129.

20. **Clarke, J. A.** *The science and technology of undulators and wigglers.* Oxford : Oxford university press, 2004.

21. Synchrotron Radiation Workshop (SRW). [Online] http://www.esrf.eu/Accelerators/Groups/InsertionDevices/Software/SRW.

22. **Chavanne, J. and Elleaume, P.** Technology of insertion devices. Chapter 5 in *Undulators, wigglers and their applications,* edited by H. Onuki and P. Elleaume. London : Francis & Taylor, 2003, p 108.

23. **Bryant, P.J.** Basic theory for magnetic measurements, in *CERN accelerator school on magnetic measurement and alignement* edited by S. Turner. Geneva : CERN, 1992.

24. **Bahrdt, J.** Insertion Devices. *Intermidiate accelerator physics.* Zeuthen : CERN, 2003.

25. **Diviacco, B. and Walker, R. P.** Recent advances in undulator performance optimization. *Nuc. Inst. Meth. Phys. Res. A368.* 1996, p. 522.

26. **Du Trémolet de Lacheisserie, E.** *Magnétisme.* Collection Grenoble Sciences, 1999.

27. **Coey, J.M.D.** *Rare-earth iron permanent magnets.*: Oxford science publications, 1996.

28. **Marcouille, O., Brunelle, P., Chubar, O., Marteau, F., Massal, M., Nahon, L., Tavakoli, K., Veteran, J., and Filhol, J.-M.** Design, Construction and Magnetic Measurements of the HU640 (OPHELIE2) Undulator dedicated to the DESIRS VUV Beamline at SOLEIL. *SRI09.* AIP Conference Proceedings, 2007, Vol. 879.

29. **Stampfer, M.** Magnetic and mechanical design calculations of a 4-5 Tesla superconductiong wavelength shifter. Zuerich : Technische Hochschule, 1955.

30. **Hallbach, K.** Physical and optical properties of rare earth cobalt magnets. *Nucl. Inst. Meth.* Elsevier, 1981, 187.

31. **Kim, K. J.** A synchrotron radiation source with arbitrarily adjustable elliptical polarization. *Nucl. Ins. Meth.* 1984, Vol. 219, 2, p. 425.

32. **Moissev, M., Nikitin, M and Fedosov, N.** Change in the kind of polarization of undulator radiation. *Sov. Phys. J.* 1978, Vol. 21, p. 332.

33. **Onuki, H.** Elliptically polarized synchrotron radiation source with crossed and retarded magnetic fields. *Nucl. Inst. Meth.* Vol. A246.

34. **Elleaume, P.** A flexible planar/helical undulator design for synchrotron sources. *Nucl. Instr. Meth. Phys. Res. A291.* 1990, p. 371.

35. **Sasaki, S.** A new undulator for generating variably polarized radiation. *Jpn. J. Appl. Phys.* 1992, Vol. 31.

36. **Chavanne, J., Van Vaerenbergh, P., Elleaume, P., and Günzel, T.** Recent achievements and future prospect for ID activities. *EPAC2000.* p. 2345.

37. **Fedurin M., Kulipanov G., Mezentsev N., and Shkaruba V.** Superconducting high-field three-pole wigglers at Budker INP. *Nucl. Inst. Meth. Phy. Res.* 2000, Vol. A448, p. 51.

38. **Chubar, O., Elleaume, P. and Chavanne, J.** A three-dimensional magnetostatics computer code for insertion devices. *Journal of synchrotron radiation.* 1998, Vol. 5, pp. 481-484.

39. **Elleaume, P., Chubar, O. and Chavanne, J.** Computing 3D magnetic fieds from insertion devices. *EPAC98.* CERN, 1998, p. 3509.

40. **Elleaume, P.** A New Approach to the Electron Beam Dynamics in Undulators and Wigglers. *EPAC92.* 1992, p. 661.

41. **Smolyakov, M. N.** Rotation invariance of electromagnetic radiation genrated by relativistic particles in magnetic fields. *Nucl. Ins. Meth. Phys. Res.* Elsevier, 2000, Vol. A, 448.

42. **Maréchal, X., Chavanne, J. and Elleaume, O.** *On 2D Periodic Magnetic fields.* 1990. ESRF-SR/ID-90-38.

43. **Chavanne, J., Elleaume, P. and Van Vaerenbergh, P.** End field stucture for linear/helical insertion devices. *PAC1999.* 1999, p. 2665.

44. **Frachon, D.** *Dévoloppement de bancs de mesure pour ondulateurs et wigglers.* PhD, Université Joseph Fourier : Grenoble, France, 1992.

45. **Guillotin, N.** *Development of HOM cavity at the ESRF.* PHD, Université d'Orsay : Orsay, France, 2008.

46. **Elleaume, P and Chavanne, J.** Latest developments on insertion devices. *EPAC2006.* 2006.

47. **Hsieh, H., Krinsky, S., Lucio, A., Pellegrini, C., and Vans Steenbergen, A.** Wiggler, undulator and free electron laser radiation sources development at the National Synchrotron Light Source. *Nucl. Inst. Meth. 208.* 1983, p. 79.

48. **Gudat, W., Pflueger, J., Chatzipetros, J., and Peatman, W.** An undulator/multipole wiggler for BESSY storage ring. *Nucl. Inst. Meth. Phys. Res. A246.* 1986, p. 50.

49. Hara, T., Tanaka, T., Tanabe, T., Maréchal, X-M., Okada, S., and Kitamura, H. In-vacuum undulators of SPring-8. *J. Sync. Rad.* 1998, p. 403.

50. **Hara, T., Tanaka, T., Tanabe, T., Maréchal, X-M., Kitamura, H., Elleaume, P., Morrison, B., Chavanne, J., Van Vaerenbergh, P., and Schmid, D.** SPring-8 in-vacuum undulator beam test at the ESRF. *J. Sync. Rad. 5.* 1998, p. 406.

51. **Hara, T., Yabashi, M., Tanaka, T., Bizen, T., Goto, S., Maréchal, X-M., Seike, T., Tamasaku, K., Ishikawa, T., and Kitamura, H.** The brightest x-ray source: A very long undulator at SPring-8. *Rev. Sci. Inst.* 2002, p. 1125.

52. **Tanaka, T., Hara, T., Tsuru, R., Iwaki, D., Marechal, X.M., Bizen, T., Seike, T., and Kitamura, H.** In-vacuum undulators. *FEL07.* 2005, p. 370.

53. **K., Bane and S., Krinsky.** Impedance of a small-gap undulator vacuum chamber. *PAC93.* 93, p. 3375.

54. **Chavanne, J., Elleaume, P. and Van Vaerenbergh, P .** Recent developments of insertion devices at the ESRF1. *PAC99.* 1999.

55. **Chavanne, J.** ESRF Machine Technical Note 1-1996/ID, 1996.

56. **Petra, M., Den Hartog P.K., Moog, E. R., Sasaki, S., Sereno, N., and Vasserman, I.B.** Radiation effects studies at the Advanced Photon Source. *Nucl. Inst. Meth.Phys. Res. A507.* 2003, p. 422.

57. **Colomp, P., Oddolaye, T., and Elleaume, P.** *Demagnetization of permanent magnets to 180MEV electron beam.* Grenoble : ESRF/MACH-ID/93-09, 1993.

58. **Bizen, T., Marechal, X. M., Seike, T., Kitamura, H., Hara, T., Tanaka, T., Asano, Y., Kim, D.E., and Lee, H.S.** Radiation damage in permanent magnets for ID. *Radiation measurements.* ELSEVIER, 2007, 41.

59. **Bizen, T., Tanaka, T., Y., Asano, E., Kim D., S., Bak J., S., Lee H., and Kitamura, H.** Demagnetization of undulator magnets irradiated high energy electrons. *Nucl. Inst. Meth. Phys. Res. A467.* 2001, p. 185.

60. **Blackmore, E. W.** Radiation effects of protons on samarium cobalt permanent magnets. *IEEE Trans. Nucl. Sci. Vol. .* 1985, Vol. NS32, p. 3669.

61. **Okuda, S., Ohashi, K. and Kobayashi, N.** Effects of electron-beam and y-ray irradiation on the magnetic flux of Nd-Fe-B and Sm-Co permanent magnets. *Nucl. Inst. Meth. Phys. Res. B94.* 1994, Vol. 227.

62. **Luna, H. B., Maruyama, X. K., Colella, N. J., Hobbs, J. S., Hornady, R. S., Palomar, B,, and Kulke, V.** Bremsstrahlung radiation effects in rare earth permanent magnets. *Nucl. Inst. Meth. Phys. Res. A285.* 1989, p. 349.

63. **Chavanne, J., Plan, B., Penel, C., and Vanvaerenbergh, P.** Magnetic design consideration for in-vacuum undulators. *EPAC2002.* CERN, 2002, p. 2604.

64. **Tanaka, T., Hara, T., Kitamura, H., Tsuru, R., Bizen, T., Maréchal, X-M., and Seike, T.** Application of high-temperature superconducting permanent magnets to synchrotron radiation sources. *Phys. Rev. Spe. Top. - Accelerators and Beams,V. 7.* 09 07 2004, pp. 1-5.

65. **Bizen, T., Maréchal, X. M., Seike, T., Kitamura, H., Hara, T., Tanaka, T., Asano, Y., Kim, D.E., and Lee, H.S.** Radiation damage in magnets for undulators at low temperature. *EPAC2004.* CERN, 2004, p. 2092.

66. **Givord, D., H.S, Li and J.M., Moreau.** Magnetic properties and crystal properties of Nd2Fe14B. *Sol. St. Com.* 1984, Vol. 50, p. 497.

67. **Hara, T., Tanaka, T., Kitamura, H., Bizen, T., and Maréchal, X.M.** Insertion devices of next generation. *APAC2004, Gyeongju, Korea.* 2004, p. 216.

68**. Kitegi, C., Chavanne, J., Cognie, D., Elleaume, P., Revol, F., Penel, C., Plan, B., and Rossat, M**. Development of a cryogenic permanent magnet in-vasuum undulator at the ESRF. *EPAC2004.* 2004.

69. **Kersevan, R., Hahn, M., Parat, I, and Schmied, D.** Machine operation issue related to the vacuum system of the ESRF. *EPAC08.* 2008, p. 3705.

70. **SHI Cryogenics Group.** See: http://www.shicryogenics.com

71. **Messer** See: http://www.messer.de

72. **Arp, V. and Weisend II, J. G.** Properties of cryogenics fluids, Chapter 1 in *Handbook of cryogenic engineering* edited by J. G. Weisend II.. London : Taylor & Francis, 1998.

73. **Herbst, J.F.** R2F14B materials: Intrinsic proprties and technological aspects. *Rev. Mod. Phys.* 1991, pp. Vol.63, No.4, p.819.

74. **Li, H. S.** Propriétés cristallographiques et magnétiques des composés R2FE14B entre les terres rares (R), le Fer et le bore. *PhD.* Grenoble : Université scientifique et médicale et l'institut national polytechnique de Grenoble, 1987.

75. **Tenaud, P.** Analyse expérimentale des mécanismes de coercivité dans les aimants NdFeB frittés. PhD, Université Joseph Fourier-Grenoble, 1988.

76. **Dufeu, D., Eyraud, E. and Lethuillier, P.** An efficient 8 T extraction vector magnetometer with sample rotation for routine operation. *Rev. Sci. Ins.* 2000, Vol. 71, 2.

77. **Givord, D., Tenaud, P. and Viadieu, T.** Analysis of hysteresis loops in Nd-Fe-B sintered magnets. *J. Appl. Phys.* Vol. 60, 9, p. 3264.

78. **Chavanne, J., Chubar, O., Elleaume, P., and Van Vaerenbergh, P.** Nonlinear numerical simulation of permanent magnets. *EPAC2000.* 2000, p. 2316.

79. **Incropera, F. P. and Dewitt, D. P.** *Introduction to heat and mass transfer, 5. Edition .*: John Wiley & Sons, 2002.

80. **Touloukian, Y.S.** Recommanded Values of The Thermophysical Properties of Eight Alloys, Major Constituents and Their Oxides. Purdue University :, 1965.

81. **Simon, N.J., Drexler, E.S. and Reed, R.P.** *Properties of Copper and Copper Alloys, NIST Monograph 177.* National Institute of Standards and Technology, 1992.

82. **Touloukian, Y. S. and Dewitt, D. P.** *Thermal radiative properties. Metallic elements and alloys.*: IFI Plenum Press, 1970.

83. **Fuji, H., Nagata, H., Uwatoko, Y., Okamoto, T., Yamamoto, H., and Sagawa, M.** Heat capacity and thermal expansion of R2Fe14B compounds (R=Y,Nd and Tm). *Journal of magnetism and magnetic materials.* Elsevier, 1987, 70, p. 332.

84. **Vedrine, P., Tixador, P., Brunet, Y., Bobo, J. C., Fevrier, A., and Leriche, A.** Mechanical characteristics of NdFeB magnets at low temperature. *Cryogenics.* 1991, Vol. 31, 1, p. 51.

85. **National Bureau of Standard. US Department of Commerce.** Thermal Expansion of Technical Solids at Low Temperature. A compilation of literature.: NBS Monograph 29.

86. Cryogenic Division, National Bureau of Standard. *LNG Materials and Fluids. 1st edition. .*

87. **Touloukian, Y. S., Kirby, R. K., Taylor, R. E., and Desai, P. D.** Thermal expansion. Metallic elements and alloys. IFI Plenum Press, 1977.

88. **Börgermann, F.-J., Blank, R. and Reppel, G.W.** Improved homogeneity of permanent magnets for undulators and wigglers. *EPAC08.* 2008.

89. **Tanaka, T., T. Seikeb and Kitamura, H.** Undulator field correction by in-situ sorting. *Nucl Inst. Meth.Phys. Res.* 2001, Vol. A465, p. 600.

90. **Bobbs, B. L., Rakowsky, G., Kennedy, P., Cover, R. A., and Slater, D.** In search of a meaningful field-error specification for wigglers. *Nucl. Inst. Meth. Phys. Res. A296.* p. 1990.

91. **Hajima, R., Takeda, N., Ohashi, H., and Akiyama, M.** Optimization of wiggler magnets ordering using a genetic algorithm. *Nucl. Ins. Meth. Phys. Res. A318.* 1992, p. 822.

92. **Chubar, O., Rudenko, O. , Benabderrahmane C., Marcouille, O., Fihol, J.-M. and Couprie, M.-E.** Application of genetic algoritms to sorting, swapping and shimming of the SOLEIL undulators magnets. *AIP Conf. Proc.* 2006, Vol. 879, p. 359.

93. **Chubar, O., Briquez, F., Couprie, M.-E., Filhol, J.-M., Leroy, E., Marteau, F., Paulin, and F., Rudenko, O.** Compensation of variable skew and normal quadrupole focusing effects of APPL-II undulators with computed-aided shimming. *EPAC08.* 2008, p. 2246.

94. **Chavanne, J., M., Hahn, R., Kersevan, C., Kitegi, C., and Penel, F.** Construction of a cryogenic permanent magnet undulator at the ESRF. *EPAC08.* 2008, p. 2243.

95. **Benabderrahmane, C, Béchu, N, Berteaud, P., Couprie, M.E., Filhol, J.M., Herbeaux, C., Kitegi, C., Marlats, J.L. , Tavakoli, K, Mary, A.** Development of cryogenic undulator CPMU at SOLEIL. *EPAC08.* 2008, p. 2225

Appendix A

The 10 T magnetometer

A.1 Principle of the magnetometer

A.1.1 Magnetometer overview

Magnetization is measured by induction; this is usually called the extraction method [76]. The magnetometer is schematically drawn in Figure A.1. The magnetic sample is mounted on a rod, the sample holder which can be moved vertically. Two pick up coils are used to measure the sample magnetization.

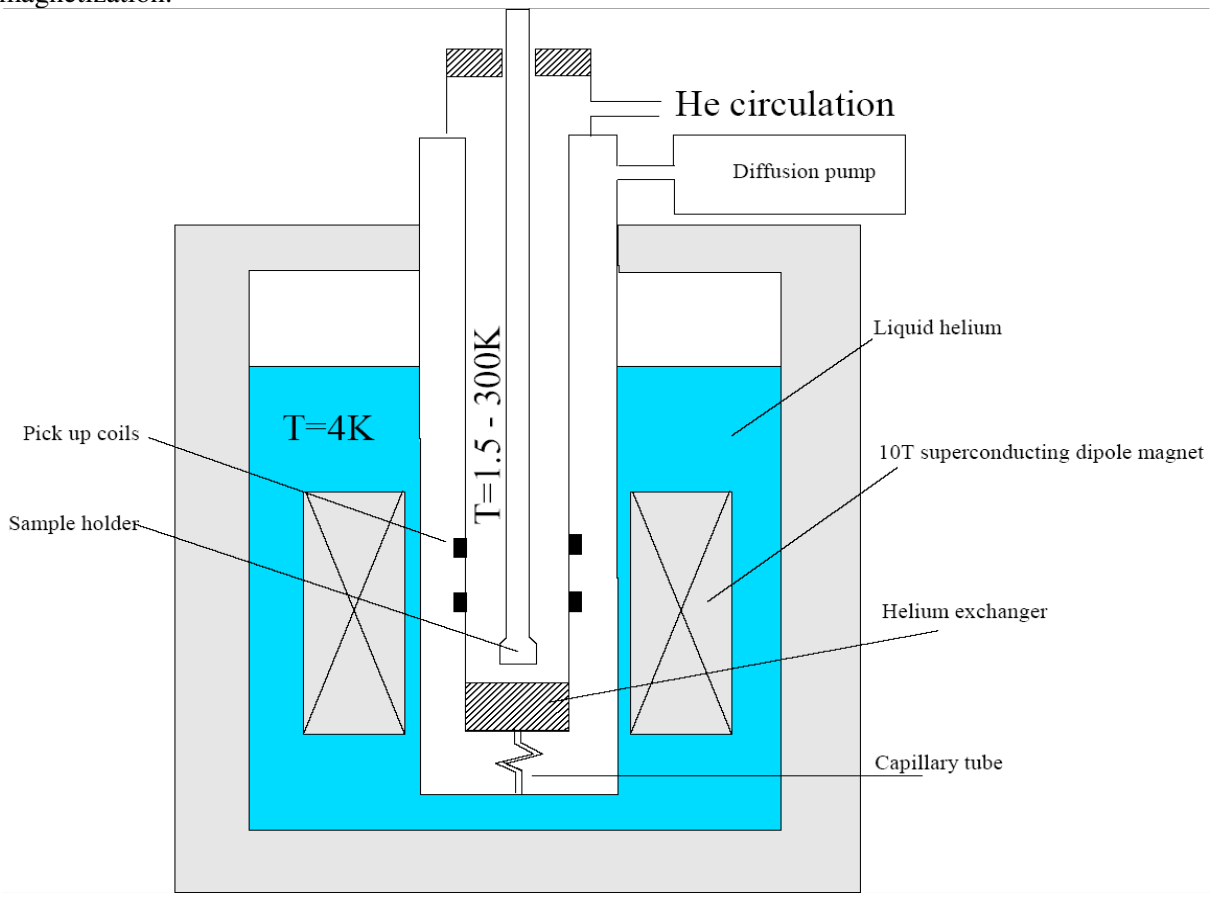

Figure A.1: Magnetometer schematic view.

To measure its magnetization, the sample is moved from one pick-up coil centre to the other one. The magnet translation induces a current in the pick-up coils, which is proportional to the magnet magnetization. The measurement of this current gives the magnetization. The distance over which the sampler holder is moved is called the extraction distance.

The superconducting dipole magnet is used to set the sample magnetization. The dipole lies in a cryostat full of liquid Helium at 4 K. It produces a static induction field between ± 10 T in the extraction region; the field produced is uniform around 80 cm in the extraction region. The minimum

field increment is 10 Oe. A vacuum chamber isolates thermally the sample from the Helium bath at 4 K.

Moreover the temperature sample is regulated between 1.5 K and 300 K thanks to the helium flux circulating through the pipe where the sample is moved. A capillary tube connects the Helium bath to the pipe; a diffusion pump ensures the Helium circulation through the capillary tube and the pipe. The temperature at the entrance to the exchanger is 1.5 K. A thermal resistance mounted on the capillary tube regulates the temperature between 1.5 K and 300 K.

A.1.1 Pick-up coils

In this part we present how the magnetization can be computed from the sample extraction. We first estimate the flux ϕ_{21} on the current loop L_1 sent by a magnet with the magnetic moment $\vec{m}$. The current in the loop L_1 is I. We suppose the magnetic moment to be punctual. According to the reciprocity theorem, $\vec{m}$ is equivalent to a current loop L_2 with a surface S and a current i such that $\vec{m} = i\vec{S}$. This is displayed in Figure A.2.

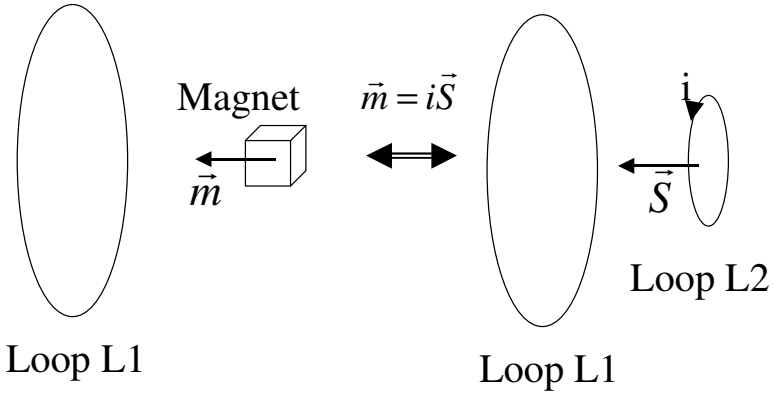

Figure A.2: A magnet with the magnetic moment is equivalent to a loop with a current i with $\vec{m} = i\vec{S}$, $\vec{S}$ is the oriented surface.

The current loop L_2 sends a flux ϕ_{21} into the loop L_1:

$$\phi_{21} = M \cdot i \tag{A.1}$$

M is the mutual inductance between loop L_2 and loop L_1. The loop L_1 creates also a flux ϕ_{12} trough the loop 2 :

$$\phi_{12} = M \cdot I = \vec{B}_1 \cdot \vec{S} \tag{A.2}$$

Eliminating M from equation (A.1) and (A.2) the flux ϕ_{21} is expressed as:

$$\phi_{21} = \frac{1}{I}\vec{B}_1 \cdot \vec{m} \tag{A.3}$$

The flux from the magnetic moment $\vec{m}$ is the scalar product of this moment with the ratio $\frac{1}{I}\vec{B}_1$. $\vec{B}_1$ is the induction created by the current I in the loop L_1. When $\vec{m}$ is not punctual, the magnetic moment is expressed as:

$$\vec{m} = V\vec{J} \tag{A.4}$$

V is the magnet volume and $\vec{J}$ the magnetization. The flux expression is generalized as:

$$\phi_{21} = \iiint_V \frac{1}{I}\vec{B}_{12}(r) \cdot \vec{J}(r) d^3r \tag{A.5}$$

The real pick-up coils cross-section is plotted in Figure A.3. The pickup coils are made of two identical sets. A set is composed of two concentric coils. The pick-up coils are connected in opposition series and are flux compensated. They are used to measure the magnetization component along the vertical axis.

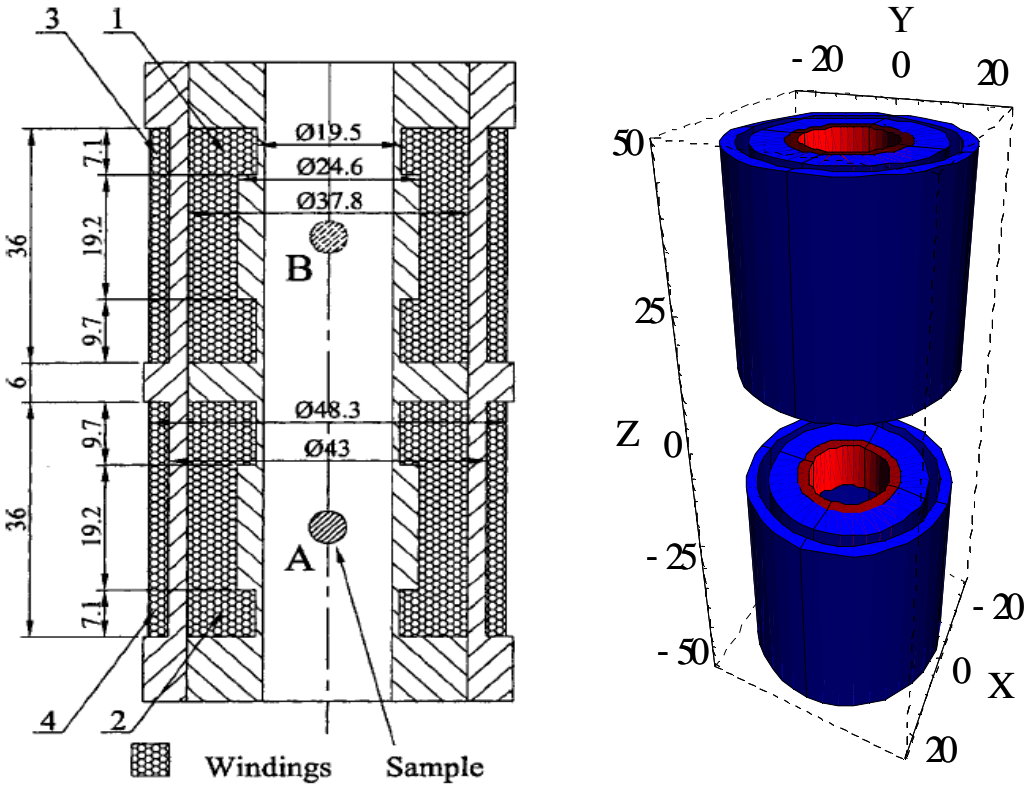

Figure A.3: Pick-up coil cross section (left) and 3D RADIA geometry (right). The left picture sources in reference [76].

The software RADIA has been used to numerically compute the pick-up coils $\frac{1}{I}\vec{B}_1$. The pick-up 3D geometry generated with RADIA is shown in Figure A.3. The $\frac{1}{I}B_z$ vertical and the $\frac{1}{I}B_x$ horizontal component computed with RADIA is displayed in Figure A.4, the vertical component $\frac{1}{I}B_z$ is constant in the coils centre, thus the magnetization measurement is not sensitive to errors on the initial and the final sample axial position. When the sample is moved from A to B, the voltage induced in the pickup coils is integrated and the resulting flux variation is:

$$\delta\phi = \left(\left(\frac{1}{I}B_z\right)_B - \left(\frac{1}{I}B_z\right)_A\right) m_z = 2m_z\left(\frac{1}{I}B_z\right)_B \tag{A.6}$$

Moreover according to Figure A.4, $\frac{1}{I}B_z$ does not depend on the radial position: the magnetization measurement has a low sensitivity to the sample radial position errors. The negligible radial component $\frac{1}{I}B_x$ ensures low sensibility to the parasitic fluxes due to magnet or to mechanical vibrations. The resolution, along the vertical axis, is 10^{-7} Am^2.

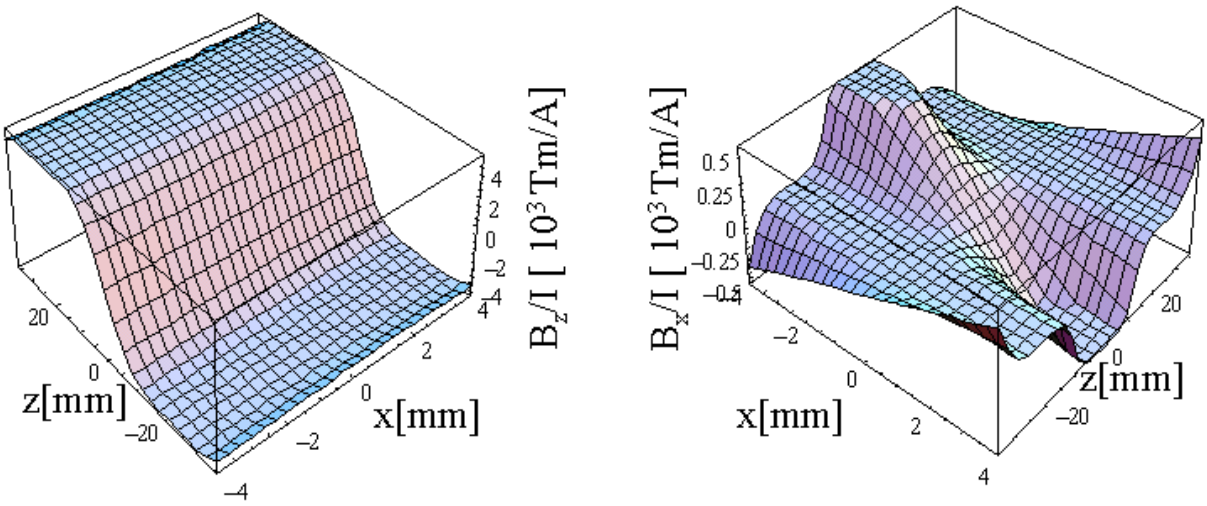

Figure A.4: $\frac{1}{I}B_z(x,z)$ and $\frac{1}{I}B_x(x,z)$ over the extraction distance for the pickup coils.

Appendix B

Heat transfer

B.1 Heat transfer by radiation

B.1.1 Emissive and absorbing properties of real surfaces

This section is inspired from [79] and [72]. Any material form at a temperature T emits thermal radiation. The radiation emitted by a solid is a surface phenomenon. Typically the emission originates from molecules which are within a distance of approximately 1 μm from the exposed surface. The radiation may be viewed as the propagation of electromagnetic waves. The wavelengths associated with the electromagnetic waves are in the range 0.1 μm 100 μm. Thus, the spectrum of thermal radiation extends from the UV to the infra-red. To understand the radiation characteristics of real surfaces, it is useful to introduce the concept of black body; the black body is an ideal surface with the following properties:

- A black body absorbs all incident radiation, regardless of wavelength and direction.
- At any temperature and wavelength, no surface can emit more than a black body.
- The emission is isotropic; the black body is a diffusive emitter.

The Stefan-Boltzmann law gives the emissive power of a black body per unit surface E_b and is expressed as:

$$E_b = \sigma T^4 \tag{B.1}$$

σ is the Stefan-Boltzmann constant and has the numerical value:

$$\sigma = 5.670 \cdot 10^{-8}\, W/m^2K^4 \tag{B.2}$$

This simple law enables the calculation of the amount of radiation emitted in all direction and over all wavelengths simply from knowledge of temperature of the black body. A black body is a perfect absorber and a perfect emitter and any radiative properties of real surfaces may be compared to this standard. Thus one defines a surface radiative property called the total hemispherical emissivity, as the total radiation emitted by the surface divided by the total radiation emitted by a black body at the same temperature. The total hemispherical emissivity is also simply named emissivity.

$$\varepsilon = \frac{E_{real}}{E_b} \tag{B.3}$$

Since no surface can emit more than a black body, the emissivity ε is always less than unity. The radiation leaving a surface might be the addition of some radiation coming from the thermal environment reflected by the surface and the radiation emitted by the surface itself at the temperature T. Therefore we need to express the reflective properties of a surface to get the total radiation leaving a surface. If a thermal radiation G [W/m^2] irradiates an opaque surface, only a portion α is absorbed. The radiation on an opaque surface is either reflected or absorbed, thus the reflected part of the radiation is connected to the absorbed one according to:

$$\alpha G + \rho G = G \tag{B.4}$$

α is the absorptivity and ρ is the reflectivity. A diffuse grey surface is a surface for which its absorptivity is equal to its emissivity (α=ε). Thus the emissivity of diffusive grey surface describes its emissive properties such as its absorber properties. The total thermal radiation leaving a diffusive and grey surface also named the radiosity J is:

$$J = \epsilon E_b + (1 - \epsilon)G \tag{B.5}$$

The net rate q at which radiation leaves the surface represents the net effect of radiative interaction occurring at the surface. It is the rate at which energy would have been transferred to the surface to maintain it at a constant temperature. It is equal to the difference between the surface radiosity and irradiation:

$$q = S \cdot (J - G) \tag{B.6}$$

For a diffusive grey surface q is expressed as:

$$q = \epsilon S \cdot \frac{E_b - J}{1 - \epsilon} \tag{B.7}$$

Therefore, to solve the radiation exchange between surfaces underlies to need to solve the radiosity for each surface.

B.2 Forced heat convection in a circular tube

On a practical level, to solve a convection heat transfer problem, one replaces the usual variables as temperature or fluid velocity by dimensionless variables [79], [72]. The solution found for dimensionless variables is called the functional form. Building dimensionless variables of a specific heat transfer problem allows using the functional form of solution found for such dimensionless variables. The dimensionless variables necessary to solve a heat transfer by convection are the Nusselt number, the Reynolds number and the Prandtl number.

The dimensionless variable which corresponds to the convection coefficient h is the Nusselt number and is defined as:

$$N_{uD} = \frac{hD}{k_f} \tag{B.8}$$

k_f is the thermal conductivity of the fluid, D is the diameter of the refrigerant channels. The Reynolds number R_{eD} is the dimensionless variable which describes the flow. R_{eD} is the ratio of the inertia and viscous forces and is defined as:

$$R_{eD} = \frac{\rho V D}{\mu} \tag{B.9}$$

V is the velocity of the fluid, ρ the mass density and μ the viscosity. In any flow there small disturbances exist which can be amplified to produce turbulent conditions. For small Reynolds number R_{eD}, viscous forces are large enough compared to the inertia forces to prevent this amplification. The flow is laminar. But, with the increasing Reynolds number, the viscous effects become less significant compared to the inertia effects, and small disturbances may be amplified so that transition occurs. The flow is then turbulent. The Prandtl number is the ratio of the momentum and thermal diffusivity. It measures the relative effectiveness of the momentum and energy transport in the fluid and is defined as:

$$P_r = \frac{c_p \mu}{k_f} \tag{B.10}$$

c_p is the thermal capacity of the fluid. The Nusselt number N_{uD} depends on the fluid and on the flow. Indeed different fluids may have different effectiveness to drive the thermal flow. Moreover the thermal transfer in the fluid may differs when the flow is either laminar or turbulent. Therefore one looks at a solution where the Nusselt number must be a functional form *f* such that [79]:

$$N_{uD} = f(R_{eD}, P_r) \tag{B.11}$$

When considering a forced convection in a circular tube, the Nusselt number is analytically determined only for laminar flow with a constant thermal flux at the surface [79]:

$$h = \frac{48}{11}\left(\frac{k}{D}\right) \tag{B.12}$$

For turbulent flow, it becomes difficult to analytically solve problems. Empirical solutions are used. The empirical solution for a turbulent flow in a circular tube is known as the Dittus-Boelter equation. The Dittus-Boelter equation is expressed as [79]:

$$N_{uD} = 0.023 R_{eD}^{4/5} P_r^{2/5} \tag{B.13}$$

The solution has been confirmed experimentally for the range of conditions:

$$0.7 \leq P_r \leq 16700 \qquad R_{eD} \geq 10000 \qquad \frac{L}{D} \geq 10 \tag{B.14))}$$

Appendix C

Heat transfer measurement

In subchapter 3.3 we detail the model we use to set the CPMU temperature. In the model the girder emissivity and the surface exchange, involved in the convection heat transfer, are undetermined. We present hereafter the measurements which have been done to experimentally determine these parameters.

C.1 Total thermal flux

The value of the girder emissivity, necessary to compute the flux which enters the girders by radiation, has been derived from the measurement of the total thermal flux.

We detail in section 3.1.2 the cooling system; it operates in 2 stages. The liquid nitrogen flowing into the closed loop carries away the total thermal power that enters into the girders. The heat exchanger, which is located between the closed loop and the sub cooler, transfers this thermal power to the sub cooler. This thermal power evaporates the liquid nitrogen in the bath. Finally the measurement of the liquid nitrogen evaporation in the bath also measures the total thermal flux that enters into the girders. Consequently a nitrogen flow meter is connected to the sub cooler bath and measures the liquid nitrogen mass rate $\dot{m}$ that is evaporated. This measurement is proportional to the total thermal flux $\dot{Q}$ that the sub cooler extracts:

$$\dot{Q} = \dot{m}L \tag{C.1}$$

L is the nitrogen heat of evaporation, the energy required to transform a given quantity of a liquid nitrogen into a gas at boiling point and at atmospheric pressure. The nitrogen heat of evaporation is 199 kJ/kg. However the thermal flux measured in such way also includes the internal loss. The internal loss is the heat transfer which is necessary to maintain the cooling system itself at cryogenic temperature. A short circuit on the closed loop allows its measurement. The thermal power is measured at the thermal balance, without heating. A total thermal power of 204 W has been measured with an internal loss of 50 W at 120 K. The total thermal flux which enters the girders is then 150 W at 120 K. A similar measurement done at 150 K gives a 135 W thermal flux.

C.2 Thermal flux through a spacer

Conduction and convection are involved in the heat transfer throughout a spacer. The conduction occurs in the slim C-shape spacers while a convective exchange at the cooling pipe surface transfers the thermal flux to the liquid nitrogen. We simply determine the thermal flux through the spacer by measuring the temperature drop with two platinum probes fixed at its extremities. Figure C.1 represents the temperature drop and thermal flux through the spacer. The thermal flux per spacer is maximum when the temperature drop is maximum; that is at the transition stage of nitrogen from liquid to gas. Once the magnetic assembly is cooled, one changes the flux extracted thanks to the heating system. The flux varies from 2 W to 4 W.

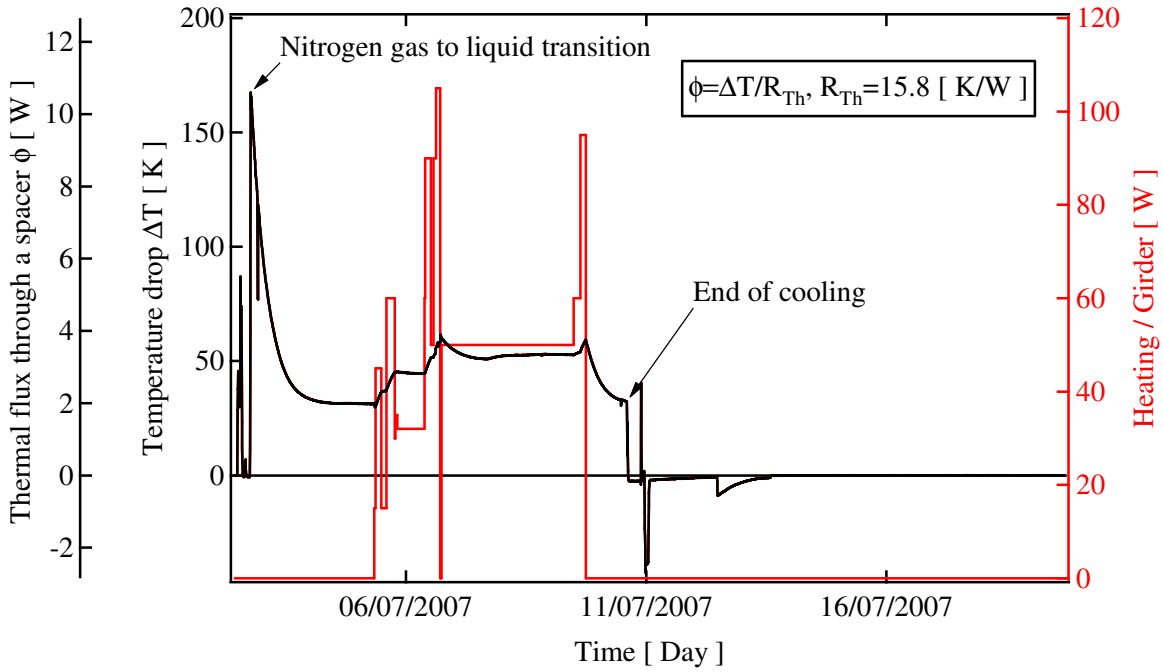

Figure C.1: Temperature measured with platinum probe on each extremity of a spacer.

Figure C.2 represents the temperature measured with the platinum probe fixed to the Copper half shell. The abrupt fall observed in Figure C.2, corresponds to the nitrogen gas to liquid transition. The temperature measured on the half shell is then 85 K; the nitrogen temperature within the inner loop is 80 K. As discussed in section 3.3.3, the convection at the cooling pipe surface causes this temperature gradient. Since the Newton law relates this temperature drop to the thermal flux, one derives from this temperature measurement the surface exchange, assuming the temperature is constant in the half shell. However the temperature measured on the half Copper shell is higher than the temperature at the interface; the surface computed with this temperature is then the upper limit. One finds a 100 mm^2 for the surface exchange. Varying the frequency changes the convection exchange parameter h while it has no effect on the thermal flux to be evacuated; finally it causes an artificial jump on the exchange surface.

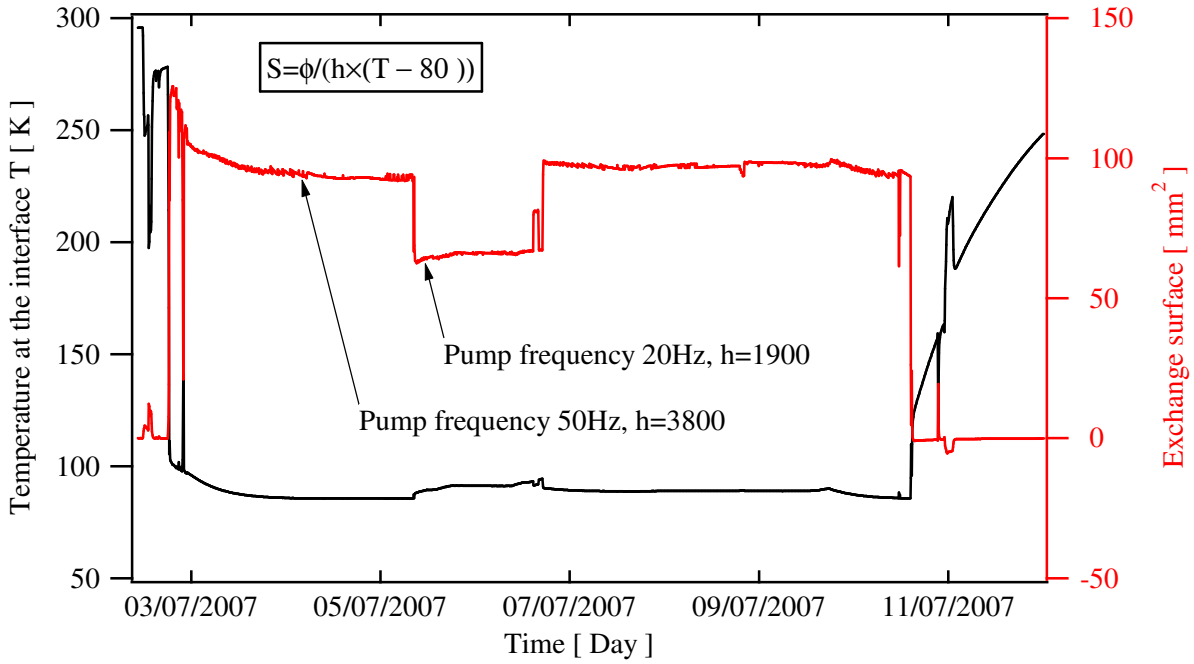

Figure C.2: Temperature at the interface (black curve) and exchange surface (red curve).

Appendix D

Measurement of the rail deflection

Three angles characterize the rail deflection: the yaw θ, the rolling ψ and the pitch ϕ. The yaw θ is the rotation angle around the vertical axis, the rolling ψ around the horizontal axis and the pitch ϕ around the longitudinal axis. They are defined in Figure D.1. The rail deflection causes positioning errors along the three axes so that one would theoretically measure these three angles to properly recover the Hall probe position. However we neglect the small horizontal position errors since we measure the planar undulator field along its axis. Indeed the planar undulator field is independent of the horizontal position around its longitudinal axis.

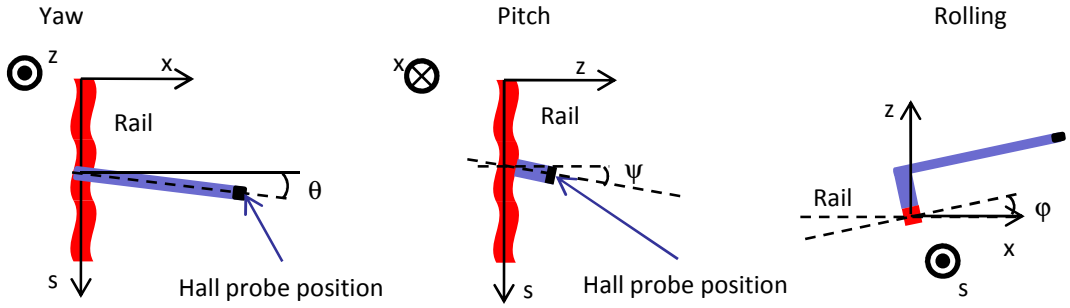

Figure D.1: The yaw, the pitch and the rolling are the three angles which fully characterize the rail deflection.

D.1 Angle measurement

On a practical level, we use laser interferometer to characterize the rail deflection. The laser is a Renishaw ML10 laser. The reflectors and the beam splitter used are schematically drawn in Figure D.2. ML10 laser allows an angular measurement with an accuracy (resolution) of 0.7 µrad (0.1 µrad). The accuracy (resolution) of the position measurement is 0.7 µm (0.001 µm). Several experimental setups allow the measurement of:

- the longitudinal position. The experimental setup build is then the so-called Michelson interferometer.
- the yaw and the pitch angles. According to the retro reflectors and the beam splitter orientation, one measures either the yaw or the pitch.

The reflector position on the Hall probe carriage is displayed in Figure D.2. L_x is the horizontal distance between the rail and the Hall probe. In the small angle approximation, the differences between the reflector and the Hall probe positions are related to the rail deflection and the distance between the Hall probe position and the rail as follows:

$$\begin{aligned} ds &= s_{Hall} - s = L_x \cdot \theta(s) \\ dz &= z_{Hall} - z = L_x \cdot \varphi(s) \end{aligned} \qquad \text{(D.1)}$$

ds and dz are respectively the longitudinal and the vertical position difference between the Hall probe position (z_{Hall}, s_{Hall}) and the reflector position (z, s). The position delay (dz, ds) has been measured with the ML10 interferometer when the Hall probe carriage is moved along the rail.

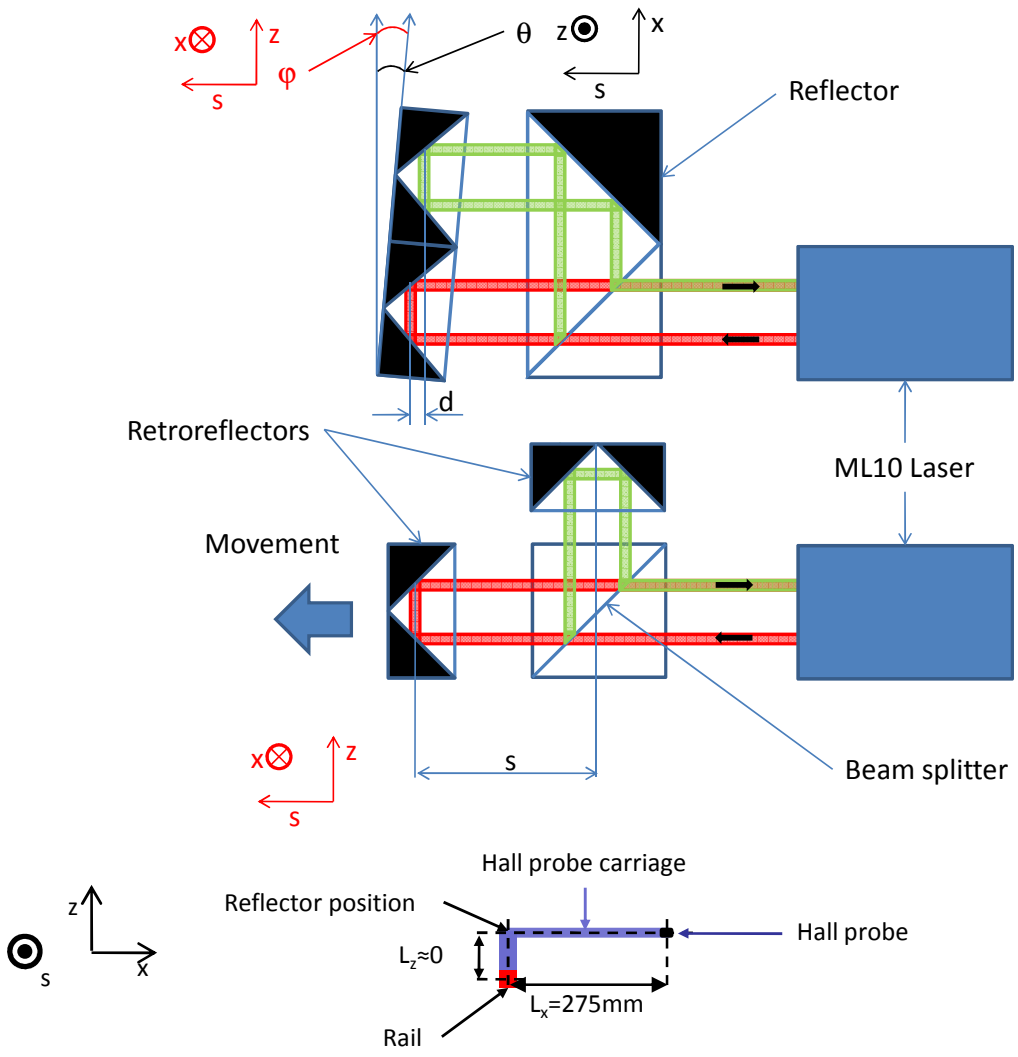

Figure D.2: ML10 laser, retro reflector and beams splitter used for the yaw, pitch and position measurement.

D.2 Straightness measurement

Another set of reflector and beam splitter allows the transverse position measurement. Usually one calls the transverse position measurement, the straightness measurement. The reflector and the beam splitter dedicated to the straightness measurement are drawn in Figure D.3. The orientation along both vertical and horizontal axis of the retro reflector and the beam splitter, allows vertical and horizontal straightness measurement. With this experimental setup, any relative displacement along the straightness axis is captured. If necessary, one deduces the rail rolling from vertical and horizontal straightness measurement. The accuracy (resolution) of the straightness measurement is 2 µm (0.01 µm).

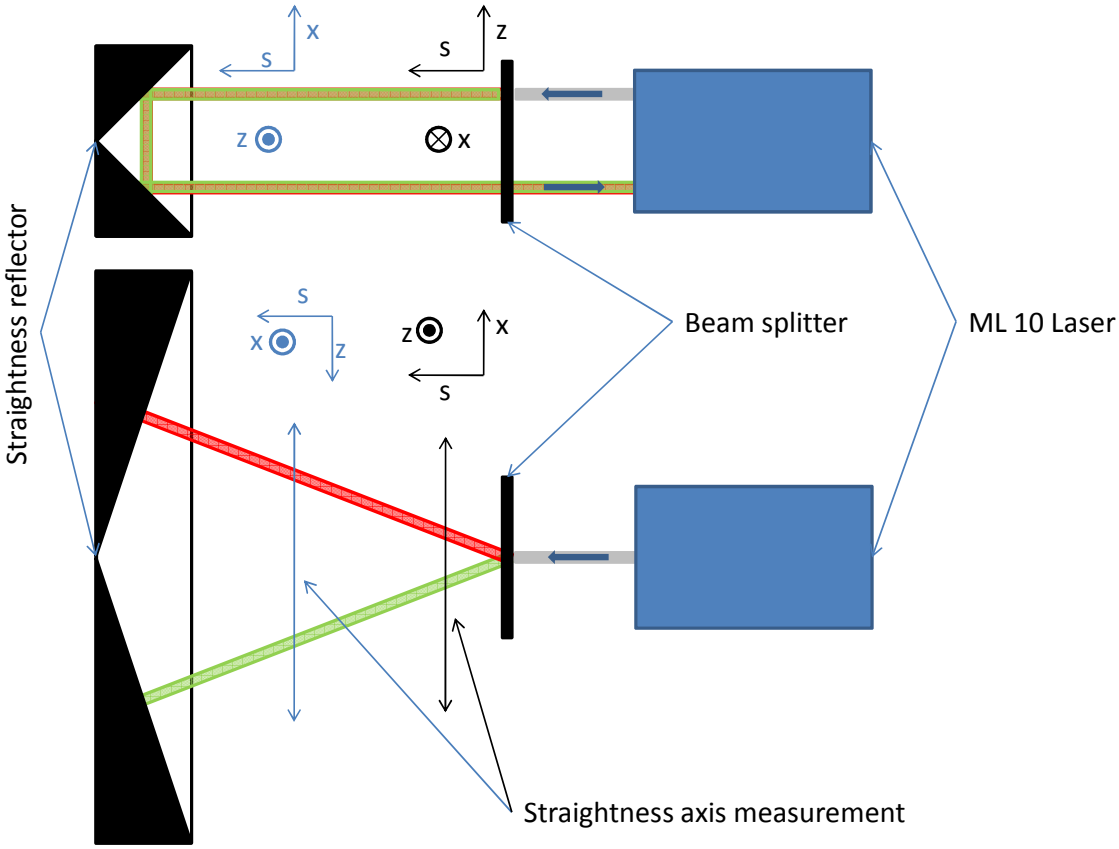

Figure D.3: Retro reflector and beam splitter for a straightness measurement.

D.3 Experimental setup

The experimental setup put into place to characterize the rail deflection is displayed in Figure D.4. The yaw and the pitch are measured closed to the optic rule position. The straightness is measured closed to the Hall probe position. The optic rule measures the longitudinal position of the mobile carriage whereas the ML10 laser measures the rail deflection at the mobile carriage. The timer system triggers both laser systems. Finally the mobile carriage is moved along the rail to record the deflection along the rail. We mount the reflector on the mobile carriage to perform the angle measurement. The beam splitter is then at a fixed position. We mount the beam splitter on the mobile carriage to perform the straightness measurement, the reflector is then at a fixed position.

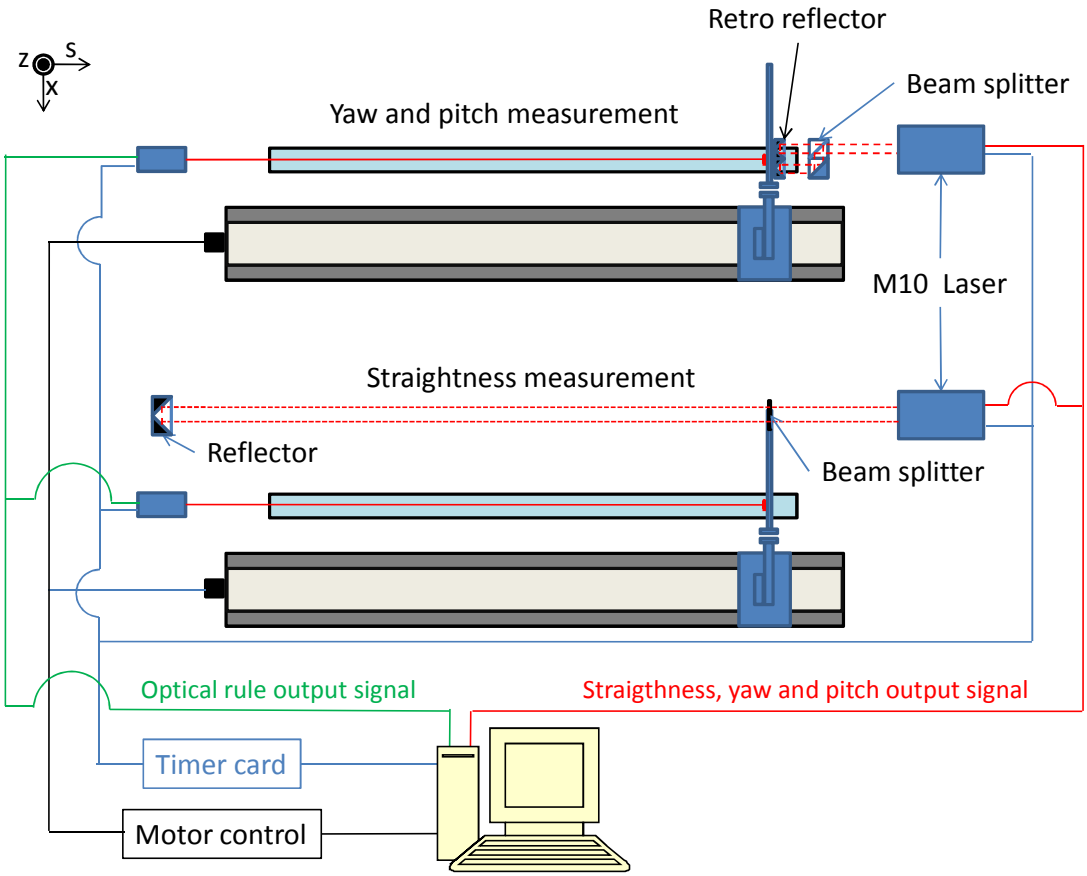

Figure D.4 : experimental setup to characterize the yaw, the pitch and the transverse straightness of the rail.

Appendix E

Measurement and control of the temperature

Alongside the in vacuum magnetic measurement bench, instrumentation is necessary to vary and measure the undulator temperature. The instrumentation presented here includes standard cryogenic elements, such as thermocouples.

E.1 Thermal sensor

Two different types of thermal sensor are installed along the girders:

- K type thermocouples made of Nickel-Chromium and Nickel-Aluminium. At cryogenic temperature, the T type thermocouple would have been the natural choice. T type thermocouples are made of Copper Constantin wires; however to avoid possible thermal leaks through the thermocouples we use a K type thermocouple since this one has a lower thermal conductivity. The suitable temperature domain for the K thermocouple is between 73 K and-1300 K.
- Platinum probes. Platinum probes are calibrated; they are commonly used as absolute thermometer. Thermocouples are more robust. Numerous thermocouples, distributed on girders and on the magnets support structure, measure the temperature profiles along the magnetic assembly.

A few platinum probes are placed closed to the thermocouples in order to calibrate measurement of the thermocouples. Figure E.1 displays two thermocouples screwed on a magnet support. Figure E.2 details the thermocouple fixation on the upper girder.

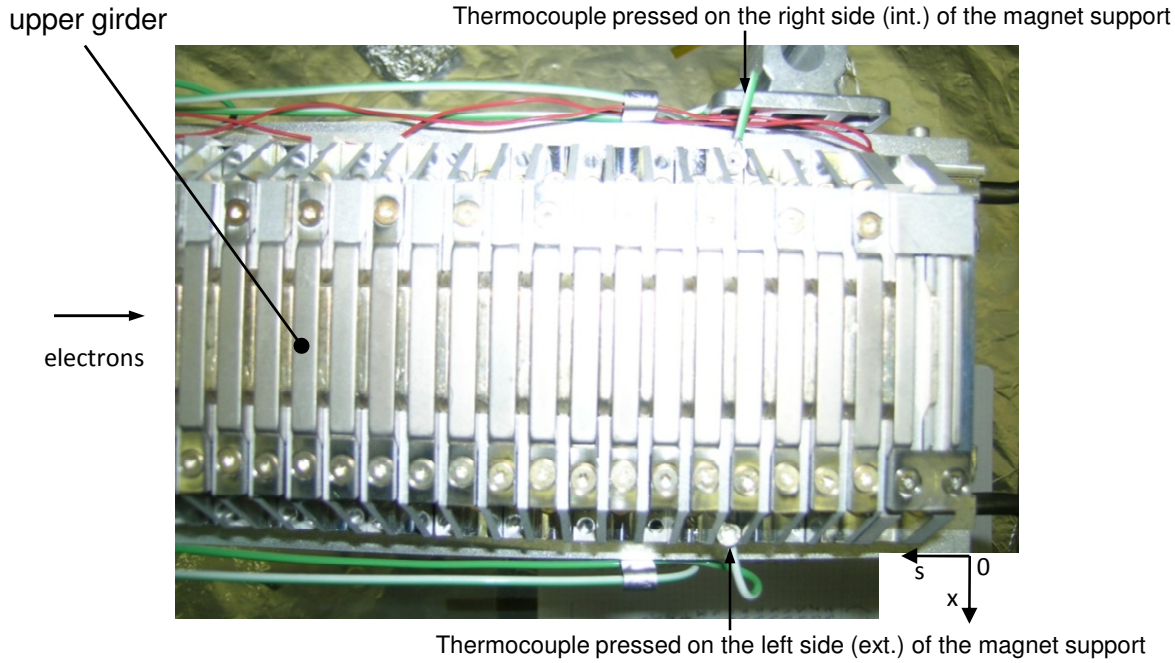

Figure E.1: Detail of two thermocouples pressed on a magnet support. The thermocouples are fixed on both sides of the magnet support. We label ext./int. the thermocouples located on the left/right of the assembly. The point 0 on the photo is the origin.

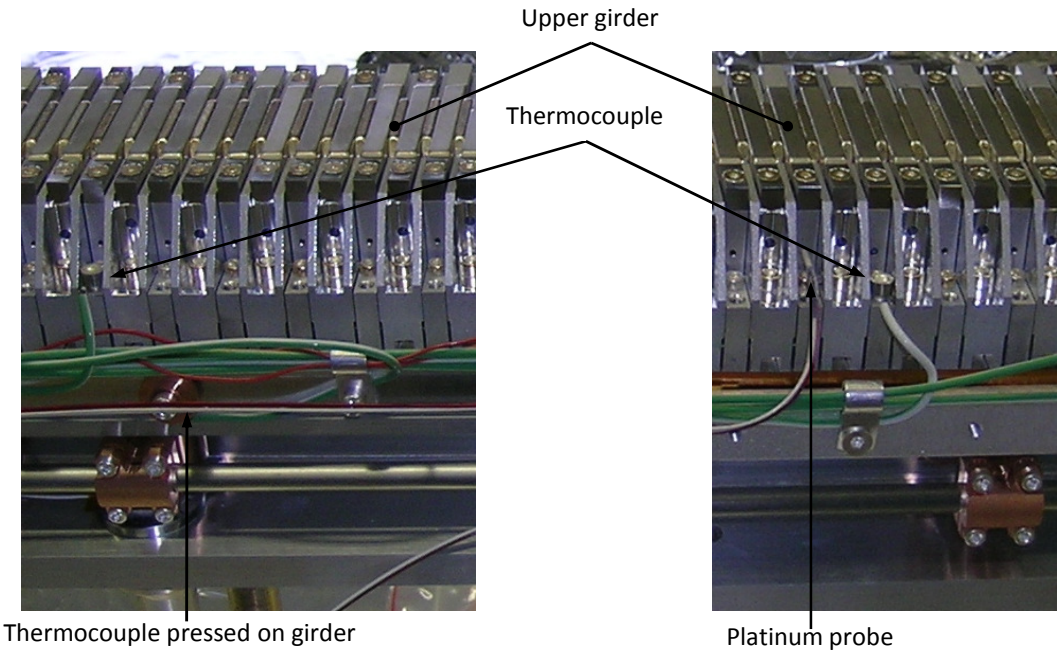

Figure E.2: Detail of thermocouples pressed on a magnet support and the upper girder (left plot). Some Pt100 are placed closed to thermocouples in order to calibrate the thermocouple measurements (right plot).

Table E.1 and Table E.2 list the different positions of the thermal sensors installed on each girder. The thermocouples located at the extremities of the girders, at the positions 0 and 2.03 m are fixed on the Copper block. As shown in Figure E.3, these Copper blocks stretch a thin Ni-Cu foil on the surface of the magnets. Actually the Cu-Ni foil wasn't installed during the magnetic measurement session as they were incompatible with the gap measurement.

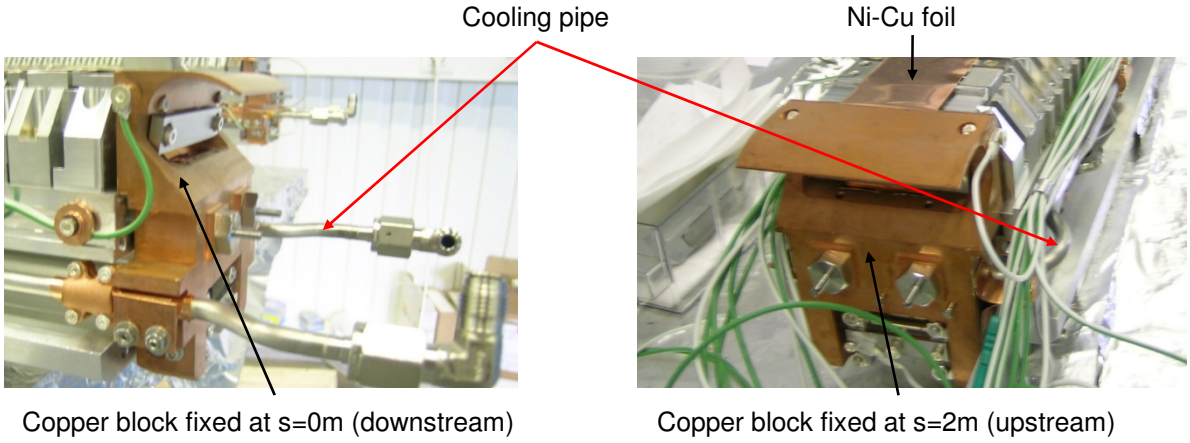

Figure E.3: Copper blocks fixed at girder extremities. The blocks ensure the tension of a thin Copper foil. These devices are necessary to protect the beam from instabilities.

Table E.1: Nature, position and label of probes fixed on magnet supports for each girder.

Magnet support-lower girder			
Therm. Pos. [mm]		Plat. probes Pos. [mm]	
Int.	Ext.	Int.	Ext.
	0.01		
0.26			
	0.58	0.58	
1			1
	1.45	1.45	
1.72			
	1.95		

Magnet support-upper girder			
Therm. Pos. [mm]		Plat. probes Pos. [mm]	
Int.	Ext.	Int.	Ext.
0.08	0.08		
0.1			
	0.3		0.28
0.6			
			1.03
1.32			
	1.45		
1.48			
	1.8		
1.97			

Table E.2: Nature, position and label of probes fixed on each girder.

Lower girder			
Therm. Pos. [mm]		Plat. probes Pos. [mm]	
Int.	Ext.	Int.	Ext.
0			
0.13			
		0.96	
	1.41		
1.52			
2.03		2.03	

Upper girder			
Therm. Pos. [mm]		Plat. probes Pos. [mm]	
Int.	Ext.	Int.	Ext.
0		0	
	0.57		
0.66	0.66		
1.56			
2.03			

E.1.1 Control of the CPMU temperature

Typically one needs to change the CPMU temperature from 120 K to 180 K in order to experimentally determine its optimal value. As explained in chapter 3, the sub cooler fixes the cooling system temperature and then prevents any control of the magnetic assembly temperature with the nitrogen temperature. The parameter to play around is the total thermal flux that the spacers evacuate; we include a heating system with the girders in order to increase the thermal flux. This scenario implies first of all cooling the magnetic assembly at 120 K; the heating system sets the CPMU temperature at a higher value. The heating system consists of 16 wire-wound silicone rubber heaters from MINCO, which are distributed along the girders. At cryogenic temperature, the 16 thermofoils provide thermal flux up to 200 W per girder. One thermofoil is shown in Figure E.4. The Aluminium bore presses the thermofoil on the girders.

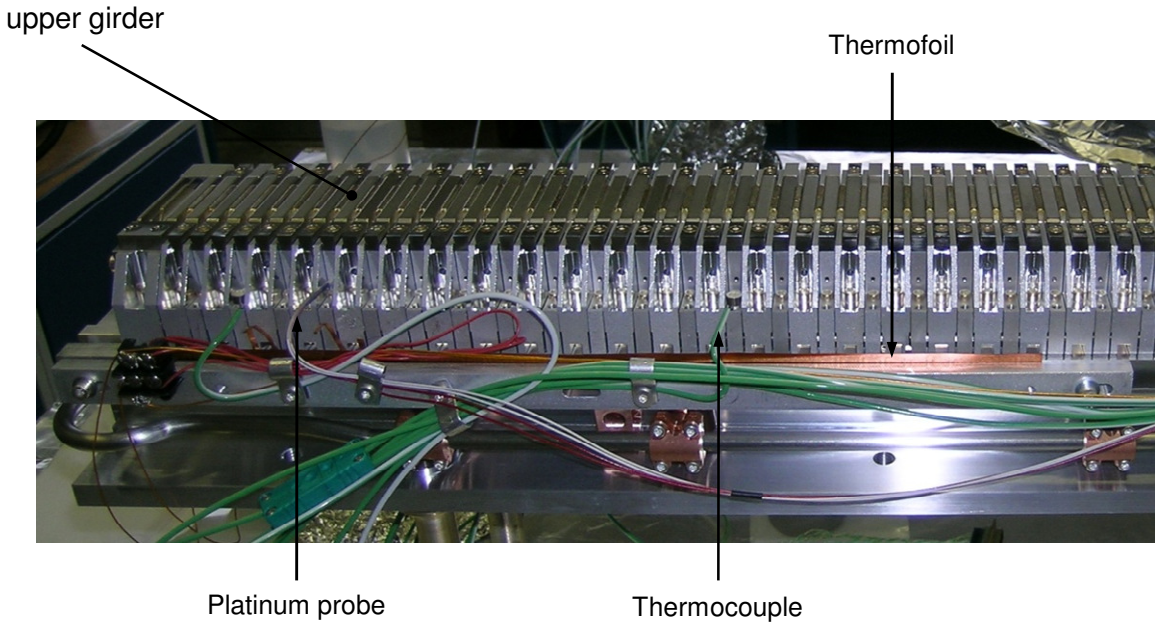

Figure E.4: Detail of a thermofoil fixation. An Aluminium bore screwed to girders, squeezes the thermofoil to ensure good thermal contact between the heating system and the girder. 6 thermofoils are distributed along each girder, 3 on the left/int. and 3 right/ext.

E.1.2 Junction inversion in K thermocouples

The junctions between the thermocouples are realized thanks to the vacuum to air throughout photographed in Figure E.6. Unfortunately, there is a mismatch: instead of providing a Ni/Ni junction, the junction ensures a Ni/Cr junction as represented in Figure E.6. Since these junctions are glued in the throughout, it is impossible to correct the inversion.

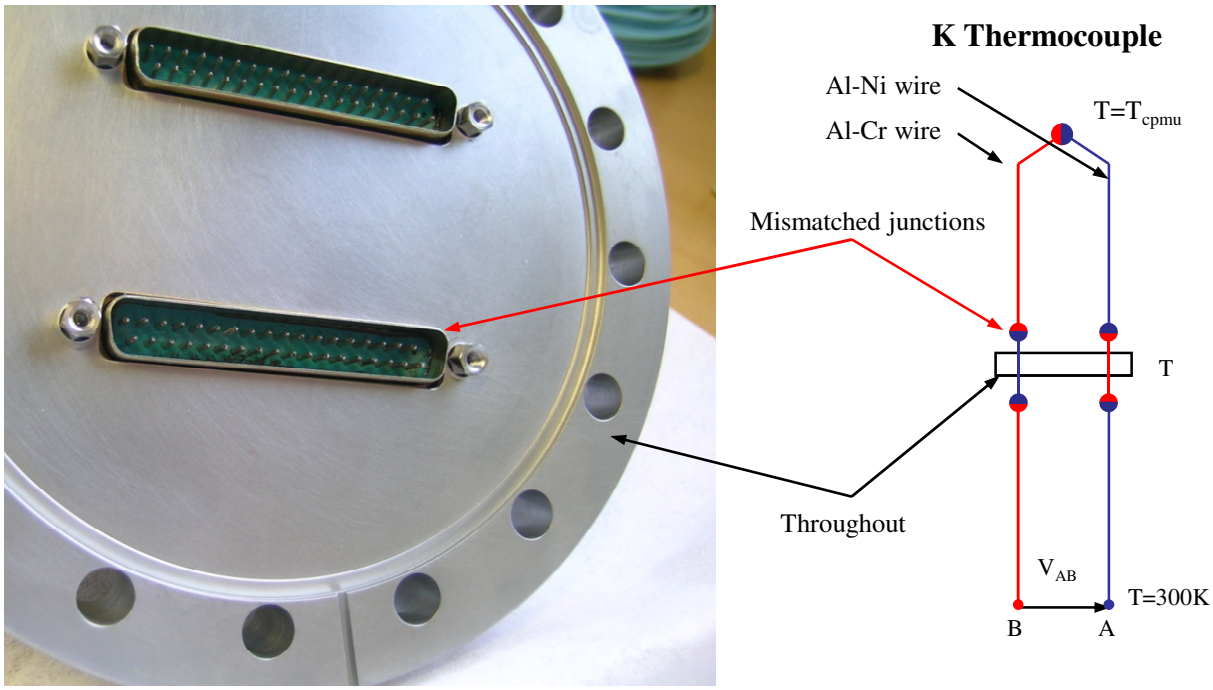

Figure E.5: throughout with mismatch junctions (left photo). The equivalent electric circuit which results from this mismatch is represented on the right.

The electrical circuit equivalent to a thermocouple is also represented in Figure E.6. The voltage along the thermocouple is:

$$V_{AB} = V_{Cr-Al}\left(T = T_{cpmu}\right) + 2\left(V_{Cr-Al}(T = 300K) - V_{Cr-Al}(T)\right) \quad \text{(E.1)}$$

Figure E.6 compares the temperature measured with a thermocouple and a Platinum probe. Both sensors are fixed on a magnet support of the upper girder, 2 cm away from each other. Hence one would expect the temperature measured with both sensors to be similar. As long as the throughout is at ambient temperature, the voltages of the junctions cancel each other out. A small temperature gradient at the throughout causes the temperature offset between the thermocouple and the platinum probe as the magnetic assembly is cooled at cryogenic temperature. In addition the alimentation wires of the heating system are located close to the thermocouples throughout. Current of several amperes goes through the wires and the thermofoils when one turns on the heating. Because of the Joule effect, the wires radiate a few joules to the thermocouples throughout and the temperature at the Ni-Cr/Ni-Al junctions increases. However the junctions measure this temperature variation as a temperature decrease since its polarity is inversed. It makes measurements of the thermocouples useless for a thermal analysis.

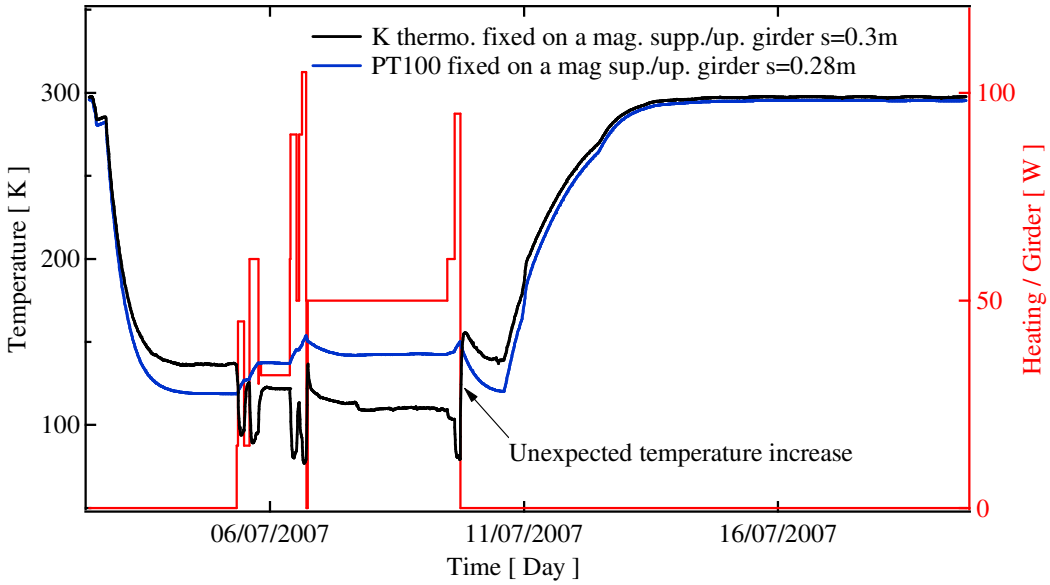

Figure E.6: Temperature measured with a Platinum probe (black curve) and a thermocouple (blue curve). The distance between both sensors is less than 3 cm. The heat provided by the thermofoils is reported (red curve).

Appendix F

Traduction et résumé des chapitres

F.1 Résumé

Un nouveau concept d'onduleur courte période et fort champ a été proposé par Toru Hara à SPring-8 en 2004 : l'onduleur cryogénique à aimants permanents (CPMU). Il s'agit de refroidir des aimants Néodyme-Fer-Bore autour de 150 K. Cela permet d'utiliser ces aimants qui ont une rémanence jusqu'à 40% supérieure à celle des aimants utilisés conventionnellement dans les onduleurs.

Pour évaluer les difficultés technologiques et la faisabilité de tels onduleurs, un CPMU de 2 m de long et de 18 mm de période a été lancé à l'ESRF. Ce travail présente le design et la réalisation du CPMU à l'ESRF. Un modèle magnétostatique du CPMU est présenté, il est basé sur des mesures de courbe d'aimantation à température cryogénique réalisées au laboratoire Louis Néel. Le modèle prévoit une augmentation du champ crête de l'onduleur de 8% autour de 150 K et de l'intégrale de champ de 20 Gcm. Un banc de mesure magnétique spécifique a également été développé à l'ESRF. Ce banc permet la mesure du champ local et des intégrales de champ sous vide. Son design et sa construction sont revus. Finalement les mesures magnétiques réalisées à température ambiante et à température cryogénique sont présentées. Ces mesures valident le modèle magnétostatique et les performances attendues.

F.2 Chapitre 1: Introduction

Les scientifiques utilisent la lumière, et en particulier les rayons X, dans de multiples domaines de recherche afin de sonder les matériaux et de découvrir leurs propriétés fondamentales. On utilisait traditionnellement des « tubes » pour produire ces rayons X, jusqu'à la découverte du Rayonnement Synchrotron (RS). Le RS, à savoir le rayonnement électromagnétique émis par un électron relativiste dans un champ magnétique, a profondément changé la manière dont les rayons X sont produits.

Les sources de Rayonnement Synchrotron

C'est en 1898 que Liénard et Wiechert ont introduit pour la première fois la théorie du RS. Ils ont alors déterminé l'expression de la perte d'énergie subie par un électron lors du mouvement circulaire induit par le RS [1]. Toutefois le RS n'a été observé en pratique que 50 ans plus tard, avec l'apparition des premiers faisceaux d'électrons ultra relativistes [2]. Après la Seconde Guerre Mondiale, les accélérateurs de particules ont connu un intense développement. C'est en 1947 que le RS a été observé grâce au tout premier synchrotron à électrons : le synchrotron à électrons de 70 MeV du laboratoire de la compagnie General Electric [3].

A l'époque, les accélérateurs avaient pour but de produire des particules à haute énergie pour la physique nucléaire et de la physique des hautes énergies. Toutefois on a rapidement considéré que l'intense lumière produite dans les synchrotrons à électrons pouvait avoir des aspects intéressants dans d'autres domaines de la physique [4]. Bien que les accélérateurs n'aient pas été dédiés au RS, les scientifiques ont d'abord profité du RS émis dans les aimants de courbure pour leurs expériences.

Au vu du nombre croissant d'utilisateurs, la deuxième génération de sources de RS a été construite à la fin des années 70. Il s'agissait d'accélérateurs dédiés à la production de RS au moyen d'aimants de courbure; le faisceau d'électrons était stocké dans un anneau de stockage à son énergie nominale. Les

utilisateurs étaient installés dans des laboratoires situés à quelques dizaines de mètres des aimants de courbure. Ils y collectaient le RS émis continuellement. Finalement, la troisième génération de source de rayonnement synchrotron a été construite à la fin des années 80. La localisation des principales sources de RS de deuxième (CHESS, HASYLAB, SSRC) et troisième génération (ESRF, SOLEIL, DIAMOND, SPring-8, APS…) est indiquée dans la Figure F.1 [5]. L'énergie des électrons dans les différentes sources de RS varie de 1 GeV à 8 GeV.

Figure F.1: Localisation des sources de RS déjà en opération ou planifiées autour du monde, image issue du site web de SOLEIL (http://www.synchrotron-soleil.fr/portal/page/portal/Soleil/Liens).

Les sources de troisième génération combinent :

1. Un faisceau d'électrons à fort courant avec une faible émittance (petite taille et faible divergence). Un tel faisceau d'électrons est nécessaire pour produire un RS ponctuel et intense. Le courant d'électrons stocké dans l'anneau de stockage est de quelques mA et l'émittance est de l'ordre du nanomètre radian.
2. L'utilisation d'Eléments d'Insertion (EI) pour produire un RS très intense. Les EI sont des assemblages magnétiques qui produisent un champ magnétique périodique. Le champ est perpendiculaire à la direction de l'électron en mouvement ce qui lui donne un mouvement oscillatoire. Comparativement aux aimants de courbure, le flux de RS émis dans un EI a une magnitude 2 à 3 fois plus forte. Les EI sont installés dans ce qui est appelée « la portion droite », i.e. une portion de l'anneau de stockage sans aimant pour focaliser et diriger le faisceau le long de l'anneau de stockage.

La Facilité Européenne pour le Rayonnement Synchrotron (ESRF) fait partie des sources de RS de troisième génération. L'accélérateur du complexe de l'ESRF est composé d'un linac, d'un booster et d'un anneau de stockage. Le faisceau d'électrons est d'abord accéléré à 200 MeV dans le linac. Il est ensuite transféré dans le booster où il est accéléré à 6 GeV, son énergie nominale. Enfin le faisceau est injecté dans l'anneau de stockage où il reste stocké à son énergie nominale. Le complexe de l'accélérateur de l'ESRF est représenté schématiquement dans la Figure F.2. Il est en opération depuis 1992. Le Tableau F.1 liste les principaux paramètres de l'ESRF.

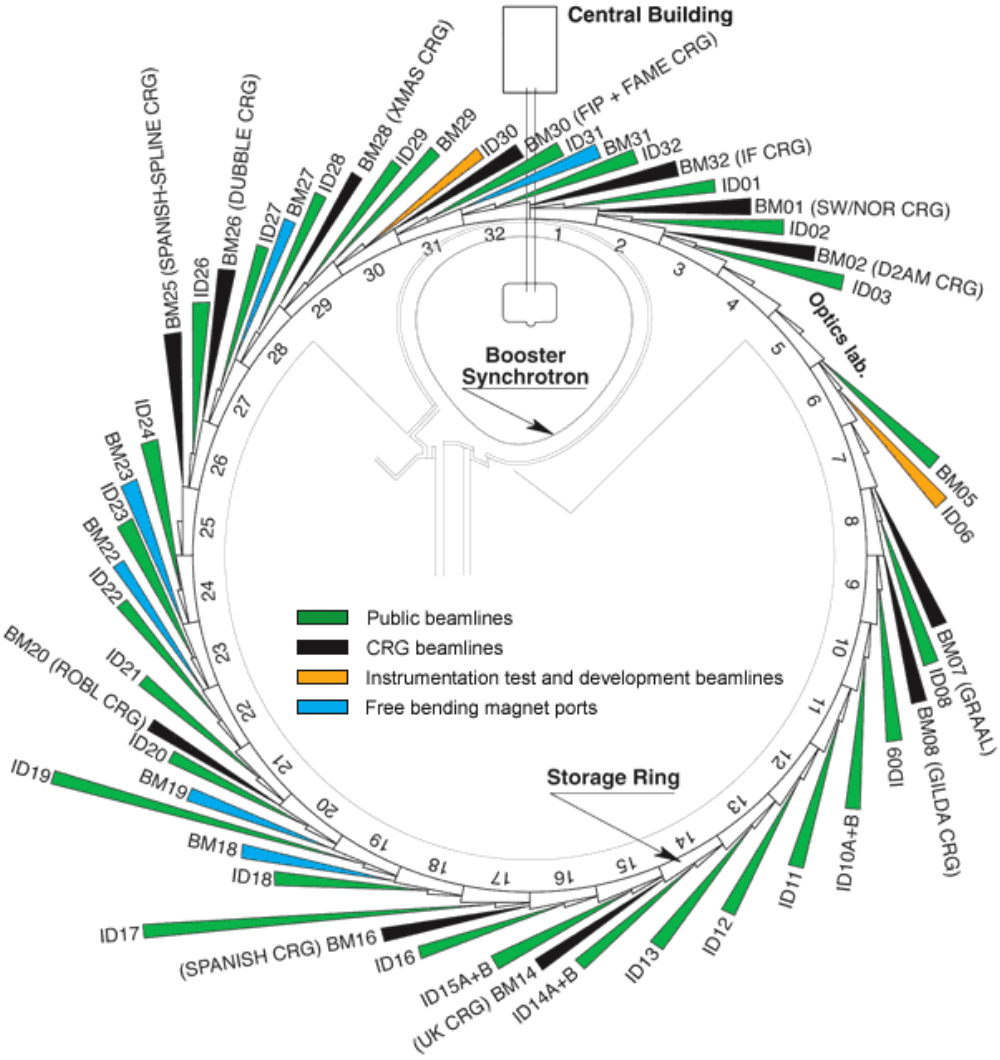

Figure F.2: Représentation schématique du complexe d'accélérateurs de l'ESRF et des lignes de lumières sur lesquelles les utilisateurs sont installés pour collecter le RS.

Tableau F.1: Principaux paramètres du faisceau d'électrons dans l'anneau de stockage de l'ESRF.

	Emittance [nm rad]	Taille RMS (section paire/impaire) [µm]	Divergence RMS (section paire/impaire) [µm]
Vertical	0.04	7.9/8.3	3.2/3
Horizontal	4	402/59	10.7/90

Développement des Eléments d'Insertion

Le RS émis par des électrons ultra relativistes soumis à un mouvement oscillatoire dans un EI a été étudié dès les premières années qui ont suivi l'observation du RS au laboratoire de la compagnie General Electric [6], [7]. Il existe deux types de RS émis dans un EI : le rayonnement de régime onduleur ou de régime wiggler.

Le régime wiggler se caractérise par un spectre large: il va de l'infrarouge aux rayons X. En ce qui concerne le régime d'onduleur le spectre se réduit à une série de pics dont l'amplitude excède celle du

régime wiggler de deux ordres de grandeur. Ceci est le résultat d'un processus d'interférence qui se produit dans ce régime.

Les EI sont appelés wigglers ou onduleur selon les propriétés du RS qu'ils émettent. Les onduleurs produisent un champ moyen de courte période, alors que les wigglers fournissent un fort champ de longue période. Les EI ont connu un fort développement technologique depuis le début des années 80, grâce à la disponibilité commerciale d'aimants ultra performants, faits de Samarium-Cobalt ($SmCo_5$, Sm_2Co_{17}) et, plus récemment, d'aimants au Néodyme-Fer-Bore ($Nd_2Fe_{14}B$). Le Tableau F.2 récapitule les propriétés majeures des onduleurs et des wigglers installés à l'ESRF.

Tableau F.2: Principaux paramètres des éléments d'insertion installés à l'ESRF.

	Period	Champ crête	Étendue du spectre
Onduleur	<40 mm	<1 T	1-100 keV
Wiggler	>70 mm	>1 T	1-150 keV

A l'ESRF, compte tenu de la technologie actuelle des onduleurs, on fournit aux utilisateurs un intense flux de photons, jusqu'à 100 keV. On utilise les wigglers pour produire un flux de photons à une énergie plus grande, ils permettent d'étendre le spectre jusqu'à 150 keV. Par conséquent, des onduleurs à période courte et fort champ sont nécessaires pour étendre le spectre de l'onduleur jusqu'à un tel niveau d'énergie. En 2004, un nouveau type d'onduleur à courte période et fort champ a été proposé à SPring-8 : l'Onduleur Cryogénique à Aimants Permanents (CPMU) [8]. Il s'agit là d'un onduleur constitué d'aimants Néodyme-Fer-Bore refroidis à température cryogénique. Cette technologie permet de sélectionner des aimants $Nd_2Fe_{14}B$, dont la rémanence peut être jusqu' à 40% plus forte que celle des aimants utilisés dans les onduleurs conventionnels. Un prototype de CPMU à l'échelle 1 pour 1 a été construit à l'ESRF afin de découvrir les difficultés technologiques inhérentes à la construction d'un EI de 2 m de long refroidi à température cryogénique. Cette thèse traite du design et de la construction de ce CPMU, à l'ESRF.

Le Chapitre 2 est consacré à la technologie des éléments d'insertion. Les propriétés des wigglers et des onduleurs y sont étudiées. Nous y présenterons les solutions pour construire, mesurer et corriger les EI.

Dans le chapitre 3, nous introduirons le concept de CPMU et nous détaillerons le design de celui-ci. Nous insisterons sur le modèle magnétostatique du CPMU et sur le modèle thermique. La sélection de la température à laquelle l'assemblage magnétique doit être refroidi est faite en fonction du modèle magnétostatique. Nous évoquerons ensuite les effets thermomécaniques sur l'assemblage magnétique.

L'onduleur est assemblé et corrigé à l'air et à température ambiante, afin d'en faciliter la production. Nous présenterons dans le chapitre 4 la méthodologie utilisée à l'ESRF pour ce faire, ainsi que l'intégrale de champ et l'erreur de phase après correction.

Toutefois, le CPMU est destiné à opérer à une température cryogénique ; de ce fait, d'autres erreurs peuvent arriver à basse température. Afin de valider les corrections effectuées à température ambiante, un banc de mesure compatible avec des températures basses est donc nécessaire. Ce point sera abordé dans le dernier chapitre, en insistant sur le banc de mesure magnétique développé à l'ESRF pour effectuer les mesures à température cryogénique. Enfin nous comparerons les mesures magnétiques avec le modèle théorique.

F.3 Chapitre 2: Propriétés et utilisation des éléments d'insertion

Nous posons ici les bases du Rayonnement Synchrotron (RS), i.e. le rayonnement émis par un électron ultra relativiste dans un champ magnétique. Les propriétés fondamentales du RS sont introduites: la brillance, le flux et la polarisation. Nous caractérisons ces propriétés pour le rayonnement d'un électron ultra relativiste dans un onduleur et dans un wiggler. Enfin nous introduisons l'erreur de phase RMS et les intégrales de champ. La première permet de mesurer la réduction d'intensité du RS due aux erreurs magnétiques ; la seconde permet de mesurer les effets des erreurs magnétiques sur le faisceau. Nous dérivons pour l'ESRF les grandeurs maximales admises. Ensuite nous abordons la technologie des Eléments d'Insertion (EI). Les différents designs permettant de produire de la lumière polarisée linéairement et circulairement sont décrits. La majorité des EI utilisent la technologie des aimants permanents, le Néodyme-fer-bore est préféré au Samarium Cobalt car il offre une plus grande rémanence pour un coût moindre.

Le design de ces EI est effectué avec RADIA, la solution numérique traditionnellement utilisée à l'ESRF. Lors de l'assemblage de l'onduleur, on évalue sa performance en mesurant ses grandeurs caractéristiques (erreur de phase RMS et intégrale de champ) au moyen de bancs de mesure : le Fil tendu et la Bobine Tournante pour la mesure des intégrales de champ et le banc à Sonde de Hall pour la mesure locale. Nous concluons ce chapitre en exposant les techniques utilisées pour corriger les erreurs magnétiques dans un onduleur. Le shimming de multipoles permet de réduire l'intégrale tandis que le shimming de phase agit sur l'erreur de phase.

F.4 Chapitre 3: Design d'un CPMU

Nous présentons l'état de l'art des EI courtes périodes/fort champ et les motivations pour la construction d'un onduleur cryogénique. Ensuite nous décrivons le projet de CPMU de l'ESRF: il s'agit d'utiliser des aimants Néodyme-fer-bore refroidis à la température de l'azote liquide. Cela permet ainsi d'utiliser des aimants avec une rémanence jusqu'à 40% supérieure à celle des aimants utilisés conventionnellement dans un onduleur. La spécificité du CPMU de l'ESRF par rapport à celui de SPring-8 est d'être destiné à opérer en conditions réelles sur l'anneau de stockage, et non pas seulement en laboratoire. L'assemblage magnétique du CPMU est un onduleur Hybride, l'HYB 18, de 107 périodes et de 18 mm de période.

Le choix pour refroidir les aimants se porte sur une boucle fermée d'azote liquide à 80 K. Le champ maximum attendu est calculé grâce à un modèle magnétostatique RADIA ; il situe le champ crête à une température de 150 K. Cette température impose de calibrer l'échange thermique entre la boucle fermée (à 80 K) et l'onduleur (à 150 K), ceci est fait via un modèle thermique. Enfin, nous avons étudié l'impact sur l'erreur de phase RMS d'un gradient thermique le long des poutres.

F.5 Chapitre 4: Assemblage et correction de l'HYB18 à température ambiante

Nous détaillons ici la réalisation et la correction de l'HYB18 à température ambiante, selon la méthodologie de l'ESRF. On caractérise les défauts des aimants en mesurant leur intégrale puis on les apparie pour construire les poutres l'une après l'autre. Enfin on corrige le champ du HYB18 à température ambiante, au plus petit gap (6 mm). En l'occurrence, il a fallu effectuer un peu plus de 90 opérations sur les aimants et les pôles pour corriger les intégrales de champ et l'erreur de phase.

Cette méthode permet de ramener l'erreur de phase RMS à 4° et de corriger les intégrales dans la limite admissible à l'ESRF. Cette erreur de phase est toutefois un peu plus élevée que celle des onduleurs standards installés à l'ESRF (2° à 3°). Cette différence s'explique par l'asymétrie Nord/Sud élevée des aimants. Cette asymétrie génère de grands défauts d'angle qui sont difficiles à corriger. Néanmoins, cette valeur de 4° reste tout à fait acceptable au vu de l'utilisation attendue. En effet, il est prévu que les utilisateurs travaillent sur les premières harmoniques du spectre.

F.6 Chapitre 5: Performance de l'HYB18 à basse température

L'HYB18 a été corrigé à température ambiante selon la méthode ESRF. Pour valider ces corrections à basse température, il a été nécessaire de développer un banc de mesure magnétique sous vide. Ce banc intègre un fil tendu et une sonde de Hall pour permettre une mesure des intégrales de champ et du champ local. Ces bancs ont également été utilisés pour mesurer l'ouverture du gap à basse température et déterminer le profil de température le long des poutres de l'onduleur.

Nous abordons ensuite les mesures d'intégrales et de champ local à basse température. En accord avec le modèle RADIA, on observe une augmentation de l'intégrale à basse température. Cette augmentation est contenue entre 300 K et 150 K (20 Gcm) et devient importante à plus basse température (60 Gcm à 120K). Le maximum de champ est obtenu à 150 K. Enfin on note un accroissement de l'erreur de phase, directement relié à un gradient de température le long des poutres. Ce gradient thermique déforme le gap de l'onduleur et change les propriétés magnétiques des aimants.

F.7 Chapitre 6: Conclusion

En 2004, T. Hara a proposé un concept de CPMU constitué d'un onduleur à aimants permanents, utilisant des aimants $Nd_2Fe_{14}B$ refroidis autour de 150 K. Ce concept soulève deux problématiques majeures : Quelle peut être la performance magnétique d'un tel onduleur ? Est-il technologiquement possible de refroidir un onduleur de plusieurs mètres de long, sans introduire d'erreur dans le champ de l'onduleur ? Afin d'y répondre, un CPMU de 2 m de long et de 18 mm de période, l'HYB18 a été proposé à l'ESRF. Ce travail présente le design du CPMU, son assemblage et l'évaluation de la performance d'un tel outil.

Nous avons tout d'abord développé un modèle numérique RADIA afin de prédire la variation du champ crête et de l'intégrale de champ avec la température. Ceci nous a permis de déterminer la température optimale à laquelle opérer. L'onduleur hybride de 2 m de long et de 18 mm de période a été assemblé puis corrigé à température ambiante. Le HYB18 a ensuite été refroidi à 150 K au moyen d'une boucle fermée d'azote liquide. Nous avons créé un banc de mesure magnétique sous vide capable d'opérer à température cryogénique afin d'évaluer la performance de ce CPMU. Ce banc de mesure est unique car il permet de réaliser à la fois des mesures magnétiques de champ local et d'intégrale de champ. Enfin ces mesures furent comparées aux calculs du modèle RADIA.

Le banc de mesures sous vide développé à l'ESRF a permis de réaliser avec succès des mesures magnétiques de 120 K jusqu'à température ambiante. Le champ local valide le modèle magnétique, tout comme l'intégrale de champ. Ainsi, le champ crête du HYB18 atteint sa valeur maximale 30 K au dessus de la température à laquelle les aimants $Nd_2Fe_{14}B$ maximisent leur aimantation rémanente ; de plus, l'intégrale de champ des extrémités du CPMU augmente à une température inférieure à 150 K. Cela s'explique par la transition de réorientation du spin qui augmente la susceptibilité des aimants $Nd_2Fe_{14}B$. Ce phénomène est donc directement à l'origine de l'accroissement de l'intégrale de champ de l'onduleur et du différentiel de température entre le niveau de magnétisation rémanente maximale des aimants $Nd_2Fe_{14}B$ et le champ crête du HYB18. On observe également que le champ crête est quasiment constant entre 140 K et 180 K, tout comme dans le modèle RADIA. C'est en accord avec ce modèle que nous avons choisi d'opérer le HYB18 à une température cible de 150 K.

On observe, lorsque la température décroît, une augmentation de l'erreur de phase RMS. Celle-ci est faible entre 300 K et 150 K : ainsi on mesure 1° supplémentaire seulement d'erreur de phase RMS lorsque le HYB18 est refroidi à 150 K. Au dessous, cette augmentation devient exponentielle. Un tel accroissement de l'erreur de phase RMS prouve l'existence d'erreurs additionnelles dans l'onduleur à basse température. Grâce à un modèle fondé sur les modèles RADIA et thermique, nous avons pu déterminer que ces erreurs additionnelles sont toutes dues à une température non uniforme le long des poutres. Ces variations de température déforment le gap magnétique et changent les propriétés magnétiques des aimants. L'erreur de phase RMS totale revient donc à la somme quadratique de l'erreur de phase RMS résiduelle à température ambiante avec l'erreur de phase RMS induite par la variation de température. Au delà de 150 K, l'erreur de champ de l'onduleur due à la déformation du

gap, et la variation des propriétés des aimants se compensent, permettant un faible accroissement de l'erreur de phase RMS. A une température inférieure, les deux effets s'additionnent, créant une augmentation substantielle de l'erreur de phase RMS.

Le CPMU a été installé avec succès sur une section droite de l'ID6 de l'anneau de stockage de l'ESRF en Janvier 2008 [94]. Il s'agissait là du tout premier CPMU installé sur une source de rayonnement synchrotron. Sans le faisceau, la température est de 143 K. Au cours des premiers mois d'opération, on s'est interrogé sur la dépendance de la température de l'onduleur au mode de remplissage de l'anneau de stockage. Dans le pire des cas (16 paquets, 90 mA) la température moyenne atteint 180 K. ; pour un tel accroissement de température, on estime un flux thermique de 80 W, soit deux fois plus que la valeur attendue. D'autre part la distribution de température le long de l'onduleur indique un dépôt de chaleur uniforme tout au long de l'assemblage magnétique, qui pourrait s'expliquer par la création de modes électromagnétiques dans la chambre à vide de l'onduleur.

Des progrès on été faits depuis, avec la mise en place d'un onduleur sous vide non étuvé [69]. Il est aujourd'hui en opération sur la section droite ID15 de l'ESRF. Au redémarrage de la machine, une augmentation de la pression du vide a été observée lors de l'injection du premier faisceau. La pression était de l'ordre de 10^{-6} mbar pour un courant de 60 mA stocké dans la machine. Toutefois, le faisceau de photons a conditionné l'onduleur non étuvé, de telle manière que quelques jours plus tard, les utilisateurs installés sur la ligne de lumière ont utilisé le faisceau de photon produit.

Ce travail pionnier sur le CPMU effectué à l'ESRF a clairement prouvé l'accessibilité technologique d'un CPMU utilisant des aimants $Nd_2Fe_{14}B$ à forte rémanence ($B_r > 1.2$ T). Les résultats obtenus permettent de mettre en évidence les améliorations nécessaires pour obtenir un onduleur CPMU avec une faible erreur de phase (<2°). Ainsi, il faut d'abord construire un onduleur à faible erreur de phase RMS à température ambiante. Le développement d'aimants à faible erreur est alors d'un grand intérêt [88]. Ensuite, à température basse, il faut éviter tout gradient de température pour maintenir l'erreur de phase RMS, ce qui implique d'isoler thermiquement le CPMU. Le design des extrémités est donc fondamental pour éviter que le flux venant des doigts RF ne se propage dans l'assemblage magnétique.

En conclusion, nous pensons que le CPMU se développera massivement dans un future proche, en particulier sur les nombreuses sources de rayonnement synchrotron de taille moyenne (E< 3 GeV), telles que SOLEIL [95], DIAMOND, NSLS-II, ALBA, etc…. Un tel onduleur à courte période/fort champ ouvre la voie aux rayons X dans ces centres de recherche.